FINAL REPORT

Sediment Volume Search Sonar Development

SERDP Project MR-2545

MAY 2021

Daniel Brown
Shawn Johnson
Cale Brownstead
Penn State University - ARL

Joeseph Calantoni
Naval Research Laboratory

Gene Fabian
US Army Aberdeen Test Center

SERDP
DOD ▪ EPA ▪ DOE

REPORT DOCUMENTATION PAGE

Form Approved
OMB No. 0704-0188

1. REPORT DATE *(DD-MM-YYYY)*
20/05/2021

2. REPORT TYPE
SERDP Final Report

3. DATES COVERED *(From - To)*
2/5/2016 - 2/5/2021

4. TITLE AND SUBTITLE
Sediment Volume Search Sonar Development

5a. CONTRACT NUMBER
16-C-0006

5b. GRANT NUMBER

5c. PROGRAM ELEMENT NUMBER

6. AUTHOR(S)
Daniel Brown, Shawn Johnson and Cale Brownstead - Penn State University - ARL

Joeseph Calantoni - Naval Research Laboratory

Gene Fabian - US Army Aberdeen Test Center

5d. PROJECT NUMBER
MR-2545

5e. TASK NUMBER

5f. WORK UNIT NUMBER

7. PERFORMING ORGANIZATION NAME(S) AND ADDRESS(ES)
Penn State University - Applied Research Laboratory
North Atherton Street, P.O. Box 30
State College, PA 16804

8. PERFORMING ORGANIZATION REPORT NUMBER
MR-2545

9. SPONSORING/MONITORING AGENCY NAME(S) AND ADDRESS(ES)
Strategic Environmental Research and Development Program (SERDP)
4800 Mark Center Drive, Suite 16F16
Alexandria, VA 22350-3605

10. SPONSOR/MONITOR'S ACRONYM(S)
SERDP

11. SPONSOR/MONITOR'S REPORT NUMBER(S)
MR-2545

12. DISTRIBUTION/AVAILABILITY STATEMENT
DISTRIBUTION STATEMENT A. Approved for public release: distribution unlimited.

13. SUPPLEMENTARY NOTES

14. ABSTRACT
Within the domain of munitions response, the problem of conducting detailed acoustic surveys in very shallow water is particularly difficult, owing to sensor deployment challenges and multi-path interference in these environments. The Sediment Volume Search Sonar (SVSS) improves buried unexploded ordnance (UXO) detection and classification performance through design, fabrication, and demonstration of a sonar system that is deployed from a shallow-draft surface vessel. The SVSS sensor produces a novel form of three-dimensional synthetic aperture sonar (SAS) imagery of both surficial and buried UXO across a range of environments. The platform and sensor are designed to operate in less than 5m water depth. These very shallow water areas are particularly important to address because of the increased likelihood of human interaction with ordnance.

15. SUBJECT TERMS
underwater munitions, unexploded ordnance, acoustic scattering, acoustic imaging, synthetic aperture sonar, sonar modeling

16. SECURITY CLASSIFICATION OF: a. REPORT	b. ABSTRACT	c. THIS PAGE	17. LIMITATION OF ABSTRACT	18. NUMBER OF PAGES	19a. NAME OF RESPONSIBLE PERSON
UNCLASS	UNCLASS	UNCLASS	UNCLASS	165	Daniel Brown
					19b. TELEPHONE NUMBER *(Include area code)* 814-865-1193

Standard Form 298 (Rev. 8/98)
Prescribed by ANSI Std. Z39.18

Table of Contents

1 Executive Summary **2**
- 1.1 Introduction . . . 2
- 1.2 Objectives . . . 2
- 1.3 Technical Approach . . . 3
- 1.4 Results and Discussion . . . 9
- 1.5 Implications for Future Research and Benefits . . . 11

2 Objective **13**

3 Background **14**

4 Materials and Methods **16**
- 4.1 Model Development . . . 16
  - 4.1.1 Phase 1 Model Development . . . 17
  - 4.1.2 Phase 2 Model Development . . . 25
- 4.2 Hardware Development . . . 29
  - 4.2.1 SVSS Hardware Configuration . . . 31
  - 4.2.2 Projector Development . . . 35
- 4.3 Signal and Image Processing Development . . . 45
  - 4.3.1 Image Reconstruction Algorithm Development . . . 45
  - 4.3.2 Image Processing Algorithm Development . . . 50
- 4.4 Test Site Development . . . 58
  - 4.4.1 Foster Joseph Sayers Reservoir . . . 60
  - 4.4.2 Aberdeen Test Center . . . 66

5 Results and Discussion **73**
- 5.1 Field Testing Results . . . 73
  - 5.1.1 In Situ Sensor Monitoring . . . 73
  - 5.1.2 Target Localization Accuracy . . . 75
  - 5.1.3 Foster Joseph Sayers Reservoir . . . 76
  - 5.1.4 Aberdeen Test Center - Littoral Warfare Environment . . . 83
  - 5.1.5 Aberdeen Test Center - Bush River . . . 88
  - 5.1.6 Target Detection . . . 94
- 5.2 Model-Data Comparison Results . . . 96
  - 5.2.1 Sayers 2-Layer Model . . . 96
  - 5.2.2 Sayers Seasonal Variation . . . 101
  - 5.2.3 Bush River . . . 104
  - 5.2.4 Discussion . . . 106

6 Conclusions and Implications for Future Research **108**

A Additional Target Details **111**
- A.1 Foster Joseph Sayers Reservoir Target Details . . . 111

A.2 Aberdeen Test Center Target Details 119

B Sensor Characterization & Calibration **122**
B.1 Sensor Noise Floor Characterization 122
B.2 Prototype Projector Calibration 123
B.3 Broadband Projector Calibration 125
B.4 Hydrophone Calibration 127

C Specular Component Modeling **130**

D Bubble Models **131**
D.1 Individual Bubble Response 131
D.1.1 ODE Formulation 131
D.1.2 Validation of the Single Bubble Response 132
D.1.3 Example Bubble Response to LFM Pulses 135
D.2 Ensemble Bubble Response 137

E List of Scientific/Technical Publications **141**

List of Figures

1 ARL/PSU's Point-based Sonar Scattering Model (a) was expanded and utilized to generate representative acoustic time series for various sediment types, and combined with APL-UW's TIER model for various target shapes. The combination of these physics-based acoustic models was used to assess the feasibility of the SVSS hardware design, and signal and image processing algorithms (b) for detection of buried UXO. 4

2 The Sound Hunter test platform is a nine-meter pontoon boat (a). The projector and receive array are shown here mounted in the forward portion of the boat. The sonar array consists of five projectors and 80 receive channels (b). 5

3 Acoustic data were collected at Foster Joseph Sayers Reservoir with the SVSS and processed with ASASIN. A slice through the 3D output at a depth of 11 cm (center) shows two solid aluminum cylinders (top) emplaced during winter draw-down, as well as two rock clutter objects (bottom) that were recovered during a subsequent draw-down. 7

4 85 objects including munitions, science targets, and clutter were selected for installation in the LWE at the Aberdeen Test Center (a). Ground truth locations were accurately measured with an RTK-GPS survey (b). 8

5 Cross-track MIPs are shown for a pair of tracks that surveyed a common set of targets in the deep field at the reservoir. It appears that surveys conducted during colder periods lead to reduced sediment scattering strength and improved target detectability. 10

6 PoSSM was configured to model the returns from the layered environment found at Sayers using the schematic provided in (a). The ensemble-averaged A-Scan over a 5 m section of track from field data (blue) and simulated data with Hamilton (red) and updated (yellow) properties is provided in (b). . . . 10

7 The SVSS data collected in the Bush River was manually screened to identify clutter objects. Depth slices for three example contacts are shown. 11

8 Flowchart of the primary constituents of the ARL/PSU Point-based Sonar Scattering Model. 18

9 Diffuse interface and volume scattering levels are shown for very fine silt (a) and medium sand (b) for a single ping, between a single transmit-receive pair (filled diamond and circle) at the corners of a sonar array. The level shown at each point includes the source level and effects of transmit and receive beam patterns, model-based scattering strength, attenuation, spreading loss, and, for volume scatterers, the two-way transmission through the interface. 19

10 Simulated received pressure time series corresponding to Figure 9. The transmitted signal was a 15 kHz–25 kHz 3 ms LFM chirp. For the very fine silt simulation, the diffuse volume scattering component dominates the combined signal, whereas the diffuse interface scattering component dominates for medium sand. 20

11 The multipath ray paths are shown for selected first and second order multipath when specular scattering is considered (a). Each ray is designated by a name that describes the order of boundary interactions [1]. The regions of specular interference are determined by the depth of the sensor and the water depth. These regions are indicated by gray boxes within the sediment that are labeled with the ray path names. (N.B. the specific depth where the specular interference appears in the reconstructed image will vary slightly from the depth indicated here due to the difference in the sediment sound speed. Use of the method of images in PoSSM (b) can simulate the presence of multipath in SVSS data. The image source and receiver are shown above the air-water interface for the *"bs"* and *"sb"* multipath rays. 21
12 Two example images of combined model results showing a 11.00 by 5.50 cm solid aluminum cylinder at 0 m cross-track and 2 m along-track, buried at 1.00 m in very fine silt (a) and medium sand (b). The interface scattering strength in the medium sand example is approximately 15 dB stronger, shifting the dynamic range of the image and revealing a noticeable multipath return at 3 m depth. 24
13 Two additional example images of combined model results showing a single small solid aluminum cylinder at the water/sediment interface (a) and a column of six buried large solid aluminum cylinders adjacent to two columns of small solid aluminum cylinders (b). The sediment in both simulations was very fine silt. The water/sediment interface can obscure flush buried targets; however, buried targets remain separable for certain target types and spacings (e.g., 0.25 cm). 25
14 Comparison between flat-interface and coherent reflection coefficients at 20 kHz for medium sand and very fine silt [2]. The typical SVSS field of view is indicated by the shaded region. The coherent component levels using 1.000 cm RMS roughness used during Phase 1 are shown as gray lines and bound the updated calculations for medium sand (blue) and very fine silt (red), which have RMS values of 1.365 cm and 0.465 cm, respectively. Note that rough-interface scattering significantly reduces the coherent component. 27
15 PoSSM models (in Figure 8) are implemented in both MATLAB and CUDA as a .dll. The user has the ability to select which models will be calculated on the CPU versus GPU, which is often beneficial when implementing a new sonar setup or acoustic component (a). The user can then select a mode that minimizes transfer of data between CPU and GPU to realize a significant speedup (b). 29
16 The Sound Hunter test platform is a nine-meter pontoon boat. The projector and receive array are shown here mounted in the forward portion of the boat. These components are mounted in a rectangular frame that is lowered into the water during testing. 30
17 A schematic diagram and photo of the Sound Hunter array configuration are shown in (a) and (b), respectively. The array consists of 80 receive channels, which are labeled R, and five projectors, which are labeled TX_X. 32

18 This diagram shows the major onboard and offboard components of the SVSS system. The majority of the equipment is COTS (green), while some specialized electronics and the wet sensors (blue) are custom designed and fabricated by ARL/PSU. 33
19 A solid model of an eight-channel SVSS hydrophone module is shown in (a). The piezoceramic elements are mounted on a mass-damping-compliance-damping isolator stack to increase the directivity of the sensor (b). 34
20 An example screen shot of the SVSS HUD taken during the Aberdeen Test Center Bush River testing. Various sonar and platform status and controls are provided, in addition to various tools and displays to help ensure precise maneuvering of the platform and complete survey coverage. 35
21 Drawing showing the cross section of the prototype projector array, mount, and housing. One of the tonpilz elements is called out as item 6, and the layered mount that provides element isolation is called out as item 3. 37
22 The fabricated prototype projectors were characterized in the ARL/PSU anechoic test facility. This figure shows one device's directivity pattern measured at 20 kHz. A full characterization can be found in Appendix B. 38
23 Projector transmit voltage response for each of the six 4x4 array units. These projectors are well matched over the 10 kHz–40 kHz frequency band. 39
24 Replicas are shown for a pair of LFM signals each spanning a 15 kHz bandwidth (a). The resonant response of the projector at 20 kHz significantly extends the length of the 12 kHz–27 kHz waveform, which results in a broader auto ambiguity function (b). 40
25 The impact of the ambiguity function width on depth resolution is seen in this pair of cross-track maximum intensity projections. The width for the signal used in the upper image is significantly longer in time, resulting in a "smearing" of the image along the depth direction. The red boxes indicate a pair of common targets. The MIP formation process is described in Section 4.3.2. 41
26 Comparison of the TVR of simulated tonpilz elements incorporating three candidate materials. The frequency axis is normalized by $f_0 = 7.5\,\text{kHz}$ . . . 42
27 A three-dimensional model (a) of the broadband projector shows the interior and exterior geometry of the device. A two-dimensional cross section (b) is labeled to show the individual projector components. 43
28 The broadband projector TVRs are compared to the finite element analysis (FEA) predicted TVR. 44
29 Broadband beam patterns are shown (a) for the broadband projector. The prototype and broadband projector's ambiguity functions are compared in (b). The improved bandwidth and lower mechanical Q_m result in a projected waveform that will substantially improve sensor resolution and reduce sidelobe level. 45
30 The field projected by a transmitter at $\bar{\chi}_T$ is scattered from an interface point at $\bar{\chi}_S$ and is received at $\bar{\chi}_R$. 46

31 A linear twenty channel receive array with three transmitters is shown above a sediment/water interface. The notional field of view for each transmitter is shown by a gray triangle. The field of view of receiver channel eight is shown by a green triangle. Only those pixels that are within the shaded region given by the logical AND of a transmitter field of view and a receiver field of view are impacted when backprojecting any single signal. 47
32 Three targets, S_P07_T2D1, S_P06_T3D1, and S_P05_T1D2, are shown in a three-dimensional animation. The animation is only supported when the document is viewed using an Adobe Acrobat reader. 51
33 A pair of two-dimensional data representations is used to visualize the three-dimensional data shown in Figure (a). Figure (b) shows slices through the three-dimensional data, which are taken at discrete positions along one of the three principal axes. Figure (c) shows MIPs along the principal axes. The along-track slice and MIP are shown in yellow. The cross-track slice and MIP are shown in light blue. The depth slice and MIP are shown in dark blue. . . 52
34 A slice is shown passing through the two cylinders seen in Figure 32. The cylinders as well as a pair of rocks recovered from the lakebed are shown. . . 53
35 A cross-track MIP is shown for data collected in the Foster Joseph Sayers Reservoir. The data is shown on a 40 dB logarithmic scale that is referenced to the peak value. A schematic diagram showing the water and layered sediment interface along with six targets is shown below the MIP. A table describing the details of these targets is also included. 54
36 Cross-track and down MIPs are shown for data collected in the Foster Joseph Sayers Reservoir. The data are shown on a 40 dB logarithmic scale that is referenced to the peak value. 55
37 The dynamic range of the data shown in Figure 36 has been compressed. This results in improved target detectability. 56
38 Illustration and sample data showing the effect of the split window normalizer in one dimension (a), and an illustration showing the SWN concept extended to three dimensions. 58
39 Ground truth on target positions is established through use of an RTK-GPS survey system. An example survey setup is shown for the ATC experiment, where an RTK base station was established adjacent to the target field (a) and aN RTK-based survey of each target (b) was conducted. 60
40 The reservoir level is varied throughout the year. In the early December timeframe the lake is lowered five feet. This is followed by a second drop in level of fifteen additional feet in late February. During the draw-down period the test sites are exposed and the target field was deployed. 61
41 The Foster Joseph Sayers Reservoir is located near Howard, PA. Two prepared fields, with water depths of 1.5 m–4.0 m at typical summer pool fill, were established within the test area identified above. 61

42 The two prepared fields are indicated on a bathymetric map of the lake. The water depth for the "shallow" field (left) is 1.5 m–2.0 m and the "deep" field (right) is 3.0 m–4.0 m when the reservoir reaches the summer pool level. Note an old railroad bed and paved road (above) separate the test area from the main part of the reservoir. 62
43 The shallow site and deep site target layouts after the 2019 field installation. Note that the orientation of the layout is provided in the lower left corner of each figure. The shallow site has 46 target positions (P01-P46), and the deep site has 35 positions (P01-P35). The target type identifier is shown below each position, and the reference can be found in Table 4. Target positions specified with a target type "xx" are mixed combinations of targets, which are specified in Table 5. 63
44 The targets described in Table 6 were installed into the LWE at the locations indicated by the white circles in this figure. During the installation of these targets the LWE water level was lowered to the draw-down waterline, which is shown by the northern line of blue squares. During testing the water level was raised to the filled waterline, which is shown by the southern line of blue squares. 68
45 A total of 86 positions including munitions, science targets, and clutter were surveyed in a site prepared in the LWE. The collected objects are shown in (a) and the target field layout prior to target burial is shown in (b). 69
46 A total of 86 positions were prepared during the test field installation. The target type at each position is indicated with T##, where Table 6 associates the target identifier with the target name. The notional depth at each position is given by D#, where the number indicates the depth in 10 cm steps. The cinder blocks (T05) were placed with either cores or a flat side oriented upward as indicated by the labels at the top of this figure. 69
47 A GPS survey of the exposed LWE sediment bed was used to create a bathymetric chart of the test area. The water depth shown here is calculated for the acoustic survey conducted 2-5 March 2020. The red 3.55 m isoline presents the waterline during installation draw-down. Typically, the LWE is filled to approximately 1.25 m and was overfilled for this test. 71
48 A series of imaging tracks were collected in the Bush River adjacent to the ATC test facility. 72
49 During data collection a number of data products are produced to verify proper sensor performance. The hydrophone and projector health are assessed with the plot shown in (a). This plot shows the RMS level on each channel of the hydrophone array for transmission with the left (TX-L) and left-center (TX-LC) projectors. The sensor speed, flight repetition interval, and DPC advance are reviewed using the plot shown in (b). Finally, a B-Scan (c) is generated for the track to assess sediment penetration. 74

50 A MIP of the cinder block located at P71 is provided in (a). A binary image (b) is created by applying a threshold at 20% of the cinder block peak level. The centroid of this green region (blue plus) is compared to the ground truth position (red x). The location error calculated across all 13 cinder block opportunities is shown in (c). 76
51 B-Scans are shown for the shallow (a) and deep (b) fields at the Foster Joseph Sayers Reservoir. Note that the horizontal-axis and vertical-axis scales are not equal. 77
52 Cross-track MIPs are shown for a pair of tracks that surveyed a common set of targets in the deep field at the reservoir. It appears that surveys conducted during colder periods lead to reduced sediment scattering strength and improved target detectability. 78
53 A selection of MIPs are presented for an image collected in the shallow field where proud pipes are present. This area spans P45, P44, P43, P15, P42 from left to right. Figure (a) is shown on a 60 dB logarithmic scale. Figures (b) and (c) are shown on a dynamic range compressed scale. Note that SP46E does not contain a target but is an empty and refilled hole. 80
54 A selection of MIPs are presented for an image collected in the shallow field where buried munitions are present. This area spans P25-P20 from left to right. Figure (a) is shown on a 60 dB logarithmic scale. Figures (b) and (c) are shown on a dynamic range compressed scale. 81
55 A selection of MIPs are presented for an image collected in the deep field where proud and buried objects are present. This area spans P12-P07 from left to right. Figure (a) is shown on a 60 dB logarithmic scale. Figures (b) and (c) are shown on a dynamic range compressed scale. 82
56 A depth slice is presented for the data cube shown in Figure 55. The pair of flush-buried shot puts, which are not visually apparent in the MIP representation, are clearly visible near 2 m along-track in this image representation. . 83
57 The cross-track MIP for P80-P84 is shown on a 60 dB log scale. This sequence of positions contains five proud objects. The ground truth along-track positions of the objects are indicated by the colored dots at the top of the figure. The object length and diameter are provided in the legend for each cylindrical target. 84
58 The cross-track MIP is shown for P03-P08 on a 60 dB log scale. This sequence of positions contains six 155 mm Howitzer shells buried in depths ranging from 10 cm–60 cm. The ground-truth along-track position of the shells are indicated by the colored dots at the top of the figure and the surveyed burial depth is shown in the legend. 85
59 A survey track was collected transiting from deep to shallow water in the LWE. At 29 m along-track there is an abrupt change in the sub-bottom scattering level observed. The dewatering draw-down level is shown as a red dashed line. 85

60 The penetration depth was estimated from the cross-track MIPs for the imaging tracks collected in the LWE. A pair of red lines are used to show the upper and lower sub-bottom margins in the MIP shown in (a). The penetration depth for this track is shown in (b). A map of the LWE penetration depth is shown in (c), where the target positions (red dots) and installation draw-down line (red diamonds) are shown. 87
61 A sub-bottom profile was collected in the Bush River over a 340 m long track. These B-Scan images show a layered riverbed where acoustic penetration frequently exceeded 1 m. 89
62 This animation shows a three-dimensional image segment collected in the Bush River. The outer static surfaces show the MIPs across the respective dimensions. When played, the animation shows the individual layers making up the full 3D image. The object in Figure 63 can be seen as the slice passes through 3 m depth. This animation can only be played if the report is viewed using Adobe Acrobat. 90
63 This image slice was taken from approximately 3 m below the sediment/water interface in the Bush River. A clutter object is clearly seen at 11.5 m along-track. 91
64 Selected clutter objects that were manually labeled in the Bush River. 92
65 Selected clutter objects that were manually labeled in the Bush River. 93
66 Performance of the detection algorithm for each data collection for (a) proud man-made targets and (b) buried man-made targets, along with the distribution of visual human assessment ratings. Above each bar are the numbers of targets detected vice opportunities, and in brackets the range of targets deemed detectable based on visual human assessment. 95
67 Left: Satellite view of target field from Google Earth. Tracks are indicated by green lines. Right: B-Scan plot of data on a track from November 8, 2019. The 5 m section of data used for the data-model comparison is indicated by the red box. 97
68 Schematic indicating the different wave paths modeled from the interaction with the mud and clay sediment layers at Sayers. 98
69 Left: Composite levels for a single ping, showing diffuse interface and volume scattering for a mud layer above a clay basement. Right: Ensemble-averaged A-Scan over the 5 m track for each model component and the total simulation response for the updated properties model. 99
70 Ensemble-averaged A-Scan over a 5 m section of track from field data (blue) and simulated data with Hamilton (red) and updated (yellow) properties. . . 99
71 B-Scan of 5 m of field (above) and simulated (below) data. 100
72 Mean A-Scan data over 5 m of collocated track for several 2019 tests. 102
73 Mean seasonal A-Scans shown in Figure 72 and peak levels from PoSSM 5 cm thick bubble layer and 5 m track simulations (◯) with air volume fractions chosen to match the field data peaks. Also shown is the expected reflected level from the clay layer (□) based on the simulated bubble layer's 2-way transmission loss subtracted from the November data's level. The symbols are color-coded to correspond to their respective field measurements. 103

74 B-Scan from Bush River test data, track 2020 0305 183020. The signature near 73 m is consistent with the presence of entrapped gas. 105
75 Average A-Scan of 3 m (66 pings) along-track in areas with (red) and without (blue) the hypothesized entrapped gas layer from field data shown in Figure 74. Also shown is the average A-Scan from a simulated bubble layer containing 0.63% air volume fraction over 5 cm. 105
76 Foster Joseph Sayers Reservoir shallow field targets. 112
77 Foster Joseph Sayers Reservoir shallow field targets. 113
78 Foster Joseph Sayers Reservoir shallow field targets. 114
79 Foster Joseph Sayers Reservoir shallow field targets. 115
80 Foster Joseph Sayers Reservoir deep field targets. 116
81 Foster Joseph Sayers Reservoir deep field targets. 117
82 Foster Joseph Sayers Reservoir deep field targets. 118
83 Photos of the eight munitions types installed in the LWE. 119
84 Photos of the nine science and clutter types installed in the LWE. 120
85 The SVSS system's noise floor was characterized for a number of operating states. As platform speed is increased, noise from the motor increases at low frequency. Note that the purple "Speed Idle" curve is obscured by the "Signal Zero" curve in this figure. 122
86 The prototype projector TVRs are well matched over the 10 kHz–45 kHz band. 123
87 Broadband beam patterns were captured for the five prototype projectors over 10 kHz–50 kHz in the ARL/PSU ATF. 124
88 The broadband projector TVRs are well matched over the 10 kHz–50 kHz band. 125
89 Broadband beam patterns were captured for the broadband projectors over 10 kHz–50 kHz in the ARL/PSU ATF. 126
90 The FFVS was measured for all eighty receive channels in the ARL/PSU ATF. 128
91 Horizontal (a) and vertical (b) beam patterns are measured at 27.5 kHz for all eighty receive channels. 129
92 Broadband beam patterns were measured for all eighty receive channels in the ARL/PSU ATF. This figure provides those patterns for the first eight channels in the array. 129
93 Left: Normalized displacement versus time for the sample bubble described by the parameters in Table 12 with initial conditions $y(0) = y_0$ and $y'(0) = 0$. Right: Response of a bubble with resonance of 27.5 kHz insonified by a continuous 20 kHz sinusoid when starting from rest. 133
94 Target strength versus frequency for a 1 mm bubble in sediment with properties described by Table 13. Our model results using the SCS equation and the numerical ODE solution evaluated for single frequency sinusoid insonification matches Figure 14.8 from [3]. 135
95 Spectrogram of the pressure response of the 25 kHz resonant bubble in sediment for insonification by the 1 ms (left) and 0.242 ms (right) LFM pulses. . 136
96 Bubble distribution for a^{-4} that results in 0.3% air by volume for a 0.7 m^3 volume of bubbles. Red squares indicate those bubbles with resonant frequencies near the frequencies of interest (for our 20 kHz–35 kHz LFM) and are selected for use in our simulations. 138

97 Bubble transmission loss at 0° incidence for an ensemble of 30 kHz resonant bubbles ($a = 0.11$ mm) with a bubble density of 4 bubbles/cm^2. 139
98 Bubble transmission loss at 0° incidence for the bubble ensemble shown in Figure 96. 140

List of Tables

1 National Instruments components utilized in the DAQ subsystem. 32
2 Summary of the relevant metrics derived from finite element model results of a single element tonpilz transducer with three different active materials used as the motor section. The number of ceramic rings in the tonpilz element are specified and k_{eff} is the effective electromechanical coupling coefficient. 42
3 ASASIN generates the Science data product, which is an HDF5 file containing processed sonar imagery as well as information about the data collection and signal processing algorithms. The output stored in /Data/ has dimensions MxNxL where M is along-track, N is cross-track, and L is depth. The image is formed using P sequential transmissions (pings) of the sonar system. The version number in the final column indicates the science file version where each dataset was added to the format. 49
4 A prepared field with 78 objects, consisting of a range of clutter, science targets, and ordnance, at a variety of burial depths, was installed in a pair of sites located at the Foster Joseph Sayers Reservoir. The notional target positions are provided in Figure 43. 64
5 Several positions in the shallow and deep fields have "mixed" target types. . 65
6 A prepared field with 85 objects, consisting of a range of clutter objects, science targets, and ordnance, at a variety of burial depths, was installed in the southeast portion of the LWE. The notional target positions are provided in Figure 46. 70
7 Properties used for PoSSM simulations of the deep field repeat track at Sayers. 97
8 Field test date, water temperature (T_{water}), difference in recorded field data level from clay interface in November (ΔL_{clay}), and the simulation-derived estimated volume of air (V_{air}) and 2-way attenuation ($2 * T_I$) through the bubble layer. Plot and symbol color is also noted. 104
9 Foster Joseph Sayers Reservoir shallow field target information. 111
10 Foster Joseph Sayers Reservoir deep field target information. 111
11 In the LWE test site, 86 positions were prepared with a range of objects. . . 121
12 Parameters for a methane bubble in fresh water with a resonance near 27.5 kHz. These parameters are used to generate Figure 93. 133
13 Parameters for a 1 mm radius methane bubble in sediment that are used to generate Figure 94. Sediment properties are representative of soft mud. . . . 134
14 Parameters for a methane bubble with a 25 kHz resonance in a soft mud sediment. These parameters are used to generate Figure 95. 136

List of Acronyms

AAF	Auto-ambiguity Function
ADC	Analog to Digital Converter
APL-UW	Applied Physics Laboratory at the University of Washington
ARL/PSU	Applied Research Laboratory at the Pennsylvania State University
ASASIN	Advanced Synthetic Aperture Sonar Imaging Engine
ATC	Aberdeen Test Center
ATF	Anechoic Test Facility
BOSS	Buried Object Scanning Sonar
CMRE	Centre for Maritime Research and Experimentation
COTS	Commercial Off the Shelf
CUDA	Compute Unified Device Architecture
DAC	Digital to Analog Converter
DAQ	Data Acquisition
DRC	Dynamic Range Compression
FCC	Federal Communications Commission
FFVS	Free Field Voltage Sensitivity
GPS	Global Positioning System
GPU	Graphics Processing Unit
HDF5	Hierarchical Data Format version 5
HUD	Heads Up Display
ITC	International Transducer Corporation
LFM	Linearly Frequency Modulated
LOA	Letter of Authorization
LWE	Littoral Warfare Environment
MIP	Maximum Intensity Projection
NAS	Network Attached Storage
NATO	North Atlantic Treaty Organization
NI	National Instruments
NRL-SSC	Naval Research Laboratory - Stennis Space Center
ODE	Ordinary Differential Equation
OPUS	Online Positioning User Service
PADCNR	Pennsylvania Department of Conservation and Natural Resources
PADEP	Pennsylvania Department of Environmental Protection
PFBC	Pennsylvania Fish and Boat Commission
PoSSM	Point-based Sonar Scattering Model
RAS	Real Aperture Sonar
RMS	Root Mean Square
RTK	Real Time Kinematic
SAS	Synthetic Aperture Sonar
SCS	Scattering Cross Section
SEDA-COG	Susquehanna Economic Development Association – Council of Governments

SVSS	Sediment Volume Search Sonar
SWN	Split Window Normalizer
TIER	Target in the Environment Response
TMO	Tone Mapping Operator
TVR	Transmit Voltage Response
USACE	US Army Corps of Engineers
USDEP	US Department of Environmental Protection
UTC	Coordinated Universal Time
UUV	Unmanned Underwater Vehicle
UXO	Unexploded Ordnance
VRS	Virtual Reference Station

Keywords

underwater munitions, unexploded ordnance, acoustic scattering, acoustic imaging, synthetic aperture sonar, sonar modeling

Acknowledgements

This research was supported in part by the U.S. Department of Defense, through the Strategic Environmental Research and Development Program (SERDP). The SERDP support was provided under the munitions response portfolio of Dr. Herbert Nelson and Dr. David Bradley. This material is based upon work supported by the Humphreys Engineer Center Support Activity under Contract No. W912HQ-16-C-0006. Any opinions, findings and conclusions or recommendations expressed in this material are those of the authors and do not necessarily reflect the views of the Humphreys Engineer Center Support Activity.

The authors were supported by numerous collaborators at ARL/PSU. First, we would like to thank Zack Lowe for designing, implementing, and operating the SVSS data acquisition system. We would also like to thank Isaac Gerg and Steve Wagner for their efforts on the ASASIN beamformer and Norm Foster and Matthew Cotter for supporting PoSSM development. Jason Philtron supported the extensive model-data comparison and bubble analysis presented in this report. The design of the projectors described in Section 4.2.2.1 was supported by Thomas Montgomery. The design of the broadband projector described in Section 4.2.2.2 was supported by Scott Brumbaugh, Douglas Markley, and Richard Meyer. The fabrication of the hydrophones and projectors used by the SVSS was supported by Brian Tussey, William Thomas, Ryan Smith, Eric Harrold, Matt Sherman, Jessica Peters, Anthony Roselli, Kurt Rheam, and Greg Granville. Finally, the development of the textured ceramic used in the broadband projectors was supported by Mark Fanton, Ed Oslosky, Brian Weiland, and Rick Gamble.

The authors would also like to thank our external collaborators as well. The application of the TIER model to simulation of the SVSS by Aubrey España and Steve Kargl (APL-UW) was critical to the Phase 1 modeling and simulation results. At NRL-SSC, Ed Braithwaite and Joe Calantoni supported characterization of the sediments collected at the Foster Joseph Sayers Reservoir. At the NATO CMRE, David Williams adapted and applied the Mondrian detector to the SVSS data.

Abstract

Within the domain of munitions response, the problem of conducting detailed acoustic surveys in very shallow water is particularly difficult, owing to sensor deployment challenges and multipath interference in these environments. The Sediment Volume Search Sonar (SVSS) improves buried unexploded ordnance (UXO) detection and classification performance through design, fabrication, and demonstration of a sonar system that is deployed from a shallow-draft surface vessel. The SVSS sensor produces a novel form of three-dimensional synthetic aperture sonar (SAS) imagery of both surficial and buried UXO across a range of environments. The platform and sensor are designed to operate in less than 5 m water depth. These very shallow water areas are particularly important to address because of the increased likelihood of human interaction with ordnance.

The sensor's hardware design is based on an acoustic modeling and simulation effort. The simulation effort was accomplished by combining The Applied Research Laboratory at the Pennsylvania State University's (ARL/PSU) point based sonar scattering model with the Applied Physics Laboratory at the University of Washington's (APL-UW) target in the environment response model. Using this integrated toolset, parameters of the sensor/environment/target space were modified to explore the expected operating conditions, and to adapt existing backprojection image reconstruction algorithms used to create three-dimensional acoustic imagery.

These model and simulation efforts informed both the sensor and signal processing design and resulted in the development of a prototype SVSS system. The system was deployed from an ARL/PSU shallow-draft research platform and tested at two trial sites: the Foster Joseph Sayers Reservoir near Howard, PA and the Littoral Warfare Environment (LWE) at the Aberdeen Test Center (ATC) in MD. Both sites were prepared with a wide range of surficial and buried man-made objects. In total, over 150 objects were emplaced, which varied in size from small shell casings to 1 m long cylinders. The geolocation of object positions was recorded with high precision, such that acoustically-detected objects could be referenced to ground truth demonstrating a localization errors less than 10 cm. Field testing conducted in the Bush River, adjacent to the ATC, demonstrated sediment penetration depths up to 3 m and imagery contained indications of likely man-made clutter from historical activity in the area.

One of the main remaining challenges to reliable detection is understanding the environmental effects that influence object detection capability. For example, a strong, seasonally-dependent acoustic response from the upper layer of sediment at the Foster Joseph Sayers Reservoir test site was shown to mask the initial acoustic response from objects within the same sediment region. Note, however, that the late-time acoustic response was still visible in imagery. Model-data comparison suggests that the strong, seasonal acoustic response is likely due to entrapped gas. During testing in the Bush River, localized regions of high-reflective seafloor were observed that occluded the sediment below, again indicating the presence of entrapped gas.

The SVSS system developed under this effort has demonstrated a prototype sensor deployed from a surface craft. This provides a means for the detection and localization of ordnance at SERDP-designated test sites. The system will fill the need for a very shallow water detection system that is currently unmet.

1 Executive Summary

1.1 Introduction

The remediation of UXO is a current environmental problem facing the United States Department of Defense. In response to this challenge, SERDP has held a series of workshops in 2007, 2013, 2014, and 2018 to discuss the underwater munitions remediation problem [4–7]. Ordnance can be found in a number of aquatic environments spanning freshwater to marine areas, and hydrodynamic processes can lead to ordnance burial [6]. Across these sites there is an extremely wide range of potential munitions. Ordnance may be as small as individual rounds whose largest dimension is greater than 7.5 cm, up to bombs that may exceed 1 m in length [8,9]. The ordnance may experience significant biofouling and corrosion after remaining in place for several decades. Finally, man-made clutter is commonly found in near-shore UXO surveys. The wide variability of the environment, range of targets sizes, variability of the target state, and presence of clutter presents a highly challenging problem for a detailed survey sensor.

Development of acoustic sensors for the detection of buried ordnance using downward-looking sonar systems is addressed in prior [10–15] and current [16] research. One advantage of the sonar sensing modality (over electromagnetic modalities) is that acoustic imaging offers the promise of higher potential area coverage rates and better localization. Within the domain of munitions response, the problem of conducting detailed acoustic surveys in very shallow water is particularly difficult, owing to sensor deployment challenges and multipath interference in these environments.

The Sediment Volume Search Sonar (SVSS) improves buried unexploded ordnance (UXO) detection and classification performance through design, fabrication, and demonstration of a sonar system that is deployed from a shallow-draft surface vessel. The SVSS sensor produces a novel form of three-dimensional synthetic aperture sonar (SAS) imagery of both surficial and buried UXO across a range of environments. The platform and sensor are designed to operate in less than 5 m water depth. These very shallow water areas are particularly important to address because of the increased likelihood of human interaction with ordnance.

1.2 Objectives

The Sediment Volume Search Sonar program was proposed in response to the Munitions Response Statement of Need MRSON-15-01 for the development of a detailed survey sensor for acoustic detection and localization of surficial and buried unexploded ordnance. The objective of the SVSS program is to improve surficial and buried ordnance detection and classification performance over that available with existing sonar systems by addressing the current gap in technology for detailed survey in shallow water depths. This gap exists because currently available systems are not well suited to shallow-water operation due to the absence of suitable platforms to host these sensors, and the challenges of multipath interference. The SVSS program's objective is achieved through simulation, design, fabrication, and demonstration of a sonar system that is deployed from a shallow-draft surface vessel and is capable of producing three-dimensional volumetric SAS imagery across a range of environments including in water depths as shallow as 1 m–2 m. Particular attention is paid to utilizing commercial off-the-shelf (COTS) hardware where possible to reduce system cost. In addition to the fabrication of the sonar system, the necessary image reconstruction algorithms and processing software are developed for the generation of three-dimensional volumetric SAS imagery. Techniques are explored for visualization and analysis of this novel three-dimensional imagery. The SVSS program will support the broader munitions remediation problem by creating data products that provide highly accurate (<10 cm) target localization. Finally, datasets from the SVSS can greatly expand the data available to the SERDP munitions response research community. An objective of the SVSS program is to provide datasets, with accompanying documentation, to those researchers identified by SERDP.

1.3 Technical Approach

The SVSS program was divided into two sequential phases: a modeling and simulation phase, followed by a design/build/demonstrate phase. The goal of the first phase of the SVSS program was to utilize modeling and simulation to provide an estimate of the proposed sensor's performance in imaging buried UXO. To carry out these simulations, existing models and signal processing tools were adapted and extended to properly account for the bistatic, sub-bottom nature of the SVSS sensor. The goal of the second phase of the SVSS program was to demonstrate, using a prototype SVSS design, the capacity for the detection of buried UXO. The prototype system was based on significant leveraging of existing sonar hardware and software.

Model Development The modeling approach used for the SVSS program has sought to build upon existing models where possible and provide extensions to address the specific needs for simulation of near-normal incidence scattering from the seafloor sub-bottom. This was accomplished by using a pair of models. The field scattered from the environment was simulated using ARL's Point-based Sonar Scattering Model (PoSSM) [17]. Figure 1a shows composite levels from the various acoustic models at calculation points at the water/sediment interface and within the sediment volume. This model was combined with the APL-UW developed Target in the Environment Response (TIER) model [18]. TIER was extended to permit simulation of the bistatic scattering geometries that are present for SVSS imaging. The integration of PoSSM and TIER provides the first high-speed, coherent model for the simulation of the field scattered from buried UXO and the surrounding environment.

The PoSSM model was used to support four principal tasks on this program: (1) predicting sensor performance, (2) developing image reconstruction algorithms, (3) informing hardware design and configuration, and (4) interpretation of field data. The sensor performance predictions are extensively detailed in the Phase 1 technical report [19]. Also during Phase 1, synthetic datasets were generated to aid development of novel volumetric SAS processing with ARL/PSU's Advanced Synthetic Sonar Imaging eNgine (ASASIN). ASASIN was modified to properly account for the bistatic sensor geometry and refraction at the sediment-water interface, and these modifications were validated using PoSSM data. An example of these simulated results is found in Figure 1b, which shows three slices through the three-

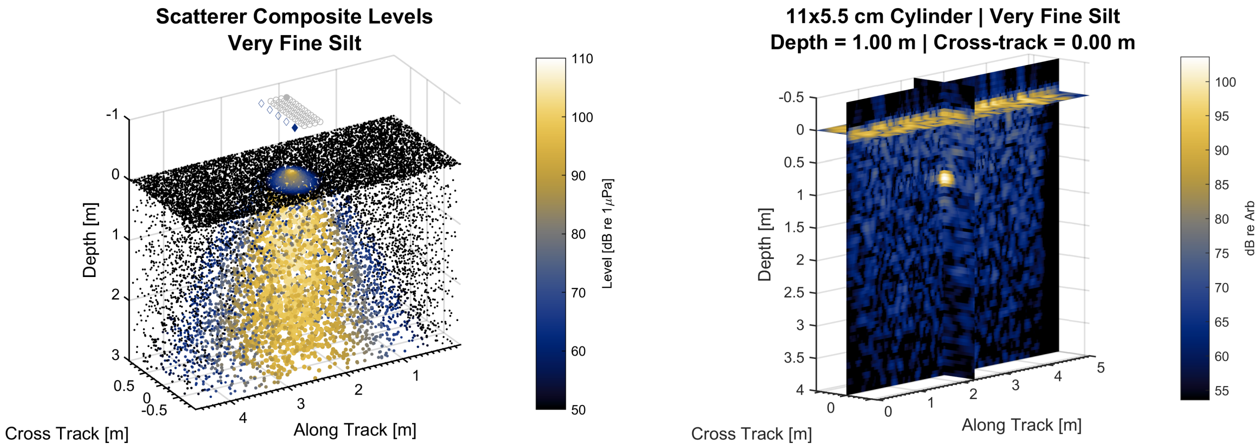

(a) PoSSM Simulation

(b) 3D Image Output

Figure 1: ARL/PSU's Point-based Sonar Scattering Model (a) was expanded and utilized to generate representative acoustic time series for various sediment types, and combined with APL-UW's TIER model for various target shapes. The combination of these physics-based acoustic models was used to assess the feasibility of the SVSS hardware design, and signal and image processing algorithms (b) for detection of buried UXO.

dimensional (3D) imagery output of ASASIN for a 1 m buried target. PoSSM modeling and simulation identified a requirement to minimize the projector sensitivity in the direction of the air-water interface. This hardware requirement directly informed the SVSS projector design. Finally, the PoSSM model was used to aid interpretation of field data collected in test sites with complex sub-bottom structure.

In combination with the SVSS program, as well as other simultaneous collaborative programs being conducted at ARL/PSU, PoSSM has continued to evolve as a sonar modeling and prediction tool [20]. These efforts have been focused on adding or expanding acoustic phenomena models, as well as improving usability, computational efficiency, and numerical stability. These advancements have enabled a detailed model-data comparison for the SVSS program.

Hardware Development Past and current research in the detection of buried ordnance has shown that normally oriented sensors provide significant penetration depth, but these sensors have typically been mounted to submerged unmanned or towed platforms [10, 16]. Addressing this problem in shallow water requires specialized hardware that is not currently commercially available. ARL/PSU addressed the problem of detailed ordnance survey in shallow water through integration of a normally oriented sensor to a shallow-draft surface craft. ARL/PSU has mitigated the complexity and technical risk in development of the prototype sensor by using an existing reconfigurable test platform known as the Sound Hunter, pictured in Figure 2a. This platform is easily adapted and modified to address lessons learned through model and simulation and/or field data analysis.

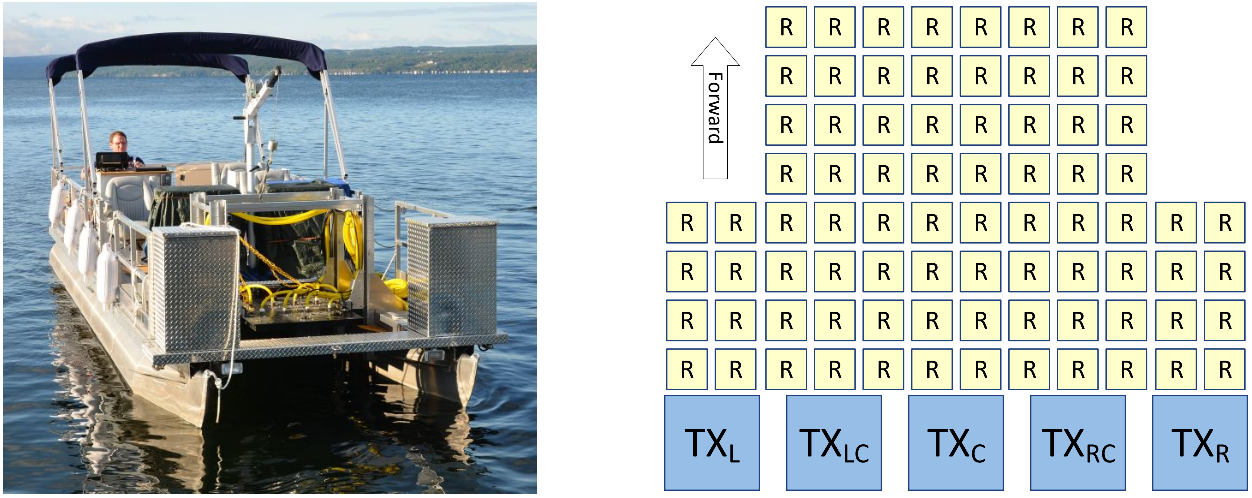

(a) Sound Hunter Platform **(b)** SVSS Sonar Array

Figure 2: The Sound Hunter test platform is a nine-meter pontoon boat (a). The projector and receive array are shown here mounted in the forward portion of the boat. The sonar array consists of five projectors and 80 receive channels (b).

The SVSS uses five discrete projectors and a two-dimensional receive array with 80 hydrophones to create high-resolution three-dimensional imagery through synthetic aperture signal processing. A schematic diagram of the projectors and receivers is shown in Figure 2b. The receiver locations are shown as small yellow squares with the letter R, and the projectors are shown as larger blue squares with TX and a subscript to indicate the position. The projectors are activated from left to right in a repeating sequence ($TX_L \rightarrow TX_{LC} \rightarrow TX_C \rightarrow TX_{RC} \rightarrow TX_R$) as the sonar system transits a survey track. This permits SAS beamforming in both the along-track and cross-track directions independently.

Signal and Image Processing Development The raw data generated by the SVSS sensor must be processed in order to form three-dimensional imagery of the seafloor and sub-bottom. The process of converting from raw sensor data to an image is called image reconstruction or beamforming. A number of reconstruction algorithms have been developed in different research areas including radar imaging [21], seismic imaging [22], and sonar imaging [23]. One technique that is known for its combination of simplicity and robustness is backprojection [24].

ARL/PSU's implementation of a backprojection beamformer is called ASASIN [25]. ASASIN was originally implemented to generate high-resolution SAS imagery from both high-frequency (>100 kHz) and mid-frequency (∼10 kHz) imaging sonar systems. Each of the imaging sonar systems supported by ASASIN generates two-dimensional imagery from one-dimensional receiver geometries. Additionally, the region imaged on the seafloor is typically in the far-field of the physical sonar system. Neither of these are true for SVSS data; consequently, several changes were made during the first phase of the SVSS program to adapt ASASIN to near-field volumetric reconstruction.

The three-dimensional data cubes generated by ASASIN require additional image processing to normalize the imagery, compress the dynamic range, and create two-dimensional representations for the screen. Normalization and dynamic range compression are needed to suppress the spatial variability of the intensity within an SVSS image that is due to the image reconstruction process and the spatial variability of the scattering strength of the imaged scene. Once normalized, two-dimensional representations such as maximum intensity projections (MIPs) or image slices can be reviewed for targets. An example of an image slice is shown in Figure 3, where a pair of solid aluminum cylinders and a pair of rocks are readily visible.

Test Site Development To support integration testing and demonstration of the SVSS system, test sites were developed at two separate geographic locations – the Foster Joseph Sayers Reservoir in Howard, PA, and the Aberdeen Test Center in Aberdeen, MD.

A test site was established at the Foster Joseph Sayers Reservoir in the early spring of 2017. This lake covers roughly 1700 acres and is eight miles in length. The test site was chosen due to its proximity to ARL/PSU and because the winter lake level is lowered sufficiently to provide ARL/PSU with the opportunity to establish an accurate ground truth of objects, clutter, and sediment types within the test bed. A test area within the reservoir for establishing target fields was approved by the Pennsylvania Department of Conservation and Natural Resources and the US Army Corps of Engineers. Within this approved test area, two sub-regions were identified that have expected water depths of 1.5 m–2.0 m and 3.0 m–4.0 m when the reservoir reaches the summer pool level. The test areas have been seeded with more than 100 objects during draw-down periods.

The SVSS conducted demonstrations at the Aberdeen Test Center's Littoral Warfare Environment and the neighboring Bush River. The LWE facility has a nominal reservoir surface area of 100 m by 140 m covering a sand sediment bed, with a 50 m by 120 m beach at the southern edge. The reservoir is dewatered by pumping its contents into the neighboring Underwater Test Facility. When dewatered, a larger portion of the beach is exposed and this allowed ARL/PSU to emplace a target field without the need for diver support.

A total of 85 objects including munitions, science targets, and clutter were selected for installation in the LWE with one-third of the objects proud and the remainder buried up to 60 cma below the sediment/water interface. The munition diameters installed in the LWE ranged from 2.0 cm to 15.5 cm (the theoretical resolution of the SVSS is 5 cm). The munitions and science targets are shown in Figure 4a prior to distribution in the field. These targets were laid out along six lines running parallel to the beach with two-meter spacing between targets. Positions were determined with a RTK-GPS survey (Figure 4b).

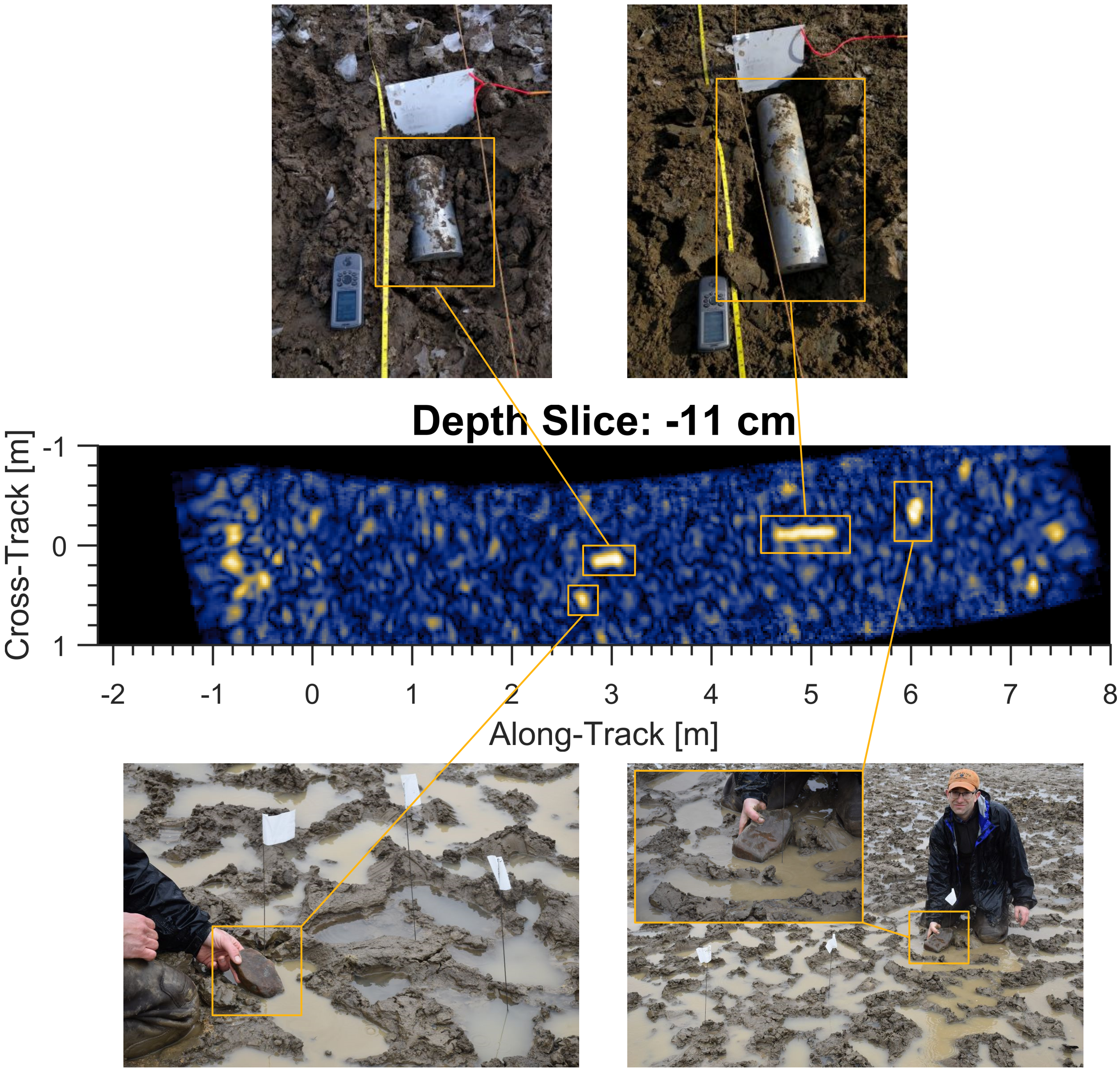

Figure 3: Acoustic data were collected at Foster Joseph Sayers Reservoir with the SVSS and processed with ASASIN. A slice through the 3D output at a depth of 11 cm (center) shows two solid aluminum cylinders (top) emplaced during winter draw-down, as well as two rock clutter objects (bottom) that were recovered during a subsequent draw-down.

(a) Munitions and Science Targets **(b)** RTK Target Survey

Figure 4: 85 objects including munitions, science targets, and clutter were selected for installation in the LWE at the Aberdeen Test Center (a). Ground truth locations were accurately measured with an RTK-GPS survey (b).

1.4 Results and Discussion

Regular testing was conducted at the Sayers Reservoir throughout 2018 and 2019. In Figure 5, a pair of cross-track MIPs are shown for the same segment of the lake bed for surveys conducted in June and November of 2019. The scene contains four cylindrical targets, whose descriptions are provided across the top of the figure. The rightmost pair of cylinders are fully buried and they are clearly visible in the November MIP. During the colder winter months, the SVSS performance was markedly better for buried target detection. ARL/PSU found the that the scattering strength of the lakebed varied throughout the year, and in the warmer months, the elevated scattering strength of the lakebed could mask the buried target returns. It is hypothesized that this seasonal variation is caused by biogenic production of methane.

To study the complex lakebed at the Sayers Reservoir, ARL/PSU utilized the PoSSM model. Figure 6a provides an overview of the PoSSM simulation used for model-data comparison. The geometry of the mud (upper) and clay (lower) sediment layers used in the model is shown. The total simulation is a combination of individual models run for the mud interface, mud volume, clay interface, and clay volume that each contribute to the combined reflected acoustic field. Additionally, for each of the interfaces, the model is split into a coherent (specular) and incoherent (diffuse) component. These six models are coherently added to simulate the entire scattered field. Also, the transmit pulse amplitude (RMS level of 183.5 dB) is adjusted by the two-way transmission coefficient and attenuation through the water/mud interface when used for the clay models, and clay/mud property ratios are used to calculate the reflection coefficient and refraction at the clay interface.

Figure 6b uses the mean A-Scan over the 5 m track to provide a model-data comparison for the simulated and field data. The simulation was configured with standard sediment properties (denoted “Hamilton” properties) found in the literature [26, Table 3, rows 7 and 6] and with properties updated from a core sample (denoted “Updated” properties). Overall, the simulation matches the field data quite well: it shows the characteristic double peak that is seen in the field data and a similar absolute level in the late return, which represents volume scattering from the clay basement. The peaks in the “Hamilton properties” simulation clearly does not match the field data: the first peak (due to the water/mud interface) is stronger than the second (due to the mud/clay interface). However, once the properties are updated to match the field site sediment’s density and velocity properties the mean amplitudes of the two peaks closely match the field data. The lower amplitude of the first peak indicates that the mud properties are more closely matched to the water column than the clay properties. When the median peak level from the mud and clay layers are calculated, the simulation is 2.4 dB and 4.6 dB lower than in the field data, respectively. It is hypothesized that this difference could mainly be due to the presence of rocks at the field test site, which are not currently considered in this simulation.

During the experiment at the Aberdeen Test Center, the SVSS surveyed a region of the Bush River adjacent to the ATC Underwater Test Facility. The bulk of the survey was collected in approximately 2.5 m of water. The ATC staff described the sediments in the portion of

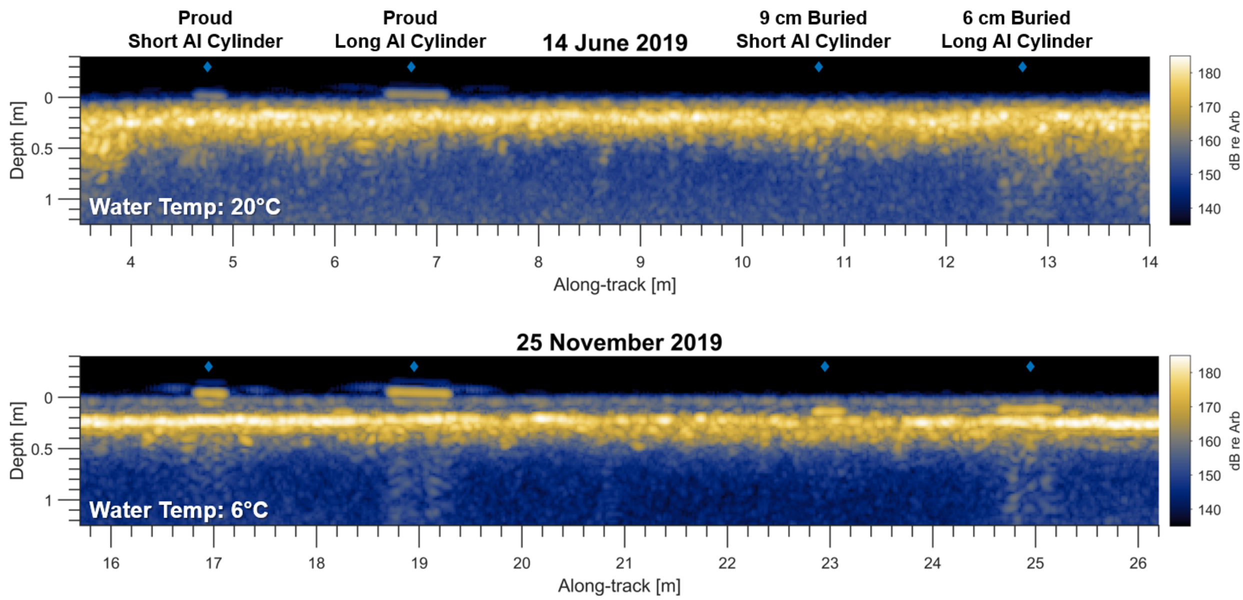

Figure 5: Cross-track MIPs are shown for a pair of tracks that surveyed a common set of targets in the deep field at the reservoir. It appears that surveys conducted during colder periods lead to reduced sediment scattering strength and improved target detectability.

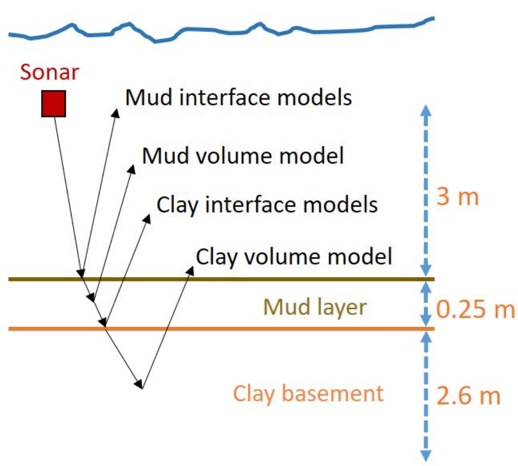

(a)

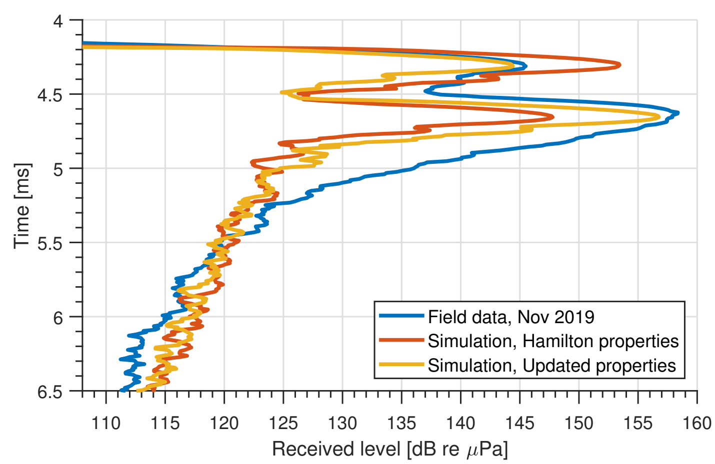

(b)

Figure 6: PoSSM was configured to model the returns from the layered environment found at Sayers using the schematic provided in (a). The ensemble-averaged A-Scan over a 5 m section of track from field data (blue) and simulated data with Hamilton (red) and updated (yellow) properties is provided in (b).

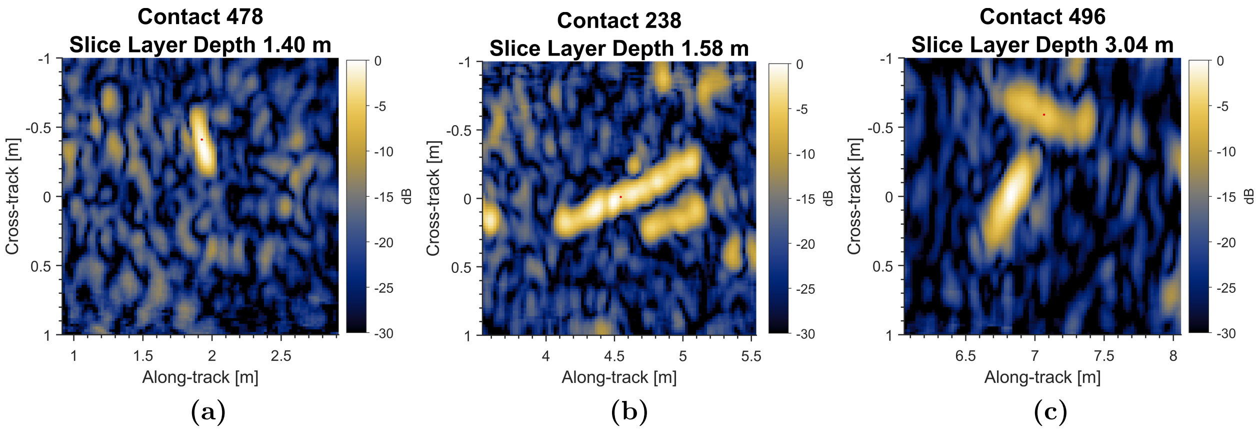

Figure 7: The SVSS data collected in the Bush River was manually screened to identify clutter objects. Depth slices for three example contacts are shown.

the Bush River as principally mud, but no sediment samples were collected to confirm this. This survey site was anticipated to have man-made clutter from historical activity in the area.

The data collected in the Bush River was manually reviewed to identify potential man-made clutter objects, and this process produced over 500 contacts. The reviewer flagged any object that either had strong geometry to suggest that it might be man-made or whose target strength significantly exceeded the background. The majority of the contacts labeled in the Bush River were buried by more than 1 m of sediment and several were buried as deep as 3 m. Three example contacts are shown in Figure 7. Each slice is shown on a 30 dB logarithmic scale and the depth beneath the sediment/water interface is indicated by the title. The small red dot in each figure shows the point selected during the image review process. The left image shows an object that is approximately 40 cm long and 10 cm wide at a burial depth of 1.4 m. The center image shows a pair of closely spaced objects at a burial depth of 1.58 m. Finally, the right image shows another pair of closely spaced objects at a burial depth of 3.04 m.

1.5 Implications for Future Research and Benefits

Overall, the research objectives of hardware development, software development, and demonstration of the SVSS were achieved. Absolute object localization errors of less than 10 cm and buried object detection at depths of 3 m illustrate the utility of the SVSS system for detection of surficial and buried UXO. The results demonstrated under this program point to three areas for future research and experimentation:

1. improving the SVSS receive hardware to increase system performance,
2. investigating advanced signal processing techniques to mitigate environmental complexity and exploit late-time target returns, and

3. conducting a field demonstration at one of the SERDP-ESTCP munitions response test beds.

The receive array currently used by the prototype SVSS was leveraged from a prior non-SERDP program. While useful for initial demonstration and testing, the receive array was not originally intended for sub-bottom imaging, and the array's design limits the achievable image resolution. A purpose-built receive array would provide increased image resolution and a wider range of sampled angles that facilitate wider azimuthal support for target strength estimation. This could be accomplished within a smaller overall footprint, potentially making the SVSS system easier to deploy from alternative surface craft.

In testing the prototype SVSS, it was found that the strength of near-normal incidence scattering from the sediment/water interface could be greater than the scattered field from smaller targets. The impact of near-normal incidence scattering has been addressed through time-gating by other normal-incidence munitions response sensors [15]. The bistatic geometry of the SVSS array may allow for windowing and exclusion of near-specular ray paths in the reconstruction process. In many of the SVSS demonstration sites, man-made objects exhibited late-time scattering phenomena. Prior research has shown that alternative reconstruction techniques can focus these late-time returns [27–29]. Application of these techniques could lead to improved target detection in challenging environments.

Finally, a field demonstration of the SVSS should be conducted at one of the SERDP-ESTCP munitions response test beds currently under development. This demonstration would provide a large research dataset and an independent measure of the SVSS performance. After performance validation, the DoD or others could use the SVSS to determine the location of proud and buried ordnance at shallow-water remediation sites.

2 Objective

The Sediment Volume Search Sonar program was proposed in response to the Munitions Response Statement of Need MRSON-15-01 for the development of a detailed survey sensor for acoustic detection and localization of surficial and buried unexploded ordnance. The objective of the SVSS program is to improve surficial and buried ordnance detection and classification performance over that available with existing sonar systems by addressing the current gap in technology for detailed survey in shallow water depths. This gap exists because currently available systems are not well suited to shallow-water operation due to the absence of suitable platforms to host these sensors, and the challenges of multipath interference. The SVSS program's objective is achieved through simulation, design, fabrication, and demonstration of a sonar system that is deployed from a shallow-draft surface vessel and is capable of producing three-dimensional volumetric SAS imagery across a range of environments including in water depths as shallow as 1 m–2 m. Particular attention is paid to utilizing commercial off-the-shelf (COTS) hardware where possible to reduce system cost. In addition to the fabrication of the sonar system, the necessary image reconstruction algorithms and processing software are developed for the generation of three-dimensional volumetric SAS imagery. Techniques are explored for visualization and analysis of this novel three-dimensional imagery. The SVSS program will support the broader munitions remediation problem by creating data products that provide highly accurate (<10 cm) target localization. Finally, datasets from the SVSS can greatly expand the data available to the SERDP munitions response research community. An objective of the SVSS program is to provide datasets, with accompanying documentation, to those researchers identified by SERDP.

3 Background

The remediation of UXO is a current environmental problem facing the United States Department of Defense. SERDP has held a series of workshops in 2007, 2013, 2014, and 2018 to discuss the underwater munitions remediation problem [4–7]. Ordnance can be found in a number of aquatic environments spanning freshwater to marine areas, and hydrodynamic processes can lead to ordnance burial [6]. Across these sites there is an extremely wide range of potential munitions. Ordnance may be as small as individual rounds whose largest dimension is greater than 7.5 cm, up to bombs that may exceed 1 m in length [8, 9]. The ordnance may experience significant biofouling and corrosion after remaining in place for several decades. Finally, man-made clutter is commonly found in near-shore UXO surveys. The wide variability of the environment, range of targets sizes, variability of the target state, and presence of clutter presents a highly challenging problem for a detailed survey sensor.

Development of acoustic sensors for the detection of buried ordnance using downward-looking sonar systems is addressed in prior [10–15] and current [16] research. One advantage of the sonar sensing modality (over electromagnetic modalities) is that acoustic imaging offers the promise of higher potential area coverage rates and better localization. The prior sonar systems that have addressed the problem of buried UXO imaging have either been towed systems or deployed from unmanned underwater vehicles. This deployment method has limited their typical operation to waters deeper than 5 m. As emphasized during the 2013 SERDP Workshop on Acoustic Detection and Classification of UXO in the Underwater Environment, the UXO detection and localization problem is particularly important to solve in water less than 5 m depth due to the prevalence of these areas and the higher likelihood of human interaction with ordnance [5]. Those environments where the ordnance is nearshore are of particular concern, and sensors capable of detailed survey are needed for detecting and localizing UXO in these environments.

A number of real aperture sonar (RAS) and synthetic aperture sonar sensors exist that may meet the wide-area survey needs outlined in MRSON-15-01. These sensors, however, are not suitable for detailed survey, especially in very shallow water and/or against buried objects. For RAS sensors to produce imagery capable of resolving small to medium sized UXO targets, whose dimension may be less than 20 cm, frequencies in excess of 100 kHz are required. There is significant sediment attenuation at these frequencies, which limits their ability to detect buried targets. For RAS sensors, a direct trade-off exists between resolution and sediment penetration capability. However, unlike a RAS, the resolution achievable by a SAS sensor is not directly determined by the operating frequency. For example, a dual frequency SAS has been demonstrated whose low-frequency band has been able to detect cylindrical targets buried up to 50 cm in favorable environmental conditions [30]. Nonetheless, two main factors limit the usefulness of a typical low-frequency side-looking SAS for detailed UXO survey in shallow water. First, SAS sensors are often deployed such that the majority of the high-frequency image is produced at low grazing angles, resulting in strong shadow contrast for proud targets. This imaging geometry limits the low-frequency effectiveness of these sensors against buried targets by leaving the majority of the swath below the critical angle for a "fast" seafloor[1], which significantly limits the probability of detection of buried targets. The second limitation is that SAS sensors are typically deployed from either unmanned underwater vehicles (UUVs) or towed by a surface craft. In very shallow water, it is difficult to operate these platforms with the stability required to form high-resolution SAS imagery.

At the 2013 SERDP workshop, there was a substantial amount of discussion of the bottom object scanning sonar (BOSS). BOSS utilizes a single, omnidirectional, low-frequency broadband transmitter and a pair of downward facing receive arrays to form three-dimensional imagery within the seafloor. In this geometry, the system operates near-normal incidence, which optimizes its operation for the detection of buried targets. The BOSS system has been evaluated by SERDP in a series of demonstration programs [14, 15]. The BOSS sensor's single omnidirectional projector transmits a sequential series of pulses as the UUV surveys the field. In the along-track direction, SAS beamforming results in a narrowing of the effective transmit and receive beam patterns. In the cross-track direction, it is not possible to apply SAS processing owing to a single transmitter; consequently, the omnidirectional projector contributes significant energy in the sidelobe structure of the receive beam pattern. This interference reduces the overall detectability of targets in the reverberation-limited environment of the seafloor. The receive array design also limits the performance of BOSS in less than 5 m of water. The arrays used on the system do not attenuate reflections from the sea surface, and this sea surface multipath return dominates the returns from within the seafloor. This limits the usable range of the sensor to be less than its depth of operation.

To achieve the technical objectives of the SVSS program, our effort will draw upon the previous successes of the sensors mentioned above, while mitigating the limitations, by developing a multi-projector, low-frequency broadband sensor array that allows high-resolution SAS image processing in both the along-track and cross-track directions while limiting multipath interference using specialized sensor design.

[1] The compressional wave speed of a "fast" seafloor is greater than the compressional wave speed of the overlaid water.

4 Materials and Methods

The SVSS program has developed sonar simulation models, sonar hardware, sonar signal processing algorithms, and test sites to support demonstration of a shallow-water, detailed-survey sensor. This section provides the details of the development in each of these areas.

4.1 Model Development

Model development has occurred throughout the SVSS program. During Phase 1, the SVSS program utilized modeling and simulation to assess the feasibility of a downward-looking SAS to generate volumetric imagery in very shallow water. A pair of modeling tools were utilized to support this analysis: ARL/PSU's Point-based Sonar Scattering Model (PoSSM) and APL-UW's Target in the Environment Response (TIER). Both models were matured and combined in order to provide data for assessing concept feasibility and for determining design requirements of a prototype sensor [Section 4.2]. Also, during Phase 1 synthetic datasets were generated to aid development of novel volumetric SAS processing with ARL/PSU's Advanced Synthetic Sonar Imaging eNgine (ASASIN) [Section 4.3]. This initial phase of the SVSS program served to provide an estimate of the proposed sensor's performance in imaging buried UXO.

The initial modeling phase also served as a risk-reduction effort, addressing several criteria presented by SERDP reviewers at the outset of the program:

- methods for mitigation of multipath reverberation,
- simulations of potential improvement in signal-to-noise ratio from the additional transmitters,
- the true gain over current SAS systems,
- the ability to detect/classify smaller targets in the presence of larger targets with stronger signals,
- the effects of platform motion on system performance, and
- the effects of variability in sediment properties on performance.

Each of these criteria were directly addressed in the SVSS Phase 1 report [19] utilizing the modeling and simulation techniques described in Section 4.1.1 (N.B. the effects of platform motion were not considered since the test platform has a high-grade inertial navigation system that is sufficient to correct for expected motion and mitigate any impact on system performance).

During execution of the second phase of this program, combined with significant interest from the sonar community and support from other programs, ARL/PSU has continued to develop and expand PoSSM. These expansions consist of both new or expanded phenomenological acoustic models, as well as improved computational efficiency. The advancements that directly impacted the SVSS program are described in Section 4.1.2. These advancements have enabled a detailed model-data comparison that is presented in Section 5.2. The fact that other sonar modeling programs contributed to PoSSM development and utilize it also serves to further validate the physics fidelity contained in PoSSM [20, 31].

4.1.1 Phase 1 Model Development

Key aspects of the Phase 1 model development effort are summarized in this section. A more complete review of those efforts can be found in the Phase 1 technical report [19].

4.1.1.1 PoSSM Summary PoSSM is a sonar modeling tool that produces calibrated, bistatic, frequency-dependent, element-level, representative time series suitable for coherent signal processing. It employs a "model of models" architecture with many of the acoustic sub-models already documented in peer-reviewed literature and textbooks. In this context, the term "points" is in reference to the discretization of the environment for calculation of the acoustic field via a variety of acoustic models. As shown in Figure 8, PoSSM combines a priori knowledge about the scene with environment models, acoustic models, and sonar properties to calculate element-level acoustic time series data.

Figure 9 shows the diffuse interface and volume scattering levels at each calculation point for a single ping and a single transmit-receive pair at the corners of the SVSS sonar array, for very fine silt (Figure 9a) and medium sand (Figure 9b). Sediment properties were derived from APL-UW TR 9407 [2]. The level shown at each point includes the source level and effects of transmit and receive beam patterns, model-based scattering strength, attenuation, spreading loss, and, for volume scatterers, the two-way transmission through the interface. The coherent component of the scattered field is modeled using Eckart's approximation, where the flat-interface reflection coefficient is reduced by an exponential factor to account for the incoherently scattered energy [3, 32].

Figure 10 shows an example output corresponding to the scene illustrated in Figure 9 where individual time series data is shown for the specular interface, diffuse interface, and diffuse volume component models, as well as the combined envelope. For the very fine silt simulation, the diffuse volume scattering component dominates the combined signal, whereas the diffuse interface scattering component dominates for medium sand. This is related to the relative impedance mismatch at the water/sediment interface, where a larger portion of the incident energy is scattered at the medium sand interface relative to the very fine silt interface.

The PoSSM architecture lends itself nicely for parallel computation, particularly on Graphics Processing Units (GPUs). Portions of the code have been implemented in C++ using the compute unified device architecture (CUDA), an application programming interface developed by Nvidia for execution on CUDA-enabled GPUs. MATLAB is the main development language for PoSSM. The computational architecture and GPU-accelerated calculations allow PoSSM to simulate millions of scatterer calculations on consumer-grade GPUs, to billions on server-grade GPUs, in a few seconds while still retaining flexibility to implement or develop any necessary physics-based models.

During Phase 1, modules for generating synthetic time series for diffuse interface scattering, specular interface scattering, and diffuse volume scattering were advanced. Additional de-

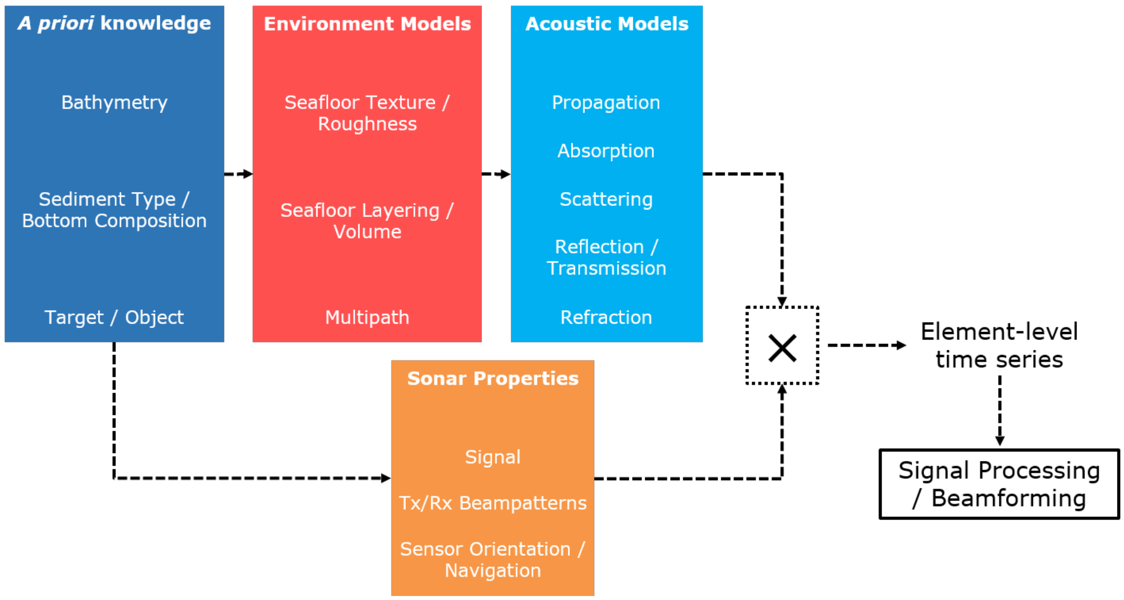

Figure 8: Flowchart of the primary constituents of the ARL/PSU Point-based Sonar Scattering Model.

tails regarding the PoSSM model, along with a validation of the diffuse interface scattering component, are found in Brown, Johnson, and Olson [17].

4.1.1.2 Multipath Modeling The signal that arises from direct-path backscattering from the target and seafloor is processed to form sonar imagery containing the targets and their surrounding environment. There are two principal sources of acoustic noise to this image reconstruction process. The first noise source is the ambient noise that is present independent of the operation of the sonar system. This noise has been characterized for the SVSS platform in Appendix B.1. The second noise source is due to multiple scattering. This type of noise is commonly referred to as multipath noise. In the definition employed here, multipath noise consists of all other acoustic signals, generated by the sonar transmitter, that propagate out and return at the same time instance as the signal of interest. The level of the multipath returns is proportional to the transmit level; therefore, increasing source level does not improve the signal-to-noise ratio in a multipath limited environment.

A model for multipath interference for mid- and high-frequency SAS imagery has been proposed by Lowe and Brown [33]. In this model, the level of multipath interference is modeled using a simple ray-based approach. Each boundary interaction accumulates a loss factor along with an additional factor associated with the beam patterns for the source and receive transducers. Additionally, the loss due to geometric spreading and absorption is calculated. The expected return level for direct backscatter is calculated and compared with the return levels calculated for various multipath geometries.

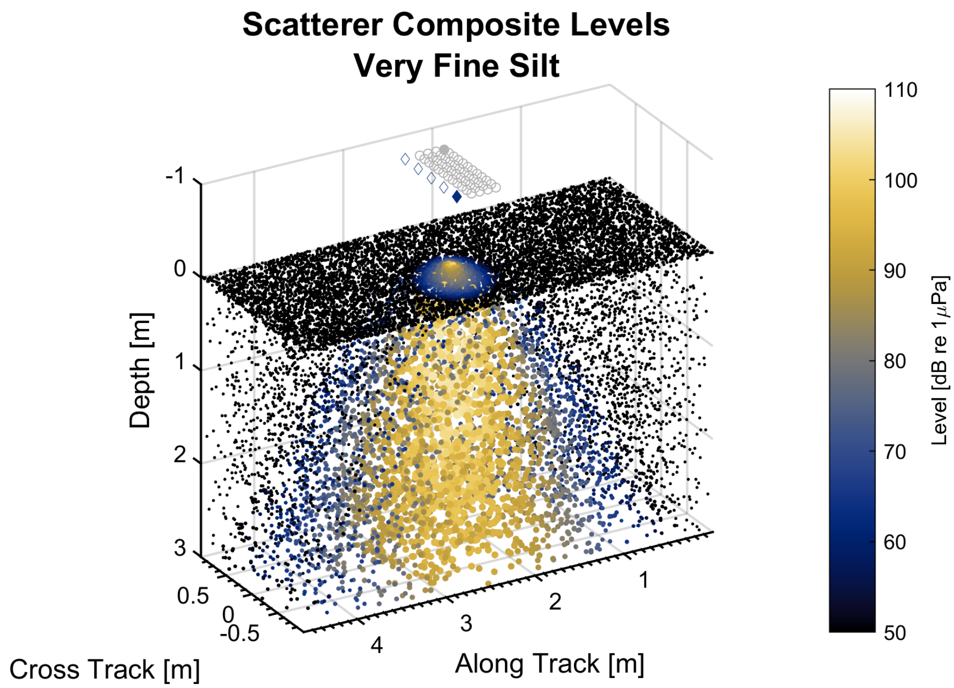

(a)

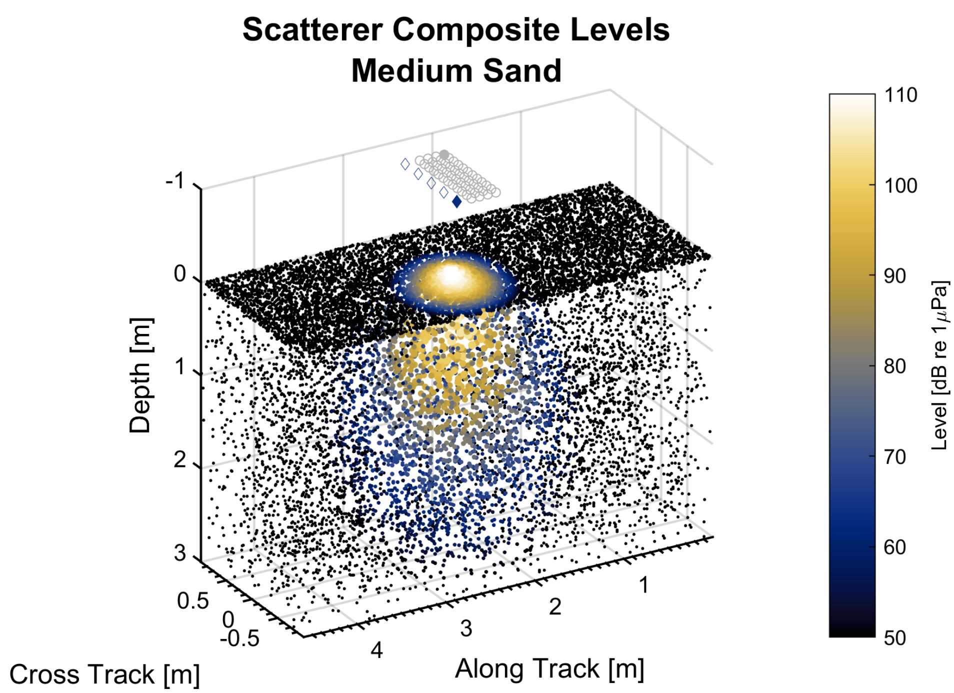

(b)

Figure 9: Diffuse interface and volume scattering levels are shown for very fine silt (a) and medium sand (b) for a single ping, between a single transmit-receive pair (filled diamond and circle) at the corners of a sonar array. The level shown at each point includes the source level and effects of transmit and receive beam patterns, model-based scattering strength, attenuation, spreading loss, and, for volume scatterers, the two-way transmission through the interface.

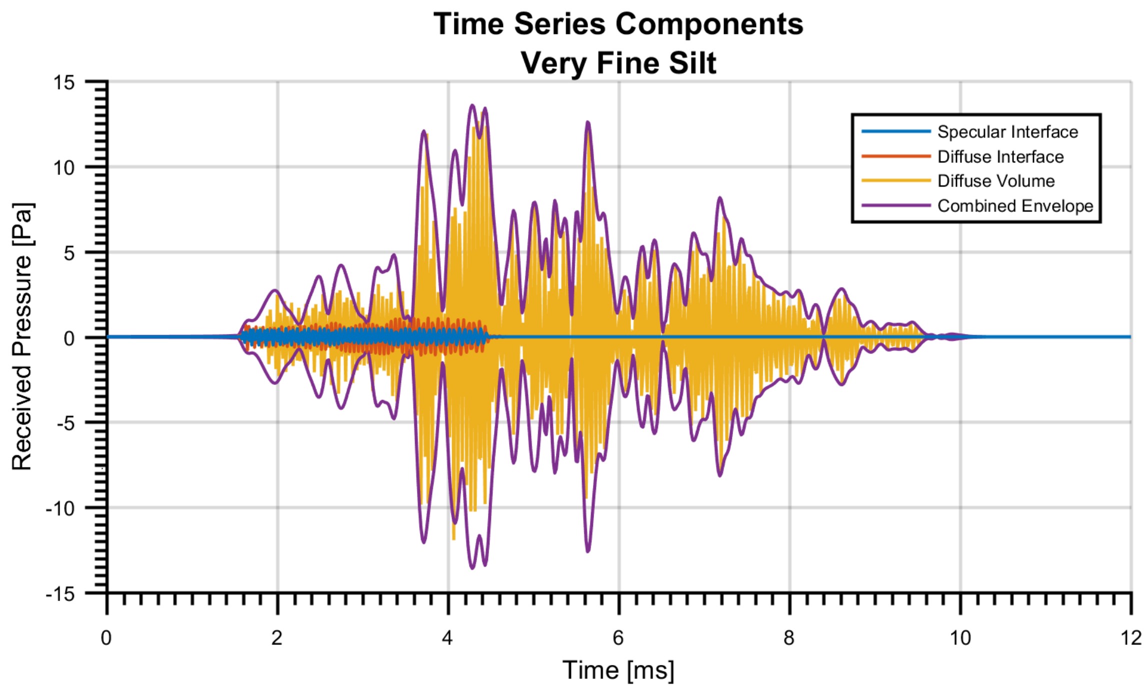

(a)

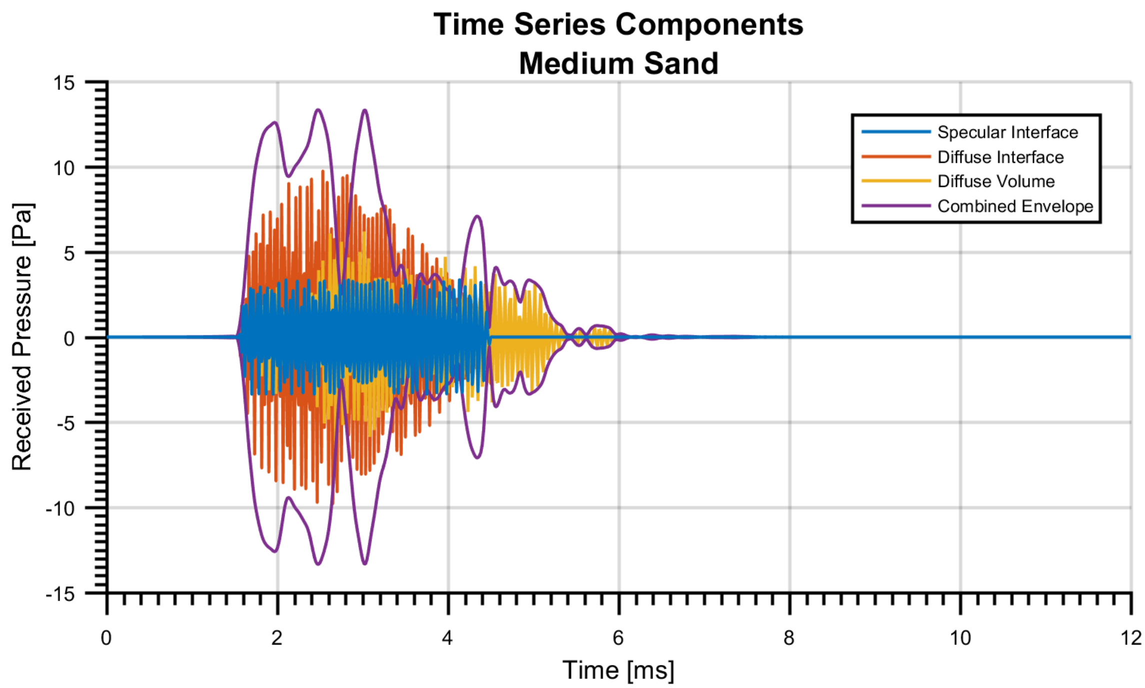

(b)

Figure 10: Simulated received pressure time series corresponding to Figure 9. The transmitted signal was a 15 kHz–25 kHz 3 ms LFM chirp. For the very fine silt simulation, the diffuse volume scattering component dominates the combined signal, whereas the diffuse interface scattering component dominates for medium sand.

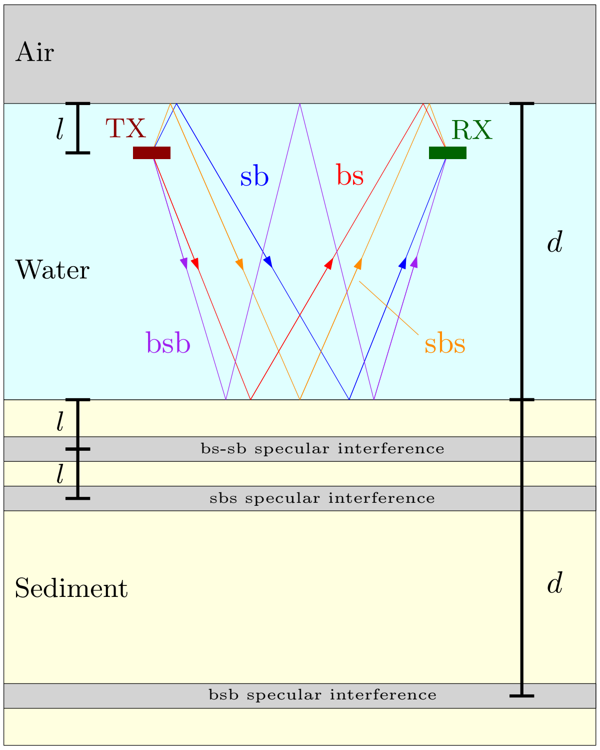

(a)

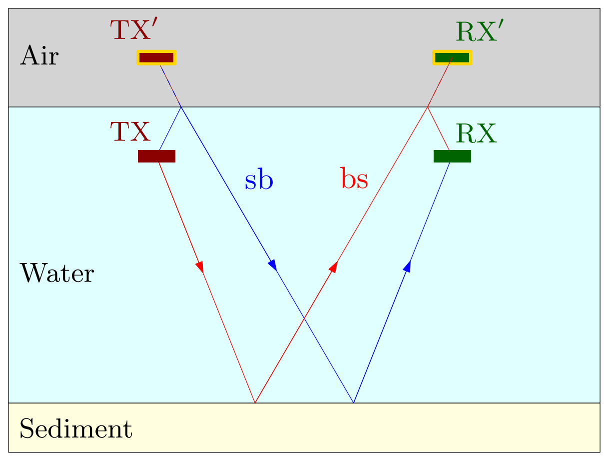

(b)

Figure 11: The multipath ray paths are shown for selected first and second order multipath when specular scattering is considered (a). Each ray is designated by a name that describes the order of boundary interactions [1]. The regions of specular interference are determined by the depth of the sensor and the water depth. These regions are indicated by gray boxes within the sediment that are labeled with the ray path names. (N.B. the specific depth where the specular interference appears in the reconstructed image will vary slightly from the depth indicated here due to the difference in the sediment sound speed. Use of the method of images in PoSSM (b) can simulate the presence of multipath in SVSS data. The image source and receiver are shown above the air-water interface for the *"bs"* and *"sb"* multipath rays.

Figure 11a shows an example of selected first and second order rays for multipath when specular scattering is considered. Each of the possible ray paths is identified using a naming convention that indicates the order of boundary interactions [1]. Surface reflections are indicated with *"s"* and bottom reflections with *"b."* As an example, the purple *"bsb"* ray first reflects from the bottom (*"b"*), followed by a surface (*"s"*) reflection, and then another bottom (*"b"*) reflection before reception at the receiver. Note that the arrival time for signals that travel the different ray paths is dependent on the sensor geometry within the water column. When multipath noise is relatively high, high amplitude horizontal stripes will be present in the beamformed SAS imagery, as indicated by the gray regions within the sediment volume. These regions of high amplitude can easily mask the desired direct-path backscatter signal if multipath noise is not effectively mitigated during sensor design.

If it is assumed that the air-water interface is perfectly flat, then the multipath model proposed by Lowe and Brown is easily merged with PoSSM by exploiting the method of images [34]. This approximates the multipath intereference in calm water conditions, when wave height (roughness) is small compared to a wavelength. As wave height increases, more of the acoustic signal will be scattered over a variety of angles, suggesting that this case is an estimate of the upper bound of multipath interference. In this approach, multipath reflections from a flat planar interface are simulated using an "image" source whose position is reflected about the boundary. An example simulation geometry that implements the method of images is shown in Figure 11b, where the transmitter position TX has been reflected about the air-water interface to TX$'$ for the simulation of *"sb"* multipath. Similarly, the receiver, RX, is shown reflected as RX$'$ for the simulation of *"bs"* multipath. Note that in both of these cases the ray paths intersecting the image transducers are incident on the lower face of the element as opposed to the upper face. By accounting for issues related to the directivity, it is possible to directly simulate the effects of multipath using the PoSSM model utilizing the method of images. Finally, experimental observations have shown that multipath interference in high-frequency SAS imagery is highest at low sea surface roughness [35]. This is because the low roughness interface minimizes forward-scattering loss at the air-water boundary. Thus, the assumption of a flat air-water interface assumption provides an upper bound on multipath interference.

4.1.1.3 TIER/PoSSM Integration In the SVSS program the PoSSM model is used to generate realistic environmental responses for scattering from the sediment interface and volume. In order to assess the ability of the SVSS system to image buried UXO, a coherent model for target scattering is also needed. This model was provided through a collaboration with APL-UW who adapted their TIER model [18]. To support SVSS modeling, TIER was modified to predict the scattered acoustic field from fully buried targets [36]. For the sonar system under development and buried targets, these modifications required TIER to consider fully bistatic scattering and refraction at the water/sediment interface [37].

The TIER model executes a numerical simulation to generate a time series result for each ping and transmitter-receiver pair. For an array containing a single transmitter and 48 receivers within a PoSSM simulation containing 51 ping locations, a total of 2448 time signatures are generated. For a simulation that includes all 5 transmitters of the SVSS configuration, 12,240 individual TIER simulations were produced. This simulation process is repeated for each desired sonar/target configuration.

TIER and PoSSM were integrated so that the same configuration files could be used for both the environmental parameters and the sensor geometry. This allowed the TIER-simulated target scattering time series to be combined with the PoSSM generated environmental scattering time series through linear superposition. Sample simulation results are shown in the next section.

4.1.1.4 Phase 1 Modeling Key Results The modeling and simulation efforts during Phase 1 successfully assessed the feasibility of a downward-looking SAS for volumetric image generation in very shallow water, and several key results were used as the basis for following phases. Figures 12 and 13 show example image formation results obtained by combining the PoSSM and TIER models, and can be used to summarize key results from the initial phase. The interested reader is directed to the Phase 1 report [19] for complete results. For each image, three planes are shown: one through the water/sediment interface (horizontal), one cross-track (vertical), and one along-track (vertical). Targets are placed at 2 m along-track.

Imagery shown in Figure 12 was generated by a simulation containing a small 11.00 cm long by 5.50 cm diameter solid aluminum cylinder at a burial depth of 1.00 m and at 0 m cross-track. The image shown in Figure 13a contains the same small cylinder, but the simulation placed the cylinder at the water/sediment interface. The image shown in Figure 13b was generated by a simulation containing six large 60.96 cm by 30.48 cm solid aluminum cylinders at burial depths of 0.25 m to 1.50 m and at 0 m cross-track, and two columns of six small 11.00 cm by 5.50 cm solid aluminum cylinders at the same burial depths and 0.50 m cross-track.

Interpretation and discussion of Figures 12 and 13 are summarized in the following list.

- Effective multipath mitigation can be realized with judicious transmitter and receiver design. A small cylinder buried at 1 m should be detectable in both very fine silt (Figure 12a) and medium sand (Figure 12b). For the medium sand case, a combination of the approximately 15 dB stronger water/sediment interface return, combined with higher acoustic attenuation in the sediment, partially obscures the target. Dynamic depth normalization developed after Phase 1 increases the target-environment contrast. Also for the medium sand case, the strong multipath return at 3 m from ray *bsb* is evident and may obscure more deeply buried targets. Additionally, multipath rays (*bs-sb*) cause interference at 0.75 m depth, which contributes to less obvious masking within the sediment.

- Sediments with similar impedance to the overlying water (e.g., very fine silt) allow for greater acoustic penetration into the sediment that results in higher signal-to-noise ratio and better image quality at greater depths.

- Sediments with a larger impedance mismatch (e.g., medium sand) inherently have a stronger scattering response at the interface and will induce greater multipath in-

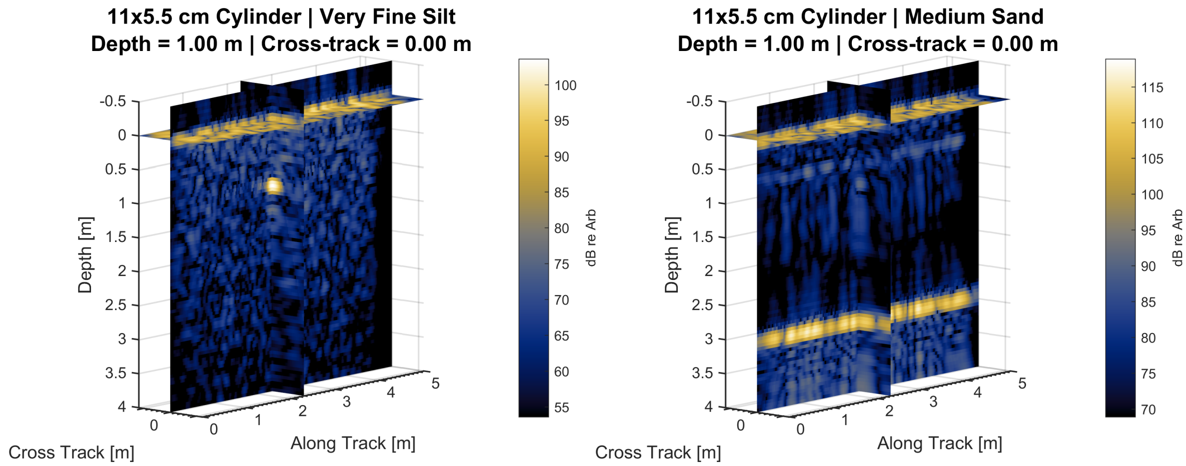

(a)

(b)

Figure 12: Two example images of combined model results showing a 11.00 by 5.50 cm solid aluminum cylinder at 0 m cross-track and 2 m along-track, buried at 1.00 m in very fine silt (a) and medium sand (b). The interface scattering strength in the medium sand example is approximately 15 dB stronger, shifting the dynamic range of the image and revealing a noticeable multipath return at 3 m depth.

terference. Judicious sensor design to limit multipath interference will be especially important in this case.

- Targets located at the water/sediment interface may be more difficult to detect when compared to more deeply buried targets (see Figure 12a in comparison to Figure 13a).
- Cross-track resolution is expected to improve when coherently combining data from five transmitters instead of a single transmitter [19]. The cross-track resolution is expected to degrade with depth; however, targets such as small solid aluminum cylinders spaced 0.25 m apart are expected to be separable (see Figure 13b).

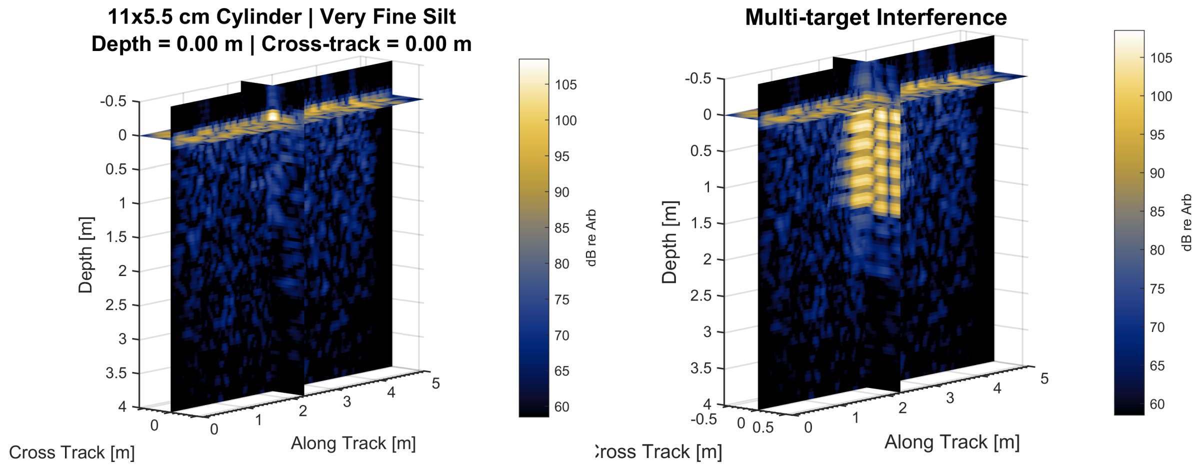

(a) **(b)**

Figure 13: Two additional example images of combined model results showing a single small solid aluminum cylinder at the water/sediment interface (a) and a column of six buried large solid aluminum cylinders adjacent to two columns of small solid aluminum cylinders (b). The sediment in both simulations was very fine silt. The water/sediment interface can obscure flush buried targets; however, buried targets remain separable for certain target types and spacings (e.g., 0.25 cm).

4.1.2 Phase 2 Model Development

Under the SVSS program, as well as other simultaneous collaborative programs being conducted at ARL/PSU, PoSSM has continued to evolve as a sonar modeling and prediction tool. These efforts have been focused on adding or expanding acoustic phenomena models, as well as improving usability, computational efficiency, and numerical stability. The following section provides a summary of recent developments. Many of these developments are utilized for the model-data comparisons presented in Section 5.2. Specifically under the SVSS program, the following topics were advanced: Sediment-Sediment Layer Interface Component, User-definable Sediment Properties, Improved Specular Component Calculation, Bubble Response, and Accelerating Volume Scattering Calculations.

4.1.2.1 PoSSM Development - Acoustic Models

- **Sediment-Sediment Layer Interface Component**
  During Phase 1, development of PoSSM was focused on acoustic returns from the water/sediment interface and the sediment halfspace. Upon further investigation of the test site at Foster Joseph Sayers Reservoir, the lakebed may be more closely approximated as a silty-clay sediment, deposited since reservoir creation, above a clay basement that existed prior to the reservoir. Since Phase 1, work has been conducted to allow calculation of the diffuse interface component from a sediment-sediment layer.

- **User-definable Sediment Properties**
  Initially, sediment properties for the bistatic scattering strength small-slope [38] calculations within PoSSM were implemented based on sediments described by APL-UW TR-9407 [2]. This limited set of sediment properties may not accurately represent the acoustic scattering, sound speed, and attenuation properties of test site sediment. The user now has the ability to define custom sediment parameters, either from other literature references or from direct physical measurements. In Section 5.2 we have combined parameters from literature [2, 39] with measurements with measurements of sediment cores made by the Naval Research Laboratory at the Stennis Space Center (NRL-SSC). Future SVSS investigations may leverage these new PoSSM components to better represent the sediment at current and future test sites.

- **Seafloor Texture and Bathymetry**
  To more appropriately simulate the diffuse interface component, the ability to account for seafloor texture and bathymetry has been included. When only the amplitude of the signal is considered, the effects of roughness are already included in the diffuse and specular interface level calculations. Therefore accounting for a non-flat seafloor is of greater importance to side-looking sonars at low grazing angles than to sonars operating at near-normal incidence. However, there may be some benefit to inclusion of roughness and bathymetry when quantifying SVSS beamforming performance over a varying bottom.

- **Improved Specular Component Calculation**
  In addition to incoherent or diffuse scattering from a rough interface, there will also be a coherent component of the transmitted signal reflected from the interface. This coherent component, often referred to as a specular reflection, can be thought of as a scaled and delayed copy of the transmitted signal, and can be modeled as the flat-interface reflection coefficient reduced by an exponential factor to account for the incoherently scattered energy (often referred to as the "Eckart Factor" [3,32]). The Eckart Factor is dependent on the interface's root mean square (RMS) roughness, among other factors. During Phase 1, the RMS roughness was assumed to be 1.0 cm for all sediments considered. This parameter approximation was improved to account for the sonar geometry, and the RMS roughness is now calculated by integrating the power law roughness from a wavenumber cutoff based on the radius of the sonar's first Fresnel zone. Figure 14 shows the impact of this improved calculation on the reflection coefficient magnitude for a sonar 3 m from the seafloor. In this example parameters from APL-UW 9407 were used in order to facilitate comparison to the Phase 1 report. The effective mean RMS value within the field of view of the SVSS was calculated. For "medium sand" the RMS value increased from 1.000 cm to 1.365 cm that *decreased* the specular component amplitude, whereas for "very fine silt" the RMS value decreased from 1.000 cm to 0.465 cm that *increased* the specular component amplitude. The range of specular component amplitudes utilized in Phase 1 (gray lines of Figure 14) bound those with this improved calculation, which will be utilized in Section 5.2. Appendix C provides a detailed description of the specular reflection coefficient calculation.

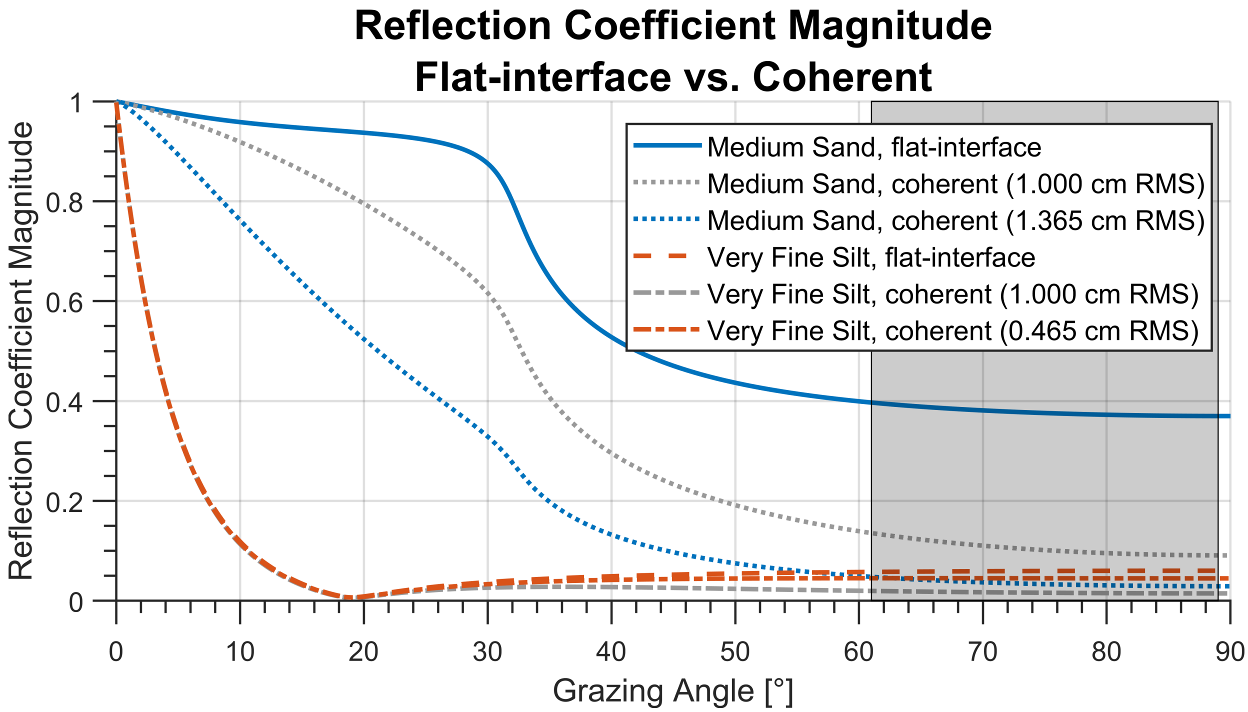

Figure 14: Comparison between flat-interface and coherent reflection coefficients at 20 kHz for medium sand and very fine silt [2]. The typical SVSS field of view is indicated by the shaded region. The coherent component levels using 1.000 cm RMS roughness used during Phase 1 are shown as gray lines and bound the updated calculations for medium sand (blue) and very fine silt (red), which have RMS values of 1.365 cm and 0.465 cm, respectively. Note that rough-interface scattering significantly reduces the coherent component.

- **Bubble Response**
  Data collected during 2019 and 2020 suggest the presence of entrapped gas within the sediment. In order to simulate the effect of entrapped gas using PoSSM, a bubble response model was developed. The following process is used to simulate acoustic scattering from bubbles. First, the bubble equation is formulated as a second order ordinary differential equation (ODE), where the bubble is assumed to act as a damped harmonic oscillator (applicable in the low-frequency regime, $ka \ll 1$). Then, the ODE is solved numerically at discrete time steps for an arbitrary forcing function (i.e., the transmit LFM chirp). Next, the velocity solution is converted to pressure. After that, the bubble's acoustic response is used as the kernel in a PoSSM simulation. Finally, the kernel is adjusted for different bubble sizes/properties so that acoustic scattering from an ensemble of bubbles (i.e., millions of bubbles) can be simulated. Additionally, the transmission loss through a bubble layer is calculated in order to apply partial occlusion to scattering that occurs beyond the bubbles. These extensions of PoSSM will be utilized in Section 5.2 and a detailed description of the bubble model can be found in Appendix D.

4.1.2.2 PoSSM Development - Usability and Computational Efficiency

- **Generic Sonar Formats**
  The sonar configuration has been generalized to allow PoSSM to simulate a wider range of sonar array designs. This is expected to benefit SVSS should a redesign feasibility study need to be conducted for future performance improvements. Additionally, simulation of other sonar systems and processing with other types of signal processing algorithms serves as implicit validation of many aspects of the tool [20, 31].

- **Accelerating Simulations with Graphics Processing Units**
  During Phase 1, computational acceleration of PoSSM simulations utilizing CUDA-enabled GPUs was limited to generation of the element-level time series. This step is the most computationally expensive, but also well suited for GPU acceleration. Prior to Phase 1, this was implemented within MATLAB first on the CPU, then GPU utilizing the MATLAB Parallel Computing Toolbox. During Phase 1, *significant* speedup was realized by writing a custom dynamic-link library (.dll) called from MATLAB. Under support from other programs, each of the other major functions needed to perform a PoSSM simulation were implemented in the custom dynamic-link library and have been accelerated using CUDA (several specific functions are also called out below). The user has the ability to select that a subset of calculations be performed on the GPU with the remainder on the CPU, which is useful for proofing during implementation of new sonar setups or acoustic components when the user desires to interact with data before and after each of the acoustic models (see schematic in Figure 15a). Once satisfied with the simulation's configuration, the user can then run all calculations on the GPU and realize significant speedup due to fewer memory transfer operations (see schematic in Figure 15b). Currently a user can calculate a representative time series including millions of acoustic calculation points in several seconds or minutes, and ever-advancing GPU hardware should continue to reduce this time.

- **Optimizations for Seafloor Texture and Bathymetry**
  In order to accurately compute the reflection of sonar signals off scatterers across a seafloor with texture or bathymetry (i.e., utilizing a height-map), the 3D normal must be computed for each calculation point. This "local acoustic slope" is combined with the geometry of the sonar transducers at each "ping" location to determine the bistatic scattering angle. This is a very important calculation for realistic simulations, particularly for high-frequency low-grazing angle sonars (like typical side-scan SAS) or for highly bistatic sonars (like SVSS). The 3D normals can either be pre-computed or computed as needed (i.e., at runtime) based on the speed and memory allocation of the particular GPU being utilized, and this option can be selected by the user, with runtime computation as the default.

- **Accelerating Volume Scattering Calculations**
  PoSSM supports simulation of returns for volume scatterers below the seafloor surface. The computation of the refracted acoustic ray from water into sediment and back is achieved using a quartic polynomial solver, based on Ferrari's solution [40]. The computation of the necessary polynomial coefficients is performed on a per-scatterer basis given the scatterer environment and position of the sonar array. The roots of the

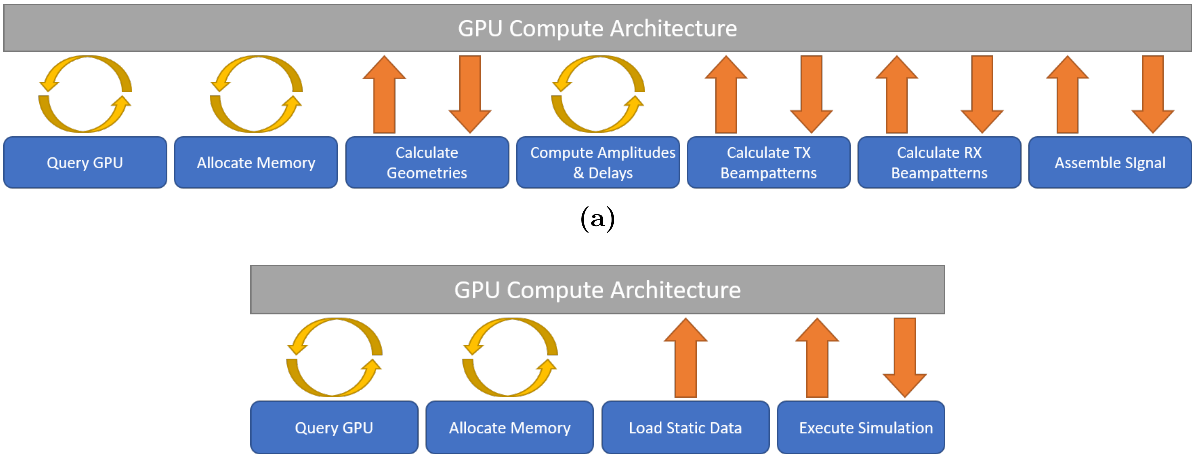

Figure 15: PoSSM models (in Figure 8) are implemented in both MATLAB and CUDA as a .dll. The user has the ability to select which models will be calculated on the CPU versus GPU, which is often beneficial when implementing a new sonar setup or acoustic component (a). The user can then select a mode that minimizes transfer of data between CPU and GPU to realize a significant speedup (b).

resulting quartic equation are then used to calculate the incident and refracted angles, as well as the distance the ray travels and the actual time of flight for the sonar pulse. For Phase 1, this was implemented in MATLAB on the CPU with several programmatic "traps" to identify the appropriate roots and correct for cases when the solution may fail (e.g., identically normal-incidence). Since Phase 1, this method has been improved significantly, including GPU-accelerated calculations, so the computational efficiency for volume scattering calculations has been significantly increased.

- **General Efficiency and Stability Improvements**
  As with any software-based product, there have been continual incremental computational efficiency improvements, and corrections for inadvertent mistakes. An additional focus has been to ensure computational stability on sufficiently capable CUDA-enabled GPUs. Many Titan, Quadro, and Tesla-class GPUs are supported. PoSSM currently utilizes a driver built against CUDA Toolkit 10.2. This focus includes ongoing strides toward establishing benchmark examples and unit tests, as well as expanding from single high-end consumer GPUs in a workstation to both multi-GPU machines and mobile workstation laptops. Work in this area is aimed at making PoSSM a capable tool for anything from basic research pursuits to large data generation tasks.

4.2 Hardware Development

Past and current research in the detection of buried ordnance has shown that normally oriented sensors provide significant penetration depth, but these sensors have typically been mounted to submerged unmanned or towed platforms [10, 16]. Addressing this problem in shallow water requires specialized hardware that is not currently commercially available.

Figure 16: The Sound Hunter test platform is a nine-meter pontoon boat. The projector and receive array are shown here mounted in the forward portion of the boat. These components are mounted in a rectangular frame that is lowered into the water during testing.

ARL/PSU addressed the problem of detailed ordnance survey in shallow water through integration of a normally oriented sensor to a shallow-draft surface craft. ARL/PSU has mitigated the complexity and technical risk in development of the prototype sensor by using an existing reconfigurable test platform known as the Sound Hunter, pictured in Figure 16. This platform is easily adapted and modified to address lessons learned through model and simulation and/or field data analysis.

The principal technical challenges with the design of the hardware for this sensor are related to the acoustic performance of the projectors and receivers. A sub-bottom ordnance survey system must:

1. operate at low frequency and high source level to provide adequate acoustic penetration of the sub-bottom,
2. operate with broad bandwidth to provide adequate image resolution and coverage for non-imaging data representations,
3. create directional responses that can passively mitigate multipath interference.

Generally, these requirements present two immediate conflicts. First, high source level is typically only achieved over a narrow range of frequencies. Second, directional transducer responses typically require high operating frequencies. In addition to the transduction challenges, the data acquisition system must synchronize the operation of several subsystems (e.g., transmit, receive, and navigation). Finally, as new test beds are surveyed and lessons are learned the system must be flexible to adapt to new environments and data acquisition strategies.

An overview of the SVSS sensor hardware is provided in Section 4.2.1. A substantial effort was made in the development of projectors for this program, and that effort is summarized in Section 4.2.2.

4.2.1 SVSS Hardware Configuration

The SVSS hardware is mounted to the Sound Hunter sonar data collection platform, which is shown in Figure 16. The platform is propelled by a 60 horsepower gasoline outboard engine, and also has a pair of 5 horsepower electric motors. The main power source is a 48 VDC battery bank that is coupled to a 2 kW inverter, which provides pure-sine 120 VAC power. The battery bank is charged from an AC source prior to a data collection. During extended field trials, a deck mounted 48 VDC propane generator is used to charge the battery bank. The Sound Hunter provides four stations for personnel on board the craft. It provides two data processing stations, one station for piloting the boat and managing the sonar coverage area, and one station for controlling and operating the sonar data collection system.

The SVSS uses five discrete projectors and a two-dimensional receive array to create high-resolution three-dimensional imagery through synthetic aperture signal processing. A schematic diagram of the projectors and receivers are shown in Figure 17a. The receiver locations are shown as small yellow squares with the letter R, and the projectors are shown as larger blue squares with TX and a subscript to indicate the position. Using the array configuration shown in Figure 17, the projectors are activated from left to right in a repeating sequence ($\mathrm{TX_L} \rightarrow \mathrm{TX_{LC}} \rightarrow \mathrm{TX_C} \rightarrow \mathrm{TX_{RC}} \rightarrow \mathrm{TX_R}$) as the sonar system transits a survey track. This permits SAS beamforming in both the along-track and cross-track directions independently. The performance gains of this design are described in detail in the Phase 1 Technical Report [19]. A photo of the rear (top) of the array is shown in Figure 17b. The ten yellow cables each lead to eight channel hydrophone modules. The five black cables lead to the acoustic projectors. In Figures 16 and 17b the array is shown in the stowed/transit position; the array is lowered into the water with a davit crane for acoustic surveys.

A block-diagram detailing the various onboard and offboard sub-systems is shown in Figure 18. Commercially available hardware is shown in green blocks, while custom designed electronics are shown in blue blocks. The wet sensors (hydrophones and projectors), which are all custom designed by ARL/PSU, are shown as blue circles. The central interface is provided by a National Instruments (NI) data acquisition (DAQ) chassis and components. The NI DAQ system is responsible for:

- interfacing with ping timing messages provided by the operator workstation,
- receiving navigation data from the navigation sensors,

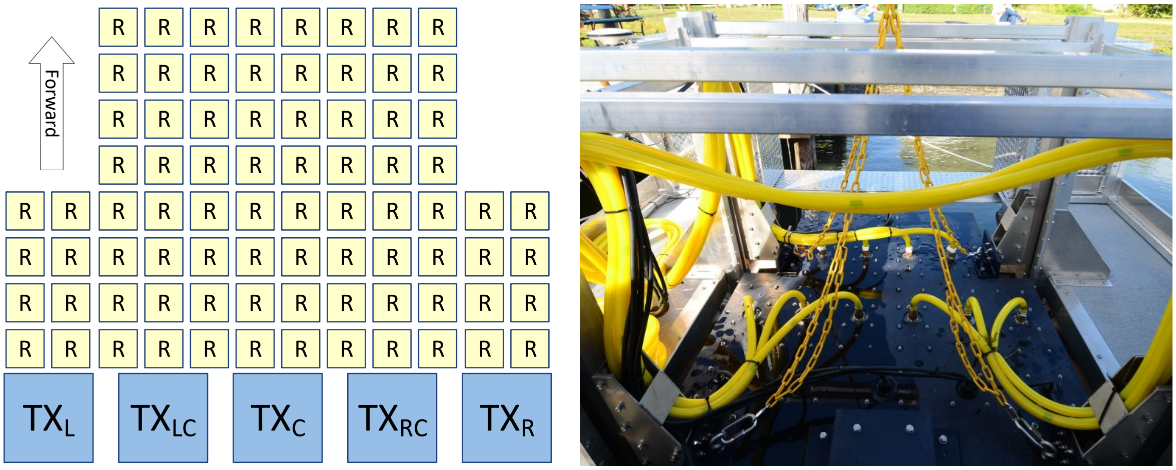

(a) **(b)**

Figure 17: A schematic diagram and photo of the Sound Hunter array configuration are shown in (a) and (b), respectively. The array consists of 80 receive channels, which are labeled R, and five projectors, which are labeled $\mathrm{TX_X}$.

Table 1: National Instruments components utilized in the DAQ subsystem.

Model	**Description**	**Function**
PXIe-1075	PXI Express Chassis	18-Slot Chassis to Host Components
PXIe-8880	Controller	Windows Core-i7 Control Computer
PXIe-6368	Multifunction DAQ	2 MHz — 16 channel ADC — 4 channel DAC
PXIe-6674T	Timing and Synchronization Module	10 MHz clock generation and distribution

- synchronizing clocks for digital-to-analog output and analog-to-digital input with a global positioning system (GPS) time reference,
- analog-to-digital conversion (ADC) of the 80 receive array channels, and
- digital-to-analog conversion (DAC) of the 5 transmit channels.

The DAQ subsystem consists of a sonar controller (PXIe-8133) that interfaces with hardware for distributing an accurate clock (PXIe-6674T), a GPS receiver to discipline this clock to a GPS reference (PXIe-6683H), and hardware for sonar signal generation and data digitization (PXIe-6368). The specific hardware components in the NI system and a short description are provided in Table 1. In addition to these sonar-specific functions, the DAQ merges the navigation and time data synchronously with the recorded acoustic data and records this to a network attached storage (NAS) device. Data may be read from this device during collection for in situ quality assessment or downloaded for detailed post-mission analysis.

The DAQ subsystem synchronizes the collected data with a GPS timestamp allowing for independent events to be measured in an absolute sense using UTC time. This is accomplished by using the PXIe-6683H as a GPS receiver, which is used to discipline the clock of the PXIe-6674T timing card. Additionally, the chassis backplane clocks are also derived

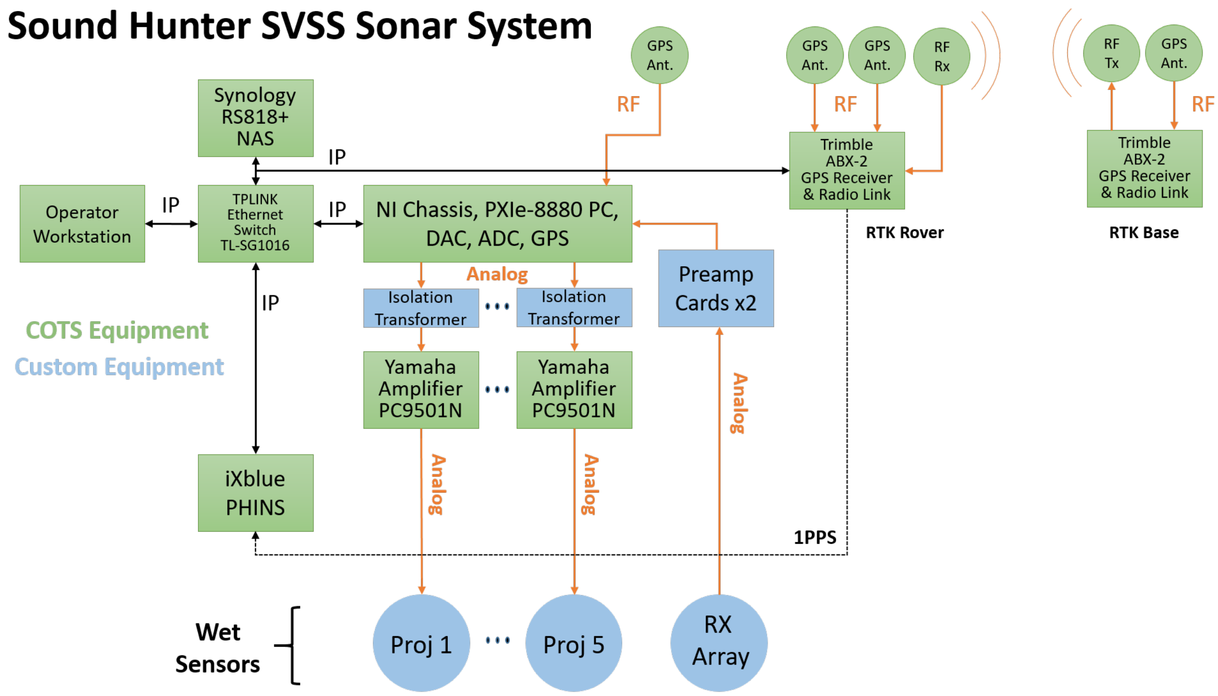

Figure 18: This diagram shows the major onboard and offboard components of the SVSS system. The majority of the equipment is COTS (green), while some specialized electronics and the wet sensors (blue) are custom designed and fabricated by ARL/PSU.

from GPS time source allowing for tight control over transmissions and reception times. This timing design provides 100 ns absolute accuracy for all sensor timestamps.

The transmit subsystem provides 5 analog channels that each consist of a DAC, a power amplifier, and an acoustic projector. Yamaha PC9501N two-channel power amplifiers support an operational band of 20 Hz to 50 kHz, and provide a maximum of 38 dB of gain to the input signal when operating in a bridged one-channel mode. Two different acoustic projectors have been designed and fabricated under the SVSS program. These projectors are detailed in Section 4.2.2. The primary projector used under this program transmitted a linear frequency modulated waveform spanning 20 kHz–35 kHz with a peak level of 186 dB re µPa @ 1m.

The receive subsystem contains 80 channels that each consist of an ADC, a signal conditioning circuit, and an acoustic hydrophone. The ADCs digitize the data at a resolution of 16-bits using successive approximation register. The digitization rate is configurable up to 2 MHz, and the majority of the SVSS data has been collected with a sample rate of 125 kHz. The signal conditioning circuit implements a single pole high-pass filter and an eight-pole, antialiasing, low-pass filter with user-selectable corner frequencies. The signal conditioning circuit also provides variable gain over the range 0 dB–40 dB. The variable gain stage gives flexibility to vary the receive sensitivity in response to changing water depth and sediment type.

The hydrophone array is constructed of ten individual hydrophone modules, each containing eight channels. The individual modules are configured in a two-channel by four-channel

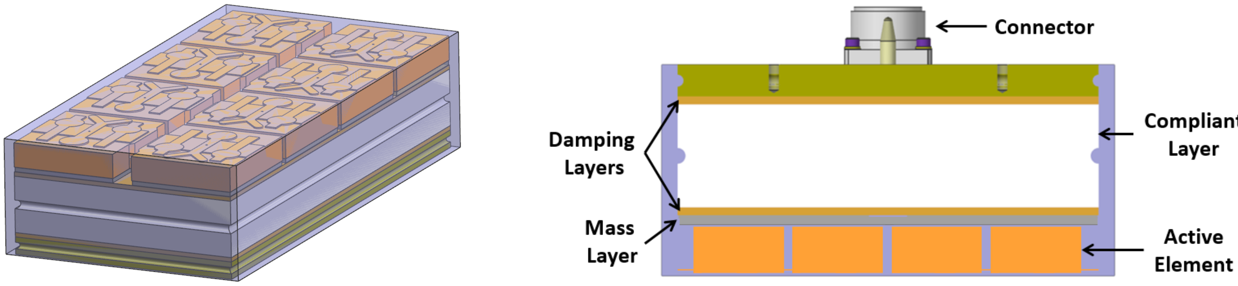

(a) (b)

Figure 19: A solid model of an eight-channel SVSS hydrophone module is shown in (a). The piezoceramic elements are mounted on a mass-damping-compliance-damping isolator stack to increase the directivity of the sensor (b).

geometry. These modules are designed so that when mounted adjacent to one another they create arrays with a 9.14 cm center-to-center hydrophone spacing in both the along-track and cross-track directions. In this arrangement, the sonar array has a total length of 73 cm in the along-track direction and a width of 1.1 m in the cross-track direction. The individual hydrophone piezoceramic elements are manufactured by ITT Exelis/EDO. ARL/PSU fabricates the hydrophone modules by bonding these elements to a baffle that provides passive multipath isolation through a controlled resonance mounting scheme. A solid model and schematic of the hydrophone mount design are provided in Figure 19. The baffle structure is schematically shown in Figure 19b where the active piezoceramic elements mounted on a mass-damping-compliance-damping isolator stack. This layered construction creates a low-frequency resonance that decouples the receiving element from the structure over the band of interest. The result is a hydrophone that is insensitive to acoustic energy incident on the "back" of the sensor, which is critical to multipath suppression.

Accurate centimeter-scale global positioning of the SVSS is achieved with a combination of a fiber-optic inertial navigation system (INS) and GPS augmented with a Real-Time Kinematic (RTK) base station. The INS used by the SVSS is an IxBlue PHINS, and it is configured to provide navigation updates at a rate of 20 Hz in the *IXBLUESTDBINV2* format [41]. The navigation solution of the INS is aided by the external GPS reference. A Trimble ABX-Two GPS receiver is used to provide a dual antenna RTK solution to the INS. RTK-aiding of the GPS removes some of the local atmospheric effects, and experimentation with and without this aiding showed that it is critical to achieve high-accuracy target localization.

The Sound Hunter includes a custom heads-up display (HUD) developed to assist the pilot in positioning the platform precisely and ensuring complete survey coverage. Figure 20 shows an example HUD screenshot taken during testing at the Aberdeen Test Center in the Bush River. The pilot can select a set of waypoints, corresponding either to known target positions for informed surveys or grid points for uninformed surveys, and has the ability to overlay waylines to aid course adjustments of the platform. As each of the waypoints come within a specified radius from the center of the sonar array, the point changes from a red X to a green square to indicate coverage of that region. The HUD includes various controls for

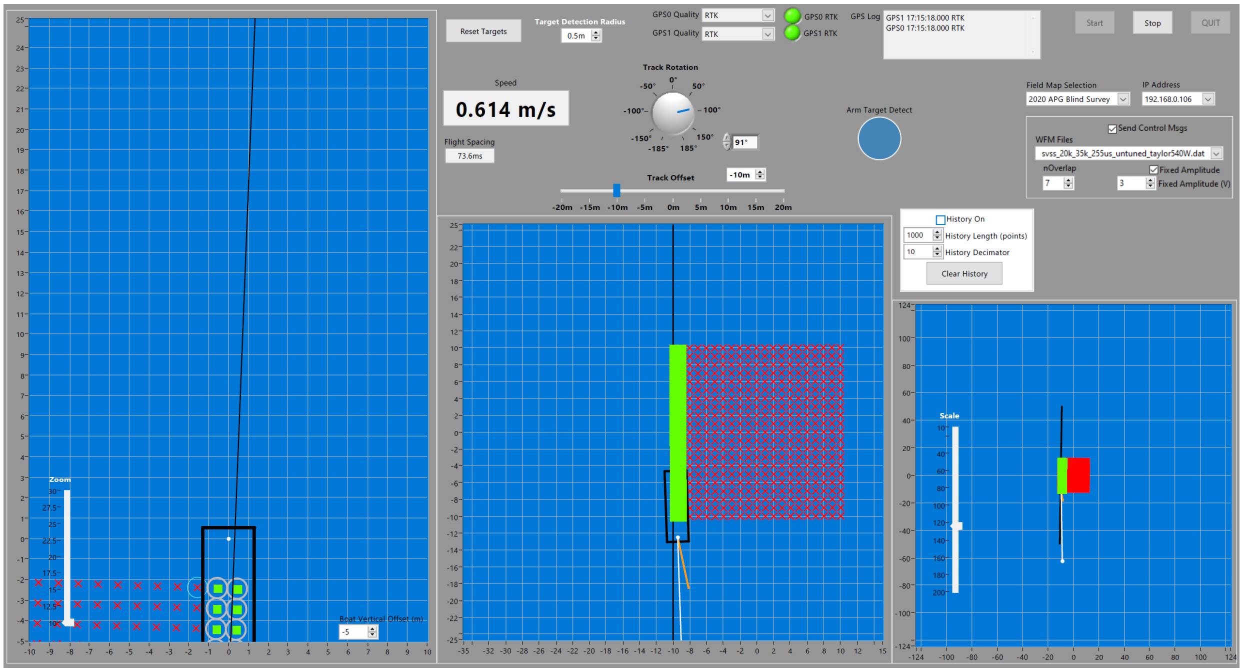

Figure 20: An example screen shot of the SVSS HUD taken during the Aberdeen Test Center Bush River testing. Various sonar and platform status and controls are provided, in addition to various tools and displays to help ensure precise maneuvering of the platform and complete survey coverage.

the sonar (e.g., waveform selection, synthetic aperture overlap), status displays (e.g., ping timing, speed, RTK-GPS status), and several displays of platform position and waypoints. Based on testing, the three most beneficial views have been a platform-referenced view where the waypoints move past the fixed sonar (Figure 20, left panel), a wayline referenced view showing the waypoints approximately centered and fixed with the platform moving (Figure 20, center panel), and a georeferenced view with waypoints centered and fixed and the platform moving (Figure 20, right panel).

4.2.2 Projector Development

Concurrent with Phase 1 modeling and simulation effort, ARL/PSU worked to identify a low-cost, commercially available transmit element, that could be modified with a mounting baffle to produce the desired beam width and passive multipath rejection. This “modified-COTS” approach was meant to provide a prototype device with lower production cost, albeit at the expense of non-ideal acoustic characteristics. The ITC-1001 transducer, which was manufactured by International Transducer Corporation (ITC), was modeled along with a number of baffle designs. Unfortunately, ITC ceased operations prior to the start of Phase 2, and ARL/PSU could not procure these transducers. ARL/PSU reached out to additional vendors; however, it was not possible to identify any commercially available transducers that could meet both our schedule and technical requirements.

To address this issue, ARL/PSU identified surplus tonpilz transducers, which were used on an unrelated project, that could be repurposed to serve as projectors for the SVSS. The design and development of this projector is described in Section 4.2.2.1. This projector design met the program's needs for a prototype sensor, and the results presented in this report are all supported with the prototype projector. Based on the results generated using this projector, ARL/PSU determined that performance would be improved with a projector that could provide increased source level over an increased operating frequency band. To address this, a second broadband projector has been designed and fabricated, and that effort is described in Section 4.2.2.2.

4.2.2.1 SVSS Prototype Projector As a fallback plan to the original "modified-COTS" design, ARL/PSU built a custom projector based on an existing tonpilz transducer element. These tonpilz elements were surplus items, and were provided to the program at no cost. A tonpilz projector is typically built from an array of tonpilz elements mounted in an air-backed housing. While the design of this housing adds additional design cost, it does have one distinct advantage: the housing's air-filled back volume creates a significant baffling effect that limits the sensitivity of the projector in the aft direction. For the current use case (downlooking), this design reduces multipath interference by attenuating the transmitted field in the direction of the air-water interface.

The tonpilz elements are connected to a mount, or "web," within the housing. The design of the web must provide the proper element location and spacing to achieve the desired beam pattern from the active face of the transducer. It must also provide acoustic isolation of the elements from the non-active surfaces of the housing and between each other. This acoustic isolation is critical to reduce unwanted radiation that may contribute to multipath interference.

The transducer element used in this design has a nodal attachment to the mount. This type of attachment assumes that the transducer element mounting plate is located at a "minimum" displacement location in the ceramic motor section, or a node. This does not mean zero displacement. As such, when the transducer is driven to produce sound from the radiating head, it must react against the mounting location. In order to reduce the amount of vibration from the nodal drive point that reaches the array housing, there must be an additional amount of isolation provided between it and the transducer elements. The mount design is a layered damping media with metallic constraining septum concept. The forward septum provides a rigid mounting surface for element alignment in the array. The middle layers consist of polyurethane and corprene (a rubberized cork) for damping. The aft septum acts as a rigid mounting surface for the array housing and a reflective layer because of the impedance mismatch. Corprene, whose characteristic impedance is five times lower than water/urethane, also provides acoustic isolation primarily through impedance mismatch. The SVSS projector design arrangement is shown in Figure 21. It should be noted that while this design is relatively inexpensive and effective, it can only be used in low hydrostatic pressure (i.e., shallow water) conditions.

The prototype projectors have been calibrated in the ARL/PSU Anechoic Test Facility

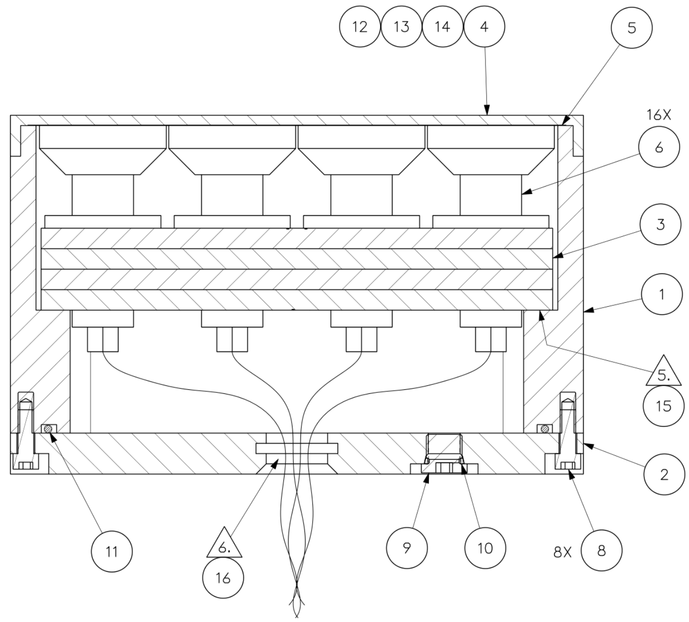

Figure 21: Drawing showing the cross section of the prototype projector array, mount, and housing. One of the tonpilz elements is called out as item 6, and the layered mount that provides element isolation is called out as item 3.

(ATF). Full details of those calibrations are provided in Appendix B; some summary results are presented here. The front-to-back ratio of the sound is greater than 30 dB and the sidelobe levels are less than −20 dB; an example transmit directivity pattern is shown in Figure 22. This indicates that the isolation system is working properly to both minimize the vibration from the projector elements that couples into the housing, and to reduce the element-to-element interaction so that it is not elevating the sidelobe energy. The corners of each projector's 4x4 array are amplitude-shaded, such that the aperture approximates a circular piston that should have a maximum of −17.8 dB secondary lobes, relative to the main lobe of the pattern at 20 kHz. Figure 22 confirms this calculation since the maximum sidelobe levels are less than −20 dB.

Figure 23 shows the measured sensitivity of each projector's 4x4 array. The six projector units are well-matched over the operating frequency band. Note that at a 300 V maximum drive voltage, the projectors are capable of a source level exceeding 200 dB re µPa @ 1m over the band spanning 18 kHz–38 kHz.

The transmit voltage response (TVR) demonstrates that this projector is capable of producing a high source level over a relatively wide band. The device has elevated sensitivity near its 20 kHz resonance, which is somewhat sharp for a sonar projector. The result is that when driven at this resonant frequency, the projector continues to vibrate for several cycles with exponentially decaying amplitude after the driving voltage is removed. The duration

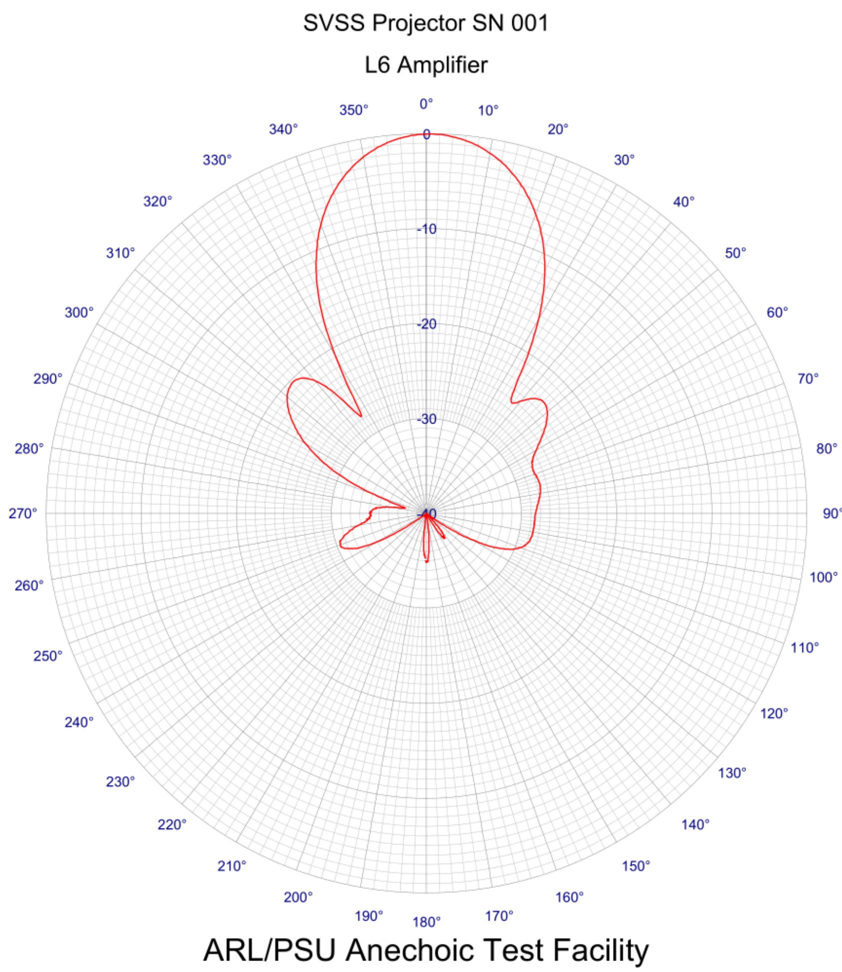

Property	Value
Peak Level (dB)	159.93
Peak Angle (deg)	0.39
Pattern Index (dB)	17.04
3 dB Beamwidth (deg)	26.92
6 db Beamwidth (deg)	37.4
10 dB Beamwidth (deg)	47.04
Max SideLobe Lvl (dB)	-20.29

Figure 22: The fabricated prototype projectors were characterized in the ARL/PSU anechoic test facility. This figure shows one device's directivity pattern measured at 20 kHz. A full characterization can be found in Appendix B.

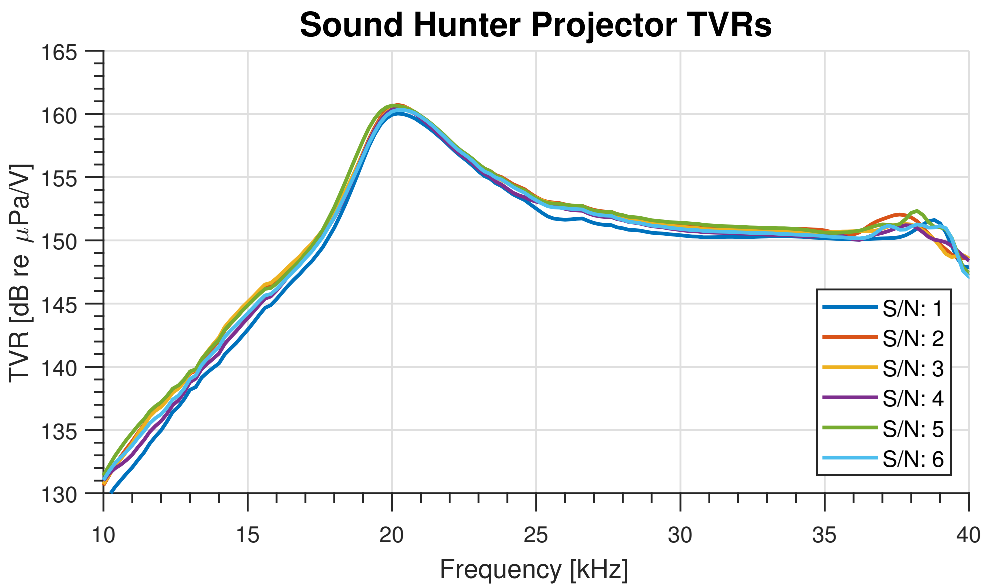

Figure 23: Projector transmit voltage response for each of the six 4x4 array units. These projectors are well matched over the 10 kHz–40 kHz frequency band.

of the exponential ring-down is determined by the device's mechanical quality factor

$$Q_m = \frac{1}{2}\omega_0\tau = \frac{\omega_0}{\omega_u - \omega_l}, \tag{1}$$

where τ is the time for the resonance to decay by e^{-1} and ω_0 is the resonance frequency. ω_l and ω_u are the frequencies of the lower and upper half-power TVR, respectively. These projectors have a Q_m of about 7. A large Q_m implies a highly resonant device where the TVR around resonance is peaked and the decay time at resonance is large. The resonance effect is apparent in Figure 24a, where waveforms are shown for a pair of transmitted signals. Both signals are linearly frequency modulated (LFM) chirps spanning 15 kHz with pulse lengths slightly greater than 0.25 ms. To reduce temporal sidelobes, the same Taylor window ($\bar{n} = 5$ and SLL $= -40$ dB) was applied to both waveforms [42]. The 12 kHz–27 kHz signal persists for significantly longer than the applied voltage, and additional analysis has shown that the exponentially decaying "tail" is due to the device responding at the 20 kHz resonance frequency. This effect is substantially reduced for the 20 kHz–35 kHz waveform because the Taylor window reduces the drive level applied at 20 kHz.

The device's resonant structure at 20 kHz impacts the vertical resolution of waveforms projected that excite this frequency. Figure 24b compares the auto-ambiguity functions (AAFs) for the pair of candidate waveforms. The auto-ambiguity function shows the temporal resolution for the pair of transmitted waveforms after replica correlation. Theoretically, the two waveforms should have the same temporal resolution because they both cover 15 kHz of bandwidth. However, this figure shows that the extended response at 20 kHz for the 12 kHz–27 kHz signal has broadened the ambiguity function significantly, by a factor of 3 or more.

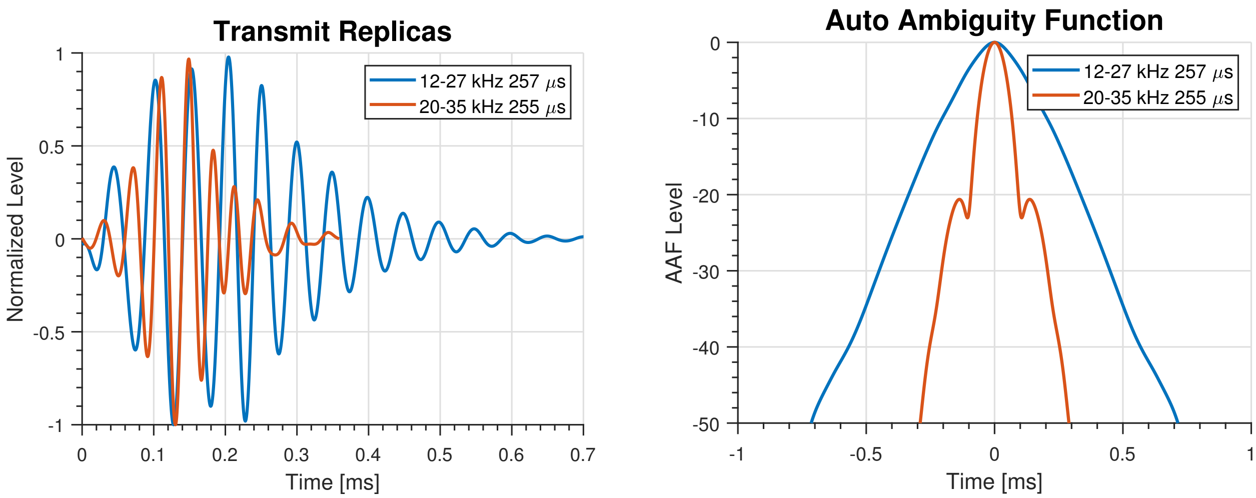

(a) **(b)**

Figure 24: Replicas are shown for a pair of LFM signals each spanning a 15 kHz bandwidth (a). The resonant response of the projector at 20 kHz significantly extends the length of the 12 kHz–27 kHz waveform, which results in a broader auto ambiguity function (b).

The qualitative impact on image resolution is shown for a pair of cross-track maximum intensity projections in Figure 25. Details regarding the formation of a two-dimensional maximum intensity projection (MIP) image are provided in Section 4.3.2. The data used to reconstruct the upper image in this pair was collected using the 12 kHz–27 kHz signal and the data for the lower image was collected using the 20 kHz–35 kHz signal. A common pair of targets are highlighted with red boxes in these two images, and the impact of the ambiguity function width is seen by comparing the depth resolution for each target. The targets appear "smeared" in the depth direction within the upper image due to the wider ambiguity function. For this reason, the bulk of SVSS testing was conducted using the 20 kHz–35 kHz operating band.

4.2.2.2 SVSS Broadband Projector Previous sections point toward the need for broader bandwidth capability and lower Q_m devices to provide fidelity to the transmit waveforms. Lower Q_m, or higher damping, reduces transducer ringing, as the device wants to ring down at its fundamental resonance frequencies. In this case, lower Q_m is achieved by optimally coupling the transducer's acoustic impedance to that of water. To do this, higher coupling materials can be used, and to some extent, the area transformation between the motor section and the head mass can be optimized. Both of these design considerations were addressed through engineering a new transducer element.

The requirements for low-Q_m and broader bandwidth capability are being addressed in many sonar areas through newer piezoelectric compositions and morphologies. The rediscovery of excessively high piezoelectric constants and electromechanical coupling coefficients of single crystalline relaxor-based ferroelectrics in the late 1990s have sparked innovation in sonar

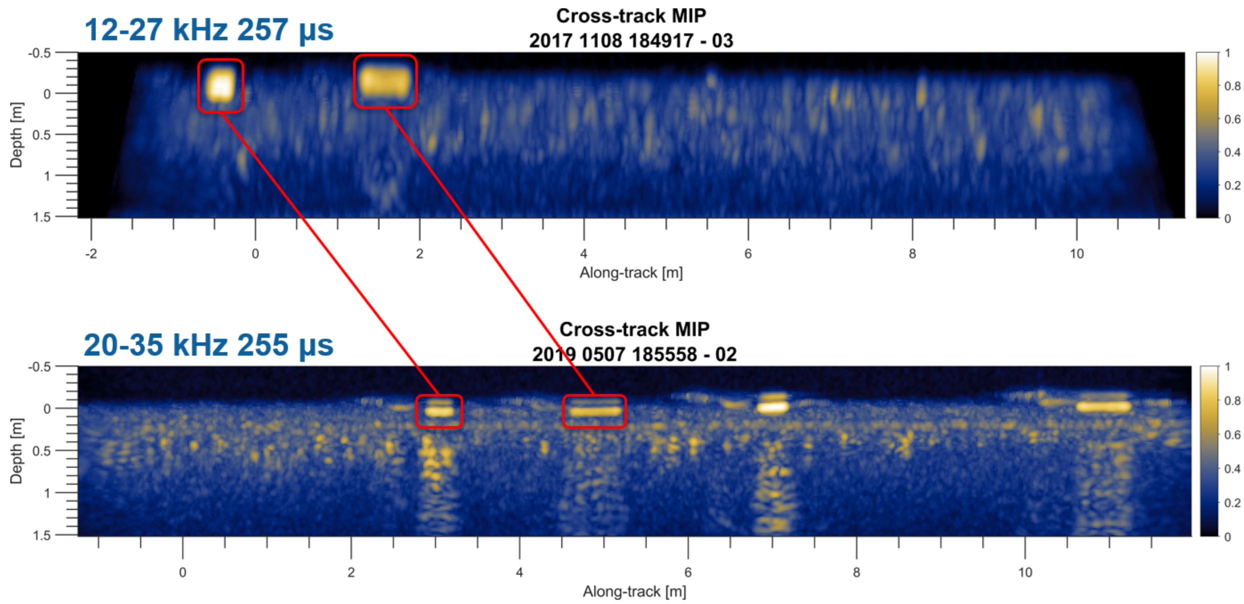

Figure 25: The impact of the ambiguity function width on depth resolution is seen in this pair of cross-track maximum intensity projections. The width for the signal used in the upper image is significantly longer in time, resulting in a "smearing" of the image along the depth direction. The red boxes indicate a pair of common targets. The MIP formation process is described in Section 4.3.2.

transducer bandwidth and packaging. More recently textured piezoelectrics have been taken from the laboratory and demonstrated in full production capacity. Textured piezoelectric ceramics are a low-cost method to control ceramic microstructures to mimic single crystal properties in one or more directions. These piezoelectrics were investigated in a traditional tonpilz element for this effort.

Three piezoelectric motor sections were modeled using finite element analysis to determine suitability for this application. Traditional lead zirconate titanate (PZT-8) ceramic, single crystal lead indium manganese niobium titanate (PIMNT), and textured PIMNT were all studied. The motor section geometry was adjusted to provide a similar resonance frequency, f_n, while keeping the head mass and tail mass constant. Figure 26 shows the comparison of single element results in terms of acoustic output referenced to $1\,\mathrm{V_{rms}}$ drive. In this comparison, single crystal provided the lowest Q_m resonance and the highest bandwidth of the three candidate materials. This performance was followed closely by textured PIMNT. Both the single crystal and textured ceramics meet the minimum Q_m and bandwidth requirements for this effort. The mechanical Q_m, electromechanical coupling and notional cost is summarized in Table 2. Given the program goals for eventual commercialization, the low-cost textured ceramic approach was chosen over single crystal for final implementation.

Further revisions of the tonpilz design were made to exploit design features to further reduce the mechanical Q_m while maintaining the necessary acoustic output and bandwidth. Stack

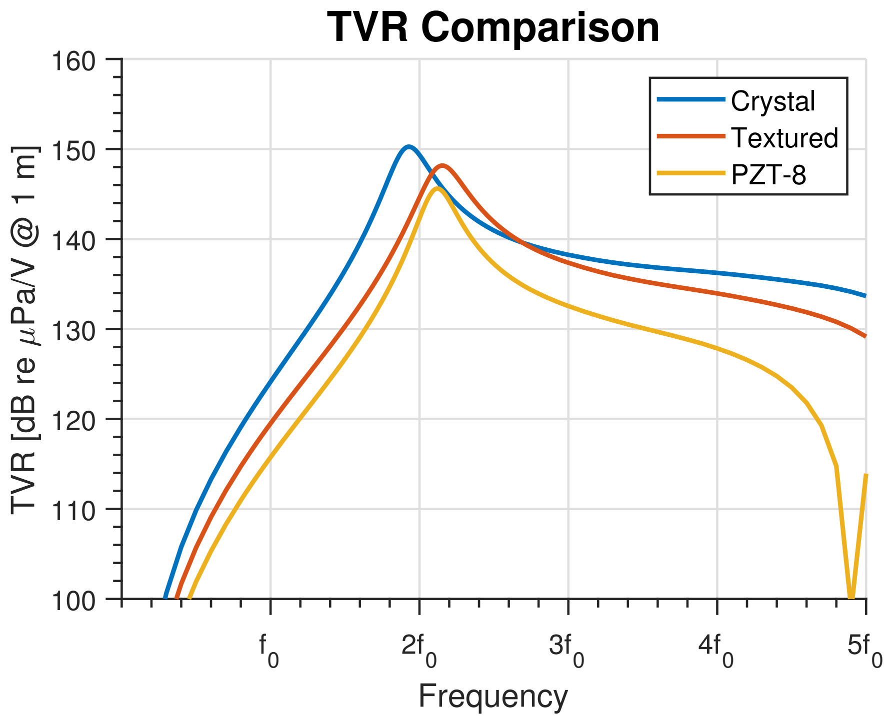

Figure 26: Comparison of the TVR of simulated tonpilz elements incorporating three candidate materials. The frequency axis is normalized by $f_0 = 10\,\mathrm{kHz}$

Table 2: Summary of the relevant metrics derived from finite element model results of a single element tonpilz transducer with three different active materials used as the motor section. The number of ceramic rings in the tonpilz element are specified and k_{eff} is the effective electromechanical coupling coefficient.

Material	# Rings	f_n	Q_m	k_{eff}	Cost
Crystal	6	$2f_0$	6.9	0.844	$$$$$
Textured	8	$2f_0$	6.9	0.72	$$$
PZT-8	12	$2f_0$	8.8	0.579	$$

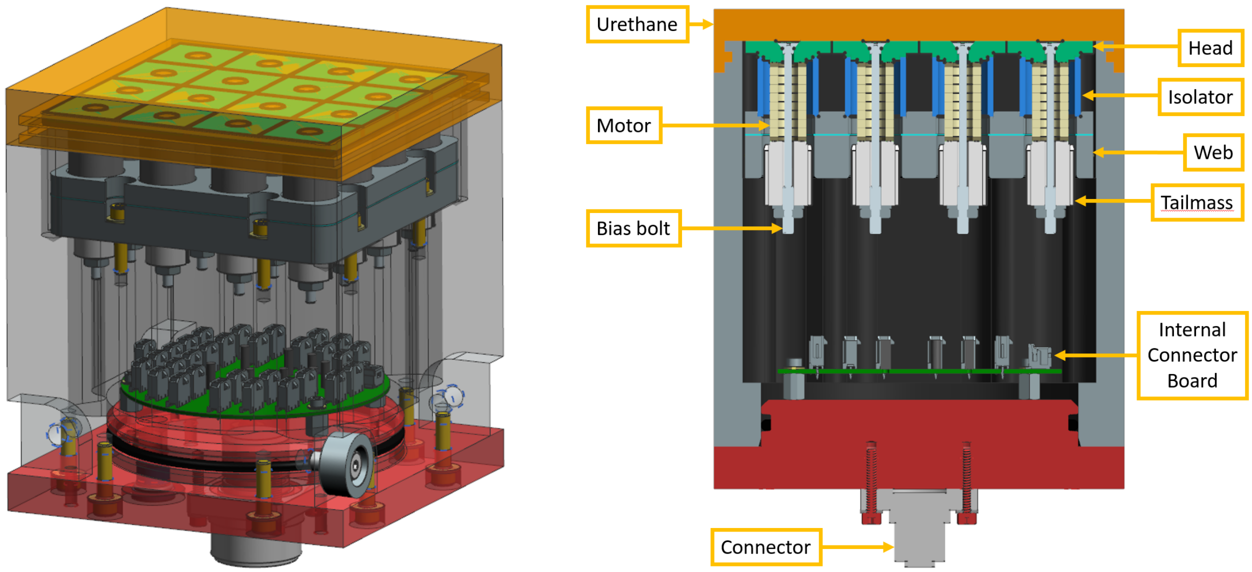

(a) (b)

Figure 27: A three-dimensional model (a) of the broadband projector shows the interior and exterior geometry of the device. A two-dimensional cross section (b) is labeled to show the individual projector components.

outside diameter, inside diameter and length coupled with head and tail mass ratios were the primary optimization variables that were tuned in the simulation. The final tonpilz design consisted of an aluminum beryllium metal matrix [43] (AlBeMet®) head mass, tungsten tail mass and textured piezoelectric stack consisting of eight rings and alumina end pieces.

The final array design had 16 tonpilz elements in a 4x4 matrix arrangement. A computer aided drafting schematic of the array is provided in Figure 27. The array consists of a housing, transducer web, isolation mount, elements and an acoustic window. To fabricate the array, over 1000 textured ceramic disks were made. During the production, each ring was serialized and all processing conditions and in-process measurements were recorded for traceability.

Array performance was evaluated in the ARL/PSU ATF. Projector calibrations consisted of frequency response, beam patterns, linearity check and waveform fidelity. Figure 28 shows the transmit voltage response of the first four serial numbers in comparison to the finite element simulation of the array. The measured data and the simulated data agree reasonably well. Each array performs within 1 dB–2 dB across the frequencies of interest for this application showing consistency of the piezoelectric material and array fabrication steps. Each array was driven to higher voltages to increase sound pressure levels to program objectives in order to evaluate the linearity. Up to cavitation thresholds, the arrays were observed to be linear; thus cavitation limits set the upper bound for achievable sound pressure levels.

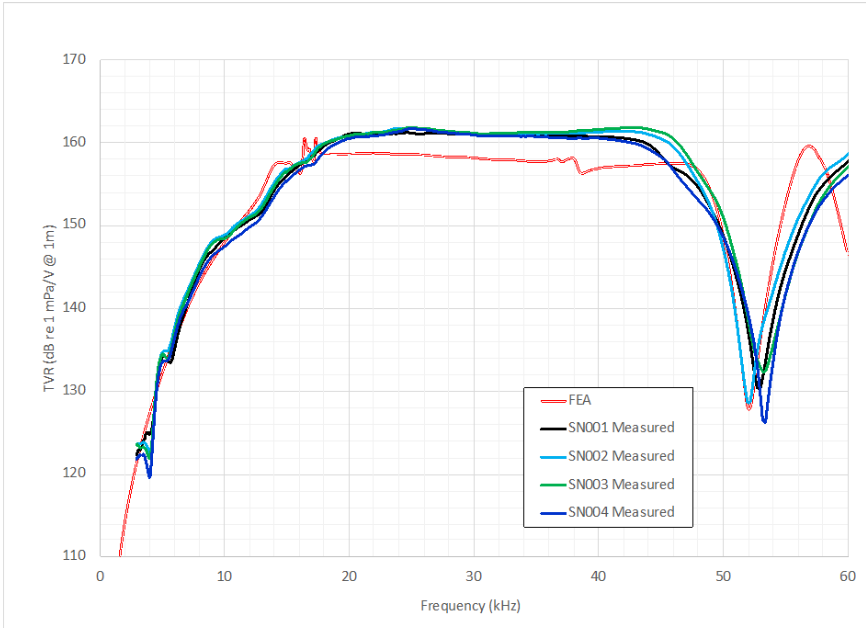

Figure 28: The broadband projector TVRs are compared to the finite element analysis (FEA) predicted TVR.

In addition to these frequency response measurements, acoustic beam patterns were evaluated by rotating the array and measuring the response off bore sight. Broad band patterns are shown in Figure 29a. Symmetry in the patterns about the main response axis as well as the depth of null between the main lobe and side lobes is an indication of the quality of the array and how well matched the individual elements are in terms of their phase and vibration velocity magnitude. The measurements of these patterns match theory with respect to main lobe width and the side lobe levels and symmetry confirm high quality array fabrication.

Finally, a replica was captured for a 0.25 ms LFM chirping 12 kHz–44 kHz with a Taylor window ($\bar{n} = 5$ and SLL $= -40$ dB). The associated ambiguity function is shown in Figure 29b compared to the standard 20 kHz–35 kHz waveform used with the prototype projector. The -3 dB width shows that in future data collections the new broadband projector will improve the SVSS vertical resolution and the greatly reduced sidelobe levels will improve sub-bottom image contrast.

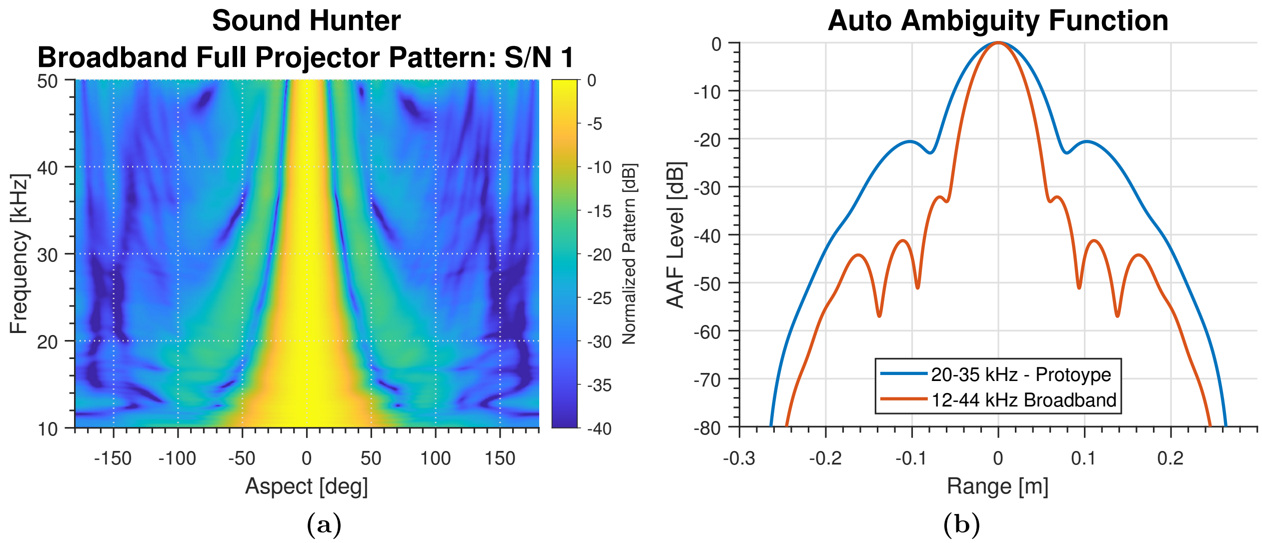

Figure 29: Broadband beam patterns are shown (a) for the broadband projector. The prototype and broadband projector's ambiguity functions are compared in (b). The improved bandwidth and lower mechanical Q_m result in a projected waveform that will substantially improve sensor resolution and reduce sidelobe level.

4.3 Signal and Image Processing Development

When conducting a survey, the SVSS sensor hardware described in Section 4.2 collects raw acoustic time series data scattered from the seabed. This raw data requires a series of signal and image processing steps to create imagery that can be analyzed for targets. These processing steps include reconstruction of three-dimensional imagery, enhancement of this imagery, and creation of two-dimensional representations for human review and analysis. In this section, the various signal processing methods applied to SVSS data are described. Three-dimensional image reconstruction is described in Section 4.3.1. Reconstructed image enhancement and reduction to two-dimensional representations is described in Section 4.3.2.

4.3.1 Image Reconstruction Algorithm Development

The raw data generated by the SVSS sensor must be processed in order to form three-dimensional imagery of the seafloor and sub-bottom. The process of converting from raw sensor data to an image is called image reconstruction or beamforming. A number of reconstruction algorithms have been developed in different research areas including radar imaging [21], seismic imaging [22], and sonar imaging [23]. One technique that is known for its combination of simplicity and robustness is backprojection [24].

The central concept in backprojection is an inversion of the forward propagation and scattering model through time-domain manipulation of the recorded signals. This inversion is performed in order to form an estimate of the scattering strength of the insonified scene.

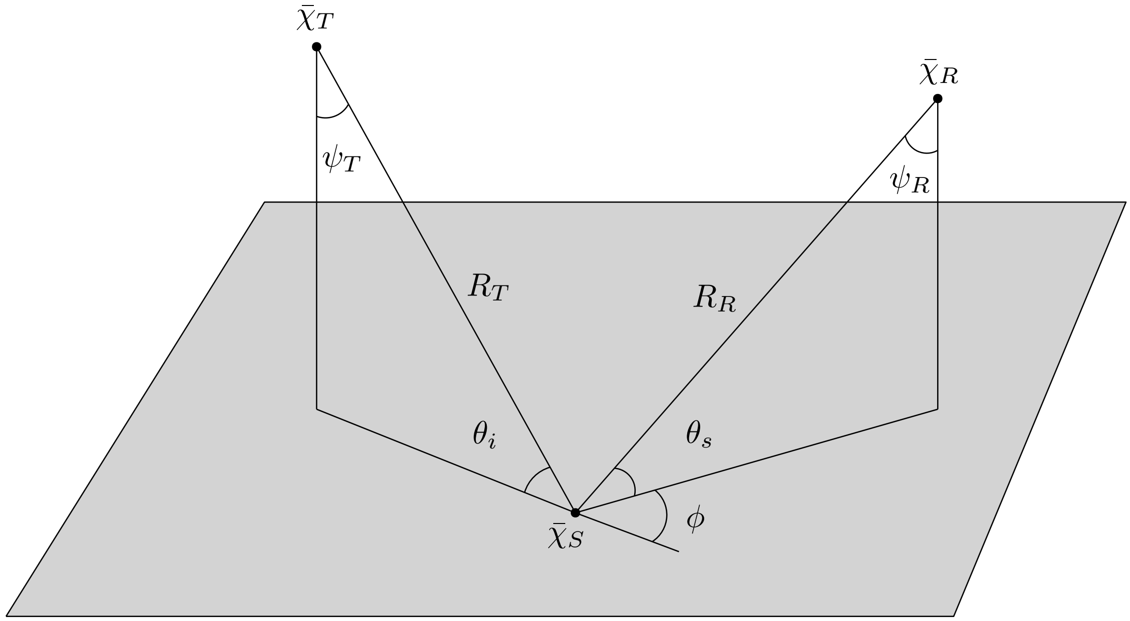

Figure 30: The field projected by a transmitter at $\bar{\chi}_T$ is scattered from an interface point at $\bar{\chi}_S$ and is received at $\bar{\chi}_R$.

The pixel at a position $\bar{\chi}_S$ is reconstructed by coherent summation of N signals according to

$$f(\bar{\chi}_S) \propto \sum_{n=1}^{N} w(\bar{\chi}_{Tn}, \bar{\chi}_{Rn}, \bar{\chi}_S) p_n \left(\frac{|\bar{\chi}_S - \bar{\chi}_{Tn}| + |\bar{\chi}_S - \bar{\chi}_{Rn}|}{c} \right) \tag{2}$$

where the geometry defined in Figure 30, c is the sound speed, and $p_n(t)$ is the n^{th} scattered field recorded for transmitter position $\bar{\chi}_{Tn}$ and receiver position $\bar{\chi}_{Rn}$. Finally, $w(\bar{\chi}_{Tn}, \bar{\chi}_{Rn}, \bar{\chi}_S)$ is a weighting function applied to the aperture.

When compared to other reconstruction techniques, the backprojection algorithm has a relatively intuitive interpretation. Equation 2 states that every beamformed pixel consists of the accumulation of a number of weighted and delayed time series. For this reason, the backprojection algorithm is often described as "delay-and-sum" reconstruction.

ARL/PSU's implementation of a backprojection beamformer is called the Advanced Synthetic Aperture Sonar Imaging eNgine (ASASIN) [25]. ASASIN was originally implemented to generate high-resolution SAS imagery from both high-frequency (>100 kHz) and mid-frequency (∼10 kHz) imaging sonar systems. Each of the imaging sonar systems supported by ASASIN generates two-dimensional imagery from one-dimensional receiver geometries. Additionally, the region imaged on the seafloor is typically in the far-field of the physical sonar system. Neither of these are true for SVSS data; consequently, several changes were made during the first phase of the SVSS program to adapt ASASIN to near-field volumetric beamforming. The primary changes were to:

1. calculate independent transmitter and receiver element field-of-views prior to backprojection,

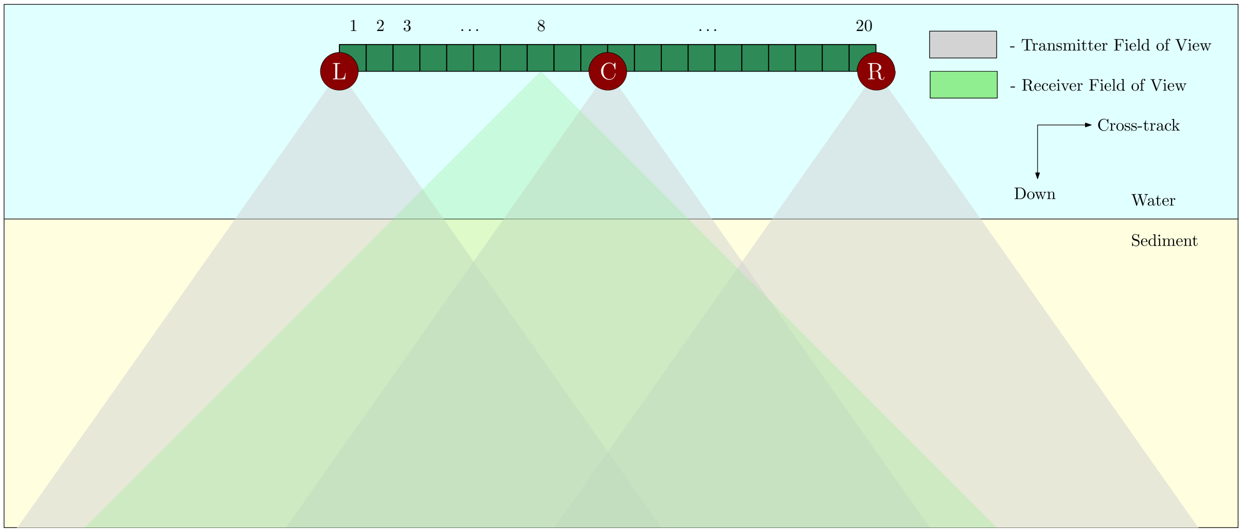

Figure 31: A linear twenty channel receive array with three transmitters is shown above a sediment/water interface. The notional field of view for each transmitter is shown by a gray triangle. The field of view of receiver channel eight is shown by a green triangle. Only those pixels that are within the shaded region given by the logical AND of a transmitter field of view and a receiver field of view are impacted when backprojecting any single signal.

2. include a sediment-water interface refraction model in determining propagation time, and

3. enable three-dimensional data output and provide three-dimensional image views.

The first change addresses the SVSS's bistatic imaging geometry. In Equation 2, the weighting function w is shown to be dependent on both the transmit position, $\bar{\chi}_T$, and the receive position, $\bar{\chi}_R$. One use of this weighting function is to restrict the integration of the raw data to those recorded signals that are in the field of view of both the transmitter and the receiver for each ping. In this way, w acts as a rectangle function that defines a subset of pixels that may be contributed to by any single recorded time series. In other applications, this binary component of the weighting is commonly made assuming a transmit/receive pair is monostatic, which reduces the beamforming complexity and reduces image formation time. This monostatic approximation is valid in the standard imaging domain because the backprojection point is frequently in the far-field of the physical transmit and receive aperture. However, this approximation is invalid for the SVSS, and the bistatic condition must be considered.

A graphical interpretation of the binary component of the bistatic function w is provided in Figure 31. Here, a hypothetical sonar system is shown with a twenty-channel receive array (dark green squares) and three transmit channels (dark red circles). Note that this array is near the sediment-water interface. The field of view of each transmitter is shown as a gray triangular region. The transmission from any specific transmitter may contribute only to the scattering from the segment of the seafloor within its field of view. The field of view of receiver channel eight is shown as a green triangular region. Data from receiver channel eight can contribute only to pixels within its field of view. Therefore, only those pixels that are within the shaded region given by the logical AND of a transmitter field of view and a receiver field of view are impacted when backprojecting any signal that arises from a single transmitter.

Traditional SAS beamforming typically assumes an isovelocity (constant sound speed) propagation path between the sensor and the imaging point. While this isovelocity approximation is rarely true, small deviations in sound speed have only a minor effect on image quality [44]. In the case of larger deviations, autofocusing techniques may be applied to recover some loss of focus quality [45]. SVSS imaging within the seafloor may present the backprojection algorithm with a discontinuity in sound speed much greater than that ever observed for propagation solely in water. Fortunately, the backprojection algorithm is well suited to this type of modification. For any desired imaging point, one only has to provide a model for the propagation time from the source to the imaging point and from the imaging point back to the receiver. This model was implemented in ASASIN as a root solver during Phase 1. Extensive testing in Phase 2 revealed numerical instability for some imaging conditions. A new implementation of the (up to) fourth-order root-finding algorithm has been developed. Under some circumstances the condition of the system can become stiff or even ill-conditioned, which can adversely affect the accuracy of the computed roots. This new root finder overcomes some of the previous difficulties encountered with its predecessor, which required special treatment in order to handle numerically challenging situations.

The primary ASASIN output data type is called the Science product. The Science product is written using the open Hierarchical Data Format version 5 (HDF5) format [46]. This data format was extended to support three-dimensional data output. A Science file includes complex output imagery, navigation information, environmental information, and system parameters. A detailed list of the data included in this format is provided in Table 3. A batch processing framework has also been established for post-processing the beamformed imagery. In this framework, a directory of raw SVSS data is recursively processed to generate data representations such as image slices or projections. These data products are discussed in Section 4.3.2.1. Where appropriate, these new output products can be georeferenced using the information provided in the /Geodesy/ group.

Finally, ARL/PSU has optimized many of the ASASIN modifications for speed or memory usage. Global memory management was improved, and a more efficient use of hardware registers resulted in increased performance. Data conditioning and FFT algorithms have been updated to be more memory efficient and provide higher performance. File I/O has been updated to reduce the likelihood of disk contention, which increases file-reading performance. Finally, logging has been improved to provide more useful information and more details on error conditions.

Table 3: ASASIN generates the Science data product, which is an HDF5 file containing processed sonar imagery as well as information about the data collection and signal processing algorithms. The output stored in /Data/ has dimensions MxNxL where M is along-track, N is cross-track, and L is depth. The image is formed using P sequential transmissions (pings) of the sonar system. The version number in the final column indicates the science file version where each dataset was added to the format.

Dataset Name	Size	Type	Units	Version
/Version	1x1	Float64		1.0
/ASASIN	3x1	UInt32		1.0
/Sensor	1x1	Enumeration		1.6
/Side	1x1	Enumeration		1.0
/Data/Imag	MxNxL	Float32		1.0
/Data/Real	MxNxL	Float32		1.0
/Environment/Salinity	1x1	Float32	PPT	1.2
/Environment/SoundSpeed	1x1	Float32	meters/second	1.2
/Environment/Temperature	1x1	Float32	Celsius	1.2
/Geodesy/WGS84				1.1
/Geodesy/WGS84/CoordinateTransformation	4x4	Float64		1.1
/ImagingGrid/Offset	1x3	Float32	meters	1.5
/ImagingGrid/Step	1x3	Float32	meters	1.5
/Metrics/DpcCorrelation	1x1	Float32		1.0
/Metrics/ImageQuality	1x1	UInt32		1.3
/Nav/Acceleration	Px3	Float32	meters/second^2	1.0
/Nav/Altitude	Px1	Float32	meters	1.0
/Nav/Course	1x1	Float64	radians	1.0
/Nav/Depth	Px1	Float32	meters	1.0
/Nav/Latitude	Px3	Float64	radians	1.0
/Nav/Longitude	Px1	Float64	radians	1.0
/Nav/Pitch	Px1	Float32	radians	1.0
/Nav/PitchRate	Px1	Float32	radians/second	1.0
/Nav/Position	Px3	Float32	meters	1.0
/Nav/Roll	Px1	Float32	radians	1.0
/Nav/RollRate	Px1	Float32	radians/second	1.0
/Nav/Time	Px1	Float64	seconds	1.0
/Nav/Velocity	Px3	Float64	meters/second	1.0
/Nav/Yaw	Px1	Float32	radians	1.0
/Nav/YawRate	Px1	Float32	radians/second	1.0
/Parameters/AdvanceLength	1x1	Float32	meters	1.8
/Parameters/AzLimit	1x1	Float32	radians	1.8
/Parameters/CenterFrequency	1x1	Float32	Hertz	1.0
/Parameters/CircleRadius	1x1	Float32	meters	1.0
/Parameters/IntermediateFrequency	1x1	Float32	Hertz	1.0
/Parameters/Pings	1x1	UInt32		1.0
/Parameters/PingsOverlap	1x1	UInt32		1.0
/Parameters/PingRange	1x2	UInt32		1.4
/Parameters/ResolutionAlongTrack	1x1	Float32	meters	1.0
/Parameters/ResolutionCrossTrack	1x1	Float32	meters	1.0
/Parameters/ResolutionDepth	1x1	Float32	meters	1.0
/Parameters/SystemSampleRate	1x1	Float32	Hertz	1.0
/Parameters/UpsampleFactor	1x1	UInt32		1.0

4.3.2 Image Processing Algorithm Development

The reconstructed three-dimensional image produced by ASASIN requires additional processing. Also, two-dimensional representations of the three-dimensional data are produced to increase human interpretability of SVSS imagery. The process of creating two-dimensional representations of three-dimensional data is covered in Section 4.3.2.1. This is followed by Section 4.3.2.2, where techniques are discussed for dynamic range compression of SVSS imagery.

4.3.2.1 Three-Dimensional Image Visualization The ASASIN beamformer is utilized to post-process SVSS data, creating imagery with voxels (i.e., three-dimensional pixels) that are 2 cm cubes. The reconstructed image forms a three-dimensional matrix of voxels that is referred to as a "data cube." An animated movie showing a reconstructed data cube is shown in Figure 32. In this animation, the x-axis (red), y-axis (green), and z-axis (blue) correspond to the along-track, cross-track, and depth dimensions, respectively, and the dimensions along these axes are 5 m, 2 m, and 2 m. Three buried targets are visible in this movie, and from left-to-right in the first frame they are a pair of solid cylinders and a buried shot put (Left: S_P07_T2D1, Center: S_P06_T3D1, Right: S_P05_T1D2). The animation is a two-dimensional rendering where any single frame is a maximum intensity projection calculated through the three-dimensional volume. The details of this type of projection are described later in this section, but the process of animating a series of frames where the data cube is rotated gives the impression of viewing the data in three dimensions. The data viewer used to create this visualization is called VAA3D [47].

Figure 33 illustrates two methods for creating two-dimensional data representations of a data cube. In Figure 33a the full three-dimensional data cube is shown. Figure 33b shows a schematic illustrating example slices through the data cube along the three principal axes. A single slice provides a two-dimensional image that can be reviewed for targets. It is important to note that any single slice excludes the majority of the data cube. Therefore, a full analysis of a single data cube requires scanning through a series of slices.

An example of a slice taken through the same data cube used to create the animation is shown in Figure 34. The slice depth was selected to pass through the pair of cylindrical targets at 3 m and 5 m along-track. There are also several additional returns that are nearly the same scattered level in the imagery. In particular, there is a strong return at 2.7 m along-track and 0.5 m cross-track, and another strong return at 6 m along-track and −0.3 m cross-track. During a subsequent test field installation period, the ends of two cylindrical targets were located and marked with flags. Using the sonar imagery, the locations of the two clutter objects relative to the two cylindrical targets were calculated. Upon placing flags at both calculated positions, the two flat rocks shown in the lower frames of Figure 34 were found and excavated. Each rock was found with a flat face oriented upward, which is the likely cause for the relatively strong acoustic return.

Another two-dimensional data representation is shown in Figure 33c. This schematic illustrates a projection of the data's maximum value along the three principal axes of the data cube to create a maximum intensity projection (MIP). Note that this type of projection is

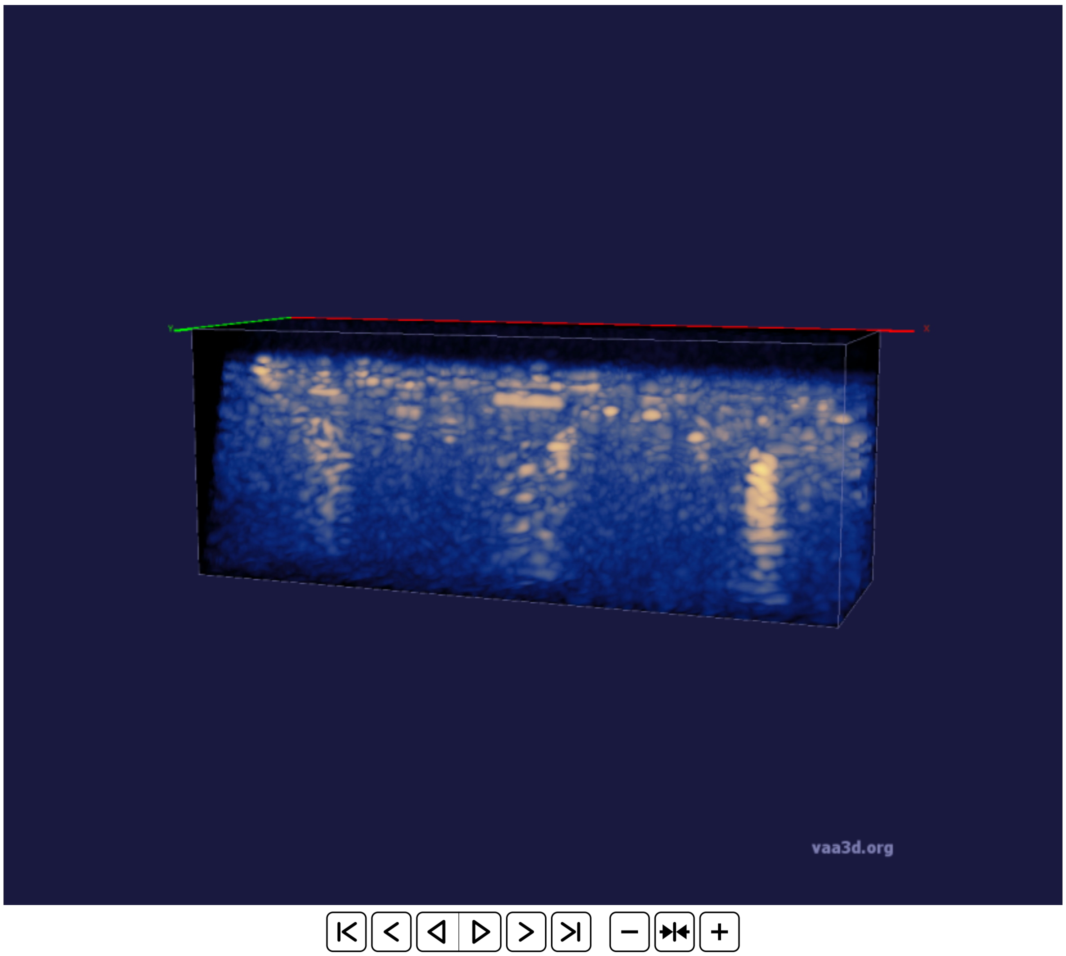

Figure 32: Three targets, S_P07_T2D1, S_P06_T3D1, and S_P05_T1D2, are shown in a three-dimensional animation. The animation is only supported when the document is viewed using an Adobe Acrobat reader.

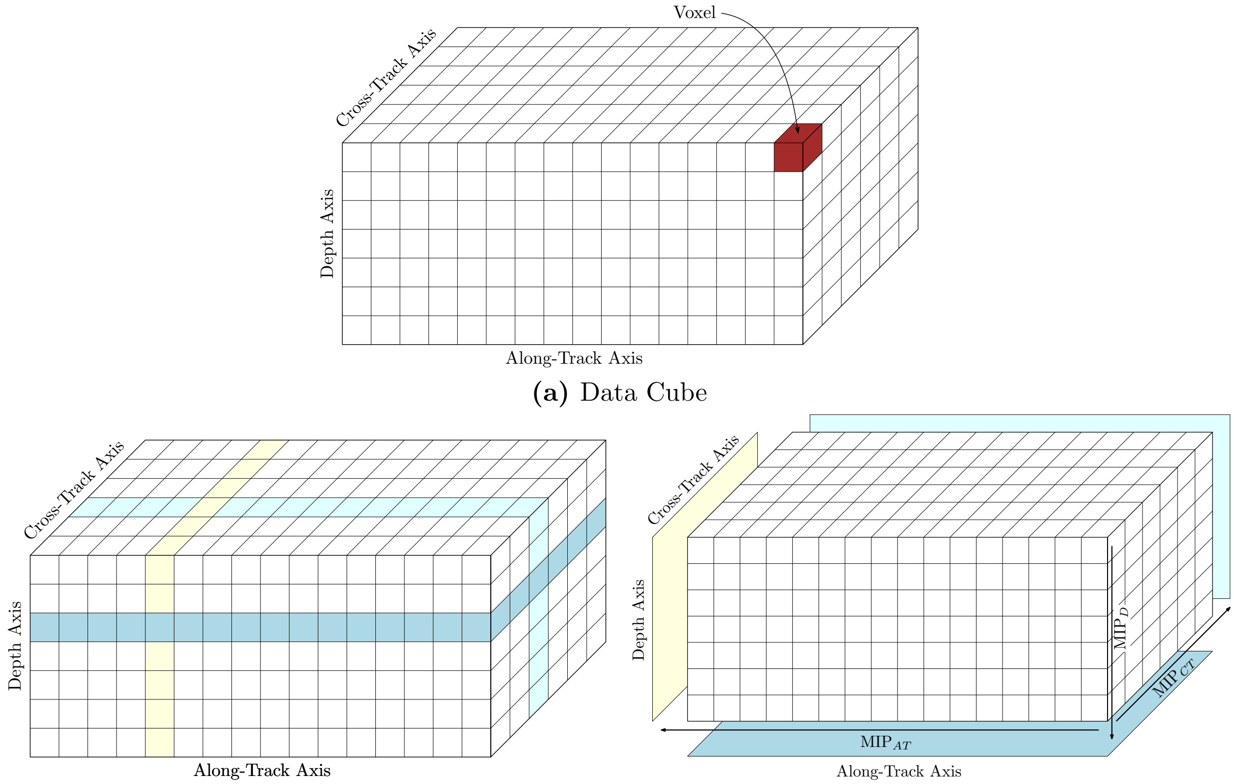

(a) Data Cube

(b) Data Cube Slice

(c) Data Cube MIP

Figure 33: A pair of two-dimensional data representations is used to visualize the three-dimensional data shown in Figure (a). Figure (b) shows slices through the three-dimensional data, which are taken at discrete positions along one of the three principal axes. Figure (c) shows MIPs along the principal axes. The along-track slice and MIP are shown in yellow. The cross-track slice and MIP are shown in light blue. The depth slice and MIP are shown in dark blue.

not necessarily confined to a principal axis, and a MIP is formed by projecting the imagery along any direction by selecting the highest intensity voxel along the axis of projection [48]. The animation in Figure 32 is created by forming a series of MIPs where the projection direction rotates around the data cube. Unlike the sliced representation, any single MIP visualization may be able to show a target regardless of its position within the data cube. However, for a target to appear within any given MIP representation it must have a higher scattering intensity than all other voxels along the direction of the projection. Because of this, it is possible that a target may be obscured in a MIP by clutter targets or environmental scattering from sub-bottom layers.

4.3.2.2 Image Dynamic Range Compression The raw data recorded by the SVSS exhibits a wide dynamic range because of propagation and scattering effects. Transmission loss over the relatively short range of the SVSS sensor is sensitive to small changes in range. For example, the difference in spherical spreading loss over the sensor's 1 m–5 m

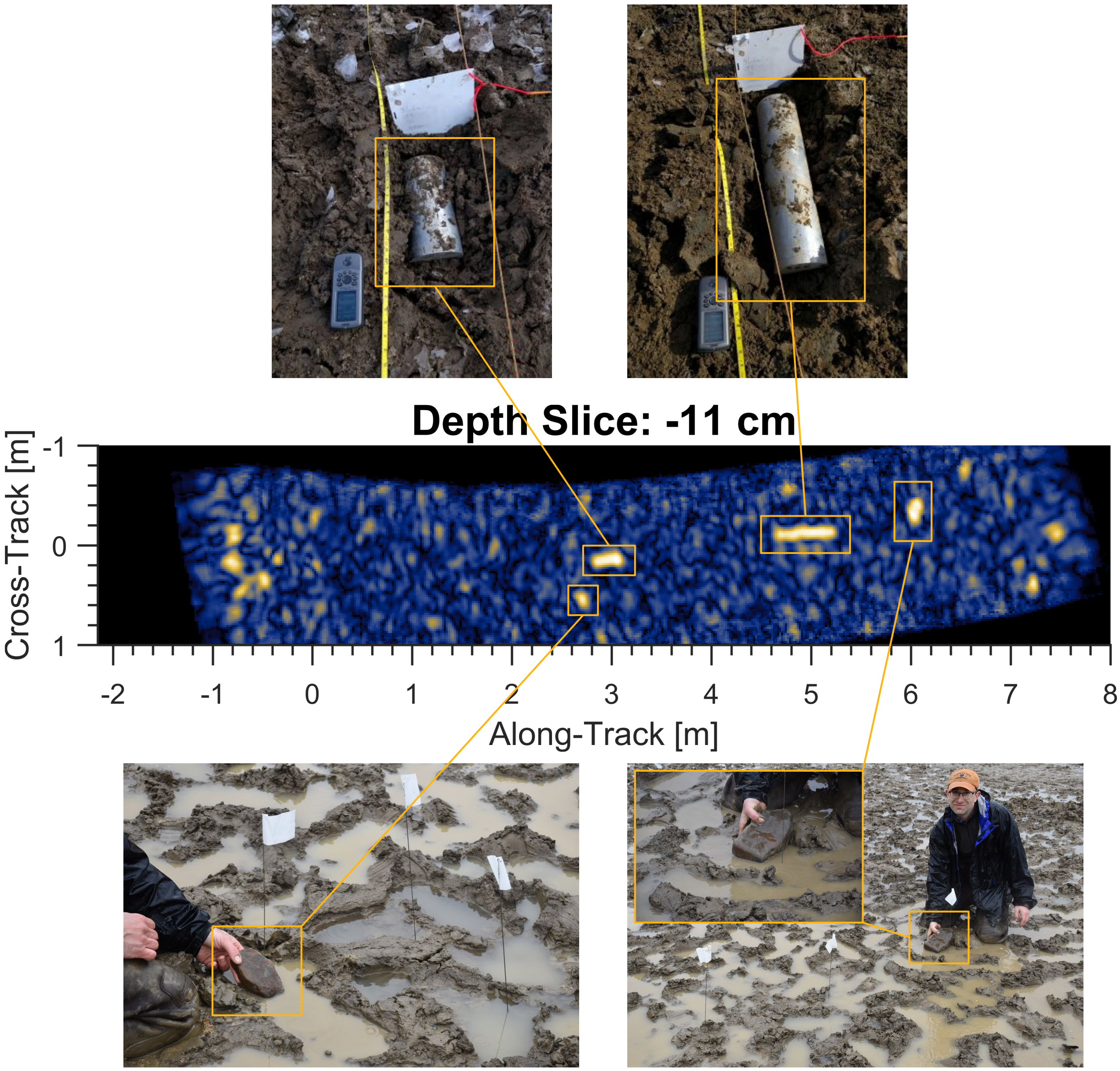

Figure 34: A slice is shown passing through the two cylinders seen in Figure 32. The cylinders as well as a pair of rocks recovered from the lakebed are shown.

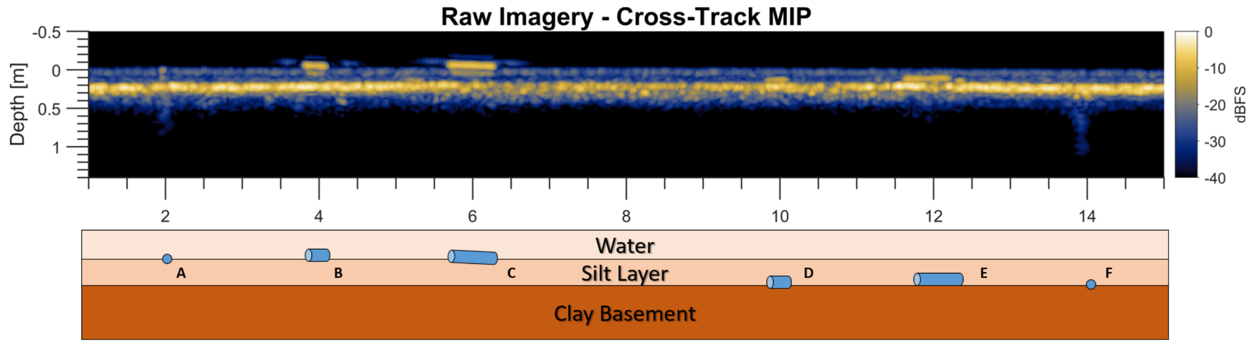

A	12 pound steel shotput	Flush Buried	D	15 x 30 cm solid aluminum cylinder	Buried 9 cm
B	15 x 30 cm solid aluminum cylinder	Proud	E	15 x 60 cm solid aluminum cylinder	Buried 6 cm
C	15 x 60 cm solid aluminum cylinder	Proud	F	12 pound steel shotput	Buried 16 cm

Figure 35: A cross-track MIP is shown for data collected in the Foster Joseph Sayers Reservoir. The data is shown on a 40 dB logarithmic scale that is referenced to the peak value. A schematic diagram showing the water and layered sediment interface along with six targets is shown below the MIP. A table describing the details of these targets is also included.

operating range is approximately 28 dB. Attenuation in sub-bottom sediments can exceed 10 dB/m (one-way) in the SVSS operating band. Additionally, spatial distribution of scattering strength can vary widely due to specular glints from targets or clutter, as well as near-normal incidence boundary scattering and reflection. In combination, these effects can lead to very wide dynamic range in the received signals.

The wide dynamic range in the raw data results in reconstructed imagery that exhibits a dynamic range frequently exceeding 80 dB. Standard display monitors are limited to approximately 50 dB dynamic range [49], so some type of compression is needed prior to display. An example of this wide dynamic range is provided in Figure 35, where a cross-track MIP is shown on a 40 dB logarithmic scale referenced to the peak value. The lakebed consists of a silt layer over a clay basement, and six targets are positioned within the scene. A schematic and a table showing the target positions and properties are shown below the MIP. The pair of proud cylinders are clearly visible, and the pair of buried cylinders are more difficult to see because of scattering from the sub-bottom silt/clay interface. The shot puts are buried at the water/silt and silt/clay boundaries, and they are not easily detected in this image. This cross-track MIP and the associated depth MIP are shown in Figures 36a and 36b, respectively. Projection across the depth axis has reduced the detectability of all of the targets in this scene. This is a consequence of calculating the maximum intensity across the depth axis, where the target must scatter more strongly than the sub-bottom silt/clay interface to be clearly visible.

To aid human interpretation of SVSS imagery, the spatially varying background scattering strength and the wide dynamic range of the imagery must be reduced. The following four-step dynamic-range-compression (DRC) process is applied to the reconstructed SVSS data

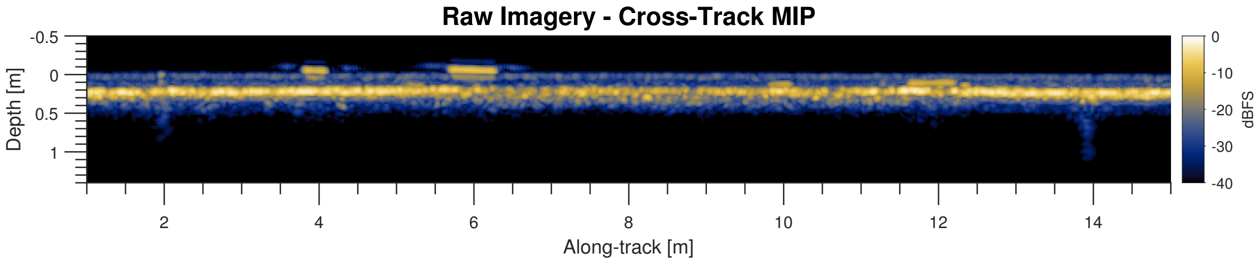

(a) Raw Cross-Track MIP

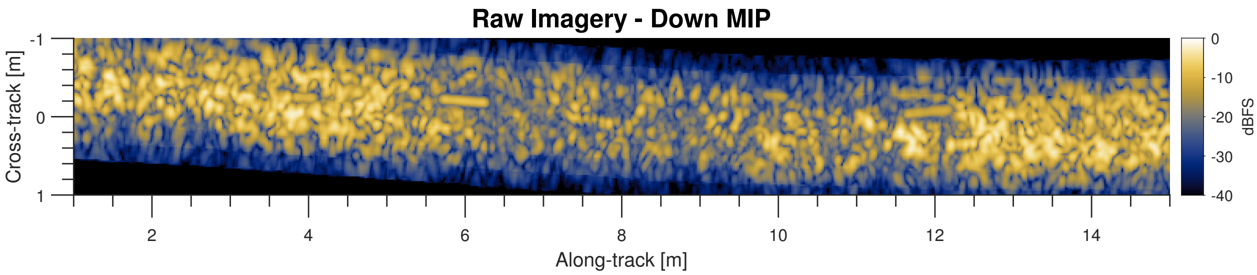

(b) Raw Depth MIP

Figure 36: Cross-track and down MIPs are shown for data collected in the Foster Joseph Sayers Reservoir. The data are shown on a 40 dB logarithmic scale that is referenced to the peak value.

cube.

1. Apply a regularized normalization based on the integration counts calculated during image reconstruction.
2. Apply a depth dependent gain to offset spherical spreading loss.
3. Apply a regularized normalization based on an estimate of the spatially variable seabed scattering strength.
4. Apply a tone mapping operator (TMO) to further compress the dynamic range.

The result of applying the DRC process can be seen by comparing the cross-track and depth MIPs in Figure 36 and 37. In the former, the MIPs of the raw reconstruction output are shown on a 40 dB logarithmic scale. In the latter, the DRC process has been applied to the raw data and the results are shown on a scale from zero to one. This DRC process has increased the intensity of the sub-bottom returns so that buried objects and the late-time returns from the targets may be more clearly recognized. The procedures and parameters used on this program were heuristically developed to create imagery to aid human review. It is unlikely that the methods developed here are "optimal," and future work on this class of sonar systems will have to address the development of robust data normalization and scaling algorithms. For the interested reader, the remainder of this section details the specific procedures and parameters of the DRC process.

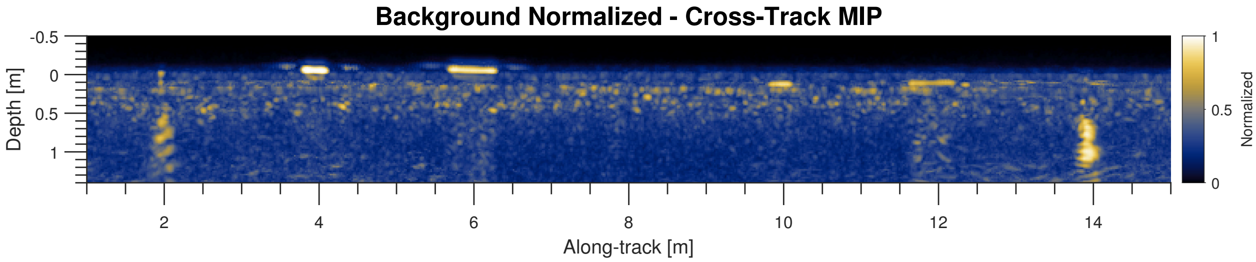

(a) Dynamic Range Compressed Cross-Track MIP

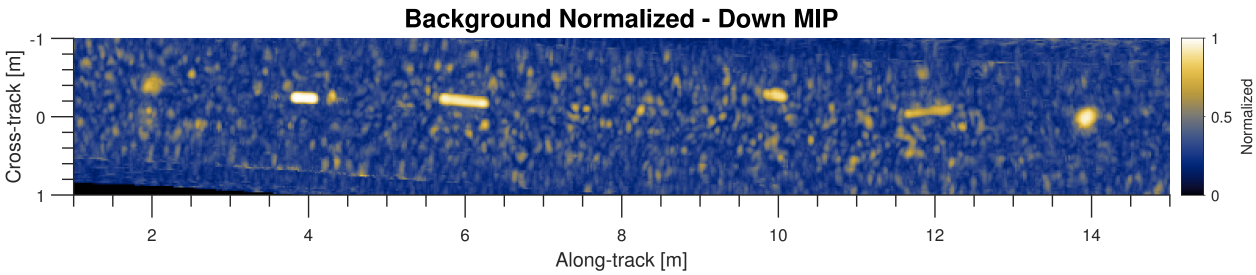

(b) Dynamic Range Compressed Depth MIP

Figure 37: The dynamic range of the data shown in Figure 36 has been compressed. This results in improved target detectability.

The spatial variability of the intensity within an SVSS image is determined in part by the image reconstruction process and in part by the spatial variability of the scattering strength of the imaged scene. Both the reconstruction and the environmental effects are addressed by estimation of the spatially varying background and dividing the data cube by this estimate to normalize their effect. While the normalization presented here is developed to aid human image interpretation, this type of background estimation is also commonly used within the sonar machine learning community [50, 51]. In parallel, Dr. David Williams has developed a volumetric image normalization algorithm for SVSS data as part of his work in applying the Mondrian detector to this system [52]. Dr. Williams's approach extends that reported here by adapting to the local slope within a scene in the estimation of the scene background. The details of the detection results are presented in Section 5.1.6.

Directly normalizing an image through division by a background estimate can introduce artifacts in those regions where the background estimate is small. Artifacts can be avoided by regularizing the normalization. This process takes the form

$$I'(x, y, z) = I(x, y, z)\frac{L}{L + \eta(x, y, z)}, \tag{3}$$

where I is the raw image, I' is the normalized image, η is the background estimate, and L is the regularization parameter. When the background estimate is much larger than the regularization parameter ($\eta \gg L$), the image is properly normalized ($I' \approx {}^{I}/_{\eta}$). However the normalization is not applied ($I' \approx I$) when the background estimate is much smaller than the regularization parameter ($\eta \ll L$). The functional form of Equation 3 provides a smooth transition across the full range of background estimate values and is effective at minimizing normalization artifacts.

The first stage of image normalization addresses the spatial variability of the image reconstruction process itself. To reconstruct an image, ASASIN coherently combines the hydrophone data recorded from transmissions from the five SVSS projectors. The bistatic field of view of a projector/receiver pair determines whether the pair contributes to any single voxel. The binary nature of this process creates spatial discontinuities in the aperture support used to reconstruct voxels. This effect is seen in sharp edges of the overlapping shaded regions in Figure 31. To mitigate this effect, ASASIN creates a metadata product as part of the reconstruction process that provides an integer count of the number of signals back-projected into each voxel.[2] Here, this is referred to as the "integration count." Normalizing the data cube by the integration count removes the reconstruction artifacts associated with discontinuities in the sensor support. Near the edges of the reconstructed image the integration count can be quite small, so the regularization method described in Equation 3 must be used. Treating the integration counts as $\eta(x, y, z)$, ARL/PSU found that $L = 100$ provides adequate regularization to prevent image artifacts.

The second stage of image normalization addresses the spatial variability of the seabed scattering strength and attenuation in the sub-bottom sediments. The background estimate should capture the spatial variability caused by sediment layering and large scale spatial structures. However, it must not be sensitive to spatial variability on length scales similar to the targets, or the normalization would obscure the targets themselves. Two approaches have been investigated on this program: a three-dimensional split window normalizer and a three-dimensional median filter. The first technique, adapted from signal detection theory, extends the filter used in a split window normalizer (SWN) to three dimensions. Traditionally, the filter implemented in a SWN captures the large-scale fluctuations in a time series through the estimate of the mean level within a pair of auxiliary data windows surrounding the normalization cell [53]. These auxiliary windows are offset from the normalization cell by a guard band whose width is set by the expected target response. This is shown schematically in Figure 38a, where the signal+noise is shown in blue and the background estimate is shown in yellow. In this example, the guard band was set based on the duration of the transient signal shown in red. This concept is directly extended to three dimensions as shown in Figure 38b. The auxiliary data is taken from a volume surrounding a guard volume whose dimensions are determined by the expected target dimensions and response. The second background estimation approach uses a similar three-dimensional filter without a guard volume. The median of the pixel values over this volume is taken as the background estimate as that will be relatively insensitive to small targets contained within the volume. ARL/PSU found that both background estimation approaches yielded similar results.

The final step in the DRC process is to apply a tone mapping operator to nonlinearly compress the dynamic range of the imagery. Tone mapping operators are commonly used to map high dynamic range imagery to a lower dynamic range for display. A good overview of a number of TMOs commonly applied to synthetic aperture radar data is found in Lambers,

[2]For those researchers working with SVSS data, this information is stored in the "normalization counts" file within the ASASIN output directory.

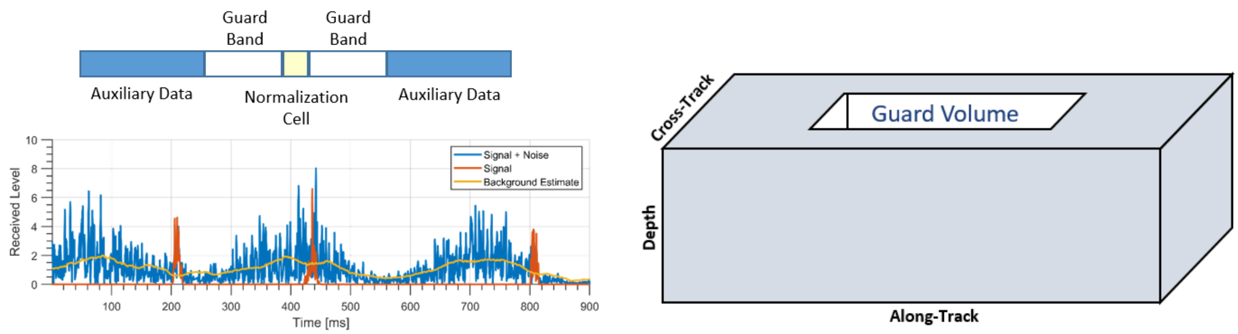

(a) One-Dimensional SWN **(b)** Three-Dimensional SWN

Figure 38: Illustration and sample data showing the effect of the split window normalizer in one dimension (a), and an illustration showing the SWN concept extended to three dimensions.

Nies, and Kolb [54]. For SVSS imagery, this step is accomplished using several sequential TMOs. First, quantile values are calculated for the 1% and 99.99% levels. The data are shifted to map the 1% quantile level to zero, and negative voxel values are replaced with NaNs (not a number) as those are rendered transparent when viewing a figure. The 1% quantile value now represent the "black point" in the imagery. Next the data are normalized by the 99.99% quantile level so that 99.99% of the voxels are on the interval $[0, 1]$. When targets are present the 0.01% of voxels greater than 1 frequently fall on the target. Clipping these values to 1 introduces obvious visual artifacts. To avoid this, the next TMO maps all of the voxels to the range $[0, 1]$ through the logistic function

$$f(x) = \frac{2}{1 + e^{-3x}} - 1, \tag{4}$$

where x is the input voxel value. Finally a gamma TMO is applied

$$f(x) = x^{\gamma}, \tag{5}$$

where again x is the input voxel value, and γ is selected to scale the median voxel value to 0.1. This final TMO provides a uniform background brightness that is insensitive to the presence of small, strong scatterers.

4.4 Test Site Development

To support both integration testing and demonstration of the SVSS system, test sites were developed at two separate geographic locations – the Foster Joseph Sayers Reservoir in Howard, PA (described in Section 4.4.1) and the Aberdeen Test Center in Aberdeen, MD (described in Section 4.4.2). The proximity of ARL/PSU to the Foster Joseph Sayers Reservoir permitted regular integration testing, with 15 test events collecting data at two prepared target fields, between October 2017 and November 2020. A demonstration event was conducted at the Aberdeen Test Center, with a week of daily testing events collecting data at a prepared target field and an unprepared field, in March 2019.

To prepare a UXO test site, the site developer must:

1. select a representative, yet finite, set of object types (inert munitions, science objects, and clutter), burial depths, orientations, etc.,
2. identify an accessible site with suitable sediment type(s) and hydrodynamic conditions where objects may be emplaced, with consideration for the deployment process (e.g., drained for excavation, diver emplaced),
3. secure the necessary permissions and permitting to establish the test site,
4. design a test site object layout that supports the objectives of the planned demonstration,
5. curate the test site objects to provide accurate dimensions, properties, and ground truth positions, and
6. collect ancillary data pertinent to the test site environment and sensing modality (e.g., sound speed) during field testing.

The remaining sections provide a summary of the site design, permissions/permitting, and curation for the test sites developed under the SVSS program. For the prepared sites, the target positions were surveyed using a RTK-aided GPS, with the base station location initialized with the NOAA Online Positions User Service (OPUS) (`https://geodesy.noaa.gov/OPUS`), KeyNetGPS VRS (Virtual Reference Station) service (provided by Keystone Precision Solutions: `https://www.keynetgps.com/`), or with a combination of methods. An RTK base station location was established adjacent to the target field, and each target's ground truth location was surveyed with an RTK rover utilizing GPS corrections from the base received over a data link. A photo of the RTK base station at the ATC experiment is shown in Figure 39a, and a photo showing an RTK rover survey of a target is shown in Figure 39b. In addition to the RTK-GPS survey, the depth of each buried target was also hand-measured relative to the sediment interface. Finally, at the ATC experiment, the orientation of each object's long axis (relative to horizontal) was measured with a digital inclinometer. This installation process provided an absolute ground truth errors of less than a few centimeters for every object placed at both sites, and less than a centimeter relative between targets within a site.

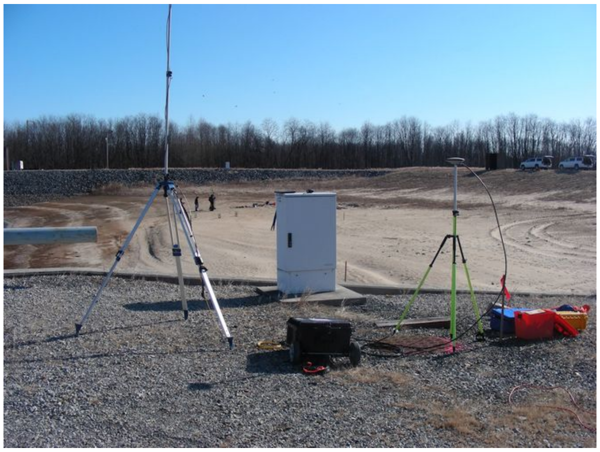

(a) RTK Base Station

(b) RTK Target Survey

Figure 39: Ground truth on target positions is established through use of an RTK-GPS survey system. An example survey setup is shown for the ATC experiment, where an RTK base station was established adjacent to the target field (a) and aN RTK-based survey of each target (b) was conducted.

4.4.1 Foster Joseph Sayers Reservoir

4.4.1.1 Site and Target Description A test site was established at the Foster Joseph Sayers Reservoir near Howard, PA in the early spring of 2017. This lake covers roughly 1700 acres and is eight miles in length. The test site was chosen due to its proximity to ARL/PSU and because the winter lake level is lowered sufficiently to provide ARL/PSU with the opportunity to establish an accurate ground truth of objects, clutter, and sediment types within the test bed.

Foster Joseph Sayers Reservoir was established for flood control by the US Army Corps of Engineers in 1971. Seasonally, the level is reduced by 1.5 m in early December and reduced another 5 m–7 m in February to provide capacity for runoff of melting snow. A historical plot of the lake level for the period of the SVSS experiments is provided in Figure 40. The lake was formed by damming Bald Eagle Creek with the creek inlet at the southwest corner of the reservoir and the dam at the northeast corner. An aerial image of the reservoir is provided in Figure 41. The lake and neighboring land was leased to the Pennsylvania Department of Conservation and Natural Resources, and Bald Eagle State Park was established.

A test area within the reservoir for establishing target fields was approved by the Pennsylvania Department of Conservation and Natural Resources and the US Army Corps of Engineers, and is approximately indicated with an orange box in Figure 41. Within this approved test area, two sub-regions were identified, which have expected water depths of 1.5 m–2.0 m and 3.0 m–4.0 m when the reservoir reaches the summer pool level, and have been seeded with a variety of objects during draw-down periods. This pair of prepared fields are referred to as the “shallow” and “deep” sites, respectively, and are shown on a

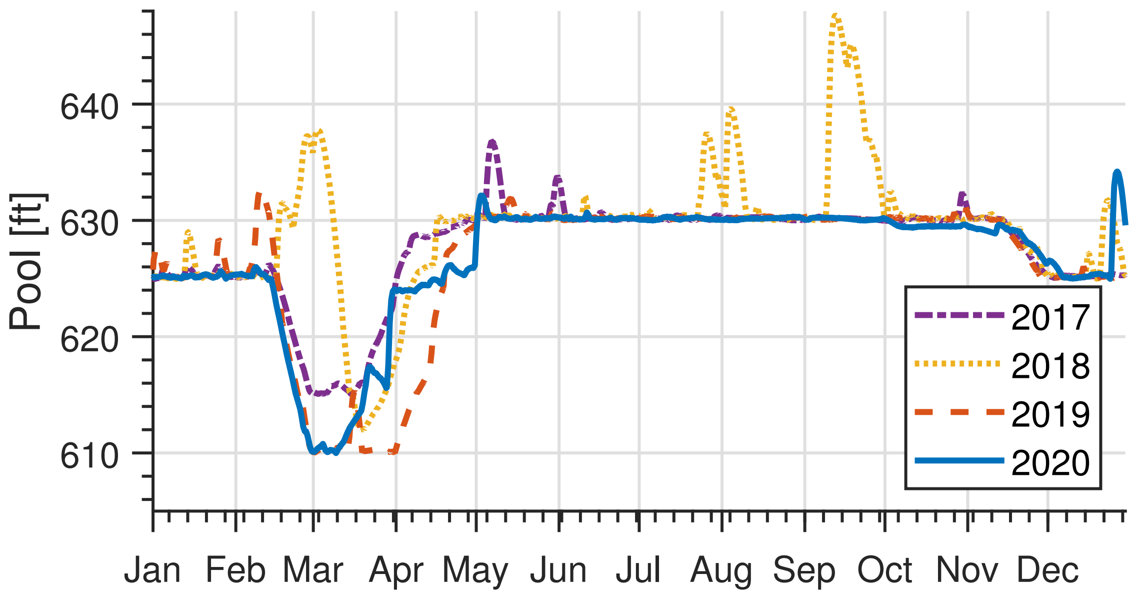

Figure 40: The reservoir level is varied throughout the year. In the early December timeframe the lake is lowered five feet. This is followed by a second drop in level of fifteen additional feet in late February. During the draw-down period the test sites are exposed and the target field was deployed.

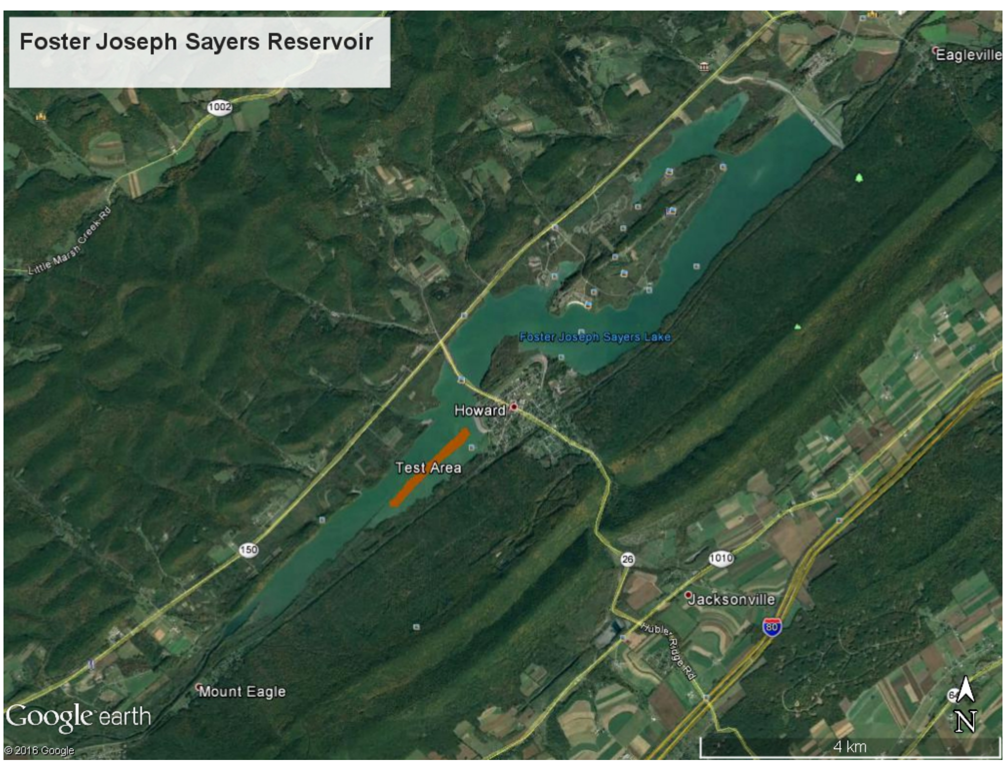

Figure 41: The Foster Joseph Sayers Reservoir is located near Howard, PA. Two prepared fields, with water depths of 1.5 m–4.0 m at typical summer pool fill, were established within the test area identified above.

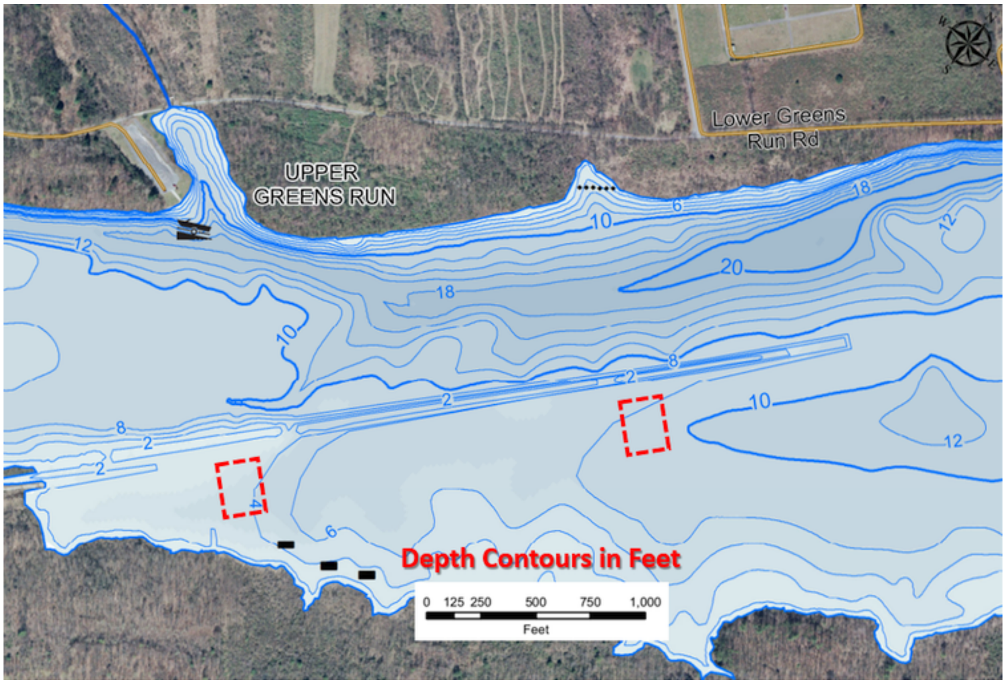

Figure 42: The two prepared fields are indicated on a bathymetric map of the lake. The water depth for the "shallow" field (left) is 1.5 m–2.0 m and the "deep" field (right) is 3.0 m–4.0 m when the reservoir reaches the summer pool level. Note an old railroad bed and paved road (above) separate the test area from the main part of the reservoir.

bathymetric chart in Figure 42.

A variety of targets were placed in the "shallow" and "deep" sites beginning in March 2017 during winter draw-down. The final test site layouts established in the March 2019 installation are provided in Figure 43. The shallow site has 46 target positions labeled P01-P46 in Figure 43a, and the deep site has 35 target positions labeled P01-P35 in Figure 43b. Concrete blocks were also placed at the four corners of each field.

Identification of target position and properties is encoded with a unique identification string. The string begins with {D,S} to indicate the deep or shallow site, followed by {P##} to indicate the position within that site, followed by {T##} to indicate the target type. A list of the target types and properties is provided in Table 4 (the diameter of cylindrical targets is listed as the target width in this table). Targets with a {Txx} designator are of "mixed" type. The target types at these locations are provided in Table 5. Finally, the identification string ends with {D#} to indicate the nominal burial depth. D0 targets are proud, D1 target are buried approximately 5 cm, D2 targets are buried approximately 10 cm, and D3 targets are buried approximately 20 cm. Actual target burial depths are determined by physical measurement and acoustic survey. Additional details, including photos and target burial depths, are provided in Appendix A.1.

Table 4 also lists the target strength for the spherical, solid cylinder, and rectangular shapes.

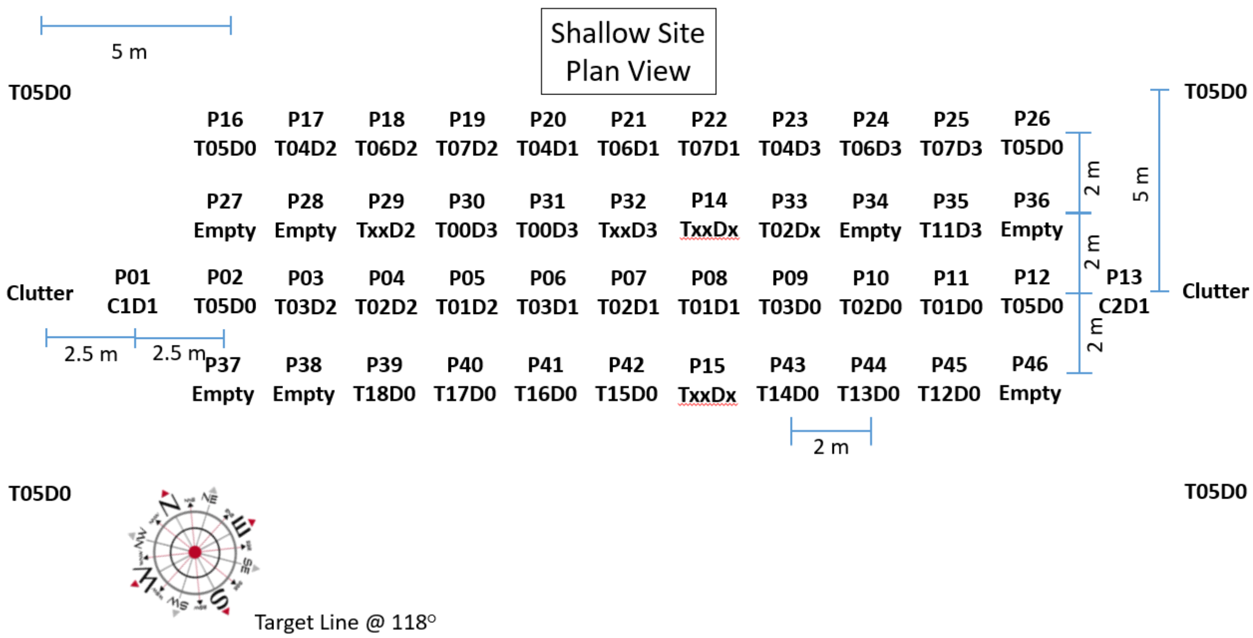

(a) Shallow Site Layout

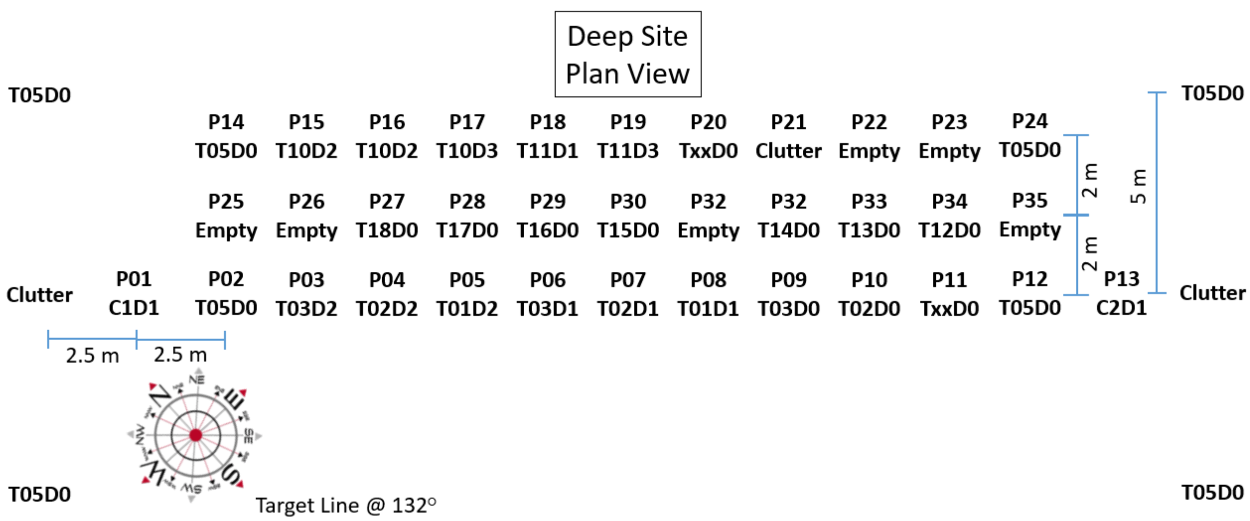

(b) Deep Site Layout

Figure 43: The shallow site and deep site target layouts after the 2019 field installation. Note that the orientation of the layout is provided in the lower left corner of each figure. The shallow site has 46 target positions (P01-P46), and the deep site has 35 positions (P01-P35). The target type identifier is shown below each position, and the reference can be found in Table 4. Target positions specified with a target type "xx" are mixed combinations of targets, which are specified in Table 5.

Table 4: A prepared field with 78 objects, consisting of a range of clutter, science targets, and ordnance, at a variety of burial depths, was installed in a pair of sites located at the Foster Joseph Sayers Reservoir. The notional target positions are provided in Figure 43.

	Target Name	**Target Identifier**	**Target Length [cm]**	**Target Width [cm]**	**Approx. Target Strength [dB @ 1 m]**[a]	**Number Installed**	**Burial Depth Range [cm]**
Science	Shot put	T01	-	10.2	-31.9	14	0-20
	Aluminum Cylinder	T02	30.5	15.2	-11.9	7	0-20
	Aluminum Cylinder	T03	61.0	15.2	-5.9	6	0-10
	Steel Pipe	T12	30.5	11.4	-13.1	2	0
	Steel Pipe	T13	61.0	11.4	-7.1	2	0
	Steel Pipe	T14	30.5	16.8	-11.4	2	0
	Steel Pipe	T15	61.0	16.8	-5.4	2	0
	Concrete Cylinder	T16	30.5	10.2	-10.6	2	0
	Concrete Cylinder	T17	61.0	15.2	-5.9	2	0
Ordnance	155 mm Howitzer	T04	87.4	15.5	-	3	0-30
	105 mm Projectile	T06	47.5	10.5	-	3	0-30
	81 mm Mortar	T07	43.5	8.1	-	3	0-30
	60 mm Mortar	T08	18.5	6.0	-	3	10-20
	37 mm Projectile	T09	22.8	3.7	-	3	10-20
Clutter	Cinder Block	T05	39.7	19.8	+3.2[b]	16	0
	Concrete Pad	T10	30.5	30.5	4.6	3	0-20
	Cinder Block Foam	T11	40.6	15.2	-	3	5-20
	Concrete Bucket	T18	30.5	26.2	-0.1	2	0
Other	Empty Hole	T00	-	-	-	2	-

[a]Calculated at 27.5 kHz using $ka \gg 1$ approximation from Urick [55, Table 9.1].
[b]Estimate for flat side of block.

These were calculated at 27.5 kHz using the high frequency ($ka \gg 1$) approximations taken from Urick [55, Table 9.1].

4.4.1.2 Permitting Process ARL/PSU has worked with various US Federal and Pennsylvania State organizations to obtain necessary permissions and to address concerns raised to emplace targets on and buried in the lakebed, and to ensure access to the test sites for curation during reservoir draw-down periods. These discussions have included US Army Corps of Engineers (USACE), Pennsylvania Department of Conservation and Natural Resources (PADCNR), Pennsylvania Fish and Boat Commission (PFBC), Pennsylvania Department of Environmental Protection (PADEP), and the Susquehanna Economic Development Association Council of Governments (SEDA-COG). The essence of the permitting process seeks to ensure the safety of researchers doing the testing and other users of the lake, provide access to researchers to otherwise restricted regions, and to abide by any pertinent environmental protection legislation. Additionally ARL/PSU has obtained a Federal Communications Commission (FCC) Radio Station Authorization for up to 35 W transmission, used for the RTK-GPS data link.

To minimize impact to other users of the state park, the test site was chosen in a less trafficked region of the reservoir, and operations have been conducted on weekdays during

Table 5: Several positions in the shallow and deep fields have “mixed” target types.

Target Identifier	**Target Description**
S_P14_TxxDx	Shot put at 31 cm depth with ladder on surface
S_P15_TxxDx	Shot put at 33 cm depth with shot put on surface
S_P29_TxxD2	Three 60 mm mortars and three 37 mm projectiles
S_P32_TxxD3	Shot put buried 24 cm in a sand filled bucket
D_P11_TxxD0	Two surface shot puts separate by 29 cm
D_P20_TxxD0	Four shot puts stacked in a pyramid

typical work hours. Numerous permissions and permits are required to support this testing. A complete list of these permissions and permits is provided below.

- **PADCNR Special Activities Agreement / Letter of Authorization**
  The PADCNR Special Activities Agreement (SAA) allows ARL to launch watercraft and conduct scientific testing within Bald Eagle State Park. This agreement outlines a summary of activities, time and location to conduct activies, and a Risk Management Plan. Additionally, an insurance rider provided by Penn State is required. The SAA replaced annual Letters of Authorization (LOA) in 2020. [SAA-0472 (2020+), LOA-2854 (2019), LOA-1979 (2018), LOA-072 (2017)]

- **USACE Special Event Permit**
  The USACE Special Event Permit is issued by the USACE Susquehanna River Project as a part of the PADCNR SAA/LOA.

- **USACE Real Estate Permit**
  The USACE Real Estate Permit is issued by the USACE Baltimore District, and allows for ARL researchers to access the test site from USACE land that may be outside PADCNR jurisdiction, and permission to emplace targets on and within the lakebed. Additionally, an insurance rider provided by Penn State is required. [License #DACW-31-3-17-0260]

- **PFBC Buoy Permit**
  The PFBC Buoy Permit allows ARL to place markers to identify the test field to facilitate testing as well as mark any potential hazard to navigation should a need arise, although none is expected since the targets are placed on the lakebed or buried. [Permit #1620].

- **SEDA-COG Joint Rail Authority License for Private Grade Crossing**
  The SEDA-COG Joint Rail Authority License for Private Grade Crossing allows ARL to cross the current Nittany & Bald Eagle Railroad tracks at the southwest edge of the park near Mount Eagle, PA and access the test sites along the now abandoned old Route 220 and railroad tracks. A temporary railroad crossing was installed by the railroad. Additionally, an insurance rider provided by Penn State is required. [License #: 00-132.0]

- **FCC Radio Station Authorization**
  This FCC radio license, issued by the Wireless Telecommunications Bureau, allows ARL to operate a radio frequency (RF) data link between an RTK-GPS base station and RTK-GPS rover(s), up to 35 W. [Call Sign: WRBW403, File #: 0008237085, FCC Registration Number (FRN): 0027550789]

ARL has received concurrence from both State and Federal authorities that the planned scientific experiments are compliant with environmental protection legislation. Several key aspects of the planned experiment were highlighted as bringing the actives into compliance *without* the need for further approval.

1. Objects being placed are for scientific purposes,
2. objects will be constructed of inert materials,
3. object positions will be recorded,
4. objects will be removed at the completion of the study, and
5. no additional sediment fill is required.

The relevant legislation and confirmation of compliance is summarized below.

- **Pennsylvania State Environmental Protection Code (Title 25)**
  Email received 5 October 2016 from Kipp Starks (PADEP); SVSS activities qualify for Waiver 12 under Chapter 105 § 105.12(a)(12).
- **United States Environmental Protection Agency Clean Water Act**
  Email received from Amy Elliott (USACE); Sec 404 states Federal authorization is assumed with State Waiver 12 (above).

4.4.2 Aberdeen Test Center

The SVSS conducted demonstrations at the Aberdeen Test Center's Littoral Warfare Environment (Figure 44) and the neighboring Bush River. The LWE facility has a nominal reservoir surface area of 100 m by 140 m covering a sand sediment bed, with a 50 m by 120 m beach at the southern edge. The reservoir is dewatered by pumping its contents into the neighboring Underwater Test Facility. When dewatered, a larger portion of the beach is exposed and this allowed ARL/PSU to emplace a target field without the need for diver support.

A total of 85 objects including munitions, science targets, and clutter were selected for installation in the LWE with one-third of the objects proud and the remainder buried up to 60 cm below the sediment/water interface. The eighty sixth prepared position was a hole that was dug and refilled without placing an object. The munition diameters installed in the LWE ranged from 2.0 cm to 15.5 cm (the theoretical resolution of the SVSS is 5 cm). The munitions and science targets are shown in Figure 45a prior to distribution in the field. These targets were laid out on a two-meter grid spacing along six lines running parallel to the beach as seen in Figure 45b.

The detailed layout of the target field is shown in Figure 46. The 86 unique positions, which are designated by P##, are shown on a two-meter grid spacing. Each position includes a target identifier, T##, and a depth indicator, D#. The target identifiers are defined in Table 6, and the depth indicator is the notional burial depth in 10 cm steps. The target strength listed in this table is calculated using the high frequency ($ka \gg 1$) approximation in Urick [55, Table 9.1]. Generally, the object's notional depths ranged from proud to 60 cm in 10 cm steps. Most targets were buried in a horizontal orientation, but some were oriented nose up 45°, nose down 45°, and nose down 90°. A more detailed description of the targets and their orientation within the test grid, burial depths, and photos is provided in Appendix A.2. Additionally, LWE depth contours and target positions during the test are shown in Figure 47.

This dewatered installation procedure reduces the cost to establish a test site and enables very accurate target ground truth measurement when compared to a diver-assisted installation. These advantages are countered by the risk associated with test site artificiality. In particular, prior to the experiment there were concerns with changes to the sediment properties associated with the regular dewatering/refilling of the LWE through its use as a test site for other programs. For the SVSS acoustic survey, the LWE was over-filled by approximately 1.25 m compared to the typical water level shown in Figure 44. Additionally, because of facility scheduling constraints, the target field was submerged for only one month between target field installation and the SVSS survey.

Owing to the diminished sediment penetration over the prepared test site at the LWE, ARL/PSU submitted a request on 4 March 2020 to the ATC staff for testing in the Bush River. This testing was approved and conducted on the afternoon of 5 March 2020. Shifting from the LWE to the Bush River required recovery and redeployment of the SVSS and the RTK base station. This process took approximately 90 minutes.

The region of the Bush River where the SVSS was tested is adjacent to the ATC Underwater Test Facility, and the surveyed track lines are shown in Figure 48. The bulk of the survey was collected in approximately 2.5 m of water. The ATC staff described the sediments in the portion of the Bush River as principally mud, but no sediment samples were collected to confirm this. This survey site was anticipated to have man-made clutter from historical activity in the area.

Figure 44: The targets described in Table 6 were installed into the LWE at the locations indicated by the white circles in this figure. During the installation of these targets the LWE water level was lowered to the draw-down waterline, which is shown by the northern line of blue squares. During testing the water level was raised to the filled waterline, which is shown by the southern line of blue squares.

(a) Munitions and Science Targets **(b)** Target Field Layout

Figure 45: A total of 86 positions including munitions, science targets, and clutter were surveyed in a site prepared in the LWE. The collected objects are shown in (a) and the target field layout prior to target burial is shown in (b).

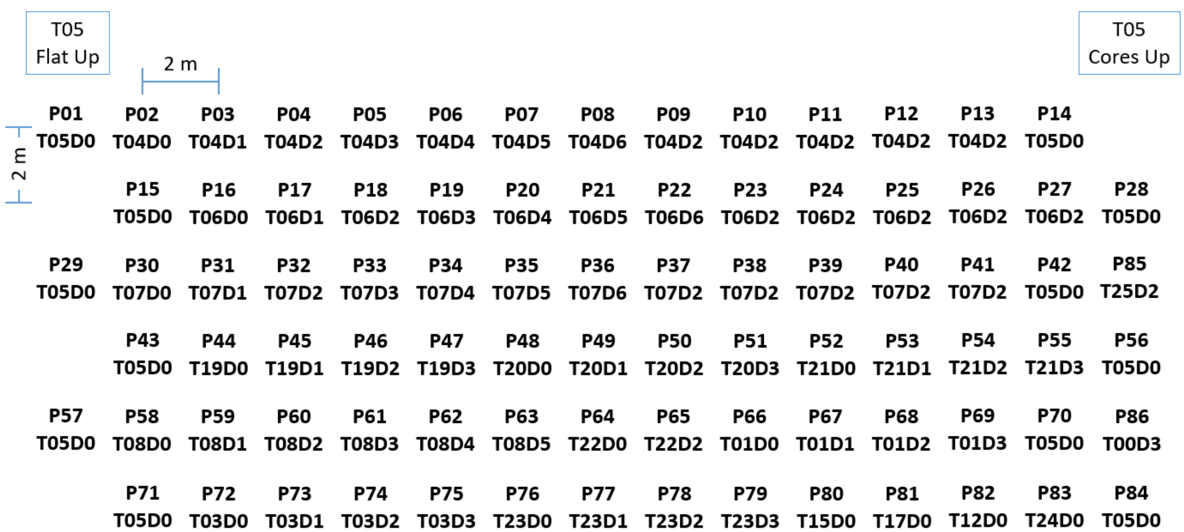

Figure 46: A total of 86 positions were prepared during the test field installation. The target type at each position is indicated with T##, where Table 6 associates the target identifier with the target name. The notional depth at each position is given by D#, where the number indicates the depth in 10 cm steps. The cinder blocks (T05) were placed with either cores or a flat side oriented upward as indicated by the labels at the top of this figure.

Table 6: A prepared field with 85 objects, consisting of a range of clutter objects, science targets, and ordnance, at a variety of burial depths, was installed in the southeast portion of the LWE. The notional target positions are provided in Figure 46.

	Target Name	**Target Identifier**	**Target Length [cm]**	**Target Width [cm]**	**Approx. Target Strength [dB @ 1 m]**[a]	**Number Installed**	**Burial Depth Range [cm]**
Science	Shot put	T01	-	10.2	-31.9	4	0-30
	Aluminum Cylinder	T03	61.0	15.2	-5.9	4	0-30
	Aluminum Cylinder	T23	30.5	10.2	-13.6	4	0-30
	Steel Pipe	T12	30.5	11.4	-13.1	1	0
	Steel Pipe	T15	61.0	16.8	-5.4	1	0
	Concrete Cylinder	T17	61.0	15.2	-5.9	1	0
	Concrete Cylinder	T24	30.5	10.2	-13.6	1	0
Ordnance	155 mm Howitzer	T04	87.4	15.5	-	12	0-60
	105 mm Projectile	T06	47.5	10.5	-	12	0-60
	81 mm Mortar	T07	43.5	8.1	-	12	0-60
	60 mm Mortar	T08	18.5	6.0	-	6	0-50
	70 mm Rocket	T19	76.0	7.0	-	4	0-30
	40 mm Projectile	T20	20.6	4.0	-	4	0-30
	25 mm Projectile	T21	21.7	2.5	-	4	0-30
	20 mm Projectile[b]	T22	7.4	2.0	-	20	0-20
Clutter	Cinder Block	T05	39.7	19.8	+3.2[c]	12	0
	Sayers Rock	T25	20.0[d]	10.0[d]	-	1	20
Other	Empty Hole	T00	-	-	-	1	-

[a]Calculated at 27.5 kHz using $ka \gg 1$ approximation from Urick [55, Table 9.1].
[b]Projectiles were installed in two clusters of 10 objects each.
[c]Estimate for flat side of block.
[d]Estimated dimensions.

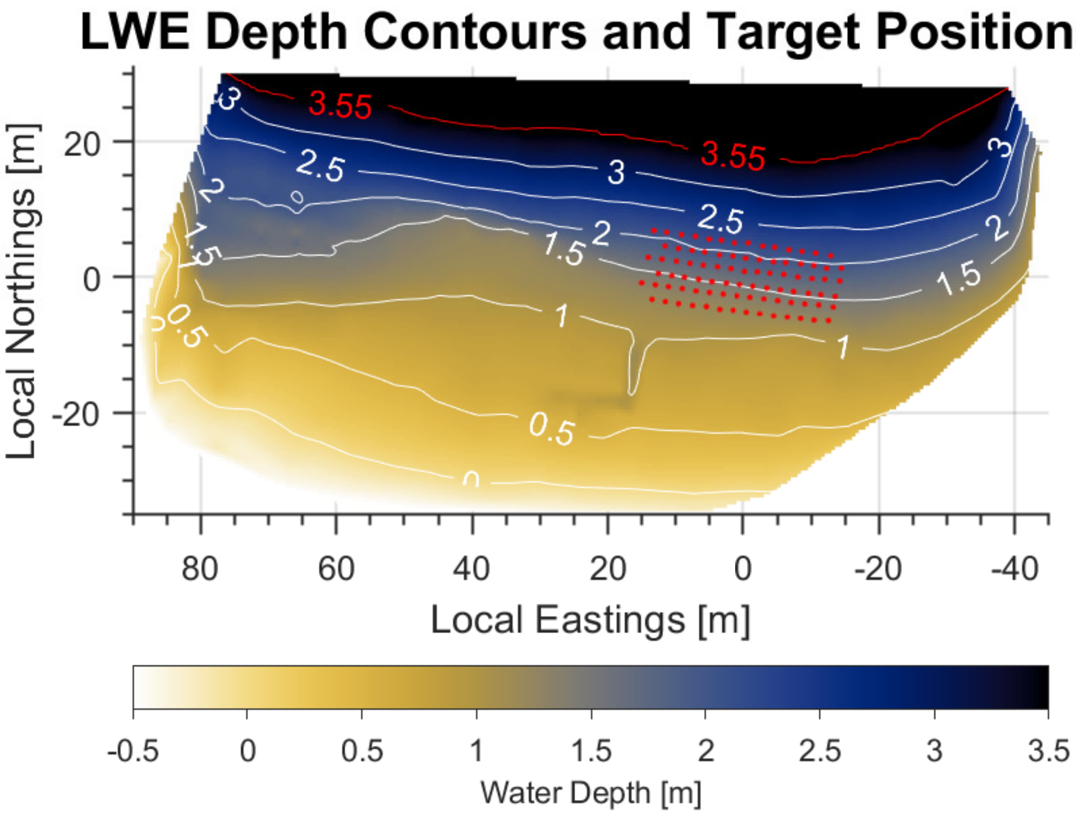

Figure 47: A GPS survey of the exposed LWE sediment bed was used to create a bathymetric chart of the test area. The water depth shown here is calculated for the acoustic survey conducted 2-5 March 2020. The red 3.55 m isoline presents the waterline during installation draw-down. Typically, the LWE is filled to approximately 1.25 m and was overfilled for this test.

Figure 48: A series of imaging tracks were collected in the Bush River adjacent to the ATC test facility.

5 Results and Discussion

5.1 Field Testing Results

Field tests of the SVSS were conducted at the Foster Joseph Sayers Reservoir and the Aberdeen Test Center during this program. This testing was conducted against both prepared fields, detailed in Section 4.4 and Appendix A, as well as an unprepared field in the Bush River adjacent to the Aberdeen Test Center. An overview of the in situ monitoring used to assess the sensor performance during a survey is provided in Section 5.1.1. The target localization accuracy of the SVSS is presented in Section 5.1.2. The target survey results from the Foster Joseph Sayers Reservoir are presented in Section 5.1.3. The survey results from the prepared and unprepared sites at the Aberdeen Test Center are presented in Sections 5.1.4 and 5.1.5, respectively.

5.1.1 In Situ Sensor Monitoring

During active survey operations the data quality and sensor performance are assessed in real-time and near real-time by two analysts. The SVSS DAQ system provides a live display of the power spectral density, sensor health, and ping timing information, as well as a near-real time display of B-Scans from selected channels. Plots containing a subset of the displayed data are shown in Figure 49. Figure 49a displays the hydrophone RMS level for transmission from the left projector (TX-L) and the left-center (TX-LC) projector. The layout of the display is chosen to mimic the physical layout of the hydrophone array, which is shown in Figure 17. While the plots here show only two projectors, in practice plots are presented for all five transmitters. The highest RMS level is on those hydrophones closest to the active projector, and the RMS level falls with increasing distance from this projector. This visualization provides a very simple way to verify that all hydrophones and projectors are operating properly.

Like many SAS systems, the SVSS uses a fixed spatial ping interval as opposed to a fixed temporal ping interval. A sequence of transmissions across the five SVSS projectors is called a "flight" of pings, and the inter-ping timing is constant within a flight. However, the flight repetition interval (FRI) is varied, determined by the platform advance speed. The near real-time analyst reviews the velocity-adaptive FRI using Figure 49b. The upper plot shows the platform speed during a track, the middle plot shows the adaptive FRI, and the lower plot shows the ping-to-ping advance in units of displaced phase centers (DPC). The FRI feedback loop is adequate to adapt to modest changes in platform speed. Large changes in velocity, like that at the end of this example track, can lead to errors in the advance per ping.

Finally, the B-Scan display shown in Figure 49c is calculated for the full track. This occurs in near real-time using an onboard workstation that processes tracks shortly after each recording is completed. Proud targets are generally visible on this display, and it can be used to assess sediment penetration and determine if there is significant water column scattering.

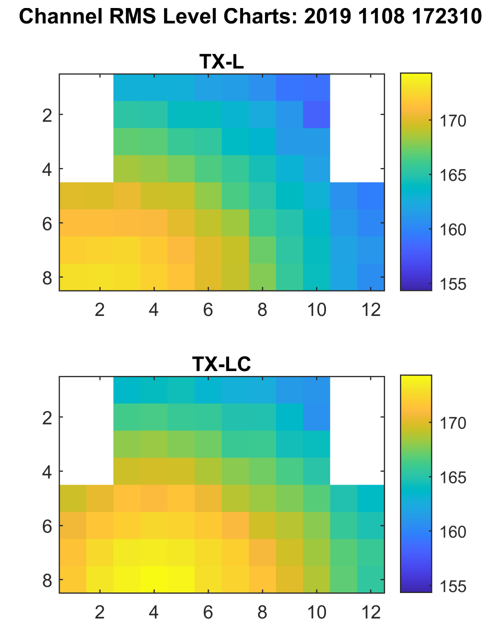

(a) Hydrophone RMS Chart

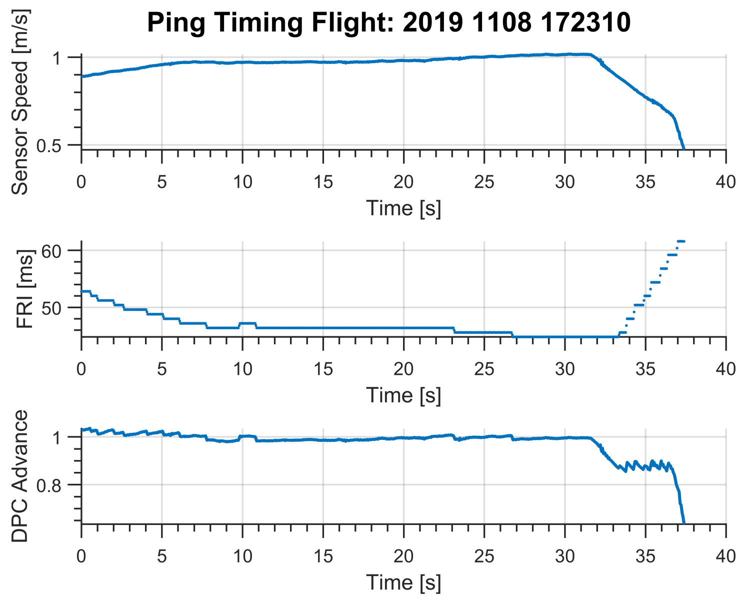

(b) Adaptive Ping Timing

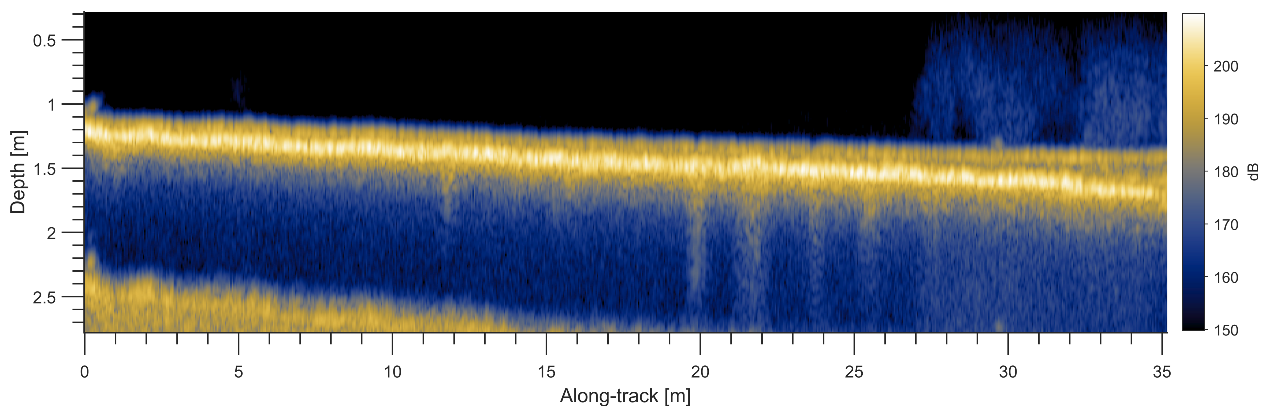

(c) B-Scan

Figure 49: During data collection a number of data products are produced to verify proper sensor performance. The hydrophone and projector health are assessed with the plot shown in (a). This plot shows the RMS level on each channel of the hydrophone array for transmission with the left (TX-L) and left-center (TX-LC) projectors. The sensor speed, flight repetition interval, and DPC advance are reviewed using the plot shown in (b). Finally, a B-Scan (c) is generated for the track to assess sediment penetration.

5.1.2 Target Localization Accuracy

The SVSS sensor is designed to provide absolute target localization errors of less than 10 cm. The SVSS's INS is aided by a RTK-GPS system, and this aiding process allows the INS to determine the absolute platform position to within a few centimeters. Unlike sensors hosted by fully submerged platforms, where the dominant localization error is caused by platform navigation drift, the SVSS errors are largely because of errors in the initial target survey, lever arm errors on the SVSS platform, or residual GPS error.

The target localization accuracy of the SVSS is quantified by comparing the image-based estimates of target location to those recorded during the RTK-GPS survey conducted during the installation of the target field. A set of cinder blocks, deployed at the ATC and with flat faces oriented upward, are selected for this analysis. These objects are located at positions P01, P15, P29, P43, P57, and P71, as shown in Figure 46. For each image containing one of these targets, the target location is determined by segmenting the pixels falling on the target and calculating the centroid of this segmented region. This algorithmic approach eliminates errors introduced by human labeling of the target centroid position. The process for quantifying localization error is as follows:

1. manually label the cinder block depth,
2. calculate a depth MIP for a 10 cm depth range centered on the target depth,
3. determine peak level scattered by the cinder block in this MIP,
4. convert the MIP into a binary image by applying a threshold at 20% of the peak MIP level, then
5. calculate the centroid of the 8-connected region spanning the cinder block.

An example of the MIP created for one contact with the cinder block at P71 is shown on a 30 dB log scale in Figure 50a. The large flat face of the cinder block is easily seen, and the associated binary image is shown in Figure 50b. The object's centroid and the ground truth survey location are shown with a blue and red mark, respectively. The separation between these marks is the localization error for this contact.

During ATC testing, a total of 13 opportunities were collected for the six cinder blocks oriented with flat sides upward. These localization errors are shown in Figure 50c, and the root-mean-square (RMS) error for target localization was 7.2 cm. This error estimate includes a single outlier (contact 3) that was caused by poor image reconstruction from a platform turn during the data collection.

Additional testing was conducted at the Foster Joseph Sayers Reservoir to further characterize the localization error, with the particular goal of determining if a bias is introduced from errors in the lever arm measurement between the inertial navigator and the sonar sensor. This type of error produces a fixed bias in the platform navigation frame and that error would be projected into the earth frame according to the platform heading.

For this additional test, a single cinder block imaged on 16 tracks was selected, with each

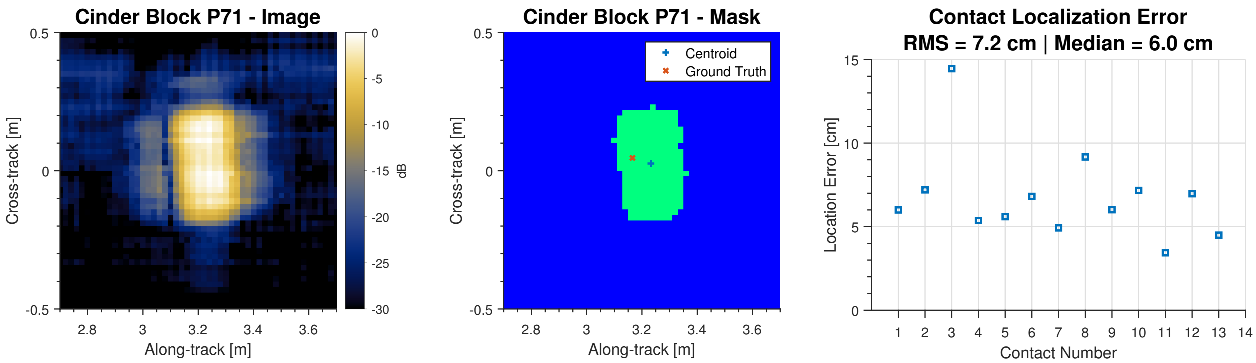

(a) (b) (c)

Figure 50: A MIP of the cinder block located at P71 is provided in (a). A binary image (b) is created by applying a threshold at 20% of the cinder block peak level. The centroid of this green region (blue plus) is compared to the ground truth position (red x). The location error calculated across all 13 cinder block opportunities is shown in (c).

image having been collected on a different heading. Analysis of the target localization error shows the navigation sensor bias due to lever arm errors is approximately 8 cm for this data set. The residual random error is approximately 2 cm. The lever arm bias is driven by two factors. First, the INS and sonar array are separated by 4.5 m (Forward: 4.385 m; Starboard: −0.453 m; Down: 0.939 m), and very accurate measurement of the separations are challenging given the hardware layout. Second, the rails used to position the array when it is raised/lowered have approximately 6 mm of slop in the forward/aft direction.

Given these results, the SVSS clearly meets the informal localization requirement of "within the width of a shovel head" that has been discussed at SERDP workshops. These results show that it is possible to further reduce the SVSS target localization errors to less than 5 cm by improving the measurement of the lever arm and reducing the variability introduced by the current array positioning hardware. For example, placing the INS in a watertight housing that is directly mounted to the array plate would minimize the lever arm length and remove any errors associated with variations in this length due to array deployment.

5.1.3 Foster Joseph Sayers Reservoir

The Foster Joseph Sayers Reservoir provides ARL/PSU with a local test site that has been critical to the success of this program. The site properties are reviewed in Section 4.4.1 and detailed information about the targets installed in this test bed are provided in Appendix A.1. In the early portion of the project, the proximity allowed ARL/PSU to make many iterative field tests to resolve issues identified in hardware integration and to refine the sensor configuration. Once the integration issues were resolved and a standard configuration was determined, ARL/PSU conducted regular field trials at the reservoir to begin establishing a large dataset with accurate ground truth that could serve the munitions response machine learning community.

The sediment structure in both the shallow and deep fields generally consists of a silt layer

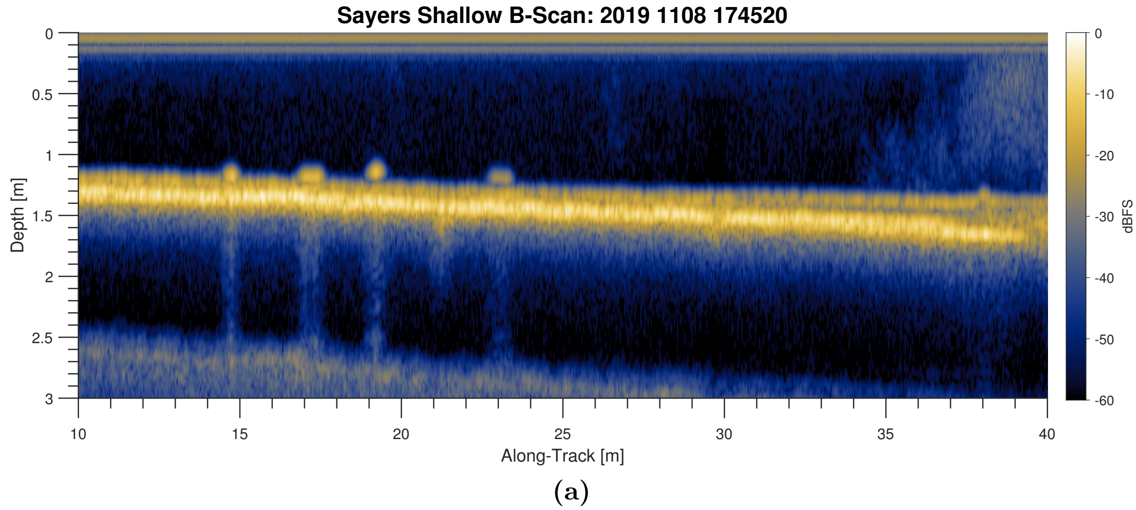

Figure 51: B-Scans are shown for the shallow (a) and deep (b) fields at the Foster Joseph Sayers Reservoir. Note that the horizontal-axis and vertical-axis scales are not equal.

over a clay basement; however, in the shallow field there are some regions where the silt layer is very thin. A pair of representative B-Scans for the shallow and deep field are shown in Figures 51a and 51b, respectively. The layered sediment structure is relatively consistent along the deep field track, while in the shallow field it thickens along the track.

Regular testing throughout 2018 and 2019 showed that the scattering strength of the lakebed varied throughout the year. An example of this is shown in Figure 52, where a cross-track MIP was generated for two tracks collected over a common set of four targets. The track in the upper portion of this figure was collected in June of 2019 when the water temperature was 20 °C, and the track in the lower portion was collected in November of 2019 when the water temperature was 6 °C. The higher sediment scattering strength during data collection in warmer months tended to mask the buried targets. It is hypothesized that this seasonal variation is caused by to biogenic production of methane, and additional discussion on this

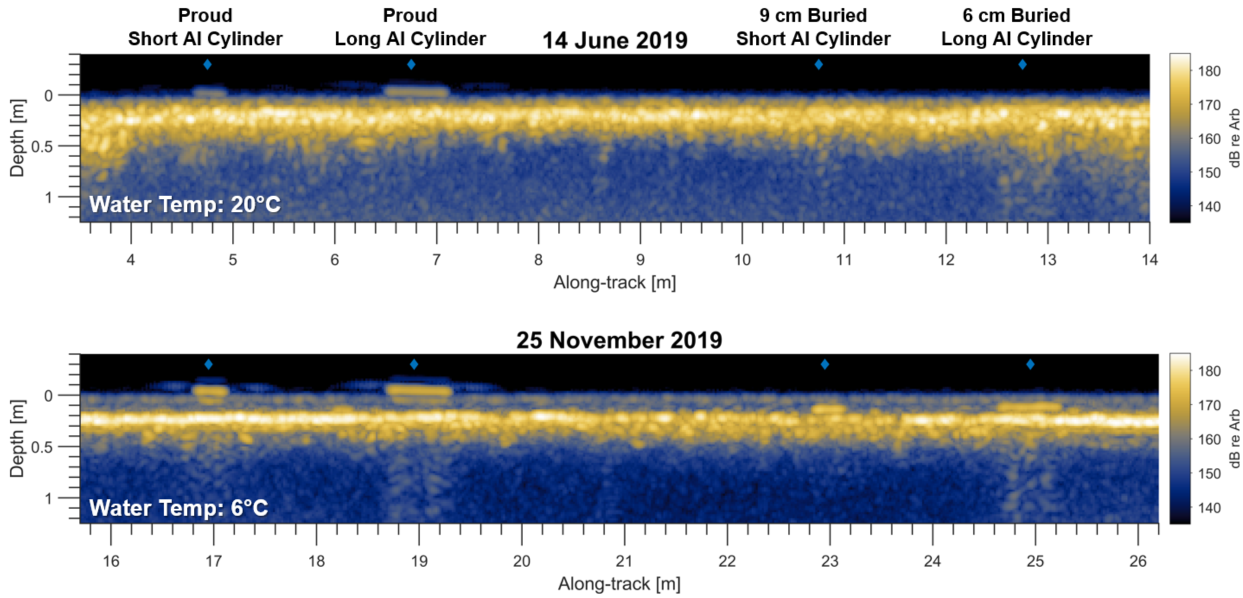

Figure 52: Cross-track MIPs are shown for a pair of tracks that surveyed a common set of targets in the deep field at the reservoir. It appears that surveys conducted during colder periods lead to reduced sediment scattering strength and improved target detectability.

topic can be found in Section 5.2.2.

A selection of depth and cross-track MIPs have been provided in Figures 53, 54, and 55. In each of these figures, the upper image (a) is a cross-track MIP shown on a 60 dB dynamic range scale. The middle image (b) is a cross-track MIP shown on a linear scale after application of the DRC described in Section 4.3.2.2. The lower image (c) is a depth MIP shown on the same linear DRC scale as (b). The cross-track MIPs have a series of colored icons along the top of the figure to indicate the along-track position of each of the targets described in the legend. The depth MIPs have the same colored icons at the cross-track and along-track positions recorded in the ground truth survey.

In Figure 53, each of the targets show a decaying return versus depth that extends far beyond the actual target dimension. These decaying returns are because of late-time scattering phenomena that are not accounted for in the image reconstruction model. The backprojection reconstruction algorithm described in Section 4.3.1 inverts a forward model that includes only geometric, single scattering. This algorithm excludes multiple scattering interactions and non-geometric (e.g., elastic or diffracted) scattering. This model is equivalent to assuming geometric-only scattering under the first Born approximation, which is accurate when the scattered field is small compared to the incident field and multiple scattering is ignored [56]. These effects produce visible artifacts in imagery as has been shown by Kargl, Williams, and Thorsos [37]. Image reconstruction in the presence of these late-time returns has also been studied [27–29]. In this image these artifacts provide a visual cue to indicate when a man-made object may be present.

In Figure 54 tracks are shown over the buried ordnance placed in the shallow field. In these figures the ordnance burial depths span 4 cm–30 cm. In Figure 54a the scattering from the water/silt and silt/clay boundaries have obscured the geometric returns from all of the targets except the shallow buried howitzer. In each case, however, the late-time scattering from the target is easily visible above the background.

Figure 55 provides a similar set of images for a track in the deep field where a mixture of clutter objects (cinder blocks) and science objects (shot put and cylinders) are both proud and buried. The silt layer is approximately 20 cm thick in this image. The short aluminum cylinder, which was buried 9 cm, is visible here because it is well-separated from both the water/silt and the silt/clay boundaries. The "mixed" target in this image is a pair of shot puts, separated by 29 cm, that are flush buried. The geometric response of these targets is not visible in the MIPs, but the non-geometric response is clearly seen. This is an example where the projection-based visualization can hinder the detection of objects whose scattering strengths are close to the surrounding sediment. A depth slice, passing through the two shot puts, has been extracted from this data cube for presentation in Figure 56. In this image, the location of the shot puts is clearly visible at 2 m along-track.

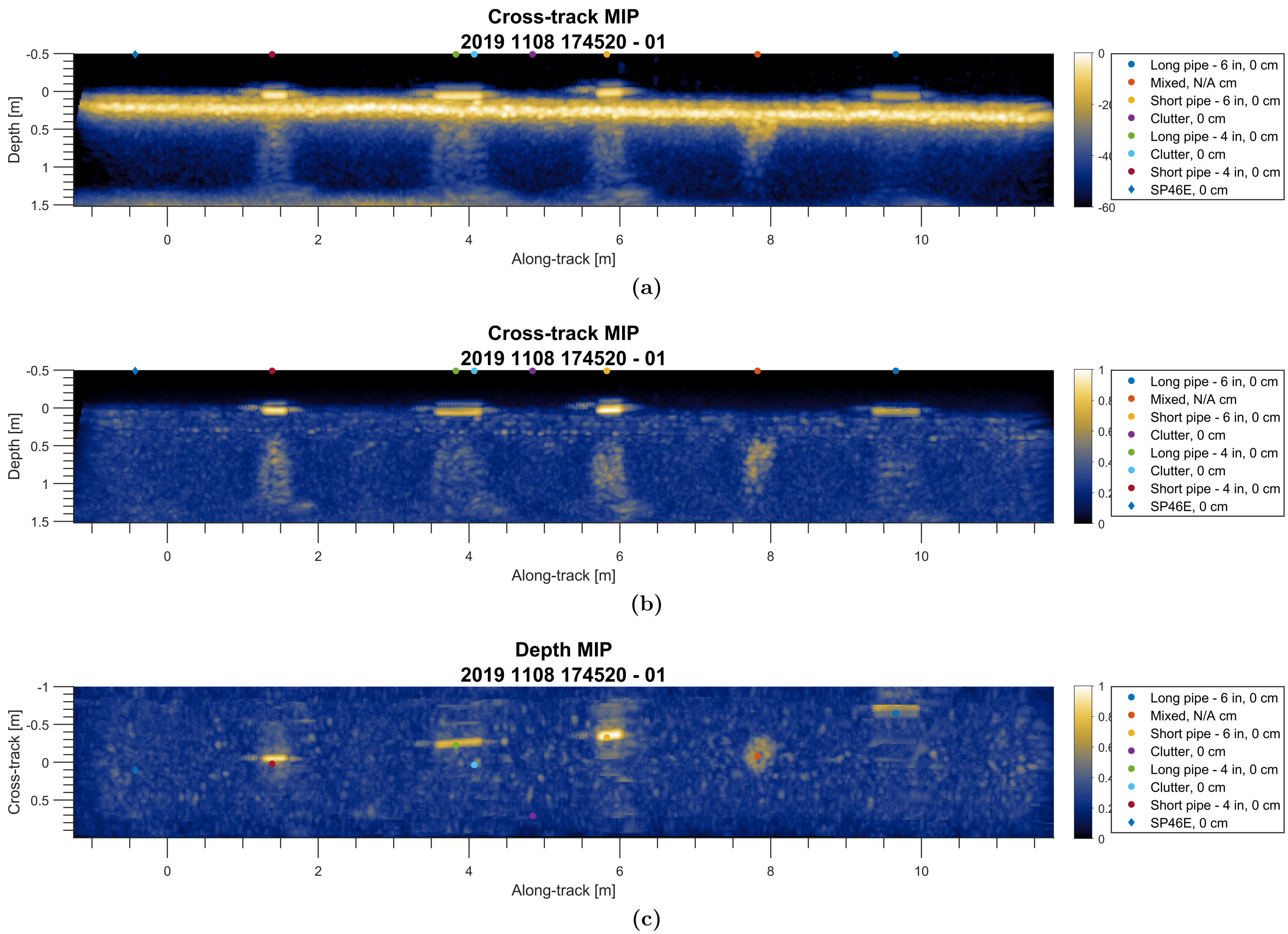

Figure 53: A selection of MIPs are presented for an image collected in the shallow field where proud pipes are present. This area spans P45, P44, P43, P15, P42 from left to right. Figure (a) is shown on a 60 dB logarithmic scale. Figures (b) and (c) are shown on a dynamic range compressed scale. Note that SP46E does not contain a target but is an empty and refilled hole.

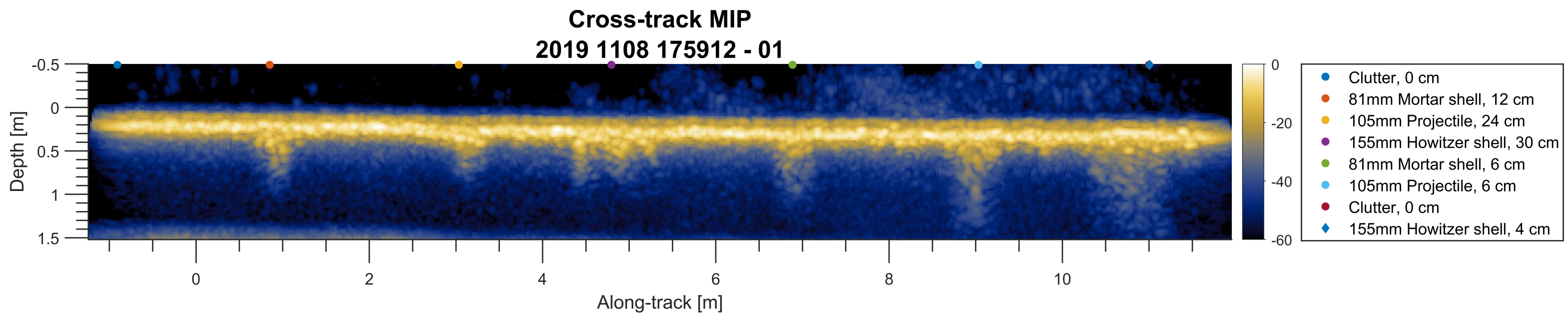

(a)

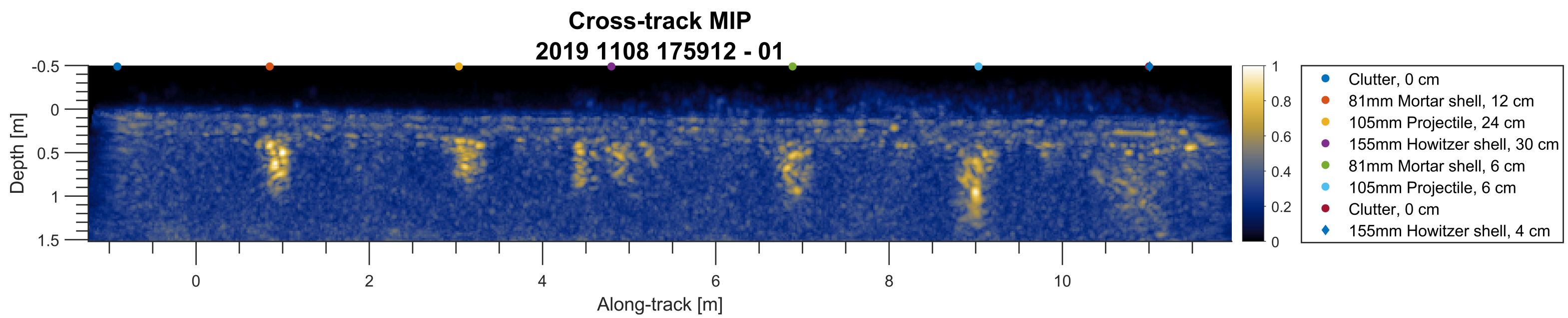

(b)

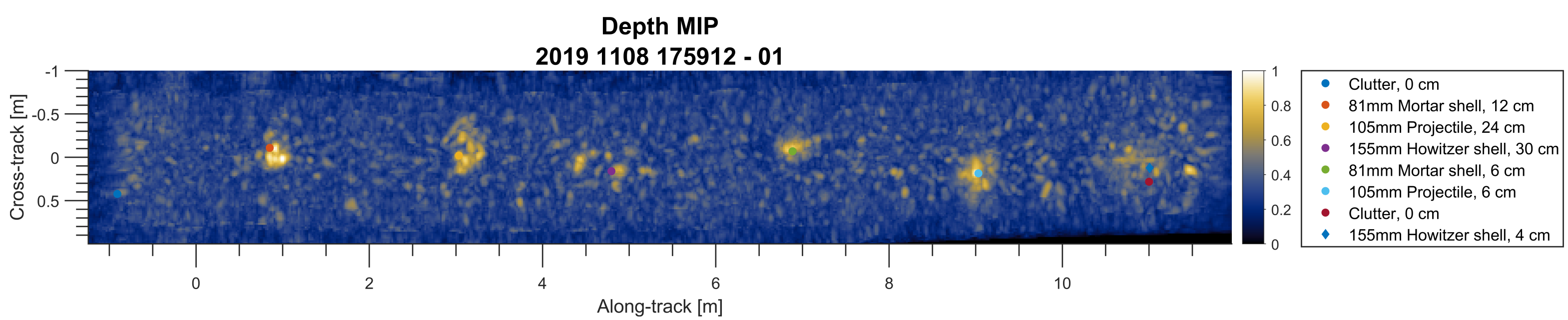

(c)

Figure 54: A selection of MIPs are presented for an image collected in the shallow field where buried munitions are present. This area spans P25-P20 from left to right. Figure (a) is shown on a 60 dB logarithmic scale. Figures (b) and (c) are shown on a dynamic range compressed scale.

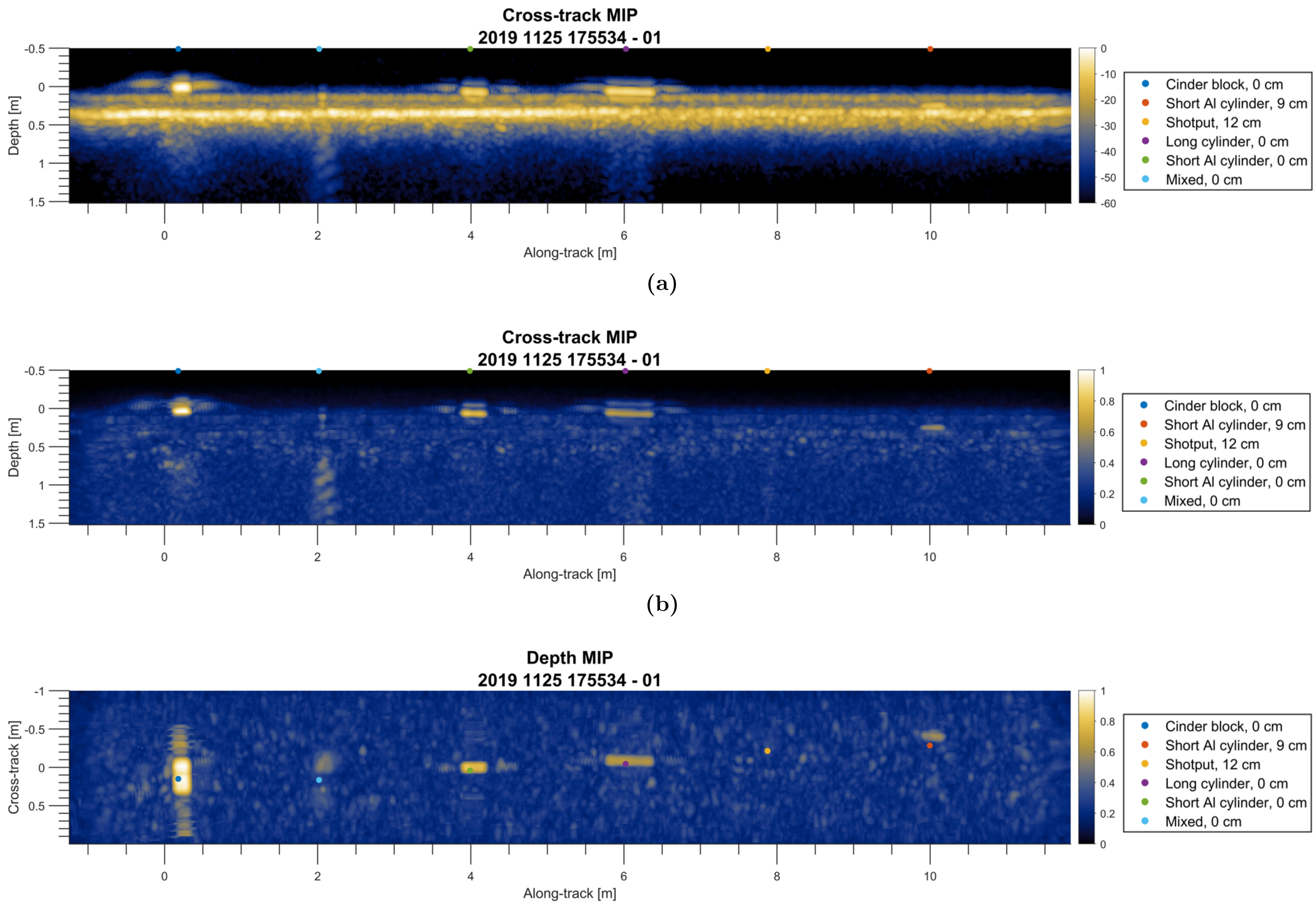

(a)

(b)

(c)

Figure 55: A selection of MIPs are presented for an image collected in the deep field where proud and buried objects are present. This area spans P12-P07 from left to right. Figure (a) is shown on a 60 dB logarithmic scale. Figures (b) and (c) are shown on a dynamic range compressed scale.

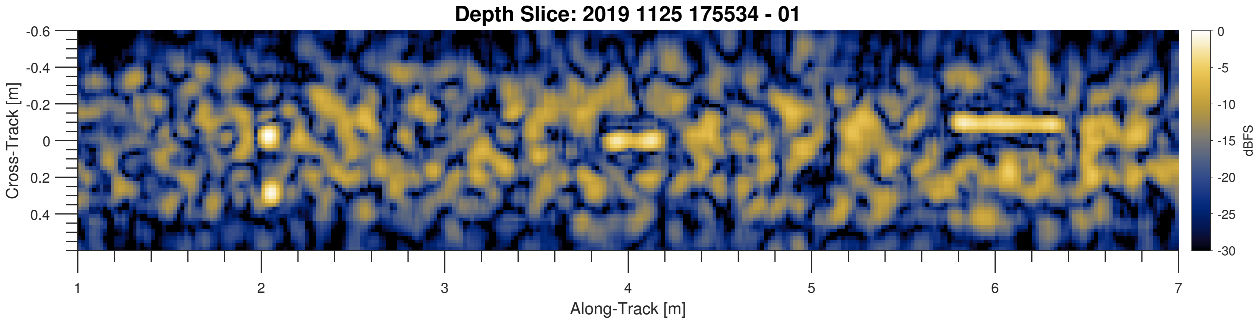

Figure 56: A depth slice is presented for the data cube shown in Figure 55. The pair of flush-buried shot puts, which are not visually apparent in the MIP representation, are clearly visible near 2 m along-track in this image representation.

5.1.4 Aberdeen Test Center - Littoral Warfare Environment

Over March 2-4, 2020 a total of 27 imaging tracks were collected against the prepared target field in the LWE. These tracks were collected by transiting the target field from west-to-east at a speed in the range of 0.5 m/s–1.0 m/s. The sonar system utilized the standard 255 µs Taylor-windowed linear frequency modulated (LFM) waveform spanning 20 kHz–35 kHz.

An example cross-track MIP of surface objects detected by the SVSS is shown in Figure 57. This image is shown on a 60 dB logarithmic scale normalized to the maximum pixel value. In this image, zero depth is referenced to an estimate of the sediment/water interface; therefore, the water column is at a negative depth and the sub-bottom is a positive depth. The five objects shown in this figure were located in positions P80-P84, where P80 is the leftmost target. Colored markers are shown at the top of this figure indicating the ground truth along-track position of the objects. The corresponding legend provides target descriptions including the length and diameter of the cylindrical objects. The elevated scattering visible at 1 m depth is from multipath interference and is not indicative of a sub-bottom layer. Similar to prior results obtained in the Foster Joseph Sayers Reservoir, the two steel pipe targets clearly show elastic ringing that is absent from the two concrete cylinders.

Across all of the objects in this figure, and many of the proud LWE objects, the sediment interface scattering level exceeded the target scattering level. This carries the risk of the interface return masking small objects. This is apparent for the small concrete cylinder, where the interface level was approximately 15 dB stronger than the target for this imaging product. Objects with smaller dimensions are both closer to the strongly scattering interface and have a lower scattering cross section. These two factors point to a challenge associated with detecting small, proud objects against high scattering strength backgrounds. A total of 27 proud objects were installed in the LWE and 23 of these objects were detected in the SVSS imagery. The four items not detected were the munitions with diameters of 20 mm, 25 mm, 40 mm, and 81 mm. Three of the four objects not detected were smaller than the vertical resolution of the transmit waveform. The 81 mm mortar is larger than the sensor's depth resolution, but this measure is only proper when comparing the minimum

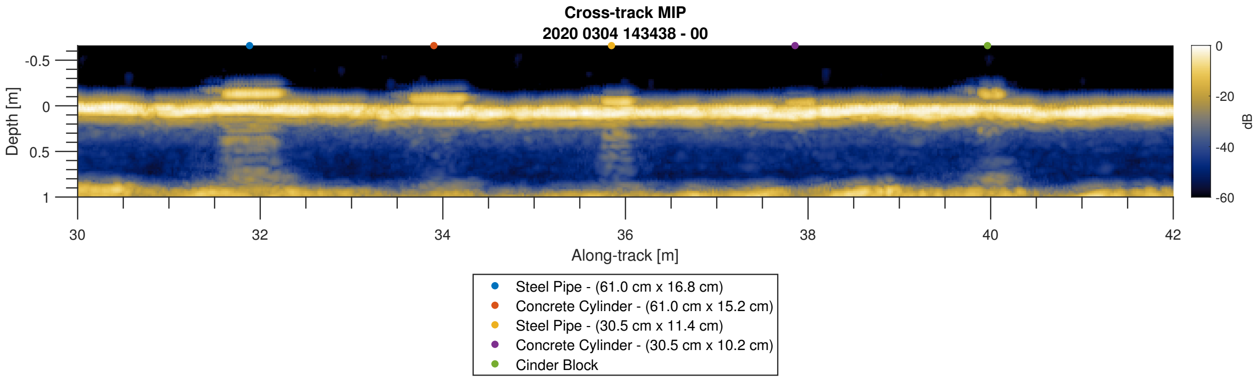

Figure 57: The cross-track MIP for P80-P84 is shown on a 60 dB log scale. This sequence of positions contains five proud objects. The ground truth along-track positions of the objects are indicated by the colored dots at the top of the figure. The object length and diameter are provided in the legend for each cylindrical target.

detectable separation of objects of equal scattering strength. In the LWE environment, the sediment's scattering level was significantly stronger than the munition's, thereby masking the munition's response.

A total of 58 buried targets were installed in the LWE and 27 imaging tracks were processed for detection of these buried targets. An example of a cross-track maximum intensity projection for a track containing buried targets is shown in Figure 58. The six colored markers shown at the top of the figure indicate the ground-truth along-track position of a set of six buried 155 mm howitzer shells, which are not visible in the image. The legend provides the ground truth burial depth for each of these targets. The scattering level below the interface falls by approximately 40 dB over just a few centimeters depth. This rapid decrease in level exceeds that expected for a standard sand environment which would be approximately 25 dB/m (two way) at the sensor's center frequency. No detections were made by the SVSS across all 58 buried targets in the LWE, and the same high-intensity scattering followed by a rapid falloff was observed throughout the target field.

The rapid attenuation of scattered level observed in the survey tracks collected 2-4 March prompted ARL/PSU to adapt the data collection plan to assess whether this elevated attenuation was prevalent across a larger portion of the LWE basin. A sub-bottom profile is shown in Figure 59 where the SVSS collected data along a track that progressed up the slope of the beach. A red dashed line is shown overlaying the sub-bottom profile at a depth equal to the lowest water level that occurred during dewatering for target field installation. This profile qualitatively indicates there is some type of environmental change near this water draw-down level that impacts sediment penetration. The ATC staff described the sediment bed as a uniform 60 cm–70 cm of sand across the face of the beach until the "drop off" seen at 15 m along-track in Figure 59. Therefore, the observed change in scattering strength and sub-bottom penetration is not because of a significant change in sediment type across the beach face.

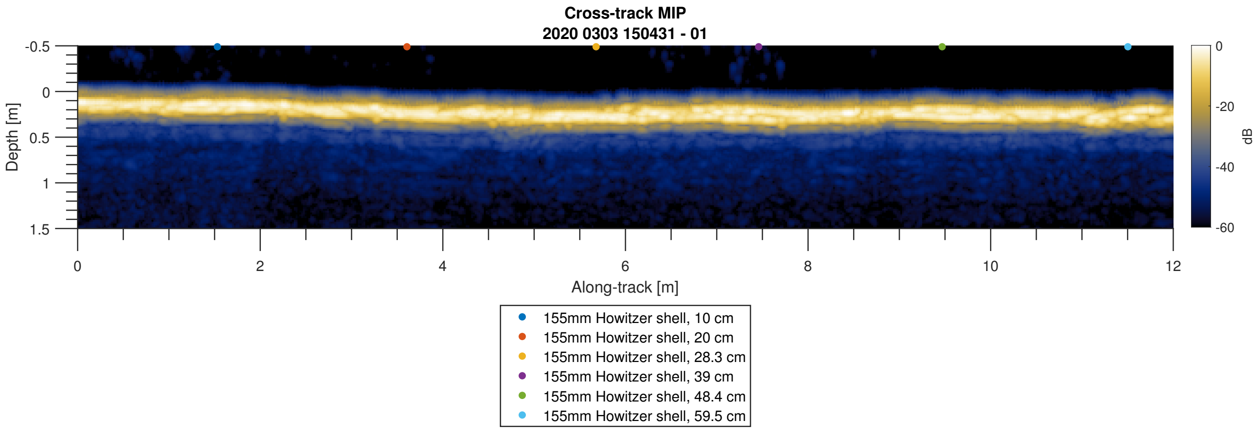

Figure 58: The cross-track MIP is shown for P03-P08 on a 60 dB log scale. This sequence of positions contains six 155 mm Howitzer shells buried in depths ranging from 10 cm–60 cm. The ground-truth along-track position of the shells are indicated by the colored dots at the top of the figure and the surveyed burial depth is shown in the legend.

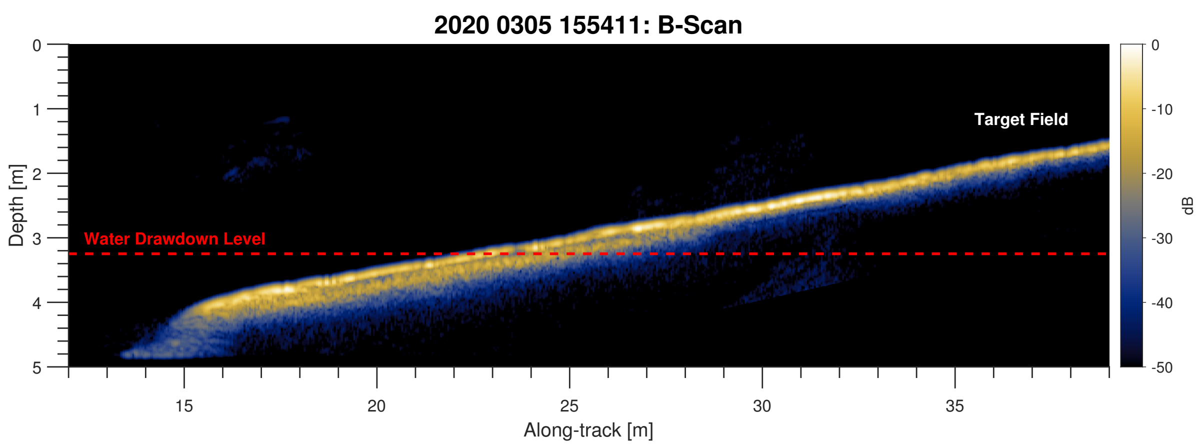

Figure 59: A survey track was collected transiting from deep to shallow water in the LWE. At 29 m along-track there is an abrupt change in the sub-bottom scattering level observed. The dewatering draw-down level is shown as a red dashed line.

The imaging tracks collected in the LWE have been processed to quantitatively estimate the spatial variation of the acoustic "penetration depth." This depth was calculated from cross-track MIPs that were analyzed to determine the upper and lower boundaries of the sediment return. These boundaries were defined to be the points approximately 20 dB less than the peak MIP intensity at each along-track position. A smoothness constraint was also imposed to reduce along-track variability. The estimated upper and lower boundaries are shown as red lines on the cross-track MIP in Figure 60a. The penetration depth cannot be simply calculated by finding the interval between these boundaries as that measure is biased upward by the width of transmit waveform's auto-ambiguity function and the cross-track slope imaged interface. In this analysis, the biasing factor has been estimated to be approximately 20 cm, and this is used to calculate the penetration depth, which is shown in Figure 60b.

The procedure for estimating penetration depth has been applied to all of the imaging tracks conducted in the LWE, and the results were compiled to create the penetration depth map shown in Figure 60c. To further reduce spatial variability, this map was smoothed with a 5 m x 5 m median filter. The target locations are shown as red dots, and the installation draw-down line is shown by filled red diamonds. This map indicates that the acoustic penetration of the sediment diminished rapidly for tracks more than 5 m south of the draw-down waterline. The specific mechanism for this change in performance is unknown; however, it is hypothesized the one month of delay between rewatering and testing was insufficient to allow entrapped air to release from the sediment that was exposed during the dewatering process.

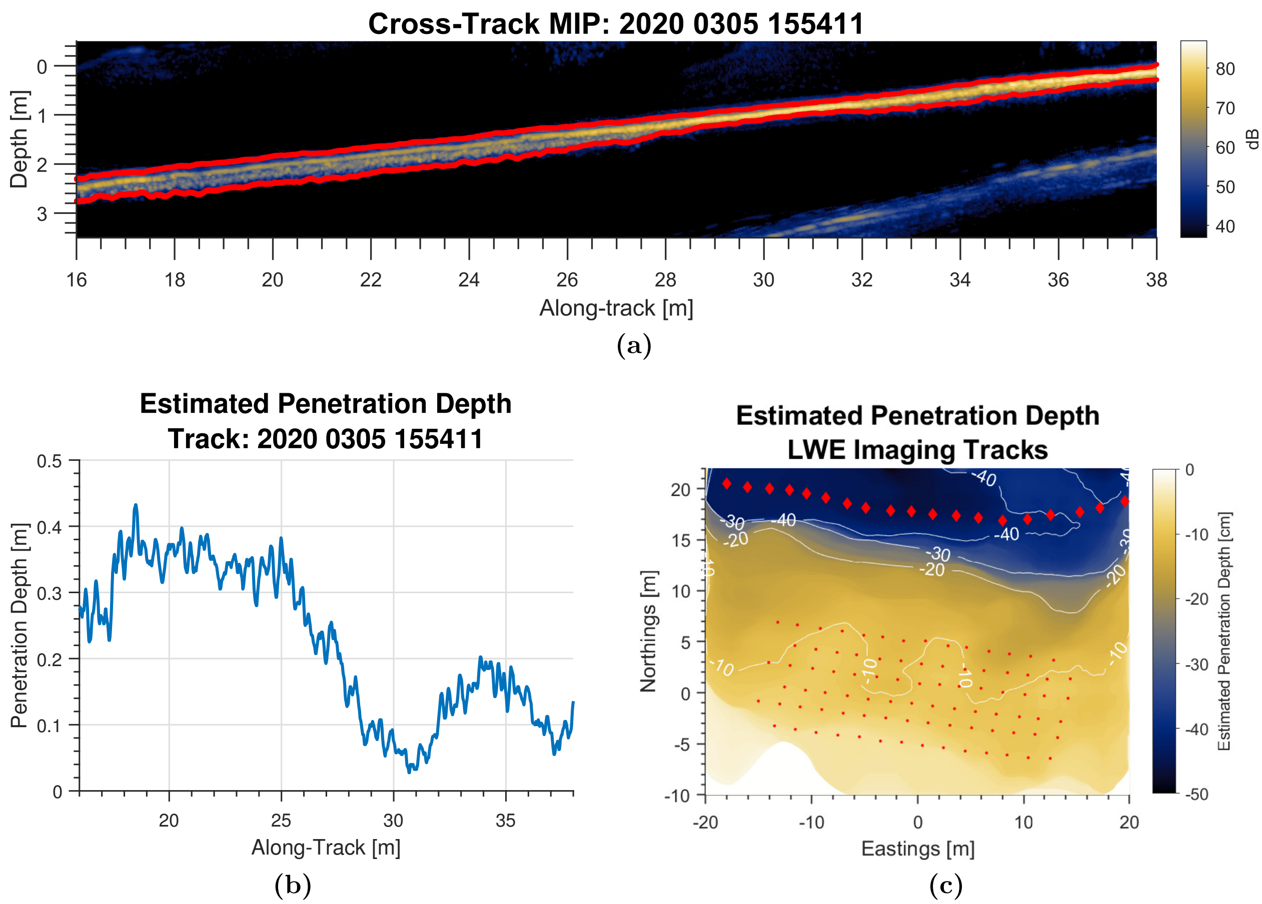

Figure 60: The penetration depth was estimated from the cross-track MIPs for the imaging tracks collected in the LWE. A pair of red lines are used to show the upper and lower sub-bottom margins in the MIP shown in (a). The penetration depth for this track is shown in (b). A map of the LWE penetration depth is shown in (c), where the target positions (red dots) and installation draw-down line (red diamonds) are shown.

5.1.5 Aberdeen Test Center - Bush River

Owing to the diminished sediment penetration over the prepared test site at the LWE, ARL/PSU requested permission to test in the neighboring Bush River. This testing was approved and conducted on the afternoon of 5 March 2020. Shifting from the LWE to the Bush River required recovery and redeployment of the SVSS and the RTK base station. This process took approximately 90 minutes.

The SVSS surveyed a region of the Bush River adjacent to the ATC Underwater Test Facility. The bulk of the survey was collected in approximately 2.5 m of water. The ATC staff described the sediments in the portion of the Bush River as principally mud, but no sediment samples were collected to confirm this. This survey site was anticipated to have man-made clutter from historical activity in the area.

The acoustic testing in this site demonstrated that the SVSS is capable of forming high-resolution imagery of deeply buried clutter in this environment. Figure 61 shows a sub-bottom profile that is broken into 4 sequential 85 m along-track segments. The sediment interface was slightly less than 2 m from the sensor. Over this track, the SVSS frequently demonstrated a penetration depth of 3 m into the sediment. Suspected entrapped gas limited the penetration of the SVSS at several points along this track, and pockets of probable sub-bottom gas are clearly seen at 64 m, 197 m, and 317 m along-track. The sediment volume above the gas layer was imaged, but the gas layer attenuates the sound and produces a shadow over the more deeply buried sediment.

An example of a region where a deeply buried clutter object was imaged is shown in Figure 63. Here, a single slice is taken from a three-dimensional image at approximately 3 m below the sediment/water interface. A 1.2 m long by 0.2 m wide clutter object is seen at the 11.5 m along-track location. The full three-dimensional data for this image segment is shown in the animated Figure 62. This animated figure shows the along-track, cross-track, and depth MIPs as a static background while an individual layer slice is incremented from above the sediment/water interface to a depth of four meters. At a depth of three meters it is possible to see the slice shown in Figure 63.

The data collected in the Bush River was manually reviewed to identify potential man-made clutter objects, and this process produced over 500 contacts. The reviewer flagged any object that either had strong geometry to suggest that it might be man-made or whose target strength significantly exceeded the background. Eighteen slices taken from the Bush River contacts are shown in Figure 64 and 65. Each slice is shown on a 30 dB logarithmic scale and the depth beneath the sediment/water interface is indicated by the title. The small red dot in each figure shows the point selected during the image review process. The majority of the contacts labeled in the Bush River were buried by more than one meter of sediment.

There were three general "classes" of objects found in this manual data review: small (∼15 cm) strong scatterers, medium (0.2 m–1.0 m) scatterers, and long (>1.5 m) cable-like

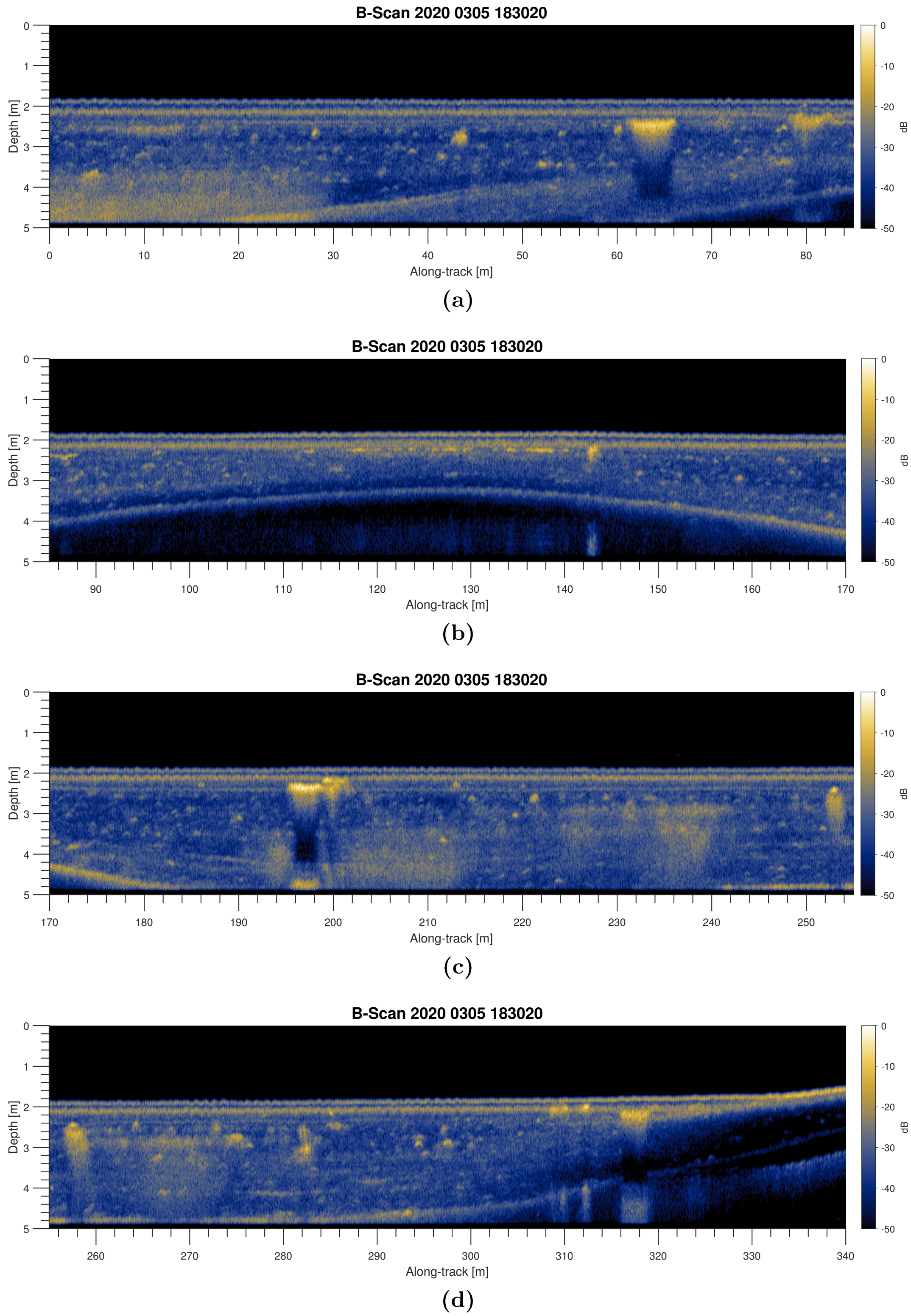

Figure 61: A sub-bottom profile was collected in the Bush River over a 340 m long track. These B-Scan images show a layered riverbed where acoustic penetration frequently exceeded 1 m.

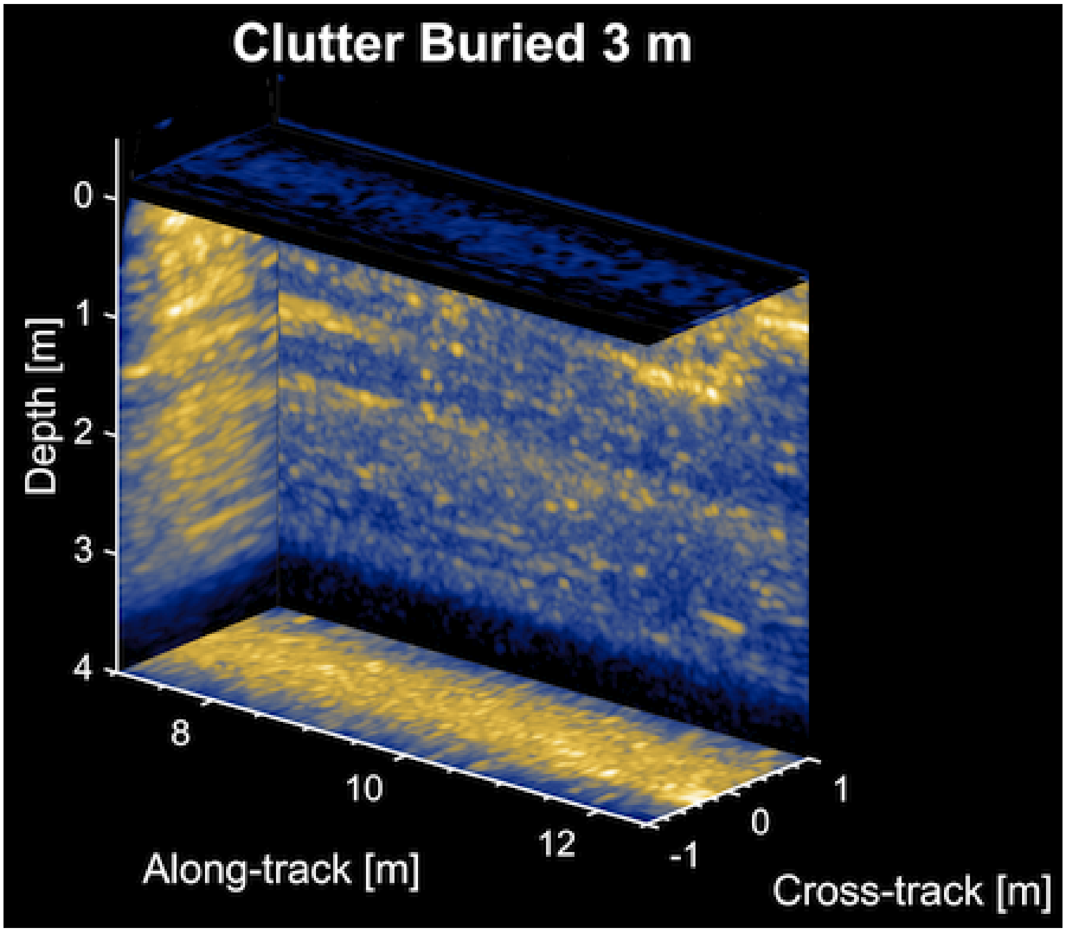

Figure 62: This animation shows a three-dimensional image segment collected in the Bush River. The outer static surfaces show the MIPs across the respective dimensions. When played, the animation shows the individual layers making up the full 3D image. The object in Figure 63 can be seen as the slice passes through 3 m depth. This animation can only be played if the report is viewed using Adobe Acrobat.

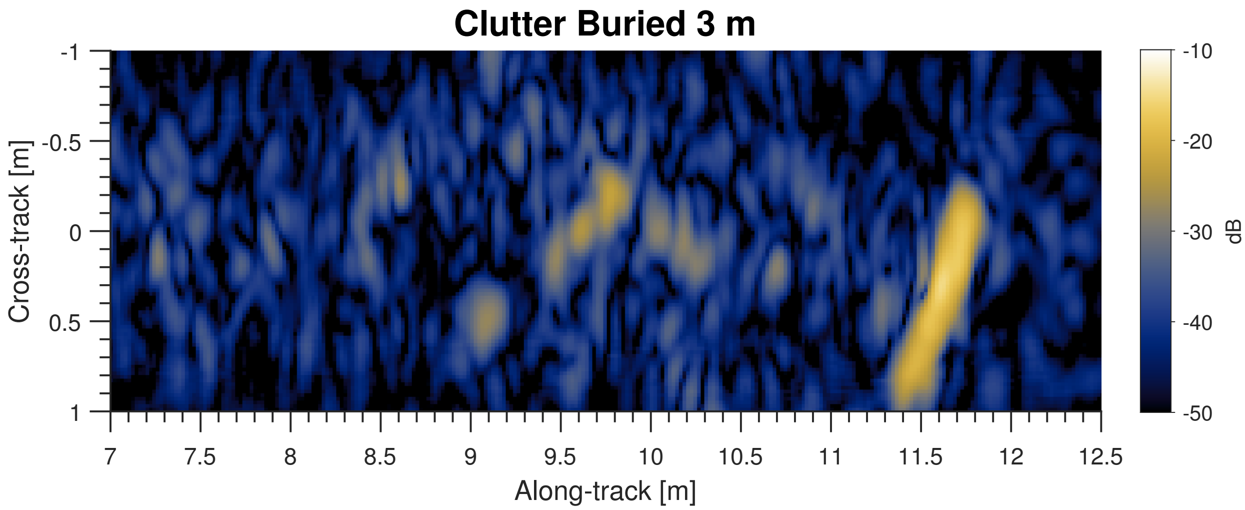

Figure 63: This image slice was taken from approximately 3 m below the sediment/water interface in the Bush River. A clutter object is clearly seen at 11.5 m along-track.

objects. Figures 64a-64c show examples of the small objects whose scattering strength exceeded the background sediment scattering level by more than 30 dB. Figures 64d-64i show examples of the cable-like objects. Finally, Figure 65 shows nine examples of the medium size scatterers. Within Figure 65, (e) and (i) both show a pair of closely spaced clutter objects.

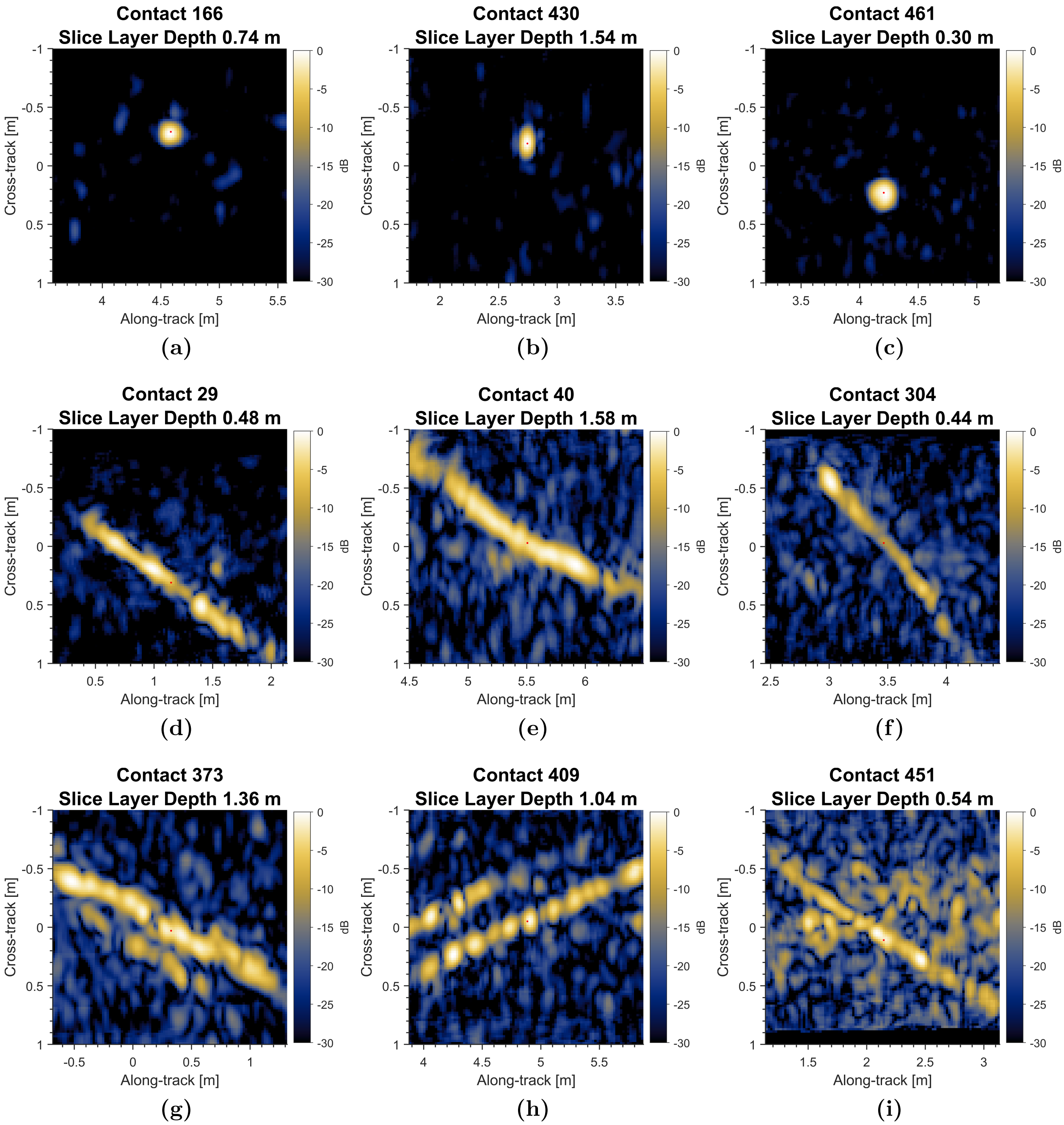

Figure 64: Selected clutter objects that were manually labeled in the Bush River.

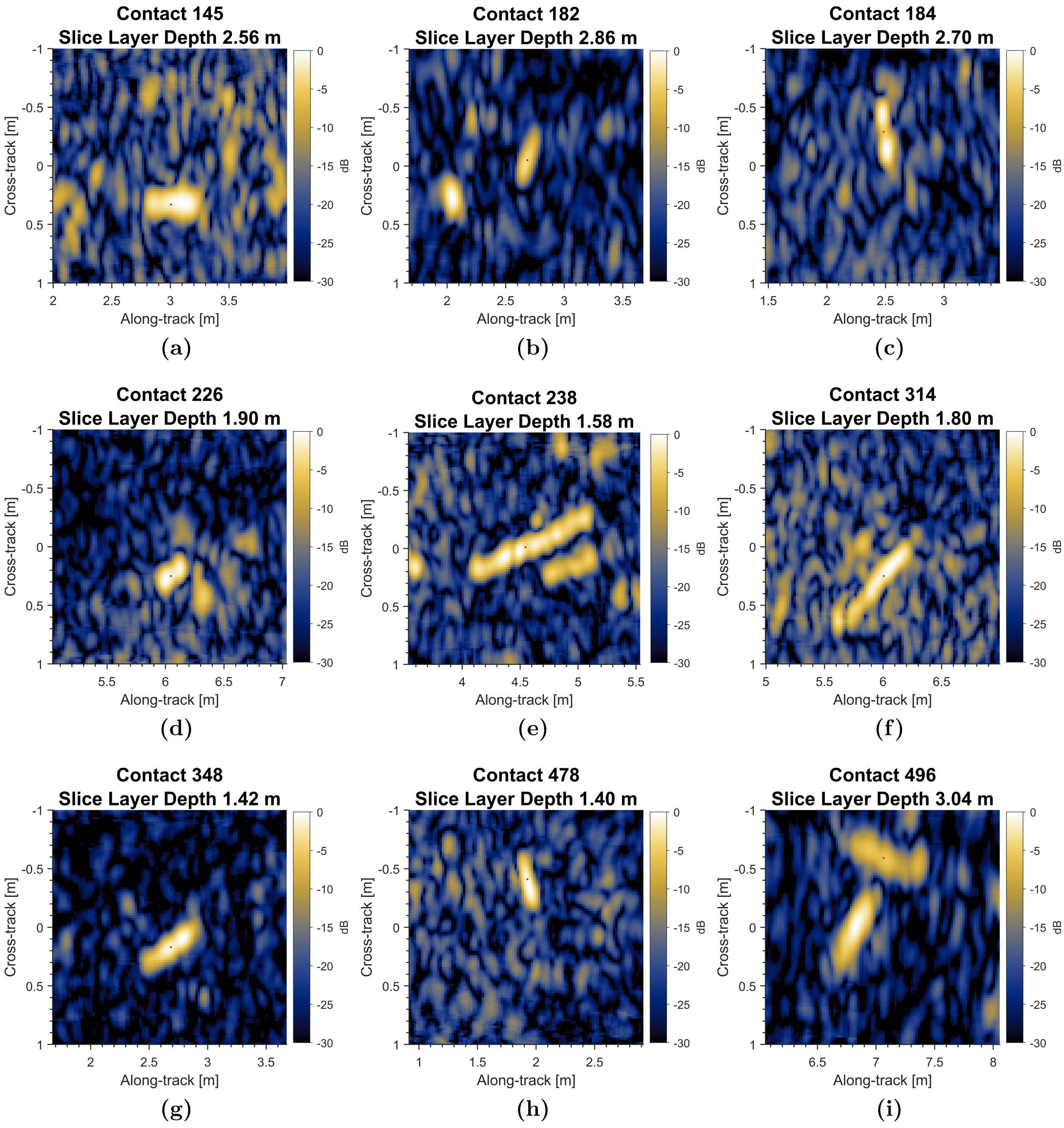

Figure 65: Selected clutter objects that were manually labeled in the Bush River.

5.1.6 Target Detection

The datasets collected at the Foster Joseph Sayers Reservoir in 2019 and at the ATC LWE in 2020 were provided to Dr. David Williams at the NATO Centre for Maritime Research and Experimentation for target detection analysis. Dr. Williams has recently developed the Mondrian detection algorithm for the detection of objects in high-frequency (and optionally dual-frequency) SAS imagery [51]. This algorithm bases its detection criteria on the spatial distribution of highlights and shadows surrounding a test point. The highlight/shadow structural requirements are based upon the sensing geometry of an imaging SAS and the expected range of target dimensions.

As part of ARL/PSU's collaboration with Dr. Williams, he adapted the Mondrian detection algorithm to the problem of proud and buried ordnance detection. This adaptation has extended the Mondrian detector to three-dimensional data, removed features based upon shadows (which are not visible in volumetric data), and expanded the range of object sizes that may be present within a scene. A more thorough review of this effort can be found in Williams and Brown [52].

The SVSS datasets were geographically segmented with the Foster Joseph Sayers Reservoir shallow and deep sites designated "A" and "B", respectively. The ATC LWE is designated site "C". The datasets were also temporally segmented with Sayers Reservoir testing "1" to "4" occurring in June, August, early November, and late November. The ATC LWE testing in March 2020 is labeled "5."

The likely entrapped gas, which creates a masking effect, at the test sites creates an upper limit on detection capability for the SVSS. To assess the Mondrian performance against a human assessment of target opportunity, the data from each target opportunity was first visually examined and rated in terms of anomaly size (large or small) and strength (strong or weak) in the imagery. Anomalies that were deemed both small and weak represent a "gray zone" in which detection may or may not actually be feasible.

With these human assessments as a backdrop, the performance of the proposed target detection algorithm at eight distinct data collections, delineated by location and time, are shown in Figure 66 for proud and buried targets. As shown in the figure, performance varies considerably across location (cf. collection letters), but also across time (cf. collection numbers), with the latter variation suggesting strong environmental dependence (e.g., water temperature, microbial activity). However, in all cases, the automated detection performance comported with the expected range based on visual inspection of the imagery indicating good detection performace. Across different locations and times, the automated detection algorithm performed at a similar level as a human capable of accurately assessing all visible large targets, all visible small targets with strong responses, and some visible small targets with weak responses. For objects deemed visible by human assessment the algorithm's probability of detection was 93% for proud objects and 68% for buried objects. Future work on the algorithm will see the development of a dedicated classification state in order to reduce the false alarm rate.

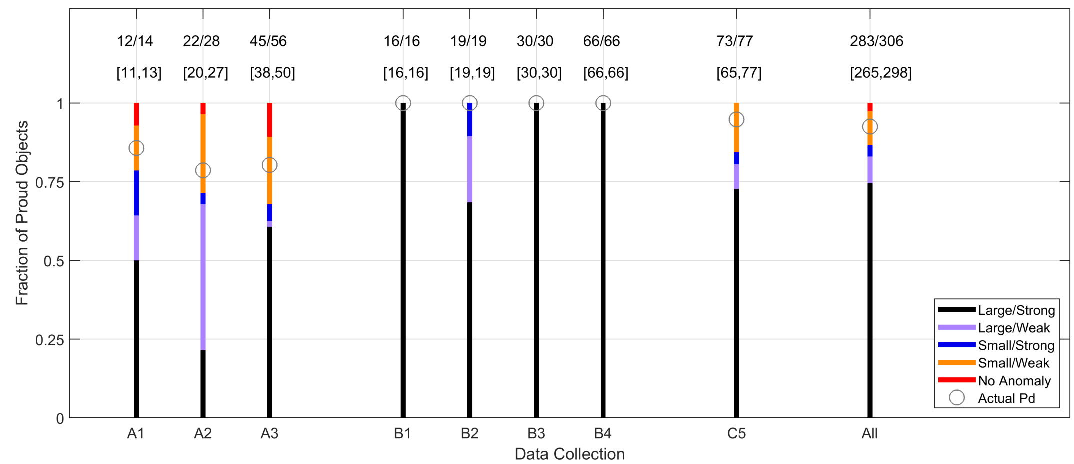

(a)

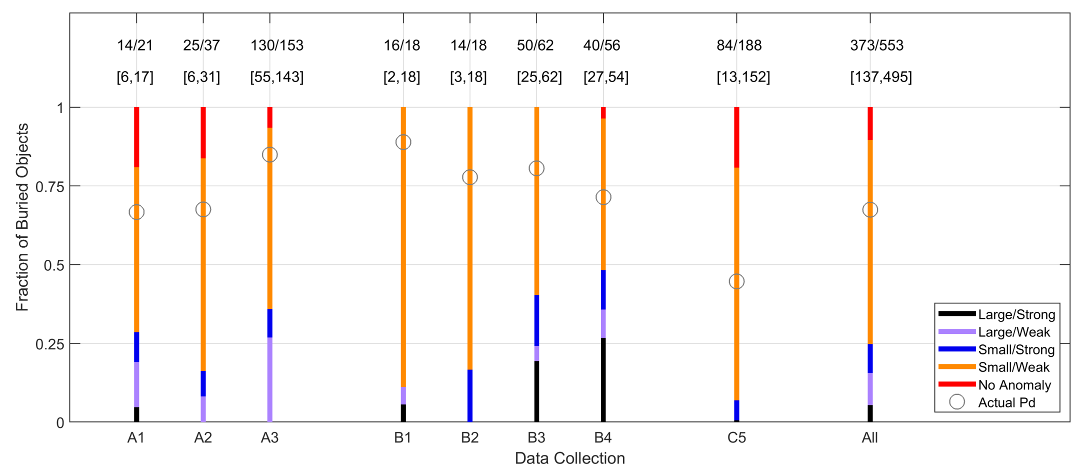

(b)

Figure 66: Performance of the detection algorithm for each data collection for (a) proud man-made targets and (b) buried man-made targets, along with the distribution of visual human assessment ratings. Above each bar are the numbers of targets detected vice opportunities, and in brackets the range of targets deemed detectable based on visual human assessment.

5.2 Model-Data Comparison Results

Effective model-data comparisons demonstrate detailed knowledge of the acoustic problem and inform the researcher about the relative importance of different physical mechanisms within the environment. In the case of the SVSS, the knowledge gained will be used to improve future system design, processing algorithms, and implementation choices. Time-series results presented here use the PoSSM model described in Chapter 4.1. Additionally, bubble response models are (also developed and) incorporated into the PoSSM framework, as described in Appendix D.

This chapter contains several model-data comparisons. First, a 2-layer model is developed and compared to field data acquired at Foster Joseph Sayers Reservoir ("Sayers"). Then, the models are used to describe unique effects observed in field data, both from Sayers Reservoir and in the Bush River. These effects were attributed to the presence of bubbles in earlier reports, and the work presented here further supports that hypothesis.

5.2.1 Sayers 2-Layer Model

This section describes a model-data comparison of the deep field test area at Sayer's Reservoir. Much of the information described here was also presented at the International Conference on Underwater Acoustics (ICUA) in September of 2020, in a presentation given by J. Philtron, D. Brown, and S. Johnson, titled "Data-model comparison of a shallow water sonar system for buried UXO detection."

During each field test day in 2019 at Sayers Reservoir, the SVSS system scanned the same section of sediment adjacent to the deep field test area. The purpose of performing this repeat track was to provide a rich dataset for quantitative model/data comparison. Figure 67 displays a satellite view of the test area, with green lines that represent the relevant repeat tracks. The red box highlights a 5 m section of data chosen for analysis. A B-Scan of data collected on November 8 is also shown. The B-Scan data indicates that the area is relatively flat and the individual A-Scans compared at different along-track positions show a similar response. The distance from the sonar to the top of the sediment is approximately 3 m, and a secondary sediment layer is clearly present that provides a stronger reflection amplitude. Note that this data, and all of the data analyzed in Chapter 5.2, has not been replica correlated (match filtered).

Figure 68 provides an overview of the PoSSM simulation used for model-data comparison. The geometry of the mud (upper) and clay (lower) sediment layers used in the model is shown. The total simulation is a combination of individual models run for the mud interface, mud volume, clay interface, and clay volume that each contribute to the combined reflected acoustic field. Additionally, for each of the interfaces, the model is split into a coherent (specular) and incoherent (diffuse) component. These 6 models are coherently added to simulate the entire scattered field. Also, the transmit pulse amplitude (RMS level of 183.5 dB) is adjusted by the two-way transmission coefficient and attenuation through the water/mud interface when used for the clay models, and clay/mud property ratios are used

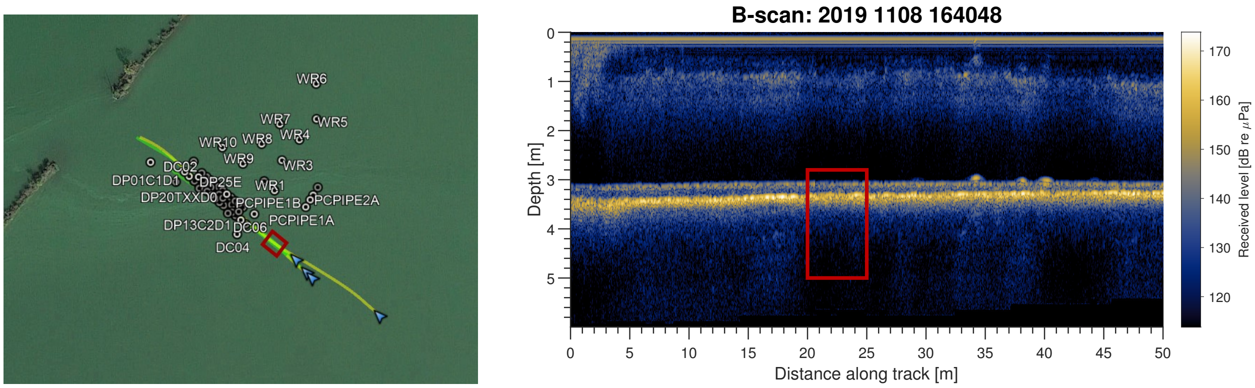

Figure 67: Left: Satellite view of target field from Google Earth. Tracks are indicated by green lines. Right: B-Scan plot of data on a track from November 8, 2019. The 5 m section of data used for the data-model comparison is indicated by the red box.

Table 7: Properties used for PoSSM simulations of the deep field repeat track at Sayers.

Variable	**Hamilton properties**		**Updated properties**	
Sediment type	Mud	Clay	Mud	Clay
ρ_s/ρ_w	1.336	1.605	1.1	1.8
c_s/c_w	1.003	1.012	1.003	1.054
δ_s	1.92e-3	3.33e-3	1.92e-3	3.33e-3
w_2 [cm^4]	5.18e-4	5.18e-4	5.18e-4	5.18e-4
γ_2	3.25	3.25	3.25	3.25

to calculate the reflection coefficient and refraction at the clay interface.

Sediment properties input into the PoSSM simulation were chosen to match available site sediment data and supplemented with values from the literature (e.g., sediment attenuation was not measured on site). The water velocity was set to $c = 1437\,\text{m/s}$ to match the November 8 field data used for the model-data comparison. Table 7 lists the properties used in the PoSSM simulation. Two main simulations with different properties were run. Sediment property values for the first simulation, labeled "Hamilton properties," used density, velocity, and attenuation for mud and clay from Hamilton [26, Table 3, rows 7 and 6] and the spectral strength and spectral exponent for silt and clay from APL-UW TR 9407 [2, Table II, p. IV-6]. Note that these properties have been revised from the initial properties used in models during Phase 1.

Sediment properties used in the second simulation are labeled "Updated properties" in Table 7. Corrections to the density and sound speed ratio were made to match core log data provided by NRL-SSC after analysis of a field sample. The updated velocity ratio for clay, based on the chosen density, is consistent with regression parameters for a collection of siliciclastic sediment field data [3, Table 5.3, p. 136]. Additionally, the volume scattering level, σ_v, was set at approximately $-21\,\text{dB}$ for mud and $-19\,\text{dB}$ for clay based on the use of $\sigma_2 = 0.004$ for the dimensionless sediment volume scattering parameter [3, pp. 381-2].

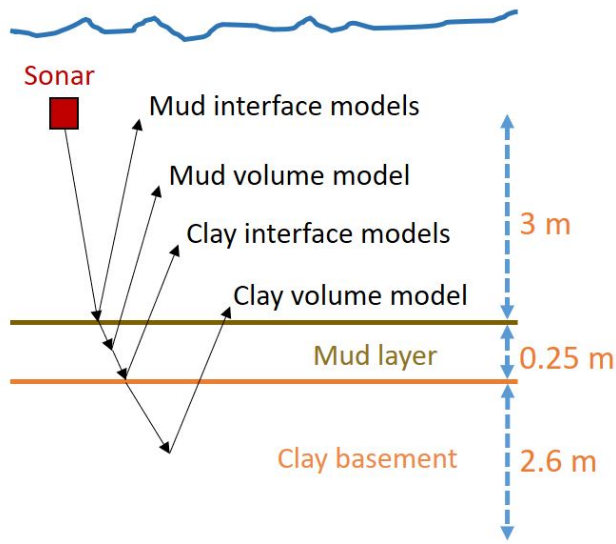

Figure 68: Schematic indicating the different wave paths modeled from the interaction with the mud and clay sediment layers at Sayers.

Figure 69 shows data from the PoSSM simulation for a single ping. On the left, the diffuse interface and volume scatterer composite levels are shown for both the mud and clay models in the simulation. Note that the interface models were calculated using 2500 calculation points per m^2, and the volume models were calculated with 2197 calculation points per m^3. On the right, the plot shows how the individual models contribute to the total PoSSM simulation result by presenting the mean of the A-Scan over the 5 m simulated track. The track contained 112 pings and the real motion (INS data) of the Sound Hunter was used for the sonar position and attitude in these simulations. This plot shows that the reflections from the mud and clay interfaces are much stronger than the volume scattering components, and that the coherent and incoherent components of the interface reflections are both significant. Note also that the kernel used in the PoSSM simulation is the transmit pulse (i.e., a 255 µs LFM chirp centered at 27.5 kHz with 15 kHz bandwidth) as measured in the ARL/PSU Anechoic Test Facility.

Figure 70 uses the mean A-Scan over the 5 m track to provide a model-data comparison for the simulated and field data. Overall, the simulation matches the field data quite well: it shows the characteristic double peak that is seen in the field data and a similar absolute level in the late return, which represents volume scattering from the clay basement. The peaks in the "Hamilton properties" simulation clearly does not match the field data: the first peak is stronger than the second. However, once the properties are updated to match the field site sediment's density and velocity properties, the mean amplitudes of the two peaks closely match the field data. The lower amplitude of the first peak indicates that the mud properties are more closely matched to the water column than the clay properties. When the median peak level from the mud and clay layers are calculated, the simulation is 2.4 dB and 4.6 dB lower than in the field data, respectively. It is hypothesized that this difference could mainly be due to the presence of rocks at the field test site, which are not currently

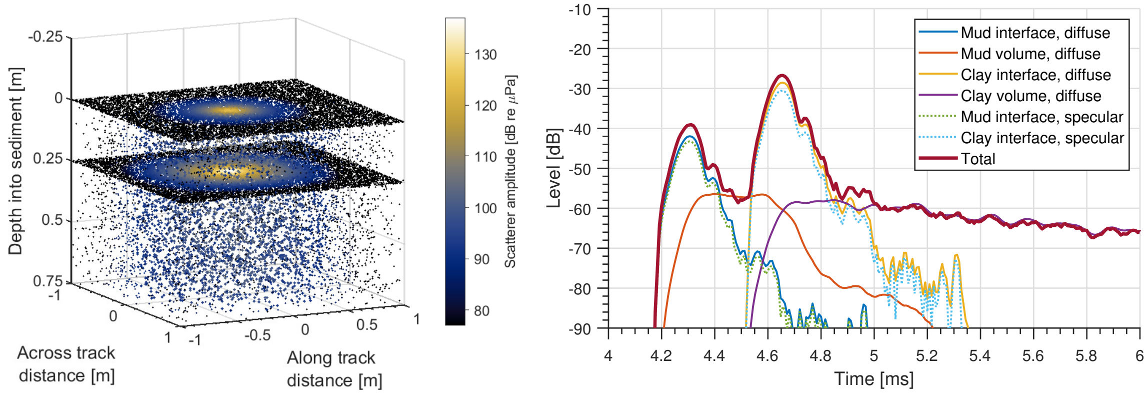

Figure 69: Left: Composite levels for a single ping, showing diffuse interface and volume scattering for a mud layer above a clay basement. Right: Ensemble-averaged A-Scan over the 5 m track for each model component and the total simulation response for the updated properties model.

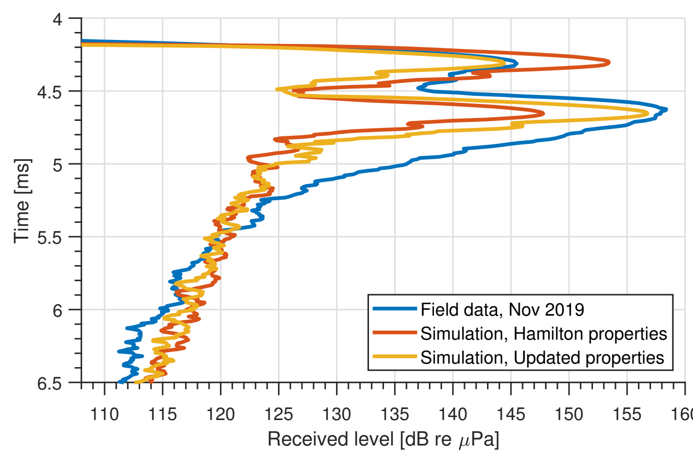

Figure 70: Ensemble-averaged A-Scan over a 5 m section of track from field data (blue) and simulated data with Hamilton (red) and updated (yellow) properties.

considered in this simulation.

Figure 71 shows the field and simulated data in B-Scan format. The dual layering of the sediment is clearly visible. Additionally, the heterogenity present in the field data is clearly visible. The simulation uses homogenous sediment layers that do not capture the ping-to-ping variability of the environment, which has variable depth to the sediment, mud layer thickness, sediment properties, and natural clutter (rocks). The stronger scattering amplitude response in the field data can also reasonably be explained by the presence of natural clutter.

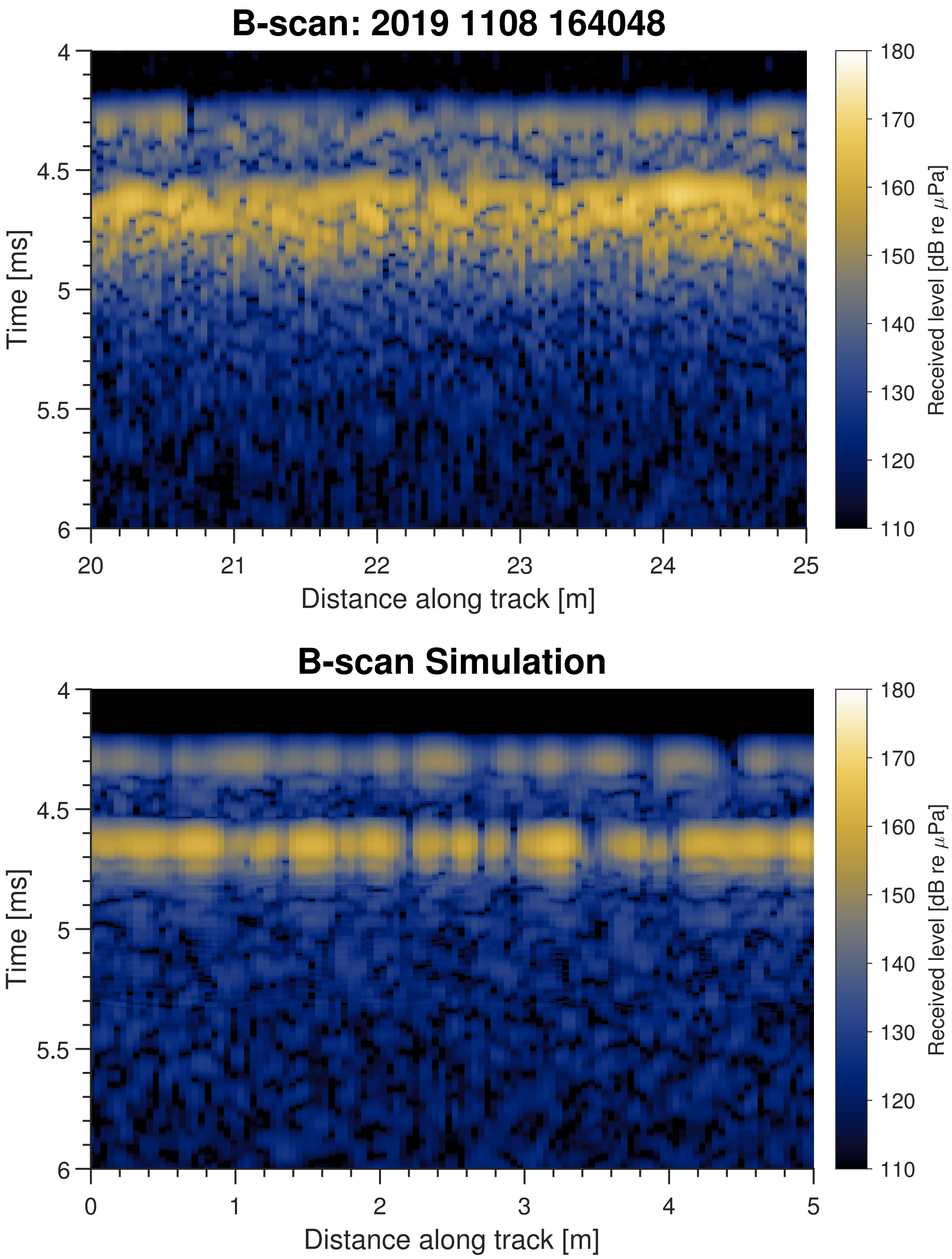

Figure 71: B-Scan of 5 m of field (above) and simulated (below) data.

5.2.2 Sayers Seasonal Variation

During each day of testing at Sayers Reservoir during 2019, data were collected along a track adjacent to the deep test field at the location indicated in Figure 67. The sediment composition in this area is a mud layer over a clay basement and a detailed model-data comparison of this region was presented in Section 5.2.1 for data collected in November. However, when data collected throughout the year is examined, it is clear that there is considerable variation in received level from the mud and clay interfaces.

Figure 72 shows the mean A-Scan data over the 5 m repeat track for tests in May, June, August, and November of 2019. The nominal distance to the mud layer is 3 m, although this distance varied by about 20 cm based on changes in the water level throughout the year (depicted previously in Figure 40). The levels shown in Figure 72 for the different tests have been adjusted to normalize for amplitude differences due to geometrical spreading so that all of the data can be presented with the first peak aligned at 3 m depth. The peak received amplitude from the mud and clay layers remains at about 3.2 m and 3.5 m depth throughout the year indicating that there was not a significant removal or addition to the sediment during this time period. However, the peak amplitudes vary dramatically—by up to 18 dB! Also, additional peaks occur *between* 3.2 m and 3.5 m, indicating that new scatterers appear and disappear throughout the summer. We hypothesize that the dramatic changes in amplitude with depth are due to entrapped gas within the sediment, which varies in depth and quantity throughout the testing season.

A small (by volume) amount of free gas in a sediment can have a very strong effect on sediment acoustic properties [57–59]. The presence of bubbles increases both the scattering strength and attenuation in the sediment. Entrapped gas can obscure very shallow buried targets due to the elevated background scattering strength as well as cloak deeply buried targets by attenuating the incident and scattered fields. In freshwater lakes, the primary mechanism by which gas bubbles form is through biogenic production of methane [60], and this process has been shown to be sensitive to temperature [61]. If the entrapped gas is due to biogenic methane, it is plausible that the seasonal dependence of the scattering strength would exhibit the trends shown in Figure 72, where the largest amplitude response in the upper mud layer occurs when the water is warmest.

PoSSM simulations were run to estimate the volume fraction of air, V_{air}, necessary to reach the peak amplitude values shown in Figure 72. The resulting transmission loss expected for the reflection from the clay interface, for which the sonar pulse travels through the bubble layer twice, was also calculated. Appendix D describes these bubble-related calculations. The sample bubble distribution shown in Figure 96 was used in the simulations. It is assumed that there is no entrapped gas during the November measurement.

The PoSSM simulation contained a layer of spherical bubbles 5 cm thick. To change the air volume fraction the number of bubbles was increased or decreased, while keeping the same a^{-4} distribution of bubble radii. The horizontal extent of the bubble layer was 1 m beyond the sonar center, which was sufficient to contain the main lobe of the composite transmit/receive beam pattern as well as the peak of the first sidelobe. For a 5 m track

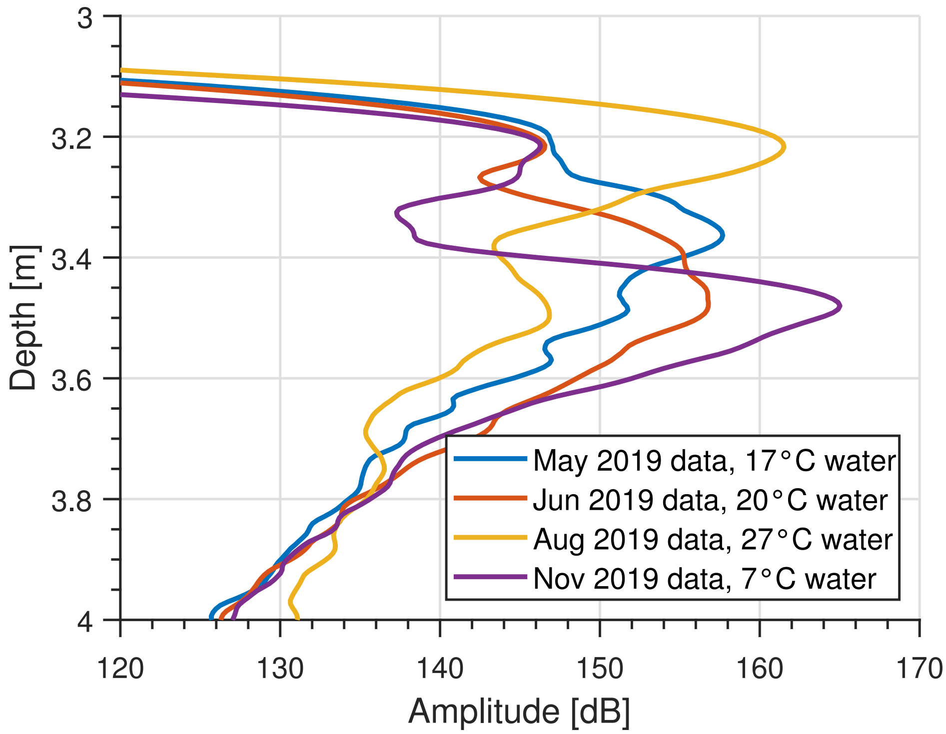

Figure 72: Mean A-Scan data over 5 m of collocated track for several 2019 tests.

length, the bubbles were evenly distributed within a 2 m x 7 m x 0.05 m volume. The bubble layer was translated vertically within the mud layer up to 20 cm to align the arrival time of the peak return from the simulation with the peak return in the field data.

The results of these simulations are summarized in Figure 73. In addition to the mean A-Scan data from different test dates, previously shown in Figure 72, circles indicate the peak level from each simulation and squares indicate the expected reflected level from the clay interface. The expected clay level was based on the November value combined with the transmission loss due to the simulated bubble layer. Table 8 provides a summary of the air volume fraction, transmission loss, and other related test information.

In Figure 73, the amplitude of the circle represents the mean A-Scan peak amplitude for the 5 m track length. The bubble layer depth and volume fraction have been adjusted so that the circles precisely align with the peak amplitude and arrival time from the field data. The squares are found to be a good estimate of the transmission loss seen in the field data, although they overestimate the clay interface reflection amplitude by 2 dB–3 dB for the May and June data. This is because the transmission loss calculated for the placement of the squares only represents the loss for the bubbles within the 5 cm thick layer, and does not account for additional bubbles within the thickness of the mud layer. A reasonable explanation of this difference is that during May and June a sufficient quantity of bubbles was present throughout the mud layer. These additional bubbles did not contribute significantly to the overall peak level but did contribute to the overall transmission loss. Overall, the PoSSM bubble simulation and transmission loss calculations accurately represent the seasonal variation seen in the field data. The maximum value of 0.28% air fraction averaged

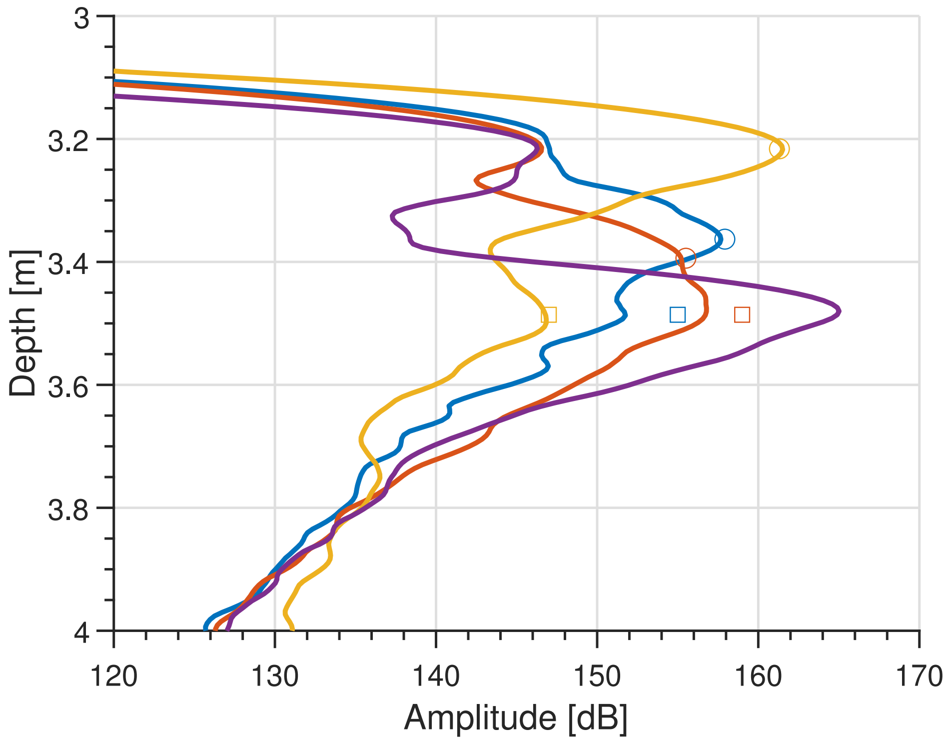

Figure 73: Mean seasonal A-Scans shown in Figure 72 and peak levels from PoSSM 5 cm thick bubble layer and 5 m track simulations (◯) with air volume fractions chosen to match the field data peaks. Also shown is the expected reflected level from the clay layer (□) based on the simulated bubble layer's 2-way transmission loss subtracted from the November data's level. The symbols are color-coded to correspond to their respective field measurements.

over 5 cm of depth is well within expected fractional levels, given that air fractions measured by X-ray micro-computed tomography (micro-CT) scans from a gassy mud sediment have been as large as 7% over a 5 cm depth [62].

Table 8: Field test date, water temperature (T_{water}), difference in recorded field data level from clay interface in November (ΔL_{clay}), and the simulation-derived estimated volume of air (V_{air}) and 2-way attenuation ($2 * T_I$) through the bubble layer. Plot and symbol color is also noted.

Field Test Date	$T_{\textbf{water}}$	ΔL_{clay}	$V_{\textbf{air}}$	$2 * T_I$	Plot color
May 5, 2019	17 °C	13 dB	0.21%	10 dB	Blue
June 14, 2019	20 °C	8 dB	0.16%	6 dB	Red
August 14, 2019	27 °C	18 dB	0.28%	18 dB	Yellow
November 8, 2019	7 °C	0 dB	0.0%	0 dB	Purple

5.2.3 Bush River

This section examines field data from track 2020 0305 183020 collected in the Bush River on March 5, 2020 and compares it to a PoSSM simulation of an entrapped gas layer to estimate the maximum air volume fraction of the entrapped gas in the Bush River sediment. Over this example track, the SVSS frequently demonstrated significant penetration in the riverbed. However, suspected entrapped gas limited the penetration of the SVSS at several points along this track. Figure 74 shows a 50 m section of the track that contains two areas of suspected entrapped gas: near 73 m and 92 m.

A-Scan data from Figure 74 was averaged over two sections of 3 m length (66 pings) along the track. The first section is from 63 m to 66 m and represents a typical return characteristic of the Bush River sediment layers. The second section is near the first, from 71.5 m to 74.5 m, but clearly demonstrates different scattering mechanisms. The strong sub-bottom reflection in this second section is hypothesized to be due to the presence of entrapped gas. To gain insight into whether this hypothesis is true, a PoSSM simulation was run with the same parameters as Section 5.2.2, but with the depth of the 5 cm bubble layer adjusted to align with the Bush River data.

Beyond comments from Aberdeen ATC employees indicating that the Bush River sediment was "soft mud," our team did not have core samples or other detailed measurements of the sediment. For this reason the team made an assumption that it is similar to the properties of the soft mud used in the Sayers Reservoir data-model comparison. The exact properties of the Bush River mud, including density, sound velocity, and shear modulus, will affect the overall scattered level from a bubble ensemble. However, using properties for a general soft mud will give us a good approximation of the air volume fraction that would produce such a strong sub-bottom reflection.

Figure 75 shows the mean A-Scans for the two sections of field data. The initial reflections at 2.0 m and 2.3 m depth are very similar in level and depth. This suggests a distinct and consistent two-layer sediment structure in this region, with the top layer approximately 30 cm thick. However, beneath 2.3 m depth the two average A-Scans diverge dramatically. The second section shows a peak of 169 dB at 2.6 m depth followed by a decay. This peak and decay is a distinctive signature commonly associated with entrapped gas [59, 62].

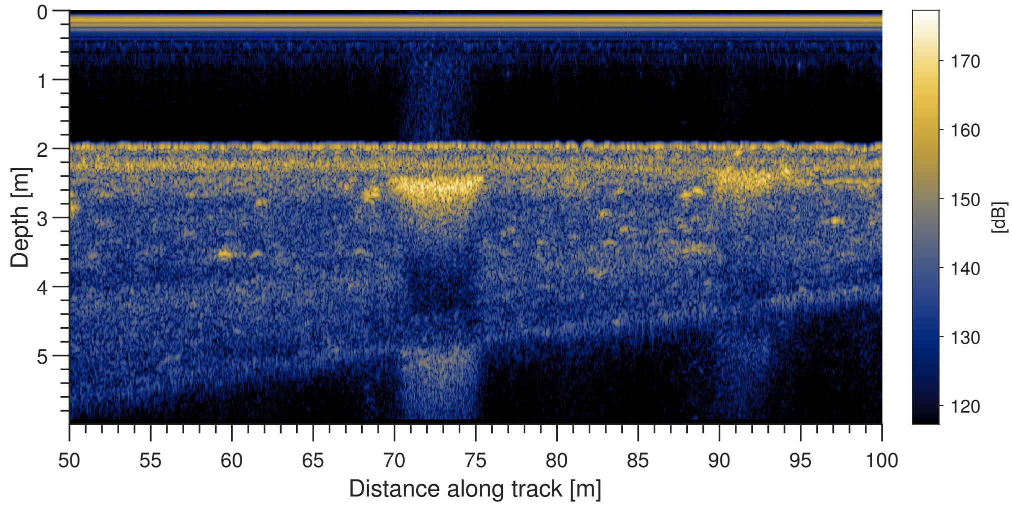

Figure 74: B-Scan from Bush River test data, track 2020 0305 183020. The signature near 73 m is consistent with the presence of entrapped gas.

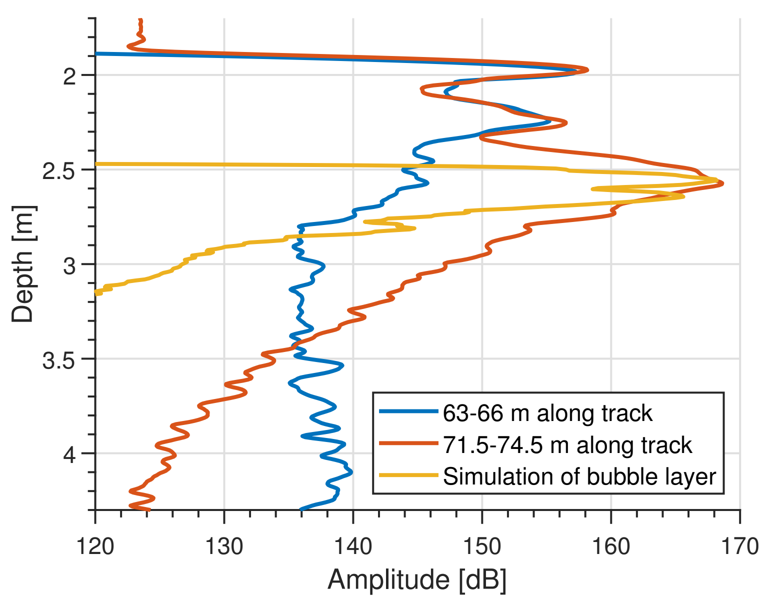

Figure 75: Average A-Scan of 3 m (66 pings) along-track in areas with (red) and without (blue) the hypothesized entrapped gas layer from field data shown in Figure 74. Also shown is the average A-Scan from a simulated bubble layer containing 0.63% air volume fraction over 5 cm.

The mean A-Scan of a PoSSM bubble simulation is also shown in Figure 75. The air volume fraction of the bubble layer in the simulation was set to 0.63%, in order to match the peak mean value shown in the field data. That a value of 0.63% was needed in order to match the peak values suggests that the average maximum air volume concentration over a 5 cm depth is approximately 0.63%. This suggests that the peak volume of entrapped gas in this section of the Bush River sediment was more than twice the peak value at Sayers (estimated as 0.28%). Since the Bush River water temperature was relatively cold, it may be that the hypothesized entrapped gas is due to a different process than at Sayers.

There is a distinct difference in the pre- and post-peak scattering level shown by the field data and the simulated bubble response data. It is hypothesized that a key reason for this difference is due to the geometric placement of entrapped gas with respect to depth. The simulation contained bubbles in only 5 cm of sediment. In contrast, it is assumed that the entrapped gas in the Bush River sediment extends over a greater depth since there is no clear sediment layering or other geometric features beyond 2.3 m depth that would inhibit gas transfer. Entrapped gas occurring in a larger range of sediment depths would induce elevated scattering over a similar range of sediment depths. This could account for both the slower rise and decay rates surrounding the peak at 2.6 m depth.

One other difference is that the PoSSM simulation does not support multiple scattering. As the volume fraction grows the implicit Born approximation will become invalid and the model will not capture the elongation that can occur owing to multiple scattering. Future collection of core samples containing entrapped gas, and tabulation of the number and size of bubbles, would greatly help to uncover additional details related to scattering from entrapped gas and lead to further validation of the bubble response model used in the PoSSM simulation.

5.2.4 Discussion

This chapter presented several model-data comparisons that furthered our understanding of the interaction between the SVSS system and the environment. The Sayers Reservoir 2-layer model was found to be a plausible representation of field data, although it lacks natural environmental clutter and variability. A new bubble response model can explain several of the more interesting effects seen in field data that were not previously described, such as the large seasonal variations in scattered amplitude from the Sayers sediment and the strong scattering occasionally seen in the Bush River. One key scientific finding is that the interaction of the sonar with entrapped gas can limit the performance of sub-bottom imaging systems.

It is clear that relatively small concentrations of entrapped gas in sediment play an outsized role in the sub-bottom acoustic response. Since scattered sound from entrapped gas can potentially mask UXO buried beneath it, it is important to understand when, where, and why entrapped gas occurs so that its effect on UXO detection and site coverage for the SVSS and other acoustic-based systems can be estimated. It is currently unknown whether entrapped gas deposits are prevalent or rare at SERDP-targeted remediation sites. As additional knowledge is gained, sonar pulses and processing methods that are less susceptible to interference could be developed for use when entrapped gas is present, or test plans can take into consideration environmental conditions (e.g., if entrapped gas is more prevalent during summer or immediately following weather events). Future work could validate our hypotheses relating to SVSS interaction with entrapped gas by performing measurements of core properties, including X-ray micro-CT scans to estimate bubble distributions, and communication with experts in biological processes that produce entrapped gas to better understand the complex role played by the environment.

6 Conclusions and Implications for Future Research

Buried UXO is a current environmental problem facing the United States and other nations. Current sensors do not exist to perform surveys to detect buried UXO in water depths less than 5 m, and these depths are critical because of the potential for human/UXO interaction. Operation in these very shallow depths complicates the use of sub-bottom imaging systems hosted on either unmanned underwater vehicles or towed platforms. Additionally, interference from acoustic multipath reverberation can be challenging in these shallow depths.

The Sediment Volume Search Sonar program was proposed to develop a detailed survey sensor for acoustic detection and localization of surficial and buried unexploded ordnance, with a particular focus on 1 m–5 m water depth. To achieve this objective, a hybrid environmental scattering and target scattering model was used to study sensor performance across a range of environments and target types. This hybrid model combined PoSSM (environmental scattering) and TIER (target scattering) to create a model capable of producing realistic time series for a range of sensor designs, environments, and UXO. These modeling results were then used to inform a prototype sensor design and the associated image reconstruction and visualization algorithms.

An initial prototype system was developed through extensive leveraging of an existing test platform and sensor hardware. This leveraged hardware was augmented with additional purpose-built components to create a sensor capable of producing three-dimensional volumetric SAS imagery across a range of environments. Additionally, software was written to process the sonar data into advantageous image representations. To support demonstration of this system, test beds were established at the Foster Joseph Sayers Reservoir and at the Aberdeen Test Center.

At both sites, the sensor demonstrated excellent target localization accuracy, with absolute positioning errors of less than 10 cm. This demonstrated that the SVSS meets the informal "within the width of a shovel head" requirement discussed at SERDP workshops. Additional analysis shows that it is possible to further reduce the SVSS target localization errors to less than 5 cm by improving the layout of the navigation and sonar hardware.

The SVSS sensor demonstrated the capacity to form high-resolution imagery of deeply buried (>3 m depth) objects during Bush River testing, which was conducted adjacent to the Aberdeen Test Center. Testing in the Littoral Warfare Environment showed good performance against proud objects, but the sediment properties over the target field precluded buried target detection. Based upon broader surveys within the LWE, the acoustic penetration diminished rapidly for tracks more than 5 m shallower than the draw-down waterline. It is hypothesized that only one month of delay between rewatering and testing was insufficient to allow entrapped air to release from the sediment.

At the Foster Joseph Sayers Reservoir the sensor demonstrated good performance against proud targets, while the detection of buried targets appeared to vary seasonally. During the summer months, when the water temperature was warm, the sediment scattering strength was elevated and the geometric response from buried targets was obscured. However, the late-time response from objects, due to resonant phenomena, was detectable in many cases.

During the late-fall and early-winter, when the water temperature was cold, the sediment scattering strength of the upper silt layer was reduced by as much as 18 dB. This reduction of sediment scattering strength resulted in improved target detectability.

The sensor data and ground truth target locations at both test sites have been curated to support other researchers in the SERDP munitions response program. To date, collaborations have been established with Dr. David Williams at the NATO Centre for Maritime Research and Experimentation, Dr. Suren Jayasuria at Arizona State University, and Dr. Vishal Monga at the Pennsylvania State University. Both Dr. Williams and Dr. Jayasuria have been provided with SVSS datasets to support their work, and ARL/PSU anticipates providing the same data to Dr. Monga later in 2021.

Overall, the research objectives of hardware development, software development, and demonstration of the SVSS were achieved. Absolute object localization errors of less than 10 cm and buried object detection at depths of 3 m illustrate the utility of the SVSS system for detection of surficial and buried UXO. The results demonstrated under this program point to three areas for future research and experimentation:

1. improving the SVSS receive hardware to increase system performance,
2. investigating advanced signal processing techniques to mitigate environmental complexity and exploit late-time target returns, and
3. conducting a field demonstration at one of the SERDP-ESTCP munitions response test beds.

The receive array currently used by the prototype SVSS was leveraged from a prior non-SERDP program. While useful for initial demonstration and testing, the receive array was not originally intended for sub-bottom imaging, and the array's design limits the achievable image resolution. A purpose-built receive array would provide increased image resolution and a wider range of sampled angles that facilitate wider azimuthal support for target strength estimation. This could be accomplished within a smaller overall footprint, potentially making the SVSS system easier to deploy from alternative surface craft. The development of a purpose-built receive array would be supported by PoSSM modeling and simulation to evaluate hardware tradeoffs during the design process.

In testing the prototype SVSS, it was found that the strength of near-normal incidence scattering from the sediment/water interface could be greater than the scattered field from smaller targets. The impact of near-normal incidence scattering has been addressed through time-gating by other normal-incidence munitions response sensors [15]. The bistatic geometry of the SVSS array may allow for windowing and exclusion of near-specular ray paths in the reconstruction process. This windowing process could be evaluated initially using synthetic data generated by PoSSM. In many of the SVSS demonstration sites, man-made objects exhibited late-time scattering phenomena. Prior research has shown that alternative reconstruction techniques can focus these late-time returns [27–29]. Application of these techniques could lead to improved target detection in challenging environments.

Finally, a field demonstration of the SVSS should be conducted at one of the SERDP-ESTCP munitions response test beds currently under development. This demonstration would provide a large research dataset and an independent measure of the SVSS performance. After performance validation, the DoD or others could use the SVSS to determine the location of proud and buried ordnance at shallow-water remediation sites.

A Additional Target Details

A.1 Foster Joseph Sayers Reservoir Target Details

This appendix provides photos of the emplaced munitions, science targets, and clutter objects installed in the Foster Joseph Sayers Reservoir. Additionally, a pair of tables are provided describing the burial depth of each object.

Table 9: Foster Joseph Sayers Reservoir shallow field target information.

Identifier	Target Type	Depth [cm]	Identifier	Target Type	Depth [cm]	Identifier	Target Type	Depth [cm]
S_P01_Clutter	Rock	10.0	S_P17_T04D2	155 mm howitzer	12.0	S_P33_T02Dx	Al. Cylinder	1.0
S_P02_T05D0	Cinder Block	0.0	S_P18_T06D2	105 mm Projectile	12.0	S_P34_Empty	No Target	0.0
S_P03_T03D2	Al. Cylinder	8.0	S_P19_T07D2	81 mm Mortar	6.0	S_P35_T11D3	Cinder Block (Foam)	22.0
S_P04_T02D2	Al. Cylinder	6.0	S_P20_T04D1	155 mm howitzer	4.0	S_P36_Empty	No Target	0.0
S_P05_T01D2	Shot put	16.0	S_P21_T06D1	105 mm Projectile	6.0	S_P37_Empty	No Target	0.0
S_P06_T03D1	Al. Cylinder	2.0	S_P22_T07D1	81 mm Mortar	6.0	S_P38_Empty	No Target	0.0
S_P07_T02D1	Al. Cylinder	4.0	S_P23_T04D3	155 mm howitzer	30.0	S_P39_T18_D0	Concrete Bucket	0.0
S_P08_T01D1	Shot put	8.0	S_P24_T06D3	105 mm Projectile	24.0	S_P40_T17_D0	Concrete Cylinder	0.0
S_P09_T03D0	Al. Cylinder	0.0	S_P25_T07D3	81 mm Mortar	12.0	S_P41_T16_D0	Concrete Cylinder	0.0
S_P10_T02D0	Al. Cylinder	0.0	S_P26_T05D3	Cinder Block	0.0	S_P42_T15_D0	Steel Pipe	0.0
S_P11_T01D0	Shot put	0.0	S_P27_Empty	No Target	0.0	S_P43_T14_D0	Steel Pipe	0.0
S_P12_T05D0	Cinder Block	0.0	S_P28_Empty	No Target	0.0	S_P44_T13_D0	Steel Pipe	0.0
S_P13_Clutter	Rock	8.0	S_P29_TxxD2	Mixed	16.0	S_P45_T12_D0	Steel Pipe	0.0
S_P14_TxxDx	Mixed	-	S_P30_T00D3	Hole	24.0	S_P46_Empty	No Target	0.0
S_P15_TxxDx	Mixed	-	S_P31_T00D3	Hole	36.0			
S_P16_T05D0	Cinder Block	0.0	S_P32_TxxD3	Mixed	26.0			

Table 10: Foster Joseph Sayers Reservoir deep field target information.

Identifier	Target Type	Depth [cm]	Identifier	Target Type	Depth [cm]	Identifier	Target Type	Depth [cm]
D_P01_Clutter	Rock	0.0	D_P13_Clutter	Rock	0.0	D_P25_Empty	No Target	0
D_P02_T05D0	Cinder Block	0.0	D_P14_T05D0	Cinder Block	0.0	D_P26_Empty	No Target	0
D_P03_T03D2	Al. Cylinder	14.0	D_P15_T10D0	Concrete Pad	0.0	D_P27_T18_D0	Concrete Bucket	0
D_P04_T02D2	Al. Cylinder	14.0	D_P16_T10D2	Concrete Pad	16.0	D_P28_T17_D0	Concrete Cylinder	0
D_P05_T01D2	Shot put	16.0	D_P17_T10D3	Concrete Pad	19.0	D_P29_T16_D0	Concrete Cylinder	0
D_P06_T03D1	Al. Cylinder	6.0	D_P18_T11D1	Cinder Block (Foam)	3.0	D_P30_T15_D0	Steel Pipe	0
D_P07_T02D1	Al. Cylinder	9.0	D_P19_T11D3	Cinder Block (Foam)	15.0	D_P31_Empty	No Target	0
D_P08_T01D1	Shot put	12.0	D_P20_TxxD0	Mixed	0.0	D_P32_T14_D0	Steel Pipe	0
D_P09_T03D0	Al. Cylinder	0.0	D_P21_Clutter	Rock	0.0	D_P33_T13_D0	Steel Pipe	0
D_P10_T02D0	Al. Cylinder	0.0	D_P22_Empty	No Target	0.0	D_P34_T12_D0	Steel Pipe	0
D_P11_T01D0	Shot put	0.0	D_P23_Empty	No Target	0.0	D_P35_Empty	No Target	0
D_P12_T05D0	Cinder Block	0.0	D_P24_T05D0	Cinder Block	0.0			

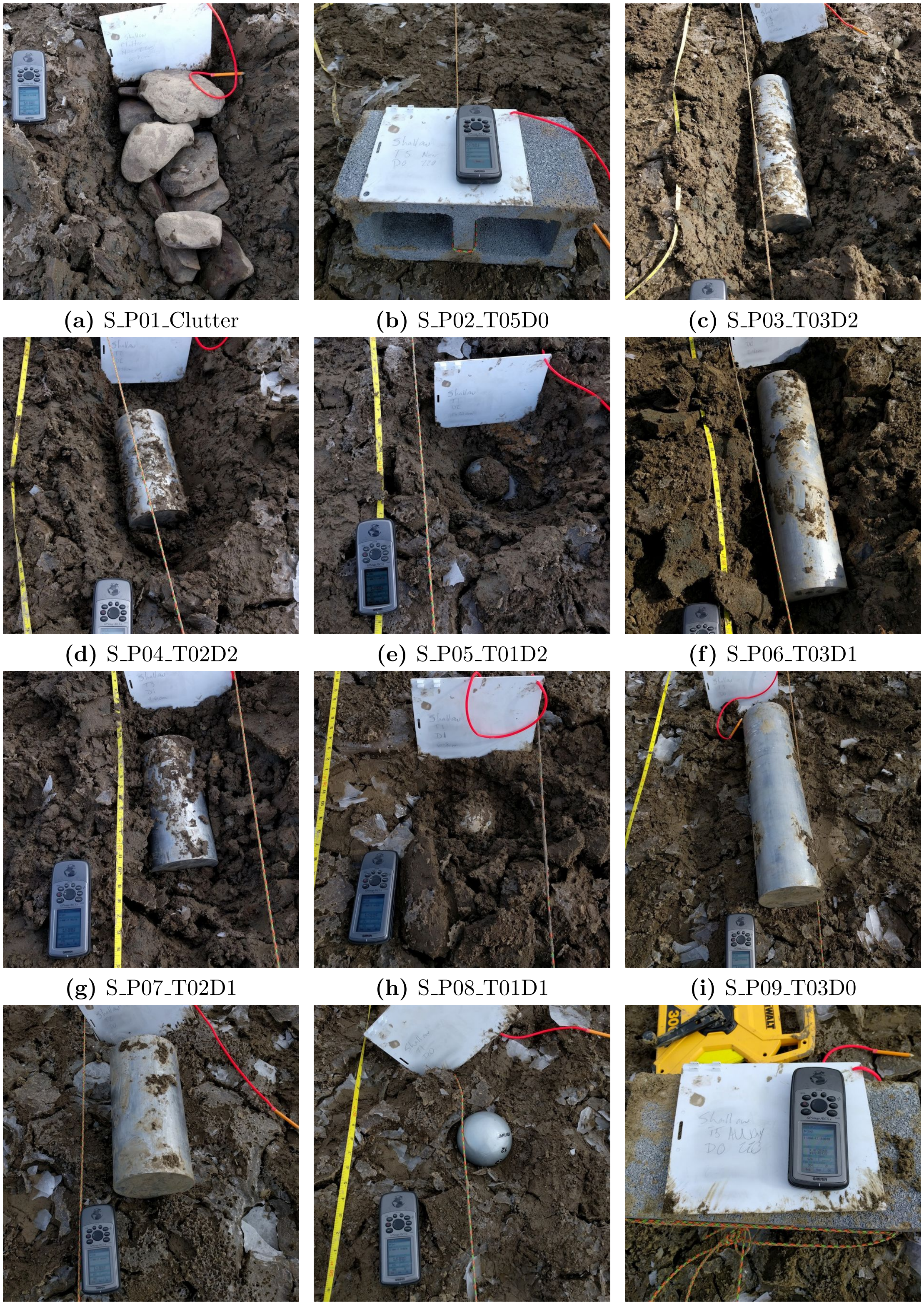

(a) S_P01_Clutter (b) S_P02_T05D0 (c) S_P03_T03D2

(d) S_P04_T02D2 (e) S_P05_T01D2 (f) S_P06_T03D1

(g) S_P07_T02D1 (h) S_P08_T01D1 (i) S_P09_T03D0

(j) S_P10_T02D0 (k) S_P11_T01D0 (l) S_P12_T05D0

Figure 76: Foster Joseph Sayers Reservoir shallow field targets.

(a) S_P13_Clutter (b) S_P14_TxxDx (c) S_P15_TxxDx

(d) S_P17_T04D2 (e) S_P18_T06D2 (f) S_P19_T07D2

(g) S_P20_T04D2 (h) S_P21_T06D2 (i) S_P22_T07D1

(j) S_P23_T04D3 (k) S_P24_T06D3 (l) S_P25_T07D3

Figure 77: Foster Joseph Sayers Reservoir shallow field targets.

(a) S_P29_TxxD2

(b) S_P30_T00D3

(c) S_P31_T00D3

(d) S_P32_TxxD3

(e) S_P33_T02Dx

(f) S_P35_T11D3

(g) S_P39_T18D0

Figure 78: Foster Joseph Sayers Reservoir shallow field targets.

(a) S_P40_T17D0

(b) S_P41_T16D0

(c) S_P42_T15D0

(d) S_P43_T14D0

(e) S_P44_T13D0

(f) S_P45_T12D0

Figure 79: Foster Joseph Sayers Reservoir shallow field targets.

(a) D_P01_Clutter

(b) D_P02_T05D0

(c) D_P03_T03D2

(d) D_P04_T02D2

(e) D_P05_T01D2

(f) D_P06_T03D1

(g) D_P07_T02D1

(h) D_P08_T01D1

(i) D_P09_T03D0

(j) D_P10_T02D0

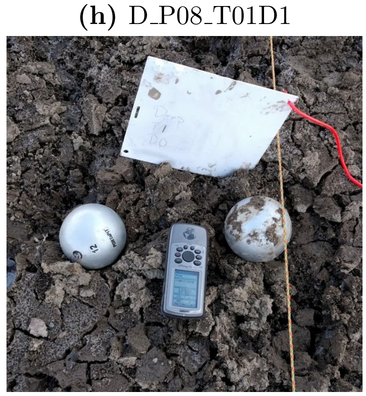

(k) D_P11_T01D0

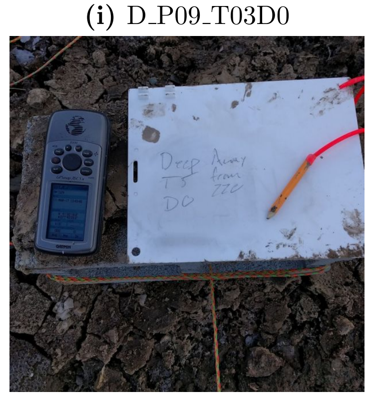

(l) D_P12_T05D0

Figure 80: Foster Joseph Sayers Reservoir deep field targets.

(a) D_P13_Clutter

(b) D_P15_T10D0

(c) D_P16_T10D2

(d) D_P17_T10D3

(e) D_P18_T11D1

(f) D_P19_T11D3

(g) D_P20_TxxD0

(h) D_P21_Clutter

(i) D_P24_T05D0

(j) D_P27_T18D0

(k) D_P28_T17D0

(l) D_P29_T16D0

Figure 81: Foster Joseph Sayers Reservoir deep field targets.

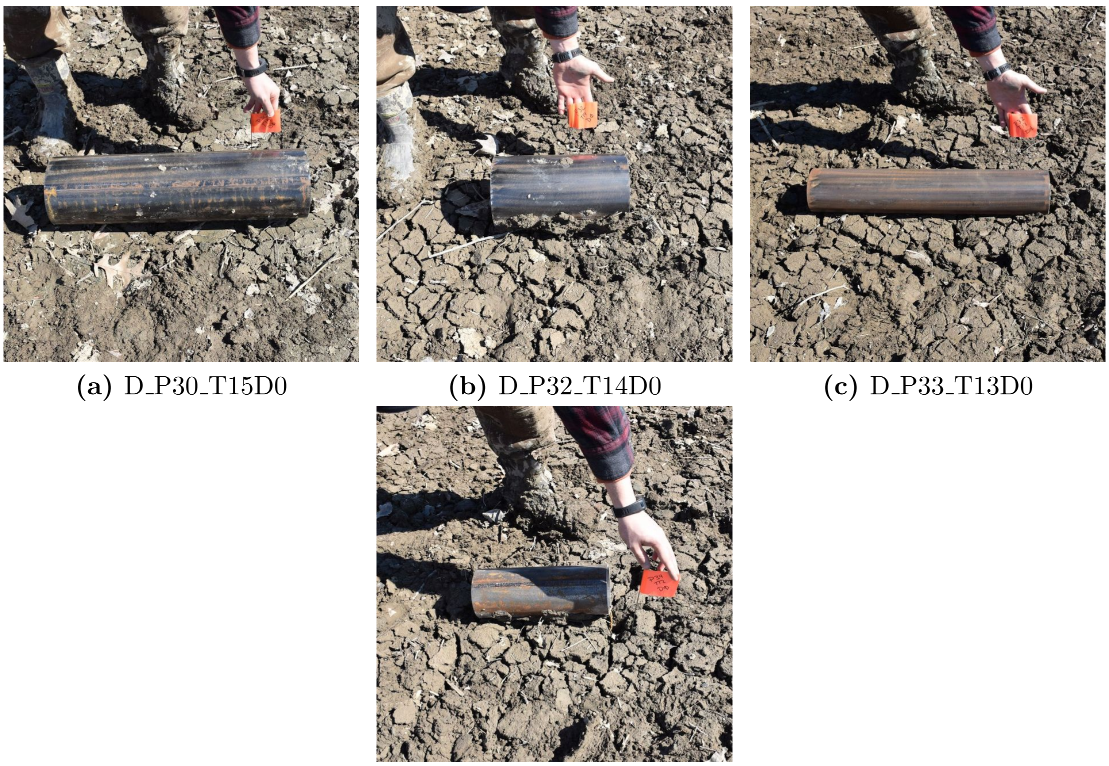

(a) D_P30_T15D0 (b) D_P32_T14D0 (c) D_P33_T13D0

(d) D_P34_T12D0

Figure 82: Foster Joseph Sayers Reservoir deep field targets.

A.2 Aberdeen Test Center Target Details

This appendix provides photos of the munitions, science targets, and clutter objects installed in the LWE. Additionally, a table is provided describing the burial depth and orientation of each of the 86 prepared positions.

(a) T04 - 155 mm Howitzer

(b) T06 - 105 mm Projectile

(c) T07 - 81 mm Mortar

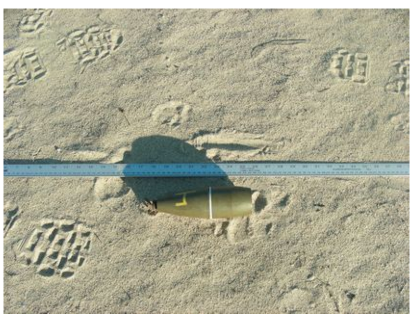

(d) T08 - 60 mm Mortar

(e) T19 - 70 mm Rocket

(f) T20 - 40 mm Projectile

(g) T21 - 25 mm Projectile

(h) T22 - 20 mm Projectile

Figure 83: Photos of the eight munitions types installed in the LWE.

(a) T01 - Shot put

(b) T03 - Al. Cylinder

(c) T23 - Al. Cylinder

(d) T12 - Steel Pipe

(e) T15 - Steel Pipe

(f) T17 - Concrete Cylinder

(g) T24 - Concrete Cylinder

(h) T05 - Cinder Block

(i) T25 - Sayers Rock

Figure 84: Photos of the nine science and clutter types installed in the LWE.

Table 11: In the LWE test site, 86 positions were prepared with a range of objects.

Identifier	Target Type	Depth [cm]	Long Axis Track Aligned	Orientation + = Nose Up	Identifier	Target Type	Depth [cm]	Long Axis Track Aligned	Orientation + = Nose Up
P01T05D0	Cinder Block	0.0	N	5.8	P43T05D0	Cinder Block	0.0	N	-1.5
P02T04D0	155 mm howitzer	0.0	Y	0.3	P44T19D0	70 mm Rocket	0.0	Y	-0.7
P03T04D1	155 mm howitzer	10.0	Y	2.7	P45T19D1	70 mm Rocket	10.7	Y	3.0
P04T04D2	155 mm howitzer	20.0	Y	6.6	P46T19D2	70 mm Rocket	18.6	Y	3.2
P05T05D3	155 mm howitzer	28.3	Y	3.4	P47T19D3	70 mm Rocket	28.7	Y	0.1
P06T04D4	155 mm howitzer	39.0	Y	0.8	P48T20D0	40 mm Projectile	0.0	Y	3.9
P07T04D5	155 mm howitzer	48.4	Y	-0.1	P49T20D1	40 mm Projectile	9.8	Y	1.0
P08T04D6	155 mm howitzer	59.5	Y	5.2	P50T20D2	40 mm Projectile	18.6	Y	7.2
P09T04D2	155 mm howitzer	19.4	Y	45.4	P51T20D3	40 mm Projectile	29.2	Y	1.3
P10T04D2	155 mm howitzer	15.0	Y	-50.1	P52T21D0	25 mm Projectile	0.0	Y	3.4
P11T04D2	155 mm howitzer	0.0	Y	-89.8	P53T21D1	25 mm Projectile	9.9	Y	7.8
P12T04D2	155 mm howitzer	20.0	N	-2.0	P54T21D2	25 mm Projectile	20.3	Y	6.1
P13T04D2	155 mm howitzer[a]	18.5	Y	1.9	P55T21D3	25 mm Projectile	29.5	Y	3.1
P14T05D0	Cinder Block	0.0	N	4.9	P56T05D0	Cinder Block	0.0	N	8.6
P15T05D0	Cinder Block	0.0	N	1.2	P57T05D0	Cinder Block	0.0	N	2.4
P16T06D0	105 mm projectile	0.0	Y	1.9	P58T08D0	60 mm Mortar	0.0	Y	-1.5
P17T06D1	105 mm projectile	10.0	Y	2.5	P59T08D1	60 mm Mortar	10.8	Y	3.1
P18T06D2	105 mm projectile	19.1	Y	3.1	P60T08D2	60 mm Mortar	19.2	Y	2.8
P19T06D3	105 mm projectile	30.5	Y	3.6	P61T08D3	60 mm Mortar	28.8	Y	6.7
P20T06D4	105 mm projectile	42.4	Y	-1.0	P62T08D4	60 mm Mortar	40.4	Y	3.0
P21T06D5	105 mm projectile	49.0	Y	3.4	P63T08D5	60 mm Mortar	50.0	Y	2.1
P22T06D6	105 mm projectile	61.0	Y	5.6	P64T22D0	20 mm Projectile	0.0	Y	N/A
P23T06D2	105 mm projectile	22.0	Y	44.8	P65T22D2	20 mm Projectile	21.4	Y	N/A
P24T06D2	105 mm projectile	18.5	Y	-52.0	P66T01D0	Shot put	0.0	N/A	N/A
P25T06D2	105 mm projectile	0.0	Y	-90.0	P67T01D1	Shot put	10.4	N/A	N/A
P26T06D2	105 mm projectile	19.0	N	-3.0	P68T01D2	Shot put	18.9	N/A	N/A
P27T06D2	105 mm projectile[a]	21.5	Y	0.9	P69T01D3	Shot put	28.5	N/A	N/A
P28T05D0	Cinder Block	0.0	N	0.5	P70T05D0	Cinder Block	0.0	N	-5.1
P29T05D0	Cinder Block	0.0	N	0.4	P71T05D0	Cinder Block	0.0	N	3.0
P30T07D0	81 mm mortar	0.0	Y	-1.7	P72T03D0	Al. Cylinder	0.0	Y	0.2
P31T07D1	81 mm mortar	11.0	Y	1.8	P73T03D1	Al. Cylinder	10.9	Y	2.3
P32T07D2	81 mm mortar	18.5	Y	1.0	P74T03D2	Al. Cylinder	19.6	Y	0.3
P33T07D3	81 mm mortar	27.5	Y	1.4	P75T03D3	Al. Cylinder	27.6	Y	1.2
P34T07D4	81 mm mortar	38.8	Y	3.3	P76T23D0	Al. Cylinder	0.0	Y	-0.7
P35T07D5	81 mm mortar	48.0	Y	0.9	P77T23D1	Al. Cylinder	10.0	Y	0.5
P36T07D6	81 mm mortar	59.4	Y	-4.7	P78T23D2	Al. Cylinder	19.9	Y	-0.9
P37T07D2	81 mm mortar	19.3	Y	41.4	P79T23D3	Al. Cylinder	29.0	Y	-3.1
P38T07D2	81 mm mortar	24.6	Y	-51.2	P80T15D0	Steel Pipe	0.0	Y	-0.4
P39T07D2	81 mm mortar	0.0	Y	-86.0	P81T17D0	Concrete Cylinder	0.0	Y	0.4
P40T07D2	81 mm mortar	19.8	N	-3.2	P82T12D0	Steel Pipe	0.0	Y	0.0
P41T07D2	81 mm mortar[a]	20.3	Y	-1.4	P83T24D0	Concrete Cylinder	0.0	Y	-2.3
P42T05D0	Cinder Block	0.0	N	0.2	P84T05D0	Cinder Block	0.0	N	-1.9
-	-	-	-	-	P85T25D2	Sayers Rock	13.0	N/A	-2.5
-	-	-	-	-	P86T00D3	Hole	30.0	N/A	N/A

[a] Clutter intentionally positioned adjacent to the target.

B Sensor Characterization & Calibration

The sonar hardware used on the Sound Hunter test platform was characterized at the Foster Joseph Sayers Reservoir test site and calibrated at the ARL/PSU Anechoic Test Facility. The ATF test facility has the capability to test sonar hardware at frequencies above 5 kHz for pulse lengths up to 2 ms. Noise characterization conducted at the reservoir test site is presented in Section B.1. The projector calibration, whose design was described in Section 4.2.2, is presented in Sections B.2 and B.3. The hydrophone calibration is presented in Section B.4.

B.1 Sensor Noise Floor Characterization

Early field testing was focused on verifying the sensor integration, and one key measurement was the characterization of the receiver noise floor. The integration of new hydrophone modules, transmit amplifiers, and projectors carries the risk of introducing new electronic self-noise mechanisms. In initial integration tests on September 13, 2017, it was discovered that the amplifier grounding scheme had introduced a ground loop responsible for a very significant increase in the noise floor. After the ground loop was identified and rectified, the system's noise floor was measured again on September 22, 2017. The results of this second test are shown in Figure 85. The operating noise floor is roughly 7 dB greater than that observed in deep water (180 m) during a separate test. It is hypothesized that the increase in noise floor in shallow water is due to scattering of the radiated self noise from the lakebed and reverberation in the shallow water column.

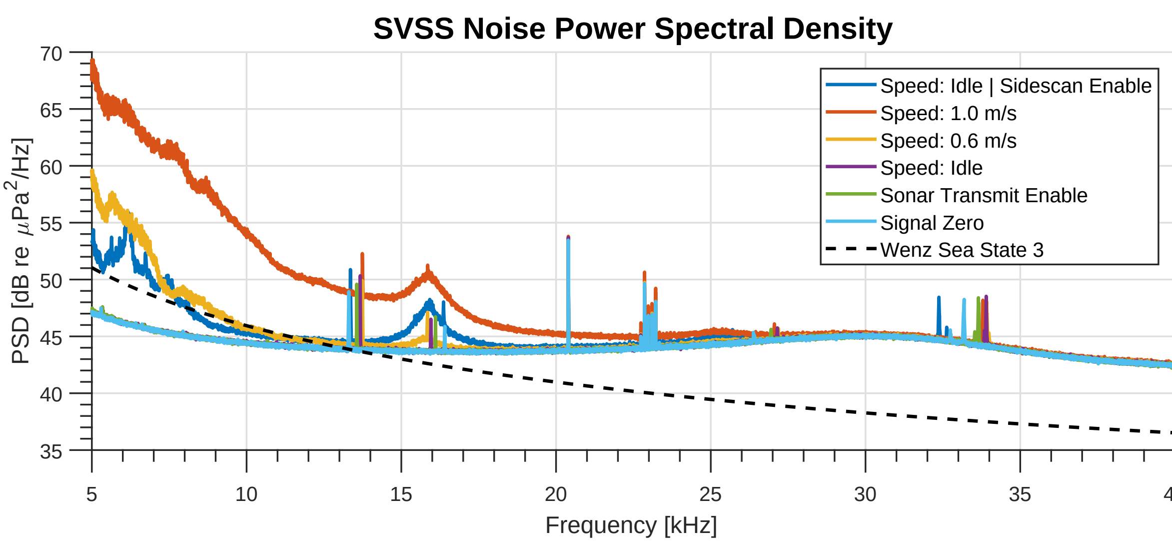

Figure 85: The SVSS system's noise floor was characterized for a number of operating states. As platform speed is increased, noise from the motor increases at low frequency. Note that the purple "Speed Idle" curve is obscured by the "Signal Zero" curve in this figure.

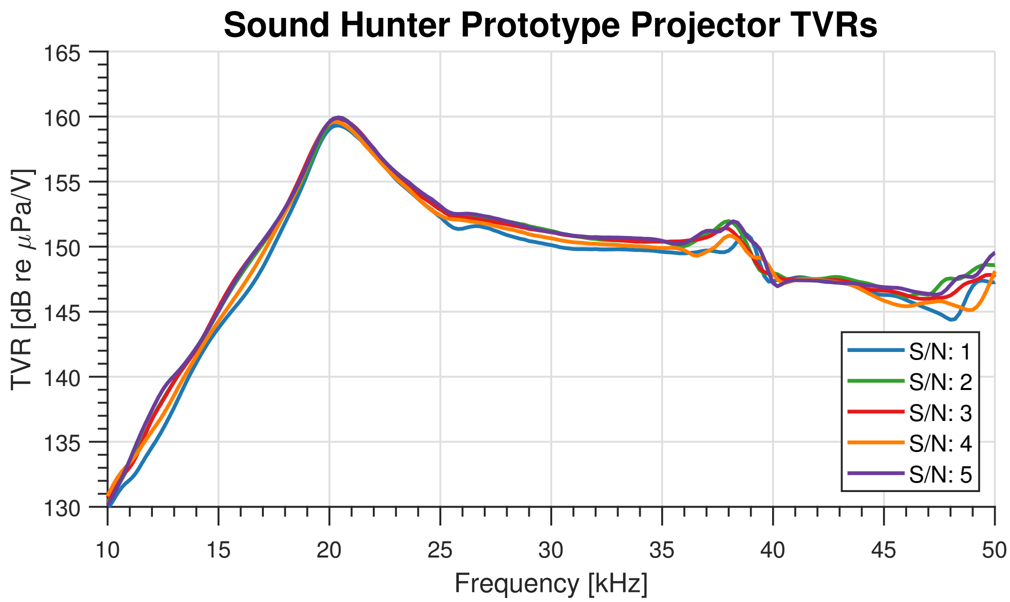

Figure 86: The prototype projector TVRs are well matched over the 10 kHz–45 kHz band.

B.2 Prototype Projector Calibration

Each of the five prototype projectors used by the SVSS were characterized in the ARL/PSU ATF using the facility's Instruments Incorporated L6 linear amplifier. Projector TVR was measured over 3 kHz–150 kHz. In the frequency band spanning 10 kHz–45 kHz the projector TVRs are well-matched, as seen in Figure 86.

Broadband transmit beam patterns were measured in the frequency band spanning 10 kHz–50 kHz. The full patterns are given in Figure 87, where the axes are transducer aspect angle and frequency, and amplitude is shown using color. The five transmitters have very similar beam patterns and are also well-behaved throughout this frequency range.

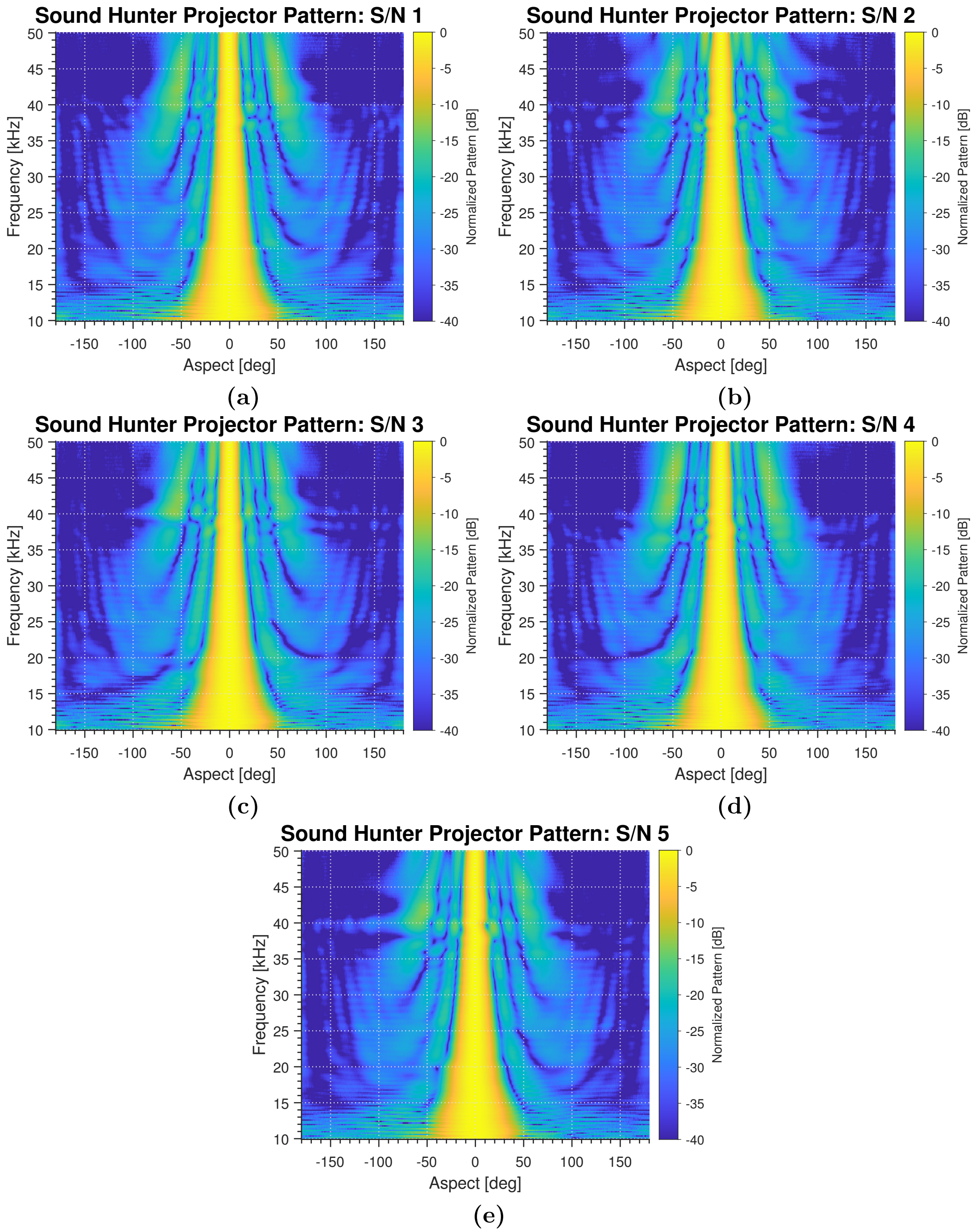

Figure 87: Broadband beam patterns were captured for the five prototype projectors over 10 kHz–50 kHz in the ARL/PSU ATF.

B.3 Broadband Projector Calibration

Six broadband projectors were fabricated for the SVSS during the program effort, and each projector was characterized in the ARL/PSU ATF using the facility's Instruments Incorporated L6 linear amplifier. The projector TVR was measured over 3 kHz–150 kHz. In the band spanning 10 kHz–50 kHz, the projector TVRs are well-matched as seen in Figure 88.

Broadband transmit beam patterns were measured in the frequency band spanning 10 kHz–50 kHz. The full patterns are given in Figure 89, where the axes are transducer aspect angle and frequency, and amplitude is shown using color. The six transmitters have very similar beam patterns and are also well-behaved throughout this frequency range.

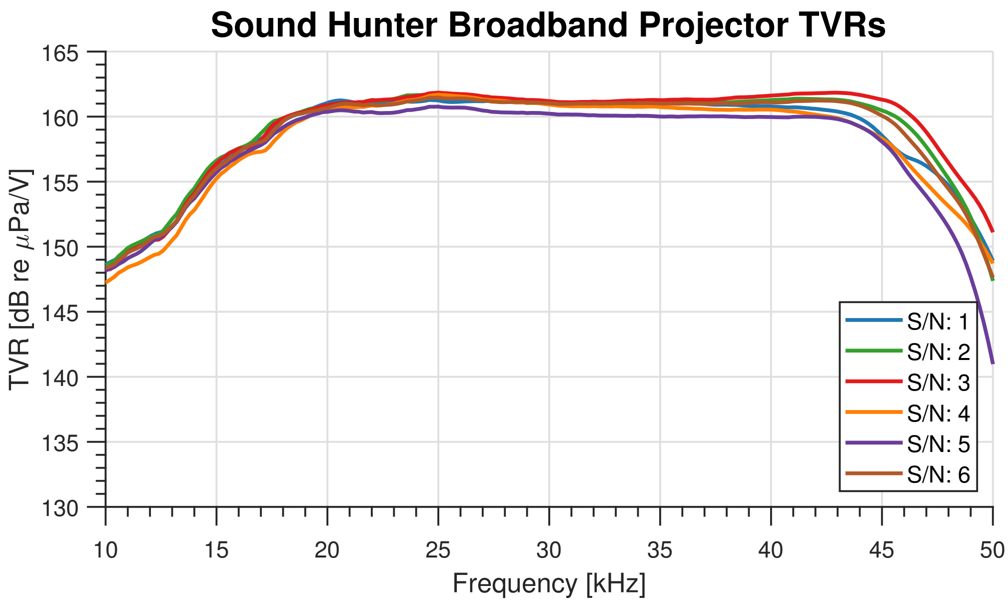

Figure 88: The broadband projector TVRs are well matched over the 10 kHz–50 kHz band.

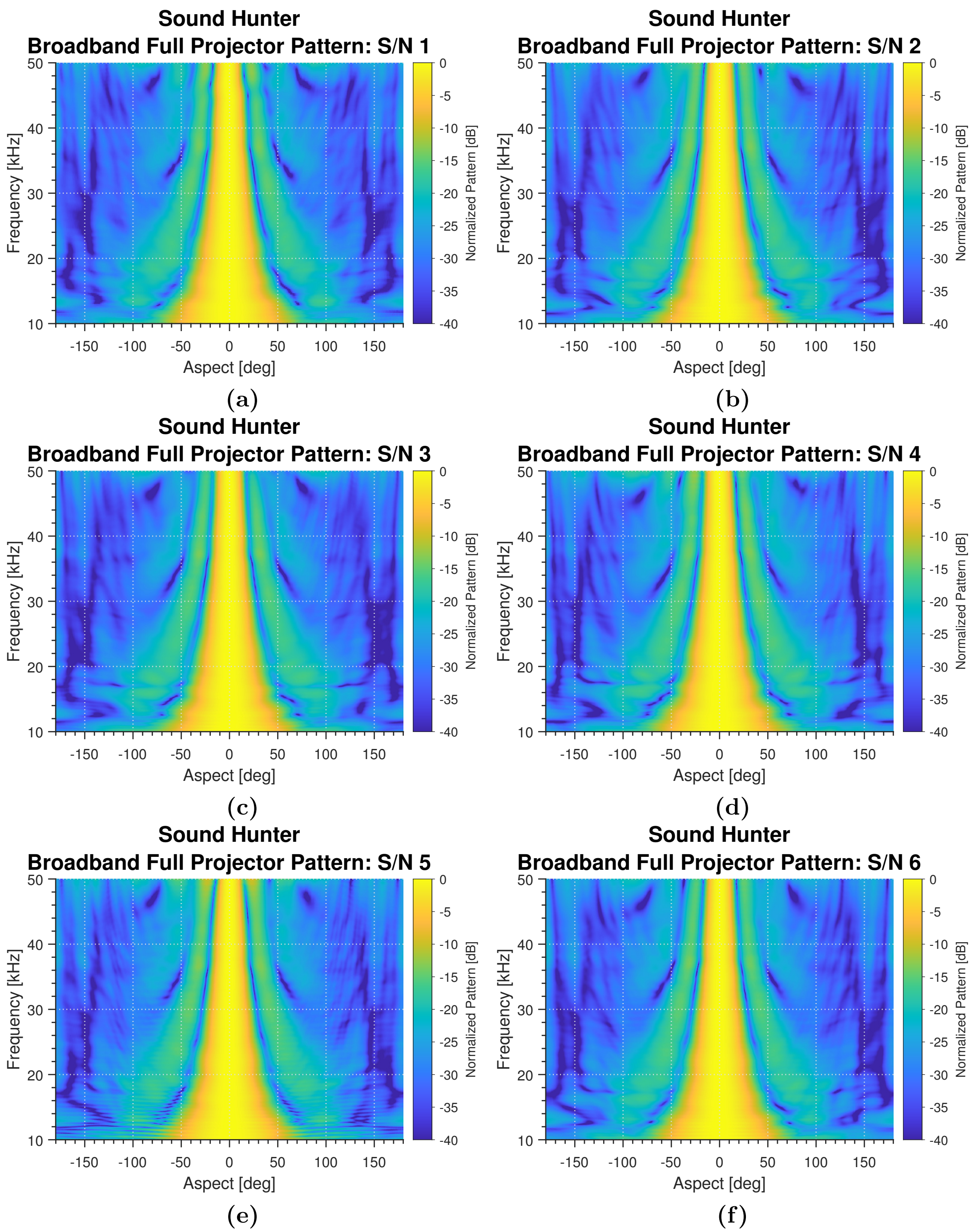

Figure 89: Broadband beam patterns were captured for the broadband projectors over 10 kHz–50 kHz in the ARL/PSU ATF.

B.4 Hydrophone Calibration

The SVSS receive array consists of ten receiver modules that each contain eight hydrophones (channels). These modules were individually calibrated to measure both on-axis sensitivity (10 kHz–50 kHz) and channel-level beam patterns (15 kHz–50 kHz). The on-axis free-field voltage sensitivity (FFVS) is shown for all eighty channels in Figure 90. The channels are generally well matched, with a few exceptions. The discontinuity in sensitivity at 30 kHz is because the data to cover the band was collected in two separate calibrations. Horizontal and vertical beam patterns measured at 27.5 kHz are provided in Figure 91 for all eighty channels. In this figure, the beam patterns are individually normalized by their peak response. The eight channel hydrophone modules are measured independently, before being integrated into the larger array configuration shown in Figure 17a. This difference will modify the baffling condition for most elements; therefore, the sidelobe structure seen here may not be an exact match for that seen in the field data. Similarly, this effect can be seen in the sidelobe structure deviations in Figure 91 because of the asymmetry in baffling for the individual hydrophone modules. Broadband beam patterns are shown for a single eight channel module in Figure 92. These figures are available for the remaining 72 channels as well, but have been omitted here for brevity.

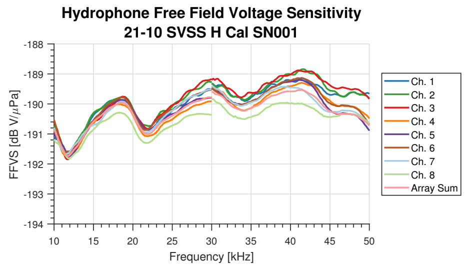

(a)

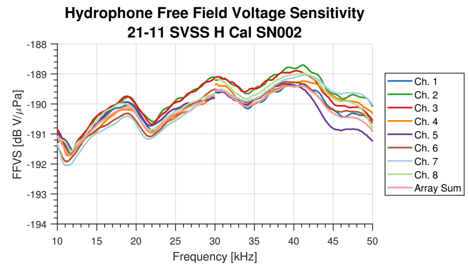

(b)

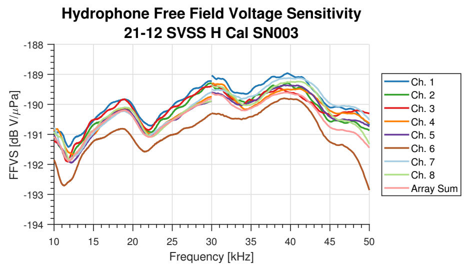

(c)

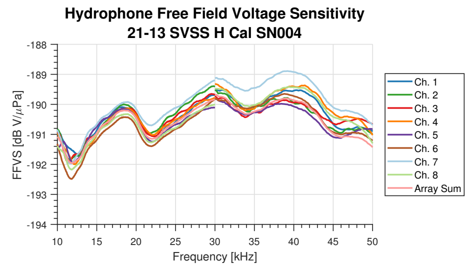

(d)

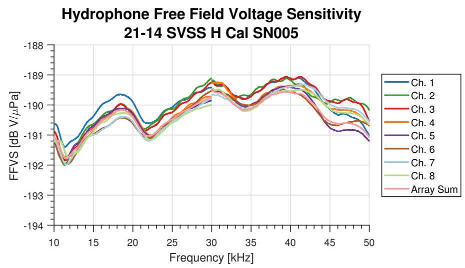

(e)

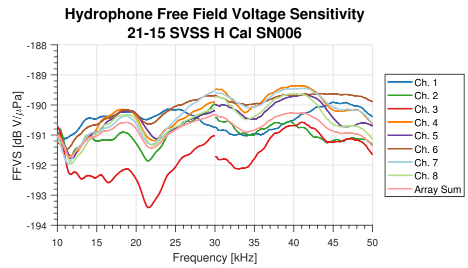

(f)

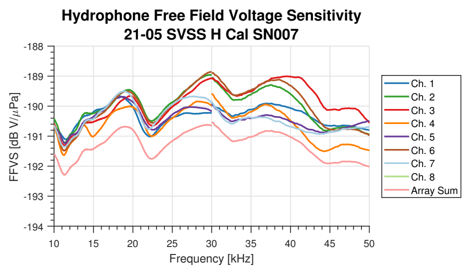

(g)

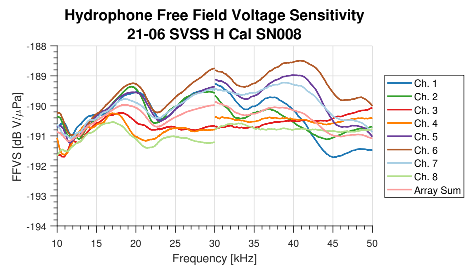

(h)

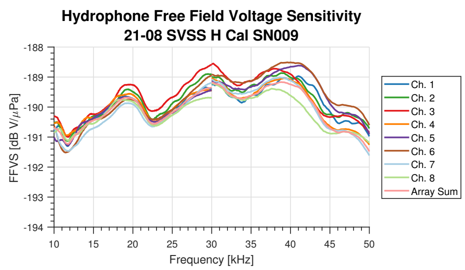

(i)

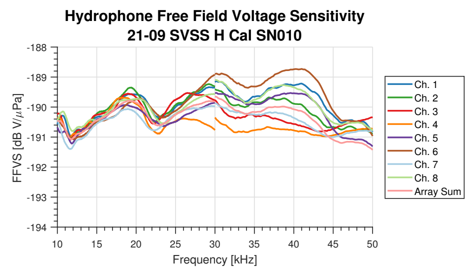

(j)

Figure 90: The FFVS was measured for all eighty receive channels in the ARL/PSU ATF.

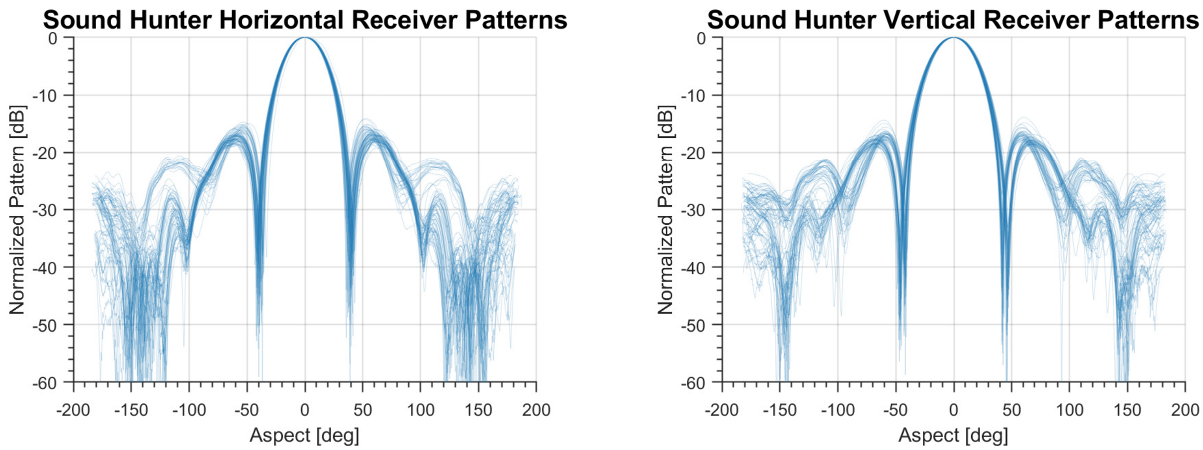

Figure 91: Horizontal (a) and vertical (b) beam patterns are measured at 27.5 kHz for all eighty receive channels.

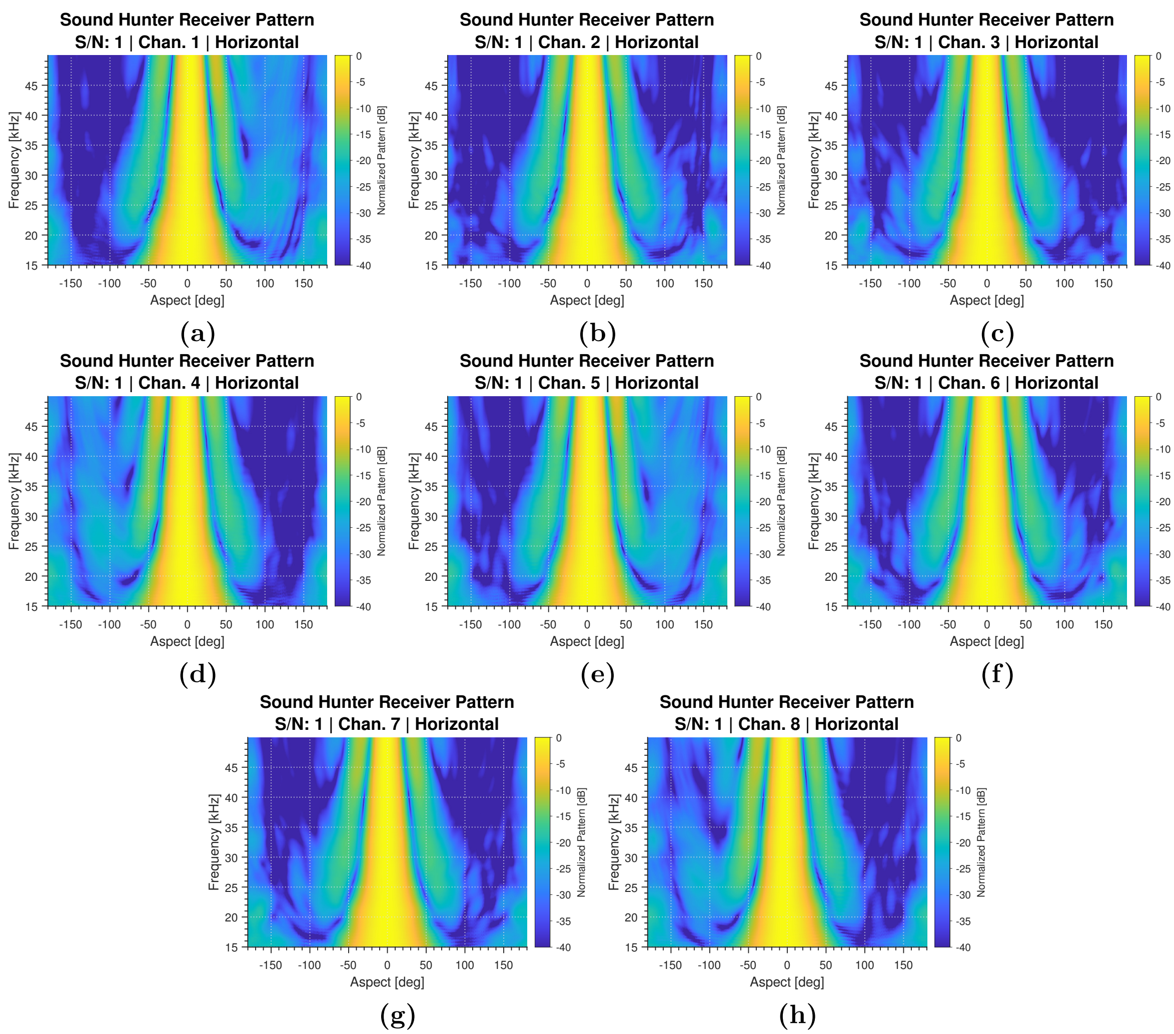

Figure 92: Broadband beam patterns were measured for all eighty receive channels in the ARL/PSU ATF. This figure provides those patterns for the first eight channels in the array.

C Specular Component Modeling

This Appendix describes the calculation for the coherent ("specular") part of the scattered field from a sediment interface. In many geometries and environments, the coherent reflection component is considered negligible and for that reason may not be calculated. However, it can become significant when at least one of the following occurs: the sediment interface is relatively smooth with respect to a wavelength, the sonar transmit/receive geometry is near-normal incidence, and the sonar is relatively close to the interface.

The coherent reflection coefficient, V_{wwc}, is defined as $V_{wwc} = V_{ww} * E$, where V_{ww} is the flat-interface reflection coefficient and E is the Eckart Factor,

$$E = e^{-2k_w^2 h^2 \sin^2(\theta_{Grz})}. \tag{6}$$

k_w is the wavenumber in the water above the sediment and θ_{Grz} is the incident grazing angle where $\theta_{Grz} = 90°$ is normal incidence. The RMS roughness of the surface, h, is calculated as

$$h = \sqrt{\frac{2\pi w_2}{(\gamma_2 - 2)K_L^{(\gamma_2-2)}}}, \tag{7}$$

and replaced an earlier version of the specular reflection coefficient calculation where h was always assumed to be 1 cm, regardless of sediment.

Equation 7 was derived by integrating the 2-D roughness spectrum from the cutoff wavenumber, K_L, to infinity, over an assumed power law distribution with w_2 as the spectral strength and γ_2 as the spectral exponent. The cutoff wavenumber is chosen as $K_L = 1/r_1$ where r_1 is the radius of the first Fresnel zone. The choice to use the first Fresnel zone was made because it approximates the area that will coherently add in phase. The radius of the first Fresnel zone is

$$r_1 = \sqrt{\frac{z_s z_r \lambda}{(z_s + z_r)\sin(\theta_{Grz})}} \approx \sqrt{\frac{z\lambda}{2\sin(\theta_{Grz})}}, \tag{8}$$

where the source height (z_s) and receiver height (z_r) from the seafloor is approximately equal ($z_s \approx z_r \approx z$).

The reflection amplitude is fed through the usual PoSSM calculation pipeline and a single scatterer is used on the sediment interface for each source-receiver pair. The location of the scatterer is chosen such that the incident and reflected angles are equal ($\theta_I = \theta_R$). The distance to the scatterer from the transmitter (R_s) and receiver (R_r) is used to calculate the term for geometric spreading loss as 20 $\log_{10}(R_1 + R_2)$, not as 20 $\log_{10}(R_1 * R_2)$, since the scatterer does not represent a re-radiation of sound but rather a continuation of the original wave. Other terms such as the attenuation and delay of the wave are calculated in the same manner as the usual PoSSM calculation pipeline.

D Bubble Models

This Appendix describes the development of a bubble response model and its implementation within the PoSSM framework. This model allows the simulation of entrapped gas within sediment layers by considering the scattering from individual bubbles and the transmission loss from sound propagation through a bubble layer. Section D.1 describes the formulation and bubble response solution to an arbitrary sonar pulse. Section D.2 describes the calculation of transmission loss from a bubble ensemble.

D.1 Individual Bubble Response

Derivation of the bubble response is a complicated topic that has seen much attention in the literature. Three resources that were helpful in the development of the formulations used here are Medwin and Clay [63], Lyons et al. [59], and Anderson and Hampton [57].

D.1.1 ODE Formulation

The oscillatory response of a bubble at low frequency ($ka \ll 1$) can be described as a classic damped harmonic oscillator. This canonical problem is expressed as a second order ODE as

$$m\frac{\partial^2 y}{\partial t^2} + R_m(t)\frac{\partial y}{\partial t} + sy = f(t), \tag{9}$$

where y is the radial displacement of the bubble surface, $f(t)$ is the forcing function (the incident acoustic plane wave), and m, R_m, and s are the effective mass, resistance, and stiffness, respectively. (See Medwin and Clay [63] for a detailed derivation of these parameters.) Note that the forcing function is written as a function of time because we are considering pulses (not simply continuous sinusoids) as well as complicated waveforms such as tapered amplitude linear frequency modulated (LFM) waveforms. In addition, the resistance term is also a function of time because the damping constant is a function of frequency and the instantaneous frequency can clearly change with time (e.g., LFM) and the bubble can also respond at multiple frequencies simultaneously. The assumption made here is to set the frequency used for the damping calculation as the instantaneous frequency of the driving force, and to set it to the damping at resonance when the forcing function is zero (to allow free decay of bubble oscillations).

Matlab is used to formulate and solve the ODE in Equation (9). It is solved using the `ode45` function, a general purpose solver based on an explicit Runge-Kutta (4,5) formula, the Dormand-Prince pair. This is a single-step solver, which only needs the solution from the immediately preceding time point to calculate the following time point. Initial conditions for radial displacement and velocity must be input, which are assumed to be zero for bubbles in sediment prior to insonification.

The numerical solution to the ODE provides the radial displacement, $y(t)$, and velocity, $y'(t)$, of the surface of the bubble. For a simple source, i.e. $ka \ll 1$, the radiated pressure, p, is

$$p(r,t) = i\rho_s c U_0 (a/r) ka e^{i(\omega t - kr)}, \tag{10}$$

where r is the distance from the center of the source, i is the imaginary unit ($i = \sqrt{-1}$), c is the speed of sound in the medium, and U_0 is the volume velocity of the source (see [64] page 172). When implementing the bubble response model in PoSSM, it handles the terms related to propagation: the geometrical spreading ($1/r$) and the delay due to travel ($e^{i(\omega t - kr)}$) to and from the bubble. We also assume unit amplitude (0 dB) for the plane wave at our bubble, in order to consider the contribution of the scattered pressure field relative to the incident field. Again, this assumption allows the PoSSM framework to account for propagation. The surface area of our bubble, which we assume is a sphere, is $4\pi a^2$. (The assumption of a spherical bubble is generally a good first order approximation, but it does break down for larger bubbles in sediment that tend to be oblate spheroids.) The volume velocity of the source is the surface area of the bubble multiplied by the velocity of the surface, $U_0 = 4\pi a^2 y'$.

From Equation (10), after substitution of $U_0 = 4\pi a^2 y'$ and $k = \omega/c$ and the removal of propagation-related terms, the equation for the radiated pressure from the oscillating bubble is

$$p(t) = 4\pi i \rho_s \omega a^4 y'. \tag{11}$$

Note that multiplication by i adds a phase shift, indicating that the pressure is 90° out of phase with the velocity, but otherwise does not effect the magnitude of the pressure. It is observed that the radiated pressure is proportional to the fourth power of the bubble radius ($p \propto a^4$), indicating that the radiated pressure level is highly dependent on bubble size. Additionally, the radiated pressure is proportional to frequency ($p \propto f$), indicating that for a given bubble size and radial velocity, the radiated pressure will be larger at higher frequencies. As a practical matter, multiplication by ω is accomplished in the frequency domain, since the instantaneous frequency can change with time.

D.1.2 Validation of the Single Bubble Response

We validate our ODE formulation and the resulting radiated pressure using three examples: a bubble undergoing free decay, a bubble with sinusoidal insonification, and by comparison to the scattering cross section equation.

The equation for a bubble's free decay is defined by Equation (9) with $f(t) = 0$. The analytical solution to this ODE for an initial displacement, $y(0) = y_0$, and no initial velocity, $y'(0) = 0$, is solved by MATLAB using the symbolic math toolbox with the following lines of code.

```
syms m Rm s y(t) y0
eqn = m*diff(y, 2) + Rm*diff(y) + s*y == 0;
Dy = diff(y);
cond = [y(0)==y0, Dy(0)==0];
ySol(t) = dsolve(eqn,cond);
```

The result can also be calculated by hand using a trial solution. Medwin and Clay show that the radial displacement is a decaying exponential multiplied by a cosine,

$$y(t) = y_0 e^{-D_b t} \cos(\omega_d t), \tag{12}$$

Table 12: Parameters for a methane bubble in fresh water with a resonance near 27.5 kHz. These parameters are used to generate Figure 93.

Parameter	Symbol	Value
Bubble radius	a	0.12 mm
Density, surrounding fluid	ρ_A	$1000\,\mathrm{kg/m^3}$
Sound speed in water	c	1500 m/s
Gas specific heat ratio	γ	1.31
Gas specific heat, at constant pressure	S_p	2256 J/(kg K)
Gas thermal conductivity	C_g	0.034 W/(m K)
Gas mass density, at 1 atm	ρ_{g0}	$0.717\,\mathrm{kg/m^3}$
Ambient pressure, at bubble depth	p_A	116 000 Pa

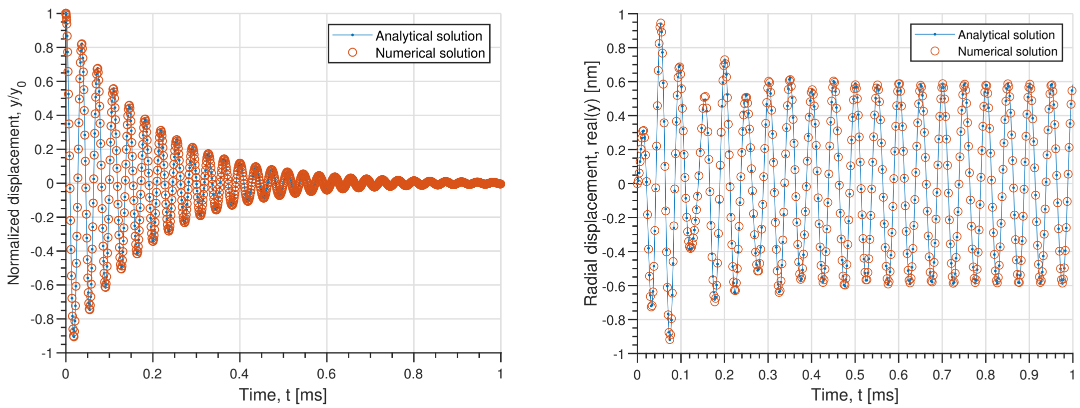

Figure 93: Left: Normalized displacement versus time for the sample bubble described by the parameters in Table 12 with initial conditions $y(0) = y_0$ and $y'(0) = 0$. Right: Response of a bubble with resonance of 27.5 kHz insonified by a continuous 20 kHz sinusoid when starting from rest.

with a damping rate, $D_b = R_m/2m$, and a damped bubble resonance frequency, $\omega_d = 2\pi f_d = \sqrt{\omega_d^2 - D_b^2}$ (see [63] pg 307). Table 12 lists parameters for a sample bubble used to demonstrate that the numerical solver gives the same displacement as the analytical solution.

The left plot in Figure 93 shows the bubble's radial surface displacement versus time, showing free decay. The numerical solution does an excellent job of capturing the bubble's motion.

The equation for a bubble insonified by a continuous sinusoid is defined by Equation (9) with $f(t) = Ae^{i\omega t}$. The analytical solution to this ODE for a bubble starting at rest, i.e., $y(0) = y'(0) = 0$, is again solved by MATLAB using the symbolic math toolbox. A plane wave excitation amplitude of 1 Pa is assumed at the bubble. This amplitude is applied equally over the bubble's surface area, since $ka \ll 1$, resulting in the forcing amplitude,

Table 13: Parameters for a 1 mm radius methane bubble in sediment that are used to generate Figure 94. Sediment properties are representative of soft mud.

Parameter	Symbol	Value
Bubble radius	a	1 mm
Sediment mass density	ρ_s	$1250\,\mathrm{kg/m^3}$
Sound speed in sediment	c_s	1486 m/s
Sound speed in water	c	1500 m/s
Gas specific heat ratio	γ	1.31
Gas specific heat, at constant pressure	S_p	2256 J/(kg K)
Gas thermal conductivity	C_g	0.034 W/(m K)
Gas mass density, at 1 atm	ρ_{g0}	$0.717\,\mathrm{kg/m^3}$
Real part of sediment shear modulus	G	1×10^6 Pa
Imaginary part of sediment shear modulus	G'	1×10^5 Pa
Ambient pressure, at bubble depth	p_A	253 000 Pa

$A = 4\pi a^2 P_{inc} = 4\pi a^2$. The forcing function is then $f(t) = 4\pi a^2 e^{i\omega t}$.

The right plot in Figure 93 shows the radial surface displacement for the sample bubble described by Table 12 when insonified at 20 kHz. The numerical solution properly represents both the transient and steady-state solutions, and again matches the analytical solution. After the initial transient effects the bubble reaches a steady-state solution that is in phase with the driving force. The analytical steady-state amplitude (see [63] page 304) matches the numerical solution.

The scattering cross section (SCS) of a bubble is the magnitude of the bubble response at a given frequency. In the literature the SCS equation is of great importance because often only the magnitude of the bubble response, and not the phase, is of interest to researchers since they are measuring scattered amplitude. Jackson and Richardson (see [3] page 392) state the SCS equation as

$$\sigma(a) = \frac{a^2}{[(\omega_0/\omega)^2 - 1]^2 + \delta^2}, \tag{13}$$

where a is the bubble radius, ω_0 is the bubble's resonance frequency, ω is the insonification frequency, and δ is the damping constant evaluated at ω. Jackson and Richardson also give a plot of the single bubble target strength (defined as $10\log_{10}(\sigma)$) versus frequency for a sample 1 mm radius bubble in sediment (see [3] pages 395-396). Their calculation is used for validation of our model. Table 13 lists the relevant parameter values for this bubble.

Equation (9) is defined using the values in Table 13 and is solved at discrete insonification frequencies. The bubble's radial velocity, calculated by the numerical solver, is evaluated 5 ms after insonification begins in order to determine the steady-state value and avoid transient effects. This velocity is converted to pressure and the pressure is converted to target strength as $20\log_{10}(p)$ to determine the scattered amplitude relative to the insonification amplitude (using a reference amplitude of 1 Pa). Figure 94 shows the calculated target strength for this individual bubble. The numerical solution and the SCS equation give identical results,

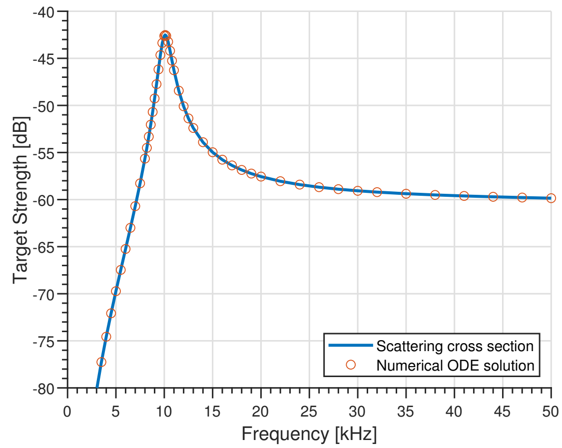

Figure 94: Target strength versus frequency for a 1 mm bubble in sediment with properties described by Table 13. Our model results using the SCS equation and the numerical ODE solution evaluated for single frequency sinusoid insonification matches Figure 14.8 from [3].

which also match Figure 14.8 from [3]. This result, along with those shown above, increases confidence that our bubble response model is valid.

D.1.3 Example Bubble Response to LFM Pulses

Linear frequency modulated (LFM) pulses are used by the SVSS. In this section, insonification by LFMs of two different lengths are used to highlight characteristics of the bubble response. The two LFM chirps are 1 ms ("long") and 0.242 ms ("short") in length, with a center frequency of 25 kHz and a bandwidth of 30 kHz. A relatively large bandwidth was chosen in order to pass through the three regions of bubble response: below, near, and above resonance. The length of the short pulse was chosen to produce an integer number of cycles in the pulse, and is similar in length to the pulse typically used by the SVSS (0.255 ms).

A methane bubble with a 25 kHz resonance frequency in a soft mud sediment is chosen to illustrate properties of bubble response. Table 14 lists the parameters that define this bubble. This bubble and properties are chosen because it is representative of bubbles believed to be present at the Sayers Reservoir test site during the summer of 2019.

Figure 95 displays the spectrogram of the pressure response of the 25 kHz resonant bubble described by Table 14 when subjected to the long (left) and short (right) LFM pulses. The bubble response during the insonification pulse shows the upward diagonal sweep representative of the instantaneous insonification frequency of the LFM, where the amplitude of the response is shaded by the resonant response of the bubble. This is particularly visible in the left plot, and indicates that the bubble has a significant response at the insonification frequency. After the pulse passes through resonance, the spectrogram shows that the bubble responds at multiple frequencies simultaneously: both at the driving frequency and at reso-

Table 14: Parameters for a methane bubble with a 25 kHz resonance in a soft mud sediment. These parameters are used to generate Figure 95.

Parameter	Symbol	Value
Bubble radius, in sediment	a	0.382 mm
Density, sediment	ρ_s	1250 kg/m^3
Sound speed, sediment	c_s	1486 m/s
Real part of sediment shear modulus	G	1×10^6 Pa
Imaginary part of sediment shear modulus	G'	1×10^5 Pa
Bubble depth	z	3 m
Gas specific heat ratio	γ	1.31
Gas specific heat, at constant pressure	S_p	2256 J/(kg K)
Gas thermal conductivity	C_g	0.034 W/(m K)
Gas mass density, at 1 atm	ρ_{g0}	0.717 kg/m^3
Ambient pressure, at bubble depth	p_A	130 700 Pa

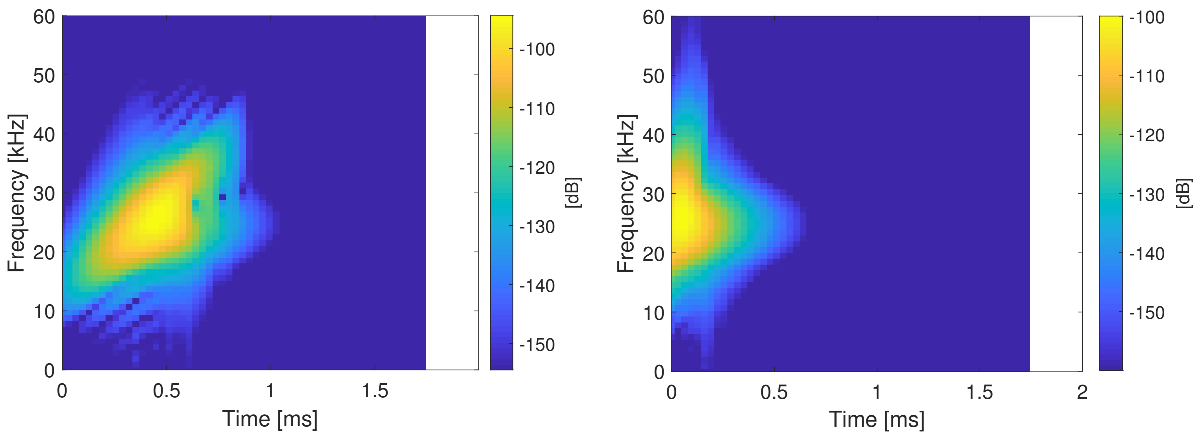

Figure 95: Spectrogram of the pressure response of the 25 kHz resonant bubble in sediment for insonification by the 1 ms (left) and 0.242 ms (right) LFM pulses.

nance. Also, the maximum pressure response occurs after the LFM passes through bubble resonance.

One significant difference between the bubble response to the long and short pulses is that the response to the short pulse is significantly longer than the pulse length. For the long pulse, the bubble's resonant decay occurs mainly during the latter half of the pulse. However, the bubble response to the short pulse is more than two times as long as the short pulse's length, on the 60 dB color scale shown. Since the SVSS uses a relatively short LFM pulse, this justifies the need to include a resonant bubble response when modeling the scattered field from a sediment containing entrapped gas.

D.2 Ensemble Bubble Response

Statistical representations are often used to describe the acoustic response from bubble clouds. However, since we have a computationally efficient framework (PoSSM) to calculate the response from a collection of acoustic point scatterers, we can use brute force to make a realization of a bubble cloud and add up each individual bubble response to determine the ensemble response. Typically this would be computationally expensive (e.g., finite element models with sufficiently small elements) but since PoSSM is GPU-accelerated, calculations for millions of bubbles can now take place in a matter of minutes.

Example bubble distributions were reviewed for ensembles in water (e.g., Boyle and Chotiros [65]) and muddy sediments (e.g., Farmer and Vaigle [66], Lyons et al. [59], and Anderson et al. [62]). After considering these field experiments, a bubble distribution following a power law that is inversely proportional to the fourth power of bubble radius (a^{-4}) was selected for use here. Note that if bubble concentration versus size data was available, this distribution could be updated. In the future, one direct path to gaining this data is to collect test site sediment core samples and perform X-ray micro-computed tomography imaging.

Figure 96 shows a realization of an a^{-4} distribution for a bubble concentration of 0.3% air by volume in a $0.7\,\mathrm{m}^3$ volume. This volume is equivalent to a 2 m x 7 m x 5 cm bubble layer, which is the size of the bubble layer simulated in Section 5.2.2. For this volume and air concentration, tens of millions of bubbles are present, as indicated in Figure 96. However, bubbles only significantly contribute to the ensemble's acoustic response when their resonance frequency is relatively close to the excitation frequency of an acoustic pulse. For this reason, when modeling the acoustic response of the bubble ensemble only a small subset of the ensemble is selected (red squares) for the PoSSM simulation. This dramatically lowers the computational burden, since now less than 2 million bubbles are simulated.

The PoSSM simulation is separated into different models to calculate the acoustic response from different sediments (e.g., mud and clay) and physical phenomena (e.g., volume and interface scattering). The inclusion of bubbles in the simulation necessitates the addition of a model accounting for the bubble scattering. Scatterers are added to the model and given the response kernel based on their properties (e.g., radius, etc.). However, an additional piece of information is needed: the cumulative effect on transmission through the bubble ensemble.

The mud layer in Sayers is relatively thin allowing for the bubbles to be approximated as a screen. Macpherson [67] provides equations for the ensemble response that are applicable when the screen thickness, s, is much less than the wavelength, $s \ll \lambda$. This approximation may not be strictly true at Sayers, but will nonetheless give a good estimate of the ensemble effect.

Macpherson derives equations for the theoretical transmission through and reflection from bubble screens and validates those equations with magnitude and phase measurements in a

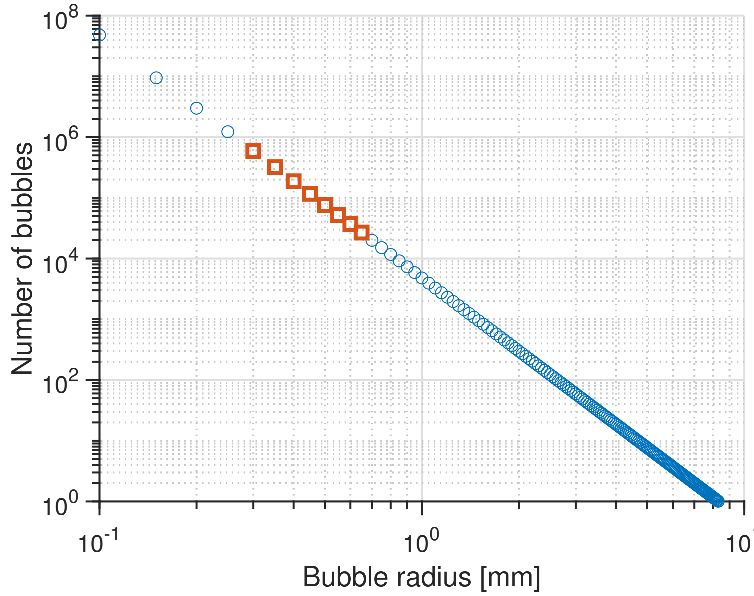

Figure 96: Bubble distribution for a^{-4} that results in 0.3% air by volume for a $0.7\,\mathrm{m}^3$ volume of bubbles. Red squares indicate those bubbles with resonant frequencies near the frequencies of interest (for our 20 kHz–35 kHz LFM) and are selected for use in our simulations.

water tank. The equation derived for the transmitted intensity is

$$T_I = 1 + \frac{K \sec\theta}{\Delta^2 + \delta^2}[K \sec\theta + 2\delta], \tag{14}$$

where $K = \lambda a/xy$, θ is the incident angle, $\Delta = \omega_r^2/\omega^2 - 1$, and δ is the frequency dependent damping constant. Note that λ is the wavelength of the incident wave, a is the bubble radius, x and y are the spacings between bubbles of a 2-D uniform rectangular lattice, ω_r is the radial resonance frequency, and ω is the excitation frequency.

Figure 97 shows the transmission loss of a bubble screen of 30 kHz resonant oxygen bubbles at a density of $4\,\mathrm{bubbles/cm^2}$. The parameters for this calculation were chosen to reproduce Figure 7 in [67]. Overall, the screen acts roughly as a band rejection filter for sound passing through it. The attenuation peaks at the bubble resonance frequency because this is the frequency with the highest bubble interaction. The width of the attenuation peak is dependent on the damping and other bubble properties. Although Macpherson formulates the equation and performs his measurement on a rectangular bubble lattice, the result can be extended to a collection of bubbles with random spacings, given the same equivalent bubble density and under the assumption that multiple scattering (bubble-to-bubble interaction) does not occur. This approximation holds for low bubble concentrations (low air volume fractions).

In natural sediments, an ensemble of bubbles will contain bubbles with a continuous distribution of radii, and therefore a wide frequency resonance. Macpherson shows that for two

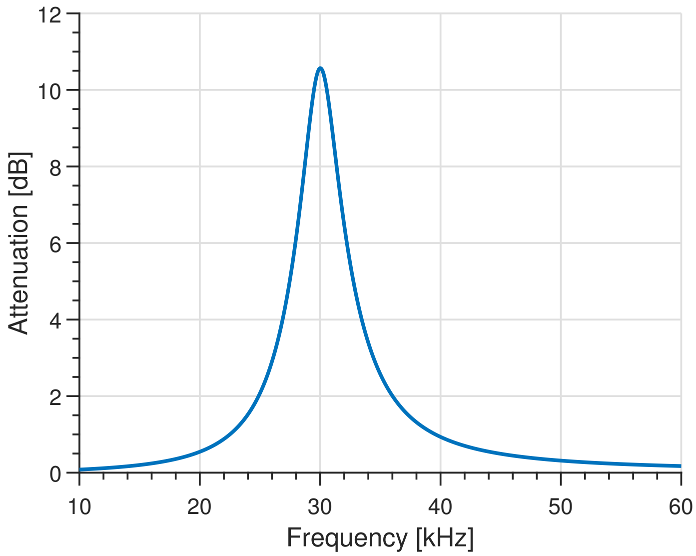

Figure 97: Bubble transmission loss at 0° incidence for an ensemble of 30 kHz resonant bubbles ($a = 0.11$ mm) with a bubble density of 4 bubbles/cm^2.

bubble screens with different bubble sizes the total attenuation is the sum of the two screens' individual responses. Using this result, Figure 98 shows the cumulative effect on the transmission loss of the selected bubble sizes from the bubble distribution shown in Figure 96. Over a limited frequency range, the total transmission loss through the bubble screen can be approximated as a constant (e.g., 9 dB). Note that the approximation of the transmission loss as a constant improves for a real-world bubble cloud since there would be a continuous, not discrete, distribution of bubble radii and resonance frequencies. Also note that when considering scattering beneath a bubble screen, the transmission loss is doubled since the wave passes through the bubble screen twice. For a PoSSM simulation, a loss of $2 * T_I$ is applied to scatterers beneath the bubble screen (e.g., in the clay models). It is clear that even small bubble concentrations (0.3% air by volume) can have dramatic attenuation effects (e.g., 18 dB) and greatly effect acoustic imaging beyond the bubbles.

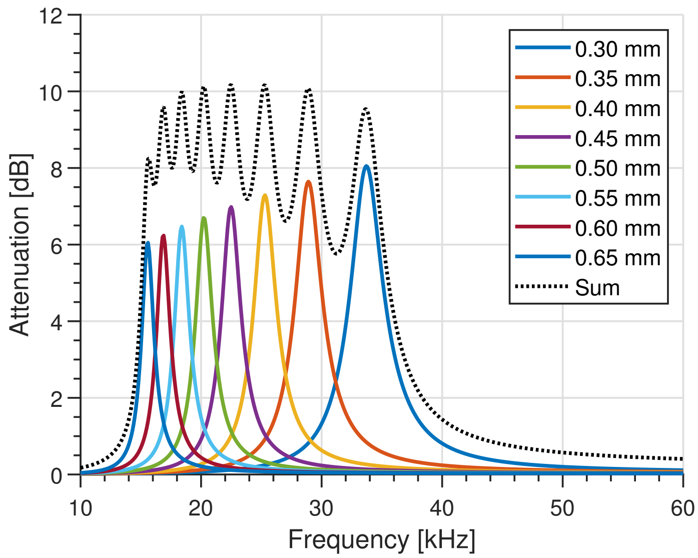

Figure 98: Bubble transmission loss at 0° incidence for the bubble ensemble shown in Figure 96.

E List of Scientific/Technical Publications

Peer Reviewed Articles

1. D. C. Brown, S. F. Johnson, and D. R. Olson, "A point-based scattering model for the incoherent component of the scattered field," *J. Acoust. Soc. Am.*, vol. 141, no. 3, pp. EL210–EL215, 2017.

Technical Reports

1. D. C. Brown, S. F. Johnson, and C. F. Brownstead, "Sediment volume search sonar: Phase 1 technical report," *SERDP Intermediate Report*, no. MR-2545, pp. 1–75, 2017.
2. ——, "Sediment volume search sonar: Phase 2 technical report," *SERDP Intermediate Report*, no. MR-2545, pp. 1–75, 2018.
3. ——, "Aberdeen Test Center experiment test report," *SERDP Intermediate Report*, no. MR-2545, pp. 1–36, 2020.

Conference Proceedings

1. D. P. Williams and D. C. Brown, "New target detection algorithms for volumetric synthetic aperture sonar data," *Proceedings of Meetings on Acoustics*, vol. 40, no. 1, pp. 1–11, Sep. 2020.
2. I. D. Gerg, D. C. Brown, S. G. Wagner, D. Cook, B. N. O'Donnell, T. Benson, and T. C. Montgomery, "GPU acceleration for synthetic aperture sonar image reconstruction," in *MTS/IEEE OCEANS Conf.*, Oct. 2020, pp. 1–9.
3. D. C. Brown, S. F. Johnson, I. D. Gerg, and C. F. Brownstead, "Simulation and testing results for a sub-bottom imaging sonar," *Proceedings of Meetings on Acoustics*, vol. 36, no. 1, pp. 1–12, May 2019.
4. T. E. Blanford, J. D. Park, S. F. Johnson, and D. C. Brown, "Experimental analysis of the effects of bistatic target scattering on synthetic aperture sonar imagery," *Proceedings of Meetings on Acoustics*, vol. 39, no. 1, pp. 1–11, Dec. 2019.
5. S. F. Johnson and D. C. Brown, "SAS simulations with procedural texture and the point-based sonar scattering model," in *MTS/IEEE OCEANS Conf.*, Oct. 2018, pp. 1–7.

Conference Abstracts

1. D. C. Brown, S. F. Johnson, C. F. Brownstead, and Z. G. Lowe, "Suppression of specular interface returns for sub-bottom imaging sonar systems," in *International Conference on Underwater Acoustics*, 2020.
2. J. H. Philtron, D. C. Brown, and S. F. Johnson, "Data-model comparison of a shallow water sonar system for buried UXO detection," in *International Conference on Underwater Acoustics*, 2020.

3. T. E. Blanford, S. F. Johnson, and D. C. Brown, “Experimental analysis of the effects of bistatic target scattering on synthetic aperture sonar imagery,” in *J. Acoust. Soc. Am.*, vol. 146, 2019, p. p. 2798.

4. S. J. Brumbaugh and D. C. Brown, “Design study of a broadband Tonpilz transducer,” in *International Workshop on Acoustic Transduction Materials and Devices*, 2019.

5. T. E. Blanford, D. C. Brown, S. F. Johnson, and C. F. Brownstead, “Sediment volume search sonar,” in *Near Surface Geoscience*, 2018.

6. D. C. Brown, S. F. Johnson, and C. F. Brownstead, “Sediment volume search sonar,” in *Symposium on the Application of Geophysics to Engineering and Environmental Problems*, 2018.

Literature Cited

[1] A. Bellettini and M. Pinto, "Design and experimental results of a 300-kHz synthetic aperture sonar optimized for shallow-water operations," *IEEE J. Oceanic Eng.*, vol. 34, no. 3, pp. 285–293, Jul. 2009.

[2] APL-UW, "APL-UW high-frequency ocean environmental acoustic models handbook," Applied Physics Laboratory - University of Washington, Tech. Rep. TR 9407, Oct. 1994.

[3] D. R. Jackson and M. D. Richardson, *High Frequency Seafloor Acoustics.* Springer, 2007.

[4] SERDP-ESTCP, "SERDP and ESTCP workshop on technology needs for the characterization, management, and remediation of military munitions in underwater environments," *SERDP-ESTCP Workshop Report*, 2007.

[5] ——, "SERDP/Office of Naval Research workshop on acoustic detection and classification of UXO in the underwater environment," *SERDP-ESTCP Workshop Report*, 2013.

[6] ——, "Informal workshop on burial and mobility modeling of munitions in the underwater environment," *SERDP-ESTCP Workshop Report*, 2014.

[7] ——, "SERDP workshop on acoustic detection and classification of munitions in the underwater environment," *SERDP-ESTCP Workshop Report*, 2018.

[8] United States, "Ammunition inspection guide," War Department, Tech. Rep. TM 9-1904, Mar. 1944.

[9] ——, "Army ammunition data sheets: Artillery, ammunition, guns, howitzers, mortars, recoilless rifles, grenade launchers, and artillery fuzes," Headquarters, Department of the Army, Tech. Rep. TM 43-0001-28, Apr. 1994.

[10] S. Schock, A. Tellier, J. Wulf, J. Sara, and M. Ericksen, "Buried object scanning sonar," *IEEE J. Oceanic Eng.*, vol. 26, no. 4, pp. 677–689, 2001.

[11] S. G. Schock and J. Wulf, "Sonar for multi-aspect buried mine imaging," in *MTS/IEEE OCEANS Conf.*, vol. 1, Oct 2002, pp. 479–484 vol.1.

[12] S. G. Schock, J. Wulf, G. Quentin, and J. Sara, "Synthetic aperture processing of buried object scanning sonar data," in *MTS/IEEE OCEANS Conf.*, Sept 2005, pp. 2236–2241 Vol. 3.

[13] S. G. Schock, J. Wulf, and J. Sara, "Imaging performance of BOSS using SAS processing," in *MTS/IEEE OCEANS Conf.*, Sept 2006, pp. 1–5.

[14] R. A. Leasko, "Munitions detection using unmanned underwater vehicles with advanced sensors," *SERDP Interim Technical Report*, 2012.

[15] B. H. Houston, M. Saniga, H. Simpson, Z. J. Waters, D. Amon, E. Williams, T. Yoder, J. A. Bucaro, and A. Sarkissian, "Structural acoustic UXO detection and identification

in marine environments - final report," Naval Research Laboratory, Tech. Rep. MR-2103, May 2016.

[16] K. L. Williams, S. G. Kargl, A. L. Espana, T. Marston, and D. S. Plotnick, "From basic research to a prototype towbody platform: Progress on underwater exploded ordnance remediation," in *Underwater Acoustics Conference and Exhibition*, 2019.

[17] D. C. Brown, S. F. Johnson, and D. R. Olson, "A point-based scattering model for the incoherent component of the scattered field," *J. Acoust. Soc. Am.*, vol. 141, no. 3, pp. EL210–EL215, 2017.

[18] S. Kargl, "Acoustic response of underwater munitions near a sediment interface: Measurement model comparisons and classification schemes," Tech. Rep. MR-2231, Apr. 2015.

[19] D. C. Brown, S. F. Johnson, and C. F. Brownstead, "Sediment volume search sonar: Phase 1 technical report," *SERDP Intermediate Report*, no. MR-2545, pp. 1–75, 2017.

[20] S. F. Johnson and D. C. Brown, "SAS simulations with procedural texture and the point-based sonar scattering model," in *MTS/IEEE OCEANS Conf.*, Oct. 2018, pp. 1–7.

[21] J. C. Curlander and R. N. McDonough, *Synthetic Aperture Radar Sensors and Signal Processing*, J. A. Kong, Ed. New York, NY: John Wiley and Sons, 1991.

[22] J. F. Claerbout, *Imaging the Earth's Interior.* Blackwell Science Inc, 1985.

[23] M. P. Hayes and P. T. Gough, "Synthetic aperture sonar: A review of current status," *IEEE J. Oceanic Eng.*, vol. 34, no. 3, pp. 207–224, Jul. 2009.

[24] R. Rau and J. H. McClellan, "Analytic models and postprocessing techniques for UWB SAR," *IEEE Trans. Aerosp. Electron. Syst.*, vol. 36, no. 4, pp. 1058–1074, Oct 2000.

[25] I. D. Gerg, D. C. Brown, S. G. Wagner, D. Cook, B. N. O'Donnell, T. Benson, and T. C. Montgomery, "GPU acceleration for synthetic aperture sonar image reconstruction," in *MTS/IEEE OCEANS Conf.*, Oct. 2020, pp. 1–9.

[26] E. L. Hamilton, "Compressional-wave attenuation in marine sediments," *Geophysics*, vol. 37, no. 4, pp. 620–646, Aug 1972.

[27] A. J. Hunter and R. van Vossen, "Sonar target enhancement by shrinkage of incoherent wavelet coefficients," *J. Acoust. Soc. Am.*, vol. 135, no. 1, pp. 262–268, 2014.

[28] D. S. Plotnick and P. L. Marston, "Multiple scattering, layer penetration, and elastic contributions to SAS images using fast reversible processing methods," in *European Conference on Synthetic Aperture Radar*, June 2016, pp. 1–3.

[29] J. D. Park, T. E. Blanford, and D. C. Brown, "Late return focusing algorithm for circular synthetic aperture sonar data," *JASA Express Letters*, vol. 1, no. 1, pp. 1–7, 2021.

[30] J. E. Piper, "Buried target detection with a synthetic aperture sonar," in *MTS/IEEE OCEANS Conf.*, vol. 1, Honolulu, HI, Nov. 2001, pp. 220–224.

[31] C. D. Monaco, S. F. Johnson, D. C. Brown, and S. N. Brennan, "Motion estimation from doppler and spatial data in SONAR images," *IEEE Journal of Oceanic Engineering*, pp. 1–10, 2020.

[32] C. Eckart, "The scattering of sound from the sea surface," *J. Acoust. Soc. Am.*, vol. 25, no. 3, pp. 566–570, 1953.

[33] Z. G. Lowe and D. C. Brown, "Multipath reverberation modeling for shallow water acoustics," in *Proc. 11th European Conference on Underwater Acoustics*, Edinburgh, Scotland, Jul. 2012, pp. 1285–1291.

[34] A. D. Pierce, *Acoustics: An introduction to its physical principles and applications.* Melville, NY: Acoustical Society of America, 1991.

[35] R. E. Hansen, H. J. Callow, T. O. Sabo, and S. A. V. Synnes, "Challenges in seafloor imaging and mapping with synthetic aperture sonar," *IEEE Trans. Geosci. Remote Sensing*, vol. 49, no. 10, pp. 3677–3687, Oct 2011.

[36] S. G. Kargl, A. L. España, K. L. Williams, J. L. Kennedy, and J. L. Lopes, "Scattering from objects at a water-sediment interface: Experiment, high-speed and high-fidelity models, and physical insight," *IEEE J. Oceanic Eng.*, vol. 40, no. 3, pp. 632–642, July 2015.

[37] S. G. Kargl, K. L. Williams, and E. I. Thorsos, "Synthetic aperture sonar imaging of simple finite targets," *IEEE J. Oceanic Eng.*, vol. 37, no. 3, pp. 516–532, July 2012.

[38] R. F. Gragg, D. Wurmser, and R. C. Gauss, "Small-slope scattering from rough elastic ocean floors: General theory and computational algorithm," *J. Acoust. Soc. Am.*, vol. 110, no. 6, pp. 2878–2901, 2001.

[39] E. L. Hamilton, "Geoacoustic modeling of the sea floor," *J. Acoust. Soc. Am.*, vol. 68, no. 5, pp. 1313–1340, 1980.

[40] S. Szénási and Á. Tóth, "Solving multiple quartic equations on the GPU using Ferrari's method," in *IEEE 13th International Symposium on Applied Machine Intelligence and Informatics (SAMI2015)*, vol. 7, 2015, pp. 333–337.

[41] IxBlue, *INS Interface Library: MU-INSIII-AN-001*, s ed.

[42] A. W. Doerry, "Catalog of window taper functions for sidelobe control," Sandia National Laboratories, Tech. Rep. SAND2017-4042, 2017.

[43] "AlBeMet property datasheet," Materion Corporation, Tech. Rep. DS-HPP-287.

[44] D. A. Cook and D. C. Brown, "Analysis of phase error effects on stripmap SAS," *IEEE J. Oceanic Eng.*, vol. 34, no. 3, pp. 250–261, Jul. 2009.

[45] H. J. Callow, “Signal processing for synthetic aperture sonar image enhancement,” Ph.D. dissertation, Department of Electrical and Electronic Engineering, University of Canterbury, New Zealand, Apr. 2003.

[46] Q. Koziol and D. Robinson, “HDF5,” [Computer Software] https://doi.org/10.11578/dc.20180330.1, Mar. 2018.

[47] H. Peng, Z. Ruan, F. Long, J. H. Simpson, and E. W. Myers, “V3D enables real-time 3D visualization and quantitative analysis of large-scale biological image data sets,” *Nature biotechnology*, vol. 28, no. 4, p. 348, 2010.

[48] J. W. Wallis and T. R. Miller, “Three-dimensional display in nuclear medicine and radiology.” *Journal of Nuclear Medicine*, vol. 32, no. 3, pp. 534–546, 1991.

[49] T. Borer and A. Cotton, “A “display independent” high dynamic range television system,” British Broadcasting Corporation, Tech. Rep. WHP 309, Sep. 2015.

[50] G. J. Dobeck, “Adaptive large-scale clutter removal from imagery with application to high-resolution sonar imagery,” in *Detection and Sensing of Mines, Explosive Objects, and Obscured Targets XV*, vol. 7664, 2010, pp. 1–10.

[51] D. P. Williams, “The Mondrian detection algorithm for sonar imagery,” *IEEE Trans. Geosci. Remote Sensing*, vol. 56, no. 2, pp. 1091–1102, Feb 2018.

[52] D. P. Williams and D. C. Brown, “New target detection algorithms for volumetric synthetic aperture sonar data,” *Proceedings of Meetings on Acoustics*, vol. 40, no. 1, pp. 1–11, Sep. 2020.

[53] D. A. Abraham, *Underwater Acoustic Signal Processing*. Springer, 2019.

[54] M. Lambers, H. Nies, and A. Kolb, “Interactive dynamic range reduction for SAR images,” *Geoscience and Remote Sensing Letters, IEEE*, vol. 5, no. 3, pp. 507–511, 7 2008.

[55] R. J. Urick, *Principles of Underwater Sound*, 3rd ed. Los Altos, CA: Peninsula Publishing, 1983.

[56] M. Born and E. Wolf, *Principles of Optics*, 7th ed. New York: Cambridge University Press, 1999.

[57] A. L. Anderson and L. D. Hampton, “Acoustics of gas-bearing sediments I. background,” *J. Acoust. Soc. Am.*, vol. 67, no. 6, pp. 1865–1889, 1980.

[58] ——, “Acoustics of gas-bearing sediments II. measurements and models,” *J. Acoust. Soc. Am.*, vol. 67, no. 6, pp. 1890–1903, 1980.

[59] A. P. Lyons, M. E. Duncan, A. L. Anderson, and J. A. Hawkins, “Predictions of the acoustic scattering response of free-methane bubbles in muddy sediments,” *J. Acoust. Soc. Am.*, vol. 99, no. 1, pp. 163–172, 1996.

[60] G. Borrel, D. Jézéquel, C. Biderre-Petit, N. Morel-Desrosiers, J.-P. Morel, P. Peyret, G. Fonty, and A.-C. Lehours, “Production and consumption of methane in freshwater

lake ecosystems," *Research in Microbiology*, vol. 162, no. 9, pp. 832 – 847, 2011, special issue on environmental microbiology.

[61] N. T. Duc, P. Crill, and D. Bastviken, "Implications of temperature and sediment characteristics on methane formation and oxidation in lake sediments," *Biogeochemistry*, vol. 100, no. 1, pp. 185–196, Sep 2010.

[62] A. Anderson, F. Abegg, J. Hawkins, M. Duncan, and A. Lyons, "Bubble populations and acoustic interaction with the gassy floor of eckernförde bay," *Continental Shelf Research*, vol. 18, no. 14, pp. 1807–1838, 1998.

[63] H. Medwin and C. S. Clay, *Fundamentals of Acoustical Oceanography*. Academic Press, 1998.

[64] L. E. Kinsler, A. R. Frey, A. B. Coppens, and J. V. Sanders, *Fundamentals of Acoustics*, 4th ed. John Wiley and Sons, 2000.

[65] F. A. Boyle and N. P. Chotiros, "A model for acoustic backscatter from muddy sediments," *J. Acoust. Soc. Am.*, vol. 98, no. 1, pp. 525–530, 1995.

[66] D. M. Farmer and S. Vagle, "Waveguide propagation of ambient sound in the ocean-surface bubble layer," *J. Acoust. Soc. Am.*, vol. 86, no. 5, pp. 1897–1908, 1989.

[67] J. Macpherson, "The effect of gas bubbles on sound propagation in water," *Proc. Phys. Soc. B*, vol. 70, no. 1, pp. 85–92, 1957.